CHEMIA

STUDIA
UNIVERSITATIS BABEŞ-BOLYAI

CHEMIA

4/2016

S T U D I A

UNIVERSITATIS BABEŞ–BOLYAI

CHEMIA

4

CUPRINS – CONTENT – SOMMAIRE – INHALT

Studia Universitatis Babes-Bolyai Chemia has been selected for coverage in Thomson Reuters products and custom information services. Beginning with V. 53 (1) 2008, this publication is indexed and abstracted in the following:

- Science Citation Index Expanded (also known as SciSearch®)
- Chemistry Citation Index®
- Journal Citation Reports/Science Edition

RADIOCARBON DATING OF A VERY OLD AFRICAN BAOBAB FROM SAVÉ VALLEY, ZIMBABWE

ADRIAN PATRUT[a,*], LASZLO RAKOSY[b], ROXANA T. PATRUT[b], ILEANA-ANDREEA RAŢIU[a], EDIT FORIZS[a], DANIEL A. LOWY[c], DRAGOS MARGINEANU[a], KARL F. VON REDEN[d]

ABSTRACT. The article reports the radiocarbon investigation results of the Humani Bedford baobab, an old African baobab from Savé Valley, Zimbabwe. Two wood samples were collected from the large inner cavity. Several segments were extracted from these samples and analysed by AMS (accelerator mass spectrometry) radiocarbon dating. We found that the age values of segments increase with the distance into the wood. This major anomaly is characteristic to multi-stemmed baobabs with a closed ring-shaped structure and a false cavity inside. The investigation of the Humani Bedford baobab evinced that the baobab consists of three fused stems. The fourth stem of the ring is missing. The oldest dated segment was found to have a radiocarbon date of 1655 ± 14 BP, which corresponds to a calibrated age of 1575 ± 30 yr. The dating results show that the stems which build the ring stopped growing toward the false cavity more than 600 yr ago. By considering the position of the oldest segment in the investigated stem, we concluded that the Humani Bedford baobab is around 1800 yr old. According to our dating results, the Humani Bedford baobab becomes the oldest living African baobab.

Keywords: AMS radiocarbon dating, Adansonia digitata, tropical trees, dendrochronology, age determination.

---

[a] *Babeş-Bolyai University, Faculty of Chemistry and Chemical Engineering, 11 Arany Janos, RO-400028, Cluj-Napoca, Romania.*
[b] *Babeş-Bolyai University, Faculty of Biology and Geology, 44 Gheorghe Bilascu, RO-400015, Cluj-Napoca, Romania.*
[c] *Nova University, 5000 Dawes Ave., Alexandria, VA 22311, U.S.A.,*
[d] *NOSAMS Facility, Dept. of Geology & Geophysics, Woods Hole Oceanographic Institution, Woods Hole, MA 02543, U.S.A.*
* *Corresponding author: apatrut@gmail.com*

INTRODUCTION

The genus *Adansonia* belonging to the Bombacoideae, a subfamily of Malvaceae, consists of nine species. Two species originate from mainland Africa, six are endemic to Madagascar and one can be found in northern Australia [1-4]. The African baobab (*Adansonia digitata* L.), which has a natural distribution in mainland Africa, especially in savanna areas, is the biggest and best-known of the *Adansonia* species [4-8].

In 2005, we started an in-depth research aimed to elucidate several controversial or poorly understood aspects concerning the architecture, growth and age of the African baobab. The research is based on our new approach which enables to investigate and date also standing live specimens. This approach consists of AMS radiocarbon dating of tiny wood samples collected especially from inner cavities, but also from deep incisions/entrances in the stems, fractured/broken stems and from the outer part/ exterior of large baobabs [9-14].

The radiocarbon investigation has revealed very interesting features of the African baobab. Due to the special ability of baobabs to produce stems periodically during their life cycle, over time they develop architectures of increasing complexity. The obtained results have demonstrated that all large baobabs are multi-stemmed. We identified the so-called open and closed ring-shaped structures, which are the most important architectures that enable African baobabs to reach old ages and large sizes. We documented the presence of false cavities, which are large natural empty spaces between fused stems disposed in a closed ring-shaped structure. The oldest dated *A. digitata* individuals were found to have ages up to 2500 years. According to these values, the African baobab becomes the angiosperm with the longest life span [14-16].

One should mention that the identification of very complex architectures and the accurate dating of large and old baobabs are not enabled by traditional dendrochronological methods, which are based on tree-ring investigation [16-19]. Old baobabs have often large cavities, especially in the central area of their trunk/stems. In normal cavities generated by wood removal, the pith/centre of the stem is located inside the cavity. For wood samples collected from normal cavities, ages decrease continuously from the cavity walls toward the outer part of the stem. Our research of large and old baobab specimens identified a major anomaly in the age sequence of samples dated by radiocarbon. In such cases, ages of samples collected from their inner cavities increase from the cavity walls up to a certain distance into the wood, after which they decrease toward the outer part. The only reasonable explanation for this finding is that

such cavities are in fact only natural empty spaces, which were never filled with wood, between several fused stems disposed in a closed ring-shaped structure. We named them false cavities [15, 18].

The closed ring-shaped structures are formed progressively and close over time, as they consist of fused stems which typically are of different ages. The stems grow faster along the outer circumference and each develops a kind of crescent shape, which is necessary for fusing. As already mentioned, false cavities are natural empty spaces between the fused stems that build the closed ring. The first noticeable difference between false and normal cavities is the presence or absence of the bark inside the cavity. While normal cavities become larger over time due to continuous decay, false cavities tend to become smaller due to stem growth [15, 18].

Recently, we documented a new anomaly in the radiocarbon dating results of samples collected from large and/or old baobabs. In several cases, we found that the outermost rings (for samples collected from the outer part) or the innermost rings (for samples collected from false cavities), which were adjacent to the bark, were found to be old, with ages of several hundreds of years, instead of being very young. We named this unexpected phenomenon growth stop. For multi-stemmed baobabs, the growth stop may occur for one, for several or for all stems. We found that the growth stop may be induced by old age, stress, the need to preserve a stable internal architecture and the collapse of stems that survived this event. The baobabs and their stems affected by growth stop may survive for several centuries, continuing to produce leaves, flowers and fruits [19].

Dated growth rings of several studied African baobab specimens, which may act as a proxy climate archive, were used for past climate reconstruction in southern Africa [20-22].

We extended our research on the architecture, growth and age of the *Adansonia* genus by starting to investigate, using the same approach, large individuals of the most representative three Malagasy species, namely the fony baobab (*Adansonia rubrostipa* Jum. & H. Perrier), the za baobab (*Adansonia za* Baill.) and the Grandidier's baobab or Reniala (*Adansonia grandidieri* Baill.) [18, 23, 24]. We found that their characteristic features are similar to those of the African baobab.

The Savé Valley Conservancy is a large wildlife area (3442 km^2), located in the semi-arid South East Lowveld of Zimbabwe at an altitude of 480–620 m, with deciduous woodland savanna, low and variable rainfall and poor-quality soils. The Conservancy comprises multiple properties held by private ranchers, local councils, government and a local community [25]. Savé Valley

hosts thousands of African baobabs, out of which 4 specimens, located all to the north of Turgwe river (in the Matendere, Chishakwe, Mokore and Humani ranches), have very large dimensions (circumference over 23 m) and are well over 1000 years old.

Here we disclose the AMS radiocarbon dating results of the oldest tree of Zimbabwe, i.e., the Humani Bedford old baobab.

RESULTS AND DISCUSSION

The Humani Bedford old baobab and its area. The Humani Bedford old baobab is located in the Bedford Block that was incorporated in 1992 in the Humani ranch (formerly known as Gumani), which is part of the Savé Valley Conservancy, Chiredzi district, Zimbabwe. Somewhat surprisingly, the old baobab was discovered only in 2011 by Roger and Anne Whittall. Its GPS coordinates are 20º24.474' S, 032º14.135' E and the altitude is 432 m. The mean annual rainfall in the area is 457 mm.

The Humani Bedford baobab has a maximum height of 18.2 m, the circumference at breast height (cbh; at 1.30 m above ground level) is 23.65 m and the overall wood volume (trunk and branches, including the cavity) is around 240 m^3 (**Figures 1 and 2**).

Its big trunk has a closed ring-shaped structure, which consists now of three fused stems that close partially a false cavity with the walls completely covered by bark. A fourth stem is missing; it toppled likely more than one century ago, thus opening the false cavity toward the west. We estimate that prior to the collapse of the fourth stem, the baobab had a circumference close to 26-27 m and a total wood volume of around 300 m^3.

The false cavity has a quasi-ellipsodial shape with the axes of 2.59 x 2.70 m at ground level and of 2.54 x 2.98 m at the height of 1.50 m. The maximum height of the cavity was of 6.10 m, but now the roof is completely missing due to the multiple transformations suffered by the tree over time. The opening toward the cavity has a width of 0.70 m at ground level, 1.77 m at 1.30 m and 2.55 m at 2.00 m above the ground. A crocodile bark tree (*Diospyros quiloensis*) grows inside the false cavity (**Figure 3**).

The baobab has very large gnarled and twisted branches, with diametres up to 2.2 m; this is usually an indicative of old age. Several branches are broken or missing. The canopy consists of three distinct units of different heights; its horizontal dimensions are 27.2 x 24.7 m.

Figure 1. General view of the Humani Bedford baobab taken from the west, at the end of the rainy season. In the middle of the trunk one can observe the false cavity which is now opened.

Figure 2. Another general view of the Humani Bedford baobab taken from the north-east.

Figure 3. The false cavity with the crocodile bark tree that grows inside. The cavity has an ellipsoidal shape and its walls are covered by bark.

Wood samples. Several wood samples were extracted from the walls of the inner cavity. Even if the penetration of the borer in the wood was almost complete, the samples were short, revealing that the trunk is mainly hollow. However, two samples (labelled 1 and 2) were considered to be sufficiently long, i.e., 0.195 and 0.250 m, for investigation. The heights of the sampling points were 1.86 and 1.45 m. The two sampling positions are shown in **Figures 4 and 5**. A number of five small pieces/segments, each of the length of 0.001 m (marked as a, b, c), were extracted from determined positions of the two samples. We also extracted a very short sample from the outer part of the same stem (labelled 11), which consisted mainly of the outermost rings. The sampling height was 1.98 m.

AMS results and calibrated ages. Radiocarbon dates of the six segments extracted from the three samples are listed in Table 1. Radiocarbon dates and errors were rounded to the nearest year. The radiocarbon dates are expressed in ^{14}C yr BP (radiocarbon years before present, i.e., before the reference year AD 1950).

Figure 4. Detail of the western flank, also showing the false cavity and the sampling points (marked by 1 and 2). One should remark the very large branches of the Humani Bedford baobab.

Calibrated (cal) ages, expressed in calendar years, are also shown in Table 1. The 1-σ probability distribution was selected to derive calibrated age ranges. For three sample segments, the 1-σ distribution is consistent with only one range of calendar years, while for the other three segments the 1-σ distribution corresponds to two ranges of calendar years. For these segments, the confidence interval of one range is considerably greater than that of the other; therefore, it was selected as the cal AD range of the segment for the purpose of this discussion. For obtaining single calendar age values of sample segments, we derived a mean calendar age of each segment from the selected range (marked in bold). Calendar ages of segments represent the difference between AD 2016 and the mean value of the selected range, with the corresponding error. Calendar ages and errors were rounded to the nearest 5 yr.

Table 1. AMS Radiocarbon dating results and calibrated calendar ages of samples/segments collected from the Humani Bedford baobab.

Sample (Segment) code	Depth[1] [height[2]] (10^{-2} m)	Radiocarbon date [error] (^{14}C yr BP)	Cal AD range 1-σ [confidence interval]	Sample age [error] (cal yr)
1a	0.5 [186]	585 [± 20]	**1398-1417 [68.2%]**	610 [± 10]
1b	19.5 [186]	1375 [± 20]	**658-682 [50.2%]** 746-757 [18.0%]	1345 [± 10]
2a	0.5 [145]	601 [± 18]	**1392-1414 [68.2%]**	615 [± 10]
2b	15.0 [145]	1230 [± 20]	778-810 [26.2%] **843-888 [42.0%]**	1150 [± 20]
2c	25.0 [145]	1655 [± 14]	**410-469 [68.2%]**	1575 [± 30]
11	0.5 [198]	303 [± 22]	1520-1536 [11.5%] **1626-1657 [56.7%]**	375 [± 15]

[1] Depth in the wood from the sampling point.
[2] Height above ground level.

Dating results of samples (segments). The most interesting investigated sample was the longest one, i.e., sample 2, out of which we dated three segments. Two segments, 2b and 2c, were found to have radiocarbon dates greater than 1000 BP. The oldest dated segment 2c originates from a distance of 0.25 m into the wood from the sampling point, which corresponds to the deepest part/end of sample 2. Its radiocarbon date of 1655 ± 14 BP corresponds to a calibrated age of 1575 ± 30 calendar yr. The second oldest segment 2b, which originates from a depth of 0.15 m into the wood, was found to have a radiocarbon date of 1230 ± 20 BP and a calibrated age of 1150 ± 20 yr. The segment 2a corresponds to the innermost rings of the cavity, which were adjacent to the bark that covers the cavity walls. Its radiocarbon date of 601 ± 18 BP corresponds to a calibrated age of 615 ± 10 yr.

We also dated two segments extracted from sample 1. The deepest segment 1b, that originates from a distance of 0.195 m into the wood, had a radiocarbon date of 1375 ± 20 BP. This value corresponds to a calibrated age of 1405 ± 20 yr. The segment 1a, which corresponds to the innermost cavity rings, had a radiocarbon date of 585 ± 20 BP and a calibrated age of 610 ± 10 yr.

The sample/segment 11, which consists of the outermost rings of the same stem, had a radiocarbon date of 303 ± 22 BP and a calendar age of 375 ± 15 yr.

Figure 5. Collecting sample 2 from the eastern wall of the cavity.

Architecture of Humani Bedford baobab. The age values of segments extracted from the two samples collected from the cavity walls of the Humani-Bedford baobab increase with the depth into the wood, as revealed by Table 1. This demonstrates that the Humani-Bedford baobab possesses a closed ring-shaped structure with an accessible false cavity inside.

According to our research on baobabs, the number of fused stems that build the closed ring varies between three and eight. In principle, the number of stems can be determined from the analysis of radiocarbon dates of many samples collected from different areas of the tree, combined with a careful visual inspection of the false cavity, the trunk and the canopy for identifying stems and possible fusion lines [15,16]. In the case of the Humani Bedford baobab, due to the hollow parts inside its trunk and to the elephant damage which has affected constantly the stems over time, the samples were short and their number was insufficient for an accurate determination of the number of stems which build the closed ring. However, after the visual inspection of the baobab and the analysis of photos taken from all directions, we have established

that the Humani Bedford baobab consists of three perfectly fused stems, while a fourth stem which toppled some time ago is missing. The false cavity, which has now a large opening on the western flank, was completely closed prior to the collapse of the fourth stem of the ring.

Age of Humani Bedford baobab. The two dated samples 1 and 2 were extracted from the eastern wall of the false cavity, more precisely from the same stem, which divides into the largest branches. For baobabs with a closed ring-shaped structure, such as the Humani Bedford baobab, the age sequence of samples collected from false cavities exhibits a continuous increase from the cavity walls up to a certain distance into the wood, which corresponds to a point/area of maximum age.

One can state without doubts that the age of the stem with the biggest branches of the Humani Bedford baobab is greater than the age of the oldest dated segment 2c, i.e., 1575 ± 30 yr. This segment corresponds to the deepest end of sample 2, which was continuous and had a length of 0.25 m. In this area, the width of the cavity wall, i.e., the distance from the sampling point 2 to the outer part of the tree is 1.20 m.

The point/area of maximum age, which is the oldest part of a stem, is typically hollow for very old baobabs, as a result of decay; the missing wood corresponds to the first years of life of the respective stem. On the other hand, for baobabs with closed ring-shaped structures, the stems which build the ring grow always faster toward the outer part than in the direction of the false cavity. Consequently, the point of maximum age is always located closer to the cavity than to the outer part.

In the case of the Humani Bedford baobab, the question to be answered is: at what distance is the point of maximum age positioned from sampling point 2 and from the outer part, respectively? For answering this question, we need also to know whether and when the investigated stem stopped growing.

The segment 2a, that consists of the innermost rings of the false cavity, had a calibrated age of 615 ± 10 yr. Meanwhile, the sample/segment 11, which corresponds to the outermost rings of the same stem, was found to be 375 ± 15 yr old. The age of segment 2a shows that the investigated stem of the Humani-Bedford baobab has stopped growing toward the false cavity around 615 yr ago. Our research on baobabs with closed ring-shaped structure has evinced that all stems, which build the ring, stopped growing toward the cavity almost simultaneously, when the false cavity reached a stable internal architecture. This growth stop is necessary for preventing the collapse of the cavity and of the entire ring. The radiocarbon investigation of the Humani-Bedford baobab shows that its stems stopped growing toward the false cavity around AD 1400.

Our previous research has also shown that, after their growth stop toward the cavity, the same stems continue growing toward the outer part, at least for a period of time [15]. The age of sample/segment 11 demonstrates that the investigated stem has continued its growth toward the outer part for almost 250 yr, until AD 1640.

According to the dating results disclosed here, we consider that the point of maximum age in the sampling direction 2 is located at 0.35 – 0.40 m from the cavity walls (sampling point 2) and 0.85 – 0.80 m from the outer part of the stem. Thus, the distance between the oldest dated segment 2c, which originates from a distance of 0.25 m from the cavity walls, and the point of maximum age of the stem, which corresponds to missing wood, was of 0.10 – 0.15 m. By considering both the sample ages and the growth stop, this distance may correspond to 250 – 350 yr of growth. Therefore, we estimate that the investigated stem of the Humani-Bedford baobab has an age of 1800 ± 100 yr and started growing around AD 200.

Over the past decade we investigated and dated almost all very large and potentially old African baobabs around the world. We dated four baobab specimens with sample ages greater than the oldest dated sample of the Humani Bedford baobab. However, all four baobabs toppled or at least their oldest stems died. Therefore, the Humani Bedford baobab is now very likely the oldest living African baobab.

CONCLUSIONS

Our research discloses the AMS radiocarbon investigation results of the Humani Bedford baobab, a very old African baobab from Savé Valley, Zimbabwe. The main aim of the research was to determine the age and the architecture of this baobab. Two wood samples were collected from the walls of the large inner cavity. The age values of the segments extracted from these samples increase with the distance into the wood. This anomalous age sequence is specific to multi-stemmed baobabs having a closed ring-shaped structure with a false cavity inside. Such structures, that enable baobabs to reach large sizes and old ages, consists of several fused stems disposed around a natural empty space which corresponds to the false cavity. The investigation of the Humani Bedford baobab shows that in present it consists of three fused stems, while a fourth stem is missing.

Three segments were found to have radiocarbon dates greated than 1000 BP. The oldest segment had a radiocarbon date of 1655 ± 14 BP, which corresponds to a calibrated age of 1575 ± 30 yr. Dating results also show that the

stems stopped growing toward the false cavity over 600 yr ago, while the investigated stem has continued growing toward the outer part for almost 250 yr. By considering the original position of the oldest dated segment in the investigated stem, we estimate that the Humani Bedford baobab is 1800 yr old and has started growing around 200 BP.

EXPERIMENTAL SECTION

Sample collection. The wood samples were collected with a Haglöf CH 600 increment borer (80 cm long, 0.54 cm inner diametre). A number of five tiny pieces/segments of the length of 0.1 cm were extracted from predetermined positions along the wood samples. The segments were processed and investigated by AMS radiocarbon dating.

Sample preparation. The standard acid-base-acid pretreatment method was used for removing soluble and mobile organic components [26]. The pretreated samples were combusted to CO_2 by using the closed tube combustion method [27]. Then, CO_2 was reduced to graphite on iron catalyst, under hydrogen atmosphere [28]. Finally, the resulting graphite samples were analysed by AMS.

AMS measurements. AMS radiocarbon measurements were performed at the NOSAMS Facility of the Woods Hole Oceanographic Institution (Woods Hole, MA, U.S.A.) by using the Pelletron ® Tandem 500 kV AMS system. The obtained fraction modern values, corrected for isotope fractionation with the normalized $\delta^{13}C$ value of -25 $^0/_{00}$, were ultimately converted to a radiocarbon date.

Calibration. Radiocarbon dates were calibrated and converted into calendar ages with the OxCal v4.2 for Windows [29], by using the SHCal13 atmospheric data set [30].

ACKNOWLEDGMENTS

R E F E R E N C E S

[1]. G.E. Wickens, P. Lowe, "The Baobabs: Pachycauls of Africa, Madagascar and Australia", Springer, Dordrecht, **2008**, pp. 232-234, 256-257, 295-296.

[2]. D.A. Baum, *Annals of the Missouri Botanical Garden*, **1995**, *82*, 440-471.

[3]. J.D. Pettigrew, L.K. Bell, A. Bhagwandin, E. Grinan, N. Jillani, J. Meyer, E. Wabuyele, C.E. Vickers, *Taxon*, **2013**, *61*, 1240-1250.

[4]. G.E. Wickens, *Kew Bulletin*, **1983**, *47*, 173-209.

[5]. J.G. Adam, *Notes Africaines*, **1962**, *94*, 33-44.

[6]. F. von Breitenbach, *Journal of Dendrology*, **1985**, *5*, 1-21.

[7]. T. Pakenham, "The Remarkable Baobab", Weidenfeld & Nicholson, London, **2004**.

[8]. R. Watson, "The African Baobab", Struik, Cape Town, **2007**.

[9]. A. Patrut, K.F. von Reden, D.A. Lowy, A.H. Alberts, J.W. Pohlman, R. Wittmann, D. Gerlach, L. Xu, C. S. Mitchell, *Tree Physiology*, **2007**, *27*, 1569-1574.

[10]. A. Patrut, K.F. von Reden, D.A. Lowy, D.H. Mayne, K.E. Elder, M.L. Roberts, A.P. McNichol, *Nuclear Instruments and Methods in Physics Research Section B*, **2010**, *268*, 910-913.

[11]. A. Patrut, D.H. Mayne, K.F. von Reden, D.A. Lowy, R. Van Pelt, A.P. McNichol, M.L. Roberts, D. Margineanu, *Radiocarbon*, **2010**, *52*, 717-726.

[12]. A. Patrut, D.H. Mayne, K.F. von Reden, D.A. Lowy, S. Venter, A.P. McNichol, M.L. Roberts, D. Margineanu, *Radiocarbon*, **2010**, *52*, 727-734.

[13]. A. Patrut, K.F. von Reden, R. Van Pelt, D.H. Mayne, D.A. Lowy, D. Margineanu, *Annals of Forest Science*, **2011**, *68*, 993-1003.

[14]. A. Patrut, K.F. von Reden, D.H. Mayne, D.A. Lowy, R.T. Patrut, *Nuclear Instruments and Methods in Physics Research Section B*, **2013**, *294*, 622-626.

[15]. A. Patrut, S. Woodborne, K.F. von Reden, G. Hall, M. Hofmeyr, D. Lowy, R.T. Patrut, *PLoS ONE*, **2015**, *10(1)*, e0117193, doi: 10.1371/journal.pone.0117193.

[16]. A. Patrut, S. Woodborne, R.T. Patrut, G. Hall, L. Rakosy, K.F. von Reden, D. Lowy, D. Margineanu, *Studia UBB Chemia*, **2015**, LX, 4, 7-20.

[17]. E.R. Swart, *Nature*, **1963**, *198*, 708-709.

[18]. A. Patrut, R.T. Patrut, P. Danthu, J.-M. Leong Pock-Tsy, L. Rakosy, D.A. Lowy, K.F. von Reden, *PLoS ONE*, **2016**, *11(1)*, e0146977. doi:10.1371/journal.pone.0146977.

[19] A. Patrut, S. Woodborne, K.F. von Reden, G. Hall, R.T. Patrut, L. Rakosy, P. Danthu, J-M. Leong Pock-Tsy, D.A. Lowy, D. Margineanu, *Radiocarbon*, **2016**, doi:10.1017/RDC.2016.92.

[20]. J. Robertson, N.J. Loader, C.A. Froyd, N. Zambatis, I. Whyte, S. Woodborne, *Applied Geochemistry*, **2006**, *21*, 1674-1680.

[21]. S. Woodborne, G. Hall, I. Robertson, A. Patrut, M. Rouault, N.J. Loader, M. Hofmeyr, *PLoS ONE*, **2015**, *10(5)*, e0124202. doi: 10.1371/journal.pone.0124202.

[22]. S. Woodborne, P. Gandiwa, G. Hall, A. Patrut, J. Finch, *PLoS ONE* **2016**, *11(7)*, e015936. doi:10.1371/journal.pone.0159361.

[23]. A. Patrut, K.F. von Reden, P. Danthu, J.-M. Leong Pock-Tsy, R.T. Patrut, D.A. Lowy, *PLoS ONE*, **2015**, *10(3)*, e0121170, doi: 10.1371/journal.pone.012170.

[24]. A. Patrut, K.F. von Reden, P. Danthu, J-M. Leong Pock-Tsy, L. Rakosy, R.T. Patrut, D.A. Lowy, D. Margineanu, *Nuclear Instruments and Methods in Physics Research Section B,* **2015**, *361*, 591-598.

[25]. P. Lindsay, R. du Toit, A. Pole, S. Romanach, Savé Valley Conservancy: A Large-Scale African Experiment in Cooperative Wildlife Management. In: H. Suich, B. Child, A. Spenceley, editors, "Evolution and Innovation in Wildlife Conservation", Earthscan, London, Sterling, VA, **2009**, pp.163-186.

[26]. I.U. Olsson, Radiometric Methods. In: B. Berglung, editor "Handbook of Holocene palaeoecolgy and palaeohydrology", Wiley, Chichester, **1986**, pp. 273-312.

[27]. Z. Sofer, *Analytical Chemistry*, **1980**, *52*, 1389-1391.

[28]. J.S. Vogel, J.R. Southon, D.E. Nelson, T.A. Brown, *Nuclear Instruments and Methods in Physics Research Section B*, **1984**, *5*, 289-293.

[29]. C. Bronk Ramsey, *Radiocarbon*, **2009**, *51*, 337-360.

[30]. A.G. Hogg, Q. Hua, P.G. Blackwell, M. Niu, C.E. Buck, T.P. Guilderson, T.J. Heaton, J.G. Palmer, P.J. Reimer, R.W. Reimer, C.S.M. Turney, R.H. Zimmerman, *Radiocarbon*, **2013**, *55*, 1889-1903.

AFRICAN BAOBABS WITH DOUBLE CLOSED RING-SHAPED STRUCTURES AND TWO SEPARATE FALSE CAVITIES: RADIOCARBON INVESTIGATION OF THE BAOBAB OF GOLCONDA FORT

ADRIAN PATRUT[a],*, ROXANA T. PATRUT[b], LASZLO RAKOSY[b], JENŐ BODIS[a], DANIEL A. LOWY[c], EDIT FORIZS[a], KARL F. VON REDEN[d]

ABSTRACT. The article discloses the results of radiocarbon investigation of the baobab of Golconda Fort, Hyderābād, India, which is the largest African baobab outside Africa. Two wood samples were collected from the large inner cavity; of these we extracted several segments for AMS (accelerator mass spectrometry) radiocarbon dating. The oldest sample segment had a radiocarbon date of 342 ± 22 BP, which corresponds to a calibrated age of 430 ± 20 yr. We estimate that the oldest part of the baobab has an age of 475 ± 50 yr. The investigation of the baobab of Golconda Fort revealed that it consists of 6 + 2 fused stems. Six stems build two rings that close two distinct false cavities, while two additional stems are located outside the rings. We called this new type of architecture double closed ring-shaped structure with two separate false cavities.

Keywords: AMS radiocarbon dating, Adansonia digitata, tropical trees, age determination, inner cavity, multiple stems.

[a] *Babeş-Bolyai University, Faculty of Chemistry and Chemical Engineering, 11 Arany Janos, RO-400028, Cluj-Napoca, Romania.*
[b] *Babeş-Bolyai University, Faculty of Biology and Geology, 44 Gheorghe Bilascu, RO-400015, Cluj-Napoca, Romania.*
[c] *Nova University, 5000 Dawes Ave., Alexandria, VA 22311, U.S.A.*
[d] *NOSAMS Facility, Dept. of Geology & Geophysics, Woods Hole Oceanographic Institution, Woods Hole, MA 02543, U.S.A.*
* Corresponding author: apatrut@gmail.com

INTRODUCTION

The African baobab (*Adansonia digitata* L.), which is the largest and best-known of the nine *Adansonia* species, has a natural distribution in continental Africa between the latitudes 16º N and 26º S. It also found outside Africa, in different areas throughout the tropics, where it was introduced [1-3]. Recent genetic research suggests multiple introduction from different regions of Africa in the Indian subcontinent, possibly extending back to prehistoric times [4].

In 2005, we started a long-term research aimed to clarify several controversial aspects of the architecture, growth and age of the African baobab. Our methodology consists of AMS (accelerator mass spectrometry) radiocarbon dating of small wood samples collected from inner cavities, but also from deep incisions in the stems, fractured stems and from the exterior of large baobabs [5-8]. According to dating results, all large baobabs are multi-stemmed. Radiocarbon investigation of big and old baobabs has demonstrated that their architectures may be very complex. We discovered the open and closed ring-shaped structures, which are the most important architectures that enable African baobabs to reach old ages and large sizes [9,10]. We identified the false cavities, which are large natural empty spaces between fused stems disposed in a closed ring-shaped structure. In a previous work, we described a new version of the closed ring-shaped structure, i.e., baobabs with two closed rings and two interconnected false cavities [11].

Here we describe another kind of closed ring-shaped structure, namely baobabs with two closed rings and two separate false cavities. As a model tree relevant to this type we selected the baobab of Golconda Fort, Hyderābād, India.

RESULTS AND DISCUSSION

The baobab of Golconda Fort and its area. This large baobab is located within the *Naya Qila* (in Hindi, i.e., "New Fort"), an extended area of the medieval Mogul Empire Golconda Fort, a famous citadel and fort, which is considered to be an archaeological treasure of the world. The *Golconda (Golkonda) Fort* (from *Golla Konda* in Telugu, i.e., "Shepherd's Hill") can be found in the metropolitan area of Hyderābād (Greater Hyderābād), the capital of the state Andhra Pradesh, India. The GPS coordinates of the baobab are 17º23.575' N, 078º24.657' E and the altitude is 518 m. Mean annual rainfall in the area is 812 mm.

The historic baobab of Golconda Fort, also called *Hatiyan ka Jhad* (in Hindi, i.e., "Elephant size tree"), has a maximum height of 19.2 m, the circumference at breast height (cbh; at 1.30 m above ground level) is 25.48 m and the overall wood volume (including the false cavitlies) is around 230 m^3 (**Figures 1 and 2**). By these dimensions, the baobab of Golconda Fort is by far the biggest baobab outside Africa.

Figure 1. General view of the baobab of Golconda during the dry season.

The impressive trunk consists of 6 + 2 fused stems. Six stems build the two rings that close two separate false cavities covered by bark. Two additional stems, called the elephant ears, are outside the rings. The largest cavity is accessible via a high somewhat trapezoidal opening, which is positioned at a height of 4.10 m above ground and has diagonals of 0.90 – 1.10 m. This high opening is the upper part of an inclined tube with stairs, which descends into a small antechamber that leads via a door into the cavity. The large false cavity has a quasi-ellipsoidal base, with four axes of 2.66 x 2.93 x 3.45 x 3.48 m, a

height of 4.28 m and a volume of around 20 m^3 **(Figure 3).** The small cavity also has a high opening in the ceiling, at the height of 4.50 m. Because its diametre is only 0.40 m, the access in the second cavity is not possible. This small cavity has a basal diametre of around 1.2 m and an appendix-like extension of 4 x 2 m. The canopy has two distinct units, which correspond to the two rings; its horizontal dimensions are 31.2 x 26.2 m.

Figure 2. The baobab of Golconda with the canopy full of leaves.

Wood samples. Two wood samples (labelled 1 and 2) were collected from the eastern and western walls of the large false cavity, at convenient heights of 1.43 and 1.35 m. The sample lengths were 0.55 and 0.52 m. A number of five small pieces/segments, each of the length of 0.001 m (marked as a, b, c), were extracted from determined positions of the two samples. We also extracted a very short sample from the outer part of the stem with the high opening toward the large cavity (labelled 11), which consisted mainly of the outermost rings. The sampling height was 1.40 m.

Figure 3. View from top to bottom of the largest false cavity of the baobab of Golconda, which is defined by 4 stems. One can remark the typical rounded ceiling. Humans had used it for decades as a shelter.

AMS results and calibrated ages. Radiocarbon dates of the six segments extracted from the three samples are displayed in Table 1. Radiocarbon dates and errors were rounded to the nearest year. The radiocarbon dates are expressed in ^{14}C yr BP (radiocarbon years before present, i.e., before the reference year AD 1950).

Table 1. AMS Radiocarbon dating results and calibrated calendar ages of samples/segments collected from the baobab of Golconda.

Sample (Segment)	Depth[1] [height[2]] (10^{-2} m)	Radiocarbon date [error] (^{14}C yr BP)	Cal AD range 1-σ [confidence interval]	Sample age [error] (cal yr)
1a	0.5 [143]	–	–	>Modern
1b	30 [143]	240 [± 24]	**1646-1665 [50.8%]** 1785-1794 [17.4%]	360 [± 30]
1c	55 [143]	342 [± 22]	1490-1524 [23.5%] **1558-1602 [30.3%]** 1601-1631 [14.4%]	435 [± 20]
2a	0.5 [135]	–	–	>Modern
2b	52 + x [135]	338 [± 22]	1494-1524 [21.7%] **1558-1602 [33.9%]** 1615-1631 [12.6%]	435 [± 20]
11a	0.5 [140]	–	–	>Modern

[1] Depth in the wood from the sampling point.
[2] Height above ground level.

Calibrated (cal) ages, expressed in calendar years, are also presented in Table 1. The 1-σ probability distribution was selected to derive calibrated age ranges. For two sample segments, the 1-σ distribution is consistent with three ranges of calendar years, while for one segment it corresponds to two ranges of calendar years. For these segments, the confidence interval of one range is considerably greater than that of the other(s); therefore, it was selected as the cal AD range of the segment for the purpose of this discussion. For obtaining single calendar age values of sample segments, we derived a mean calendar age of each segment from the selected range (marked in bold). Calendar ages of segments represent the difference between AD 2016 and the mean value of the selected range, with the corresponding error. Calendar ages and errors were rounded to the

nearest 5 yr. For three segments, ages fall after AD 1950 (0 BP), namely the ^{14}C activity, expressed by the ratio $^{14}C/^{12}C$, is greater than the standard activity in the reference year 1950. Such values correspond to negative radiocarbon dates and are termed greater than Modern (>Modern). In these cases, the dated wood is young, being formed after AD 1950.

Dating results of samples (segments). We extracted and dated three segments from sample 1, which was continuous/unbroken. The deepest and oldest segment 1c, which was also the sample end, originates from a distance of 0.55 m from the sampling point. Its radiocarbon date of 342 ± 22 BP corresponds to a calibrated age of 435 ± 20 calendar yr. The segment 1b, originating from a distance of 0.25 m into the wood, had a radiocarbon date of 240 ± 24 BP and a calibrated age of 435 ± 20 yr. Two segments were extracted and dated from sample 2, which was 0.52 m long; given that sample 2 was broken, it consisted of three parts. The sample end 2b, corresponding to a distance of (0.52 + x) m into the wood (where x = length of the two missing parts from sample 2), had a radiocarbon date almost identical with that of segment 1c, i.e., 338 ± 22 BP, and a calibrated age of 435 ± 20 yr. The ages of three segments, which consist of the innermost rings (for 1a and 2a) and outermost rings (for 11), fall after AD 1950. These values demonstrate that the corresponding stems continued growing toward the interior and exterior at least for a time period after 1950.

Architecture of the baobab of Golconda Fort. The large trunk has a kind of irregular platform at the height of 4.0 – 4.5 m, where the openings toward the two cavities are located and from where the tree can be inspected. From this platform we counted the stems, which still show some obvious fusion lines. We found that there are six stems which build the two rings, while two other younger stems are outside the rings. The two separate false cavities are both covered by bark. The first false cavity is defined by four stems and the second cavity by three stems, while one stem is shared by both cavities. For the two samples collected from the largest cavity, the age values of segments increase with the depth into the wood; this anomaly is characteristic only to false cavities [10-16]. We called this new type of baobab architecture double closed ring-shaped structure with two separate false cavities.

Age of the baobab of Golconda Fort. For baobabs with closed rings, the age sequence of samples collected from false cavities shows a continuous increase from the cavity walls up to a certain distance into the wood, which corresponds to a point/area of maximum age [10,11]. It is obvious that the age of the oldest part of the baobab must be greater than the age of the oldest dated sample(s), i.e., 435 ± 20 yr. The lengths of the two samples collected from the largest false cavity, namely 0.55 and 0.52 m, were considerably shorter

than the increment borer (0.80 m), revealing that both samples end in hollow parts. The width of the cavity walls is between 1.40-1.60 m for the western wall (sample 1) and is unknown for the eastern wall (sample 2). These data suggest that the end of sample 1 is relatively close to the point of maximum age. Therefore, we believe that in this point, which is hollow, the age would be of around 450 – 500 yr. By also considering the errors, we estimate that the age of the western stem of the largest cavity, which could be one of the oldest, is 475 ± 50 yr. According to the shape and dimensions of stems and cavities, we also estimate that the six stems which build the two rings have close ages, probably between 400 – 500 yr. On the other hand, the two stems outside the rings, the so-called elephant ears, must be younger. The ages of samples 1b and 1c, namely 435 and 360 yr, demonstrate that the western stem of the large cavity grew very fast when it was young, i.e., by 0.25 m toward the cavity in 75 yr, after which it grew by only 0.30 m over the next 360 yr.

CONCLUSIONS

The research reports the AMS radiocarbon investigation of the largest African baobab outside Africa, i.e., the baobab of Golconda Fort, Hyderābād, India. Two wood samples were collected from the walls of the largest inner cavity. The age values of segments extracted from these samples increase with the distance into the wood, showing an anomaly which is specific to false cavities. The oldest segment had a radiocarbon date of 342 ± 22 BP and a calibrated age of 430 ± 20 yr. We estimate that the big baobab has an age of 475 ± 50 yr and was planted outside the old Golconda Fort around AD 1540. Naya Quila was built more than a century later, in 1656. Our investigation has identified a new type of the closed ring-shaped structure, which was called double closed ring-shaped structure with two separate false cavities. The baobab of Golconda Fort consists of eight stems. Six stems build the two rings with two false cavities inside.

EXPERIMENTAL SECTION

Sample collection. Sample preparation. *AMS measurements*. See our first article in this issue [17].

Calibration. Radiocarbon dates were converted into calendar ages with OxCal v4.2 for Windows [18], using the IntCal13 atmospheric set [19].

ACKNOWLEDGMENTS

R E F E R E N C E S

[1]. G.E. Wickens, P. Lowe, "The Baobabs: Pachycauls of Africa, Madagascar and Australia", Springer, Dordrecht, **2008**, pp. 232-234, 256-257, 295-296.
[2]. D.A. Baum, *Annals of the Missouri Botanical Garden*, **1995**, *82*, 440-471.
[3]. J.D. Pettigrew, L.K. Bell, A. Bhagwandin, E. Grinan, N. Jillani, J. Meyer, E. Wabuyele, C.E. Vickers, *Taxon*, **2013**, *61*, 1240-1250.
[4]. K.L. Bell, H. Rangan, C.A. Kull, D. Murphy, R. Soc. Open Sci., 2015, 2(9): 150370. doi: 10.1098/rsos.150370.
[5]. A. Patrut, K.F. von Reden, D.A. Lowy, A.H. Alberts, J.W. Pohlman, R. Wittmann, D. Gerlach, L. Xu, C. S. Mitchell, *Tree Physiology*, **2007**, *27*, 1569-1574.
[6]. A. Patrut, D.H. Mayne, K.F. von Reden, D.A. Lowy, R. Van Pelt, A.P. McNichol, M.L. Roberts, D. Margineanu, *Radiocarbon*, **2010**, *52*, 717-726.
[7]. A. Patrut, D.H. Mayne, K.F. von Reden, D.A. Lowy, S. Venter, A.P. McNichol, M.L. Roberts, D. Margineanu, *Radiocarbon*, **2010**, *52*, 727-734.
[8]. A. Patrut, K.F. von Reden, R. Van Pelt, D.H. Mayne, D.A. Lowy, D. Margineanu, *Annals of Forest Science*, **2011**, *68*, 993-1003.
[9]. A. Patrut, K.F. von Reden, D.H. Mayne, D.A. Lowy, R.T. Patrut, Nuclear *Instruments and Methods in Physics Research Section B*, **2013**, *294*, 622-626.
[10]. A. Patrut, S. Woodborne, K.F. von Reden, G. Hall, M. Hofmeyr, D. Lowy, R.T. Patrut, *PLoS ONE*, **2015**, *10(1)*, e0117193, doi: 10.1371/journal.pone.0117193.
[11]. A. Patrut, S. Woodborne, R.T. Patrut, G. Hall, L. Rakosy, K.F. von Reden, D. Lowy, D. Margineanu, *Studia UBB Chemia*, **2015**, LX, 4, 7-20.
[12]. S. Woodborne, G. Hall, I. Robertson, A. Patrut, M. Rouault, N.J. Loader, M. Hofmeyr, *PLoS ONE*, **2015**, *10(5)*, e0124202. doi: 10.1371/journal.pone.0124202.
[13]. S. Woodborne, P. Gandiwa, G. Hall, A. Patrut, J. Finch, *PLoS ONE* **2016**, *11(7)*, e015936. doi:10.1371/journal.pone.0159361.
[14]. A. Patrut, K.F. von Reden, P. Danthu, J.-M. Leong Pock-Tsy, R.T. Patrut, D.A. Lowy, *PLoS ONE*, **2015**, *10(3)*, e0121170, doi: 10.1371/journal.pone.012170.
[15]. A. Patrut, K.F. von Reden, P. Danthu, J-M. Leong Pock-Tsy, L. Rakosy, R.T. Patrut, D.A. Lowy, D. Margineanu, *Nuclear Instruments and Methods in Physics Research Section B,* **2015**, *361*, 591-598.

[16]. A. Patrut, R.T. Patrut, P. Danthu, J.-M. Leong Pock-Tsy, L. Rakosy, D.A. Lowy, K.F. von Reden, *PLoS ONE*, **2016**, *11(1)*, e0146977. doi:10.1371/journal.pone.0146977.
[17]. A. Patrut, L. Rakosy, R.T. Patrut, I.A. Ratiu, E. Forizs, D.A. Lowy, D. Margineanu, K.F. von Reden, *Studia UBB Chemia*, **2016**, LXI, 4, 7-20.
[18]. C. Bronk Ramsey, *Radiocarbon*, **2009**, *51*, 337-360.
[19]. P.J. Reimer, E. Bard, A. Bayliss, J.W. Beck, P.G. Blackwell, C. Bronk Ramsey, C.E. Buck, H. Cheng, R. Lawrence Edwards, M. Friedrich, P.M. Grootes, T.P. Guilderson, H. Haflidason, I. Hajdas, C. Hatté, T.J. Heaton, D.L. Hoffmann, A.G. Hogg, K.A. Hughen, K.F. Kaiser, B. Kromer, S.W. Manning, M. Niu, R.W. Reimer, D.A. Richards, E.M. Scott, J.R. Southon, R.A. Staff, C.S.M. Turney, J. van der Plicht, *Radiocarbon*, **2013**, *55*, 1869-1887.

ISOTOPIC COMPOSITION INFLUENCE OF IRRIGATION WATER ON SOME AROMATIC PLANTS

ROMULUS PUŞCAŞ[a], DANA ALINA MAGDAS[a], ILDIKO LUNG[a], GABRIELA CRISTEA[a*], MARIA LOREDANA SORAN[a], IOANA FEHER[a], ADRIANA DEHELEAN[a]

ABSTRACT. In this paper, three species of aromatic herbs (*Petroselinum crispum*, *Ocimum basilicum*, and *Origanum vulgare)* were investigated, by mean of stable isotopes (deuterium, oxygen and carbon) and total phenol content, in order to study the influence of irrigation water. The results revealed the fact that there is a strong correlation between the isotopic compositions of irrigation water (deuterium enriched water or tap water) and δD, $\delta^{18}O$, $\delta^{13}C$ values and total polyphenol content of studied plants. Multielemental content was subjected to analysis of variance (ANOVA). It was found that *Ocimum basilicum* plant was characterized by a higher level of As and Co as compared to other two species, while *Origanum vulgare* had the highest content of Cu. Also, a correlation between the irrigation water content and toxic metal uptake had shown that the Pb concentration is influenced by the water isotopic composition.

Keywords: *irrigation water, aromatic herbs, stable isotopes, total polyphenols, chemometrics.*

INTRODUCTION

Commonly found in edible as well as inedible plants, polyphenolic compounds have been reported to have numerous biological effects, such as antioxidant activity [1]. Herbs are used in many domains, including medicine, nutrition, flavoring, beverages, dyeing, repellents, fragrances, cosmetics [2]. Numerous species have been identified as having medicinal properties as well as

---

[a] *National Institute for Research and Development of Isotopic and Molecular Technologies, 67-103 Donat Str., 400293, Cluj-Napoca, Romania,*
[*] *Corresponding author: gabriela.cristea@itim-cj.ro*

a valuable impact on health, e.g. antioxidant activity, digestive stimulation action, anti-inflammatory, antimicrobial, hypolipidemic, antimutagenic effects and anticarcinogenic potential [3-4]. Raw extracts of herbs and spices, and other plant materials abundant in phenolics provide a high concern in the food industry due to the fact that they decelerate oxidative degradation of lipids and therefore enhance the quality and nutritional value of food.

Recently, medicinal plants have drawn an interest against oxidative stress. The existence of different natural antioxidants in herbs is known. Phenolic compounds, like flavonoids, can give away oxygen to the damaging free radicals to avoid the oxidative damage at the first initiation step. They are not roaming radicals, but constraining their genesis [5]. Parsley (*Petroselinum crispum*) is a widely known culinary plant and medicinal herb used in Europe since ancient times. Many biological activities are associated to its leaf and seed, and it is easy to grow. Consuming the leaf is beneficial to cardiovascular and diabetic diseases due to its anti-hyperglycemic, anti-inflammatory and anti-hyperlipidimic properties [6]. The conveniences are primarily related to the flavonoids and their antioxidant activity but the synergistic effect of all chemicals is important in the therapy [7-9]. Flavonoids are a varied group of polyphenolic compounds with diversified health effects.

On the other hand, it is of major interest to establish the levels of some metallic elements in common used plants, because at elevated levels, these metals could be toxic [10-11]. Determination of metals in aromatic plants is a part of quality control to establish their purity, safety and efficacy according to the World Health Organization (WHO). Although several attempts have been reported for determination of elemental content of aromatic plants from all over the world, but reports of aromatic plants irrigated with different type water (especially, tropical water) are scanty.

In this preliminary study three species of aromatic herbs, commonly used in cooking, were chosen as follows: *Petroselinum crispum, Ocimum basilicum* and *Origanum vulgare.*

Petroselinum crispum variety moss curled 2 (curly parsley) and *Petroselinum crispum classic* (parsley) – Parsley, including both leaf and root type, is a Mediterranean plant, member of the *Umbelliferae* family. *Ocimum basilicum* (basil), originating in tropical Asia is a classic culinary herb of Mediterranean and Southeast Asian cuisines, from *Lamiaceae* family. Many cultivars exist, selected for fragrance, flavor, color and size. *Origanum vulgare* (oregano) is an herb of the family *Lamiaceae*, too. Oregano is native to the mountainous parts of Mediterranean region and warm-temperate regions of Eurasia. All these plants are widely cultivated commercially and in kitchen gardens, having culinary and therapeutically properties.

The aim of this paper was the study of the irrigation water influence, having different isotopic content, on the isotopic composition (deuterium, oxygen and carbon), total polyphenol, essential nutrients, heavy metals and some rare earth content of the investigated aromatic herbs.

Previously studies regarding the influence of water isotopic content on living organisms were mainly related to the use of depleted water in cancer treatment. It was observed, that the use of deuterium depleted water in cancer treatment indicated a decrease of tumor sizes [12-13]. Also, the influence of depleted water and/or enriched water in studies regarding the plant growth indicated a direct relationship between isotopic composition of irrigated water and plant metabolic process [14-16].

RESULTS AND DISCUSSION

Stable isotope analysis

The δD and $\delta^{18}O$ values of leaf water were enriched in deuterium and oxygen-18 relative to the isotopic composition of irrigation water for both groups of aromatic herbs, (Table 1). Generally, the deuterium source for plants is irrigation water. This is taken through roots and moves upward in the xylem to the leaves. The transpiration process from plant leaves leads the fractionation of xylem water. As a result, leaf water is often considerably enriched in deuterium [20].

Table 1. Isotopic compositions of plants samples

Group no.	Plant leaf	$\delta D_{irrigation}$ water (‰)	$\delta^{18}O_{irrigation}$ water (‰)	δD (‰)	$\delta^{18}O$ (‰)	$\delta^{13}C$ (‰)
I	Petroselinum crispum classic	-16.3	-1.2	1.5	11.1	-32.8
	Petroselinum crispum variety moss curled			1.1	10.8	-33.4
	Ocimum basilicum			5.3	13.8	-35.9
	Origanum vulgare			-1.5	6.3	-34.6
II	Petroselinum crispum classic	-70.6	-10.2	-22.0	2.3	-32.2
	Petroselinum crispum variety moss curled			-22.6	2.1	-33.2
	Ocimum basilicum			-13.2	5.9	-34.9
	Origanum vulgare			-25.1	1.3	-34.4

The differences observed between the two parsley varieties (*Petroselinum crispum classic* and *Petroselinum crispum* variety moss curled), within the same group, fit in experimental errors. Instead, isotopic differences were observed between the plants watered with water having different isotopic compositions, by nearly 20 ‰ for δD and 8 ‰ for $δ^{18}O$, due to the used irrigation water.

The most important isotopic difference, caused by the irrigation water, was observed for the *Origanum vulgare* of nearly 23 ‰ for δD, and 8 ‰ for $δ^{18}O$ for *Ocimum basilicum*, and the smallest isotopic difference was about 18 ‰ in the case of δD, for *Ocimum basilicum*, and of 5 ‰ in terms of $δ^{18}O$ for *Origanum vulgare*.

The differences between the δD and $δ^{18}O$ isotopic values of the irrigation water and the water extracted from the studied plants leaves are very well highlighted in both groups. Compared to the irrigation water, the most significant difference in the heavy isotopes of oxygen and hydrogen was recorded in group II for the *Ocimum basilicum* leaf, the isotopic enrichment being up to 57.4 ‰ for δD, and 12.7 ‰ for $δ^{18}O$. For the first group, this enrichment of leaf water is about 21.6 ‰ for δD and 15 ‰ for $δ^{18}O$. The smallest difference was recorded for the *Origanum vulgare* leaf in group II, having values of 45.5 ‰ for δD and 11.5 ‰ for $δ^{18}O$, and 14.8 ‰ for δD and 7.5‰ for $δ^{18}O$ in group I, respectively. These differences of the δD and $δ^{18}O$ isotopic values between the irrigation water and the water extracted from the leaves are caused most likely by the morphology of the leaf.

The isotopic composition of carbon is not significantly influenced by the isotopic composition of the irrigation water, but is directly related to the studied plant species. Thus, the differences recorded for the same type of plant belonging to group I or II, the maximum difference recorded was 1 ‰, while between different species (parsley and basil) the difference may reach 3 ‰. This fact confirms that $δ^{13}C$ is a better indicator for plant species, reflecting much less the isotopic composition of the irrigation water.

Total polyphenols analysis

Total polyphenols content from the studied plants was analyzed by the conventional spectrophotometric Folin-Ciocalteu method. The content in polyphenolic compounds was proportional with the intensity of the blue color. The quantities of the total polyphenols (Figure 1), expressed as mg gallic acid/g fresh weight (FW) was calculated using the linear equation of the standard calibration curve:

$$y = 3.296\,x + 0.0137\ (R^2 = 0.9987) \tag{1}$$
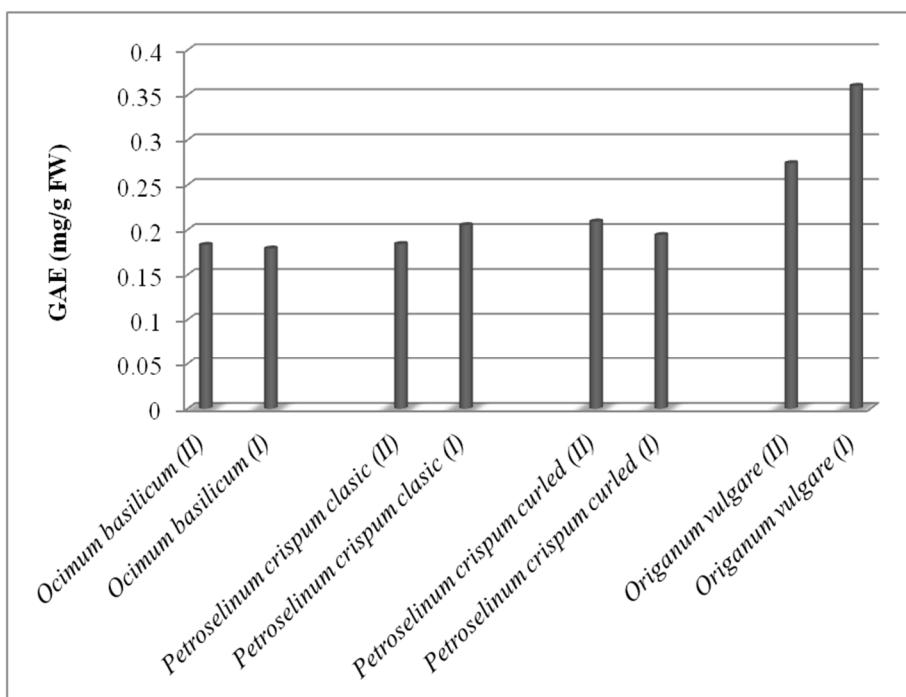
Figure 1. Total polyphenols content expressed as gallic acid
equivalents in the studied plants**.**

It was observed that the amount of total polyphenols increases in some plants when they are watered with tropical water, while in other plants this quantity decreases. Thus, the amount of the total polyphenols increases in parsley and oregano and in the case of basil and curly parsley the amount of total polyphenols decreases in plant watered with tropical water compared with control plants group. The amount of polyphenols in irrigated plants with tropical water increased by 11.41 % in parsley, with 31.39 % in oregano, while in basil and curly parsley decreased by 2.02 %, respectively 1.95 % compared to control plants group.

ICP-MS analysis

The concentrations of some essential plant nutrients (P, K, Mg, Na, Fe, Mn, Cu, Zn) and toxic heavy metals (Co, Cd, Cr, Ni, Pb, As, Al, In) and some rare earth elements of plant species under investigation are presented in Table 2, 3 and 4, respectively. The obtained results are presented as mean ± standard deviation.

Table 2. The concentrations of nutrients in the investigated plants

Nutrient element [mg/kg]	*Petroselinum crispum* classic	*Petroselinum crispum* variety moss curled 2	*Ocimum basilicum*	*Origanum vulgare*
	Group I			
Na	263.58±10.33	109.05±2.78	128.70±3.54	343.90±22.54
Mg	2689.96±95.63	919.13±32.25	2080.75±59.44	1657.03±58.09
P	6156.75±161.94	3586.04±72.89	3351.51±236.96	4599.10±163.30
K	31458.43±1648.80	33792.30±1724.57	38572.32±1368.98	16187.87±527.26
Mn	67.31±1.76	57.40±0.79	36.55±2.52	20.78±1.60
Fe	55.10±1.54	74.78±4.31	73.09±8.12	61.69±10.30
Cu	7.39±0.11	8.13±0.39	9.90±0.68	18.22±1.74
Zn	90.34±2.07	52.20±1.23	26.60±1.97	79.19±6.19
	Group II			
Na	286.85±9.54	117.35±11.60	14.80±0.21	24.39±1.79
Mg	1482.84±37.12	1398.83±39.96	1963.78±69.82	1478.55±48.13
P	858.86±24.50	5132.43±436.91	2663.12±70.05	5415.18±138.26
K	30655.50±967.73	34868.24±1552.47	32172.69±1460.95	20847.17±662.66
Mn	57.57±0.85	69.42±6.56	42.59±1.38	20.96±2.41
Fe	61.53±1.92	69.42±7.54	45.04±2.45	45.74±6.38
Cu	7.67±0.07	7.54±0.48	10.04±0.06	14.81±1.39
Zn	94.77±1.28	77.72±7.04	47.01±0.60	79.12±5.50

Table 3. The concentrations of toxic elements [mg/kg] in the investigated plants

Toxic elements	*Petroselinum crispum* classic	*Petroselinum crispum* variety moss curled 2	*Ocimum basilicum*	*Origanum vulgare*
	Group I			
Co	0.487±0.113	0.805±0.372	2.350±0.383	1.489±0.331
Cd	1.668±0.085	0.198±0.009	0.091±0.014	0.045±0.007
Cr	1.018±0.047	0.722±0.057	0.448±0.045	0.035±0.024
Ni	1.712±0.159	0.864±0.038	0.489±0.028	0.593±0.153
Pb	0.183±0.017	0.087±0.005	0.212±0.016	0.153±0.014
As	0.112±0.032	0.042±0.043	0.739±0.077	0.178±0.035
Al	9.410±0.759	14.841±1.691	8.287±0.945	30.063±2.264
In	0.0047±0.0005	0.0024±0.0013	0.0008±0.0003	0.0012±0.0014

	Group II			
Co	0.916±0.257	1.326±0.203	1.935±0.456	1.129±0.047
Cd	0.630±0.017	0.119±0.006	0.042±0.011	0.024±0.002
Cr	0.745±0.126	0.974±0.070	0.422±0.062	0.251±0.072
Ni	1.366±0.093	0.998±0.038	0.377±0.081	0.436±0.134
Pb	0.060±0.002	0.092±0.015	0.109±0.010	0.055±0.004
As	0.156±0.015	0.048±0.009	0.829±0.068	0.074±0.013
Al	9.539±0.376	4.933±0.489	4.744±0.223	6.367±0.385
In	0.0038±0.0013	0.0007±0.0003	0.0011±0.0005	0.0005±0.0000

Table 4. The concentrations of rare earth elements [mg/kg] in the investigated plants

Rare earth elements	*Petroselinum crispum* classic	*Petroselinum crispum* variety moss curled 2	*Ocimum basilicum*	*Origanum vulgare*
	Group I			
Y	0.0579±0.0444	0.0163±0.0026	0.0056±0.0008	0.0308±0.0037
La	0.0850±0.0031	0.0109±0.0025	0.0919±0.0204	0.0112±0.0020
Ce	0.1672±0.0188	0.0114±0.0013	0.1627±0.0073	0.0073±0.0036
Pr	0.0173±0.0047	0.0016±0.0003	0.0161±0.0014	0.0030±0.0007
Sm	0.0003±0.0005	0.0022±0.0031	ND	0.0003±0.0005
Eu	0.0071±0.0013	0.0025±0.0011	0.0020±0.0009	0.0012±0.0009
Gd	0.0017±0.0015	0.0027±0.0023	0.0013±0.0023	*ND
Dy	ND	ND	0.0003±0.0006	ND
Ho	ND	ND	ND	ND
Yb	ND	ND	ND	ND
	Group II			
Y	0.1193±0.0899	0.0745±0.0942	0.0103±0.0060	0.0090±0.0008
La	0.0152±0.0021	0.0160±0.0017	0.0151±0.0054	0.0031±0.0020
Ce	0.0292±0.0059	0.0217±0.0045	0.0112±0.0058	0.0005±0.0086
Pr	0.0032±0.0003	0.0028±0.0015	0.0011±0.0007	0.0008±0.0008
Sm	ND	ND	0.0008±0.0005	ND
Eu	0.0059±0.0011	0.0049±0.0015	0.0014±0.0008	ND
Gd	0.0004±0.0008	ND	ND	ND
Dy	0.0003±0.0005	ND	ND	ND
Ho	0.0003±0.0003	ND	ND	ND
Yb	0.0004±0.0008	ND	ND	ND

*ND – not detectable

The essential primary plant nutrients (P, K, Mg, and Na) are important for plant production and vital for growth and development of all living bodies. Some metals (such as Cr, Mn, Zn, Fe, Co, Cu, Ni) are essentials plant nutrients, but, they are phytotoxic at higher concentrations. Heavy metals are present in aromatic plants at different concentrations and the uptake of these by plants is influenced by various factors (i.e. type of plant, soil nature, climate, etc).

The biogeochemical behavior of rare earth elements (REEs) is not fully understood. Until recently, REEs were not characterized either as essential plant nutrients or as environmentally hazardous metals [21]. However, the last experimental studies demonstrated toxic effects of REEs for plants [22-23].

The obtained results indicated that the concentration of elements in investigated aromatic plants depends on the species of plant and irrigated water. For efficient processing of experimental data ANOVA test was employed.

For the first case, the matrix employed for statistical analysis was formed by all analyzed multielements in eight samples. For evidencing the elements that can separate the two investigated groups, according to irrigation water, ANOVA was applied. Only one element, namely Pb ($p < 0.05$) was found to be a good discriminator for these groups. It can be concluded that tropical water may facilitate the Pb intake by all analyzed herbs, except curly parsley, where the concentration is smaller.

For the second purpose, ANOVA was applied on the same matrix, this time having as independent variable, the species, and means of four groups were compared. The most important elements that can distinguish investigated aromatic group plants are: K (0.012), Cr (0.022), Mn (0.005), Co (0.037), Ni (0.005), Cu (0.005), Zn (0.034), As (0.001), In (0.027), Eu (0.018). *Ocimum basilicum* plant was characterized by the highest levels of As and Co, compared to other three plant types, while *Origanum vulgare* had the highest content of Cu and the lowest content of K. Other important parameters that can differentiate the above mentioned species was represented by total phenolic content ($p = 0.038$). Higher values for this parameter may be found in *Origanum vulgare* samples compared to *Ocimum basilicum* plant. The *Petroselinum crispum* classic had a high content of Ni, Zn, In and Eu, respectively. The highest concentrations for Cr and Mn were obtained for the *Petroselinum crispum* group, compared to *Origanum vulgare samples*.

CONCLUSIONS

This paper presents original data concerning the leaf isotopic content in two aromatic herbs groups, irrigated with water having two different isotopic compositions. The δD value of extracted leaf water for both groups was positively

related to the δD value of irrigation water, and all leaf samples were enriched in deuterium and oxygen-18 relative to irrigation water.

Another important observation is that the value of the isotopic composition of the input water contributes to the modification of the content of total polyphenols, differently for the studied plants. So, for the parsley and oregano irrigated with water with isotopic composition specific to the tropical areas, the content of total polyphenols rises and for basil and curly parsley the content of total polyphenols decreases compared to the plants from the reference lot.

These preliminary results show that, by modifying the isotopic composition of the irrigation water, one can obtain plants with a larger contribution of total polyphenols, beneficial to the human body. Also, it is of interest that studies like these should be conducted on more species of herbs and other plants.

The isotopic content of irrigation water may have influence on Pb content assimilation by all studied plants. Regarding the comparison among investigated species, ANOVA highlighted the elements that differentiate the species. It was observed that parsley is characterized by the highest concentration of Ni, Zn, In and Eu. For both, parsley and curly parsley samples, the highest levels for Cr and Mn were founded as compared to oregano samples.

EXPERIMENTAL SECTION

Sampling and stable isotope analysis

Three species of aromatic herbs, consisting of 8 samples, were grown during twelve weeks. The samples were divided into two groups, depending on the irrigation water. Thus, the plants from first group (I) were watered with deuterium - enriched water (tropical water). This water has a similar isotopic composition of rainwater in the tropics (δD = -16.3 ‰, δ^{18}O = -1.2 ‰). The second group (II), for control, was irrigated with drinking water from the public network (δD = -70.6 ‰, δ^{18}O = -10.2 ‰). In this experiment, for both plant groups, the same soil type (commercial soil) was used.

Water from plant parts (leaf) was extracted without any isotopic fractionation by cryogenic distillation. The δ^{18}O and δD values in water extracted from leaf were determined by using a liquid-water isotope analyzer (DLT – 100, Los Gatos Research). For δ^{13}C analysis, the plant samples were dried at 55 ^{0}C. Carbon isotope analyses were performed using a Delta V Advantage mass spectrometer (Thermo Scientific) operated in dual inlet mode [17-18]

The stable isotope values were express in delta (δ) notation:

$$\delta X = \left(\frac{R_{sample}}{R_{std}} - 1\right) \times 1000$$

(2)

where X is the heavy isotope (D, ^{13}C, ^{18}O), δ is in parts per thousand (‰) deviation relative to a standard gas, and R_{sample} and $R_{standard}$ are the ratios of the heavy to the light isotopes for sample and standard, respectively. The isotopic compositions were expressed relative to standard V-SMOW for D and ^{18}O measurements, and V-PDB for ^{13}C measurements, respectively. The limit of uncertainty of the isotopic analysis was ± 0.2 ‰ for δ^{13}C and δ^{18}O and ± 1.0 ‰ for δD.

Preparation of plant extracts and determination of total polyphenols content

One gram of fresh leaves was ground and fin pulverized by adding liquid nitrogen. 1 g of the fresh plant material with 2 mL 60 % ethanol was subjected to sonication for 30 minutes using an ultrasound device (Elmasonic S 15H, 37 kHz). After extraction, the sample was filtered by nylon syringe filter (0.45 µm), after which, the final volume was adjusted to 2 mL with the same solvent mixture used for extraction. Each extract was performed in three parallel samples.

The Folin-Ciocalteu reagent was used for total polyphenols content determination, according to the Slinkard method [19]. According to this method 5 mL of distilled water and 0.5 mL Folin-Ciocalteu reagent were added to 1 mL of extract. After 3 min, 1.5 mL of sodium carbonate (5 g/L) was added to the mixture and distilled water up to 10 mL. The sample was kept in a water bath at 50 °C for 16 min and after cooling, the absorbance was read at 765 nm against distilled water as the blank, using a Shimadzu UV-160A spectrophotometer (Kyoto, Japan). The total polyphenols were expressed as mg/g gallic acid equivalents, concentration of gallic acid ranging from 0.001 to 0.40 mg/mL. All measurements were taken in triplicates and mean values were calculated.

Determination of essential plant nutrients and heavy metals concentrations

For ICP-MS method from each dried samples, 0.1 g was weighed and transferred to a Teflon receptacle. Afterward, 2.5 mL of concentrated ultrapure nitric acid (65 %) was added and were subjected to mineralization by oven at 180 °C for 12 hours. Then clear solutions were transferred quantitatively into

the volumetric flasks (50 mL) and made up with ultrapure water. Plant nutrient elements and heavy metal concentrations were determined with ELAN DRC (e) instrument. Calibration standards solutions and internal standards were prepared by successive dilution of a high-purity ICP multielement calibration standard 10 µg/mL of Al, As, Ba, Be, Bi, Ca, Cd, Co, Cr, Cs Cu, Fe, Ga, In, K, Li, Mg, Mn, Ni, Pb, Rb, Se, Na, Ag, Sr, Ti, V, U, Zn (Perkin Elmer Life and Analytical Sciences).

Statistical approach

Many analytical techniques provide large amount of experimental data, which might became difficult to interpret or to extract the most meaningful conclusions. In this case, ANOVA was applied on multielemental concentrations obtained from ICP-MS, having two important purposes: i) to evidence elements that may distinguish two plants groups weathered with water having different isotopic content and ii) to highlight the elements that can differentiate the four investigated plant types (curly parsley, parsley, basil, oregano). All statistical analysis was made using specific software.

ACKNOWLEDGMENTS

R E F E R E N C E S

[1]. M.P. Kähkönen, A.I. Hopia, H.J. Vuorela, J.-P. Rauha, K. Pihlaja, T.S. Kujala et al., *Journal of the Agricultural and Food Chemistry*, **1999**, *47*, 3954.
[2]. A. Djeridane, M. Yousfi, B. Nadjemi, D. Boutassouna, P. Stocker, N. Vidal, *Food Chemistry*, **2006**, *97*, 654.
[3]. K. Aaby, E. Hvattum, G. Skrede, *Journal of the Agricultural and Food Chemistry*, **2004**, *52*, 4595.
[4]. Y. Luo, Q. Cai, M. Sun, H. Corke, *Life Science,* **2004***, 74,* 2157.
[5]. R.J. Nijveldt, E. van Nood, D.E. van Hoorn, P.G. Boelens, K. van Norren, P.A. van Leeuwen, *American Journal of Clinical Nutrition,* **2001**, *74(4)*, 418.
[6]. R. Yanardag, S. Bolkent, A. Tabakoglu-Oguz, O. Ozsoy-Sacan. *Biological and Pharmaceutical Bulletin,* **2003**, *26(8)*, 1206.
[7]. S. Fejes, A. Blázovics, É. Lemberkovics, G. Petri, É. Szöke, Á. Kéry, *Phytotherapy Research,* **2000**,*14(5)*, 362.

[8]. P.Y.Y. Wong, D.D. Kitts, *Food Chemistry,* **2006**, *97(3)*, 505.
[9]. H. Zhang, F. Chen, X. Wang, H.-Y. Yao, *Food Research International,* **2006**, *39(8)*, 833.
[10]. S. Jabeen, M.T. Shah, S. Khan, M.Q. Hayat, *Journal Mededicinal Plant Research*, **2010**, *4*, 559.
[11]. S. Yagi, A.E. Abd Rahman, G.O.M. ELhassan, A.M.A. Mohammed, *Journal of Applied and Industrial Sciences*, **2013**, *1(1)*, 49.
[12]. G. Somlyai, G. Jancso, G. Jákli, K. Vass, B. Barna, V. Lakics, T. Gaál*, FEBS (Federation of European Biochemical Societies) Letters*, **1993**, *317* (1-2), 1.
[13]. H. Wanga, B. Zhu, Z. He, H. Fu, Z. Dai, G. Huang, B. Li, D. Qin, X. Zhang, L. Tian, W. Fang, H. Yang, *Biomedicine & Pharmacotherapy,* **2013**, *67*, 489.
[14]. P. Berdea, S. Cuna, C. Cuna, G. Balas, *Studia UBB Geologia,* **2007**, *52(1)*, 6.
[15]. C. Tanase, A. Stingu, I. Volf, V.I. Popa, *Scientific Annals of "Al. I. Cuza" University*, **2011**, *XII*, 115.
[16]. Z. Balazs, D. Ristoiu, D.A. Magdas, G. Cristea, A. Dehelean, C. Voica, R. Puscas, A. Pirnau, I. Feher, S. Radu, M. Vadan, *Analytical Letters,* **2016**, *49(3)*, 364.
[17]. V. Avram, D.A. Magdas, C. Voica, G. Cristea, C. Cimpoiu, A. Hosu, C. Marutoiu, *Analytical Letters,* **2014**, *47(4)*, 641.
[18]. A. Dehelean, D.A. Magdas, G. Cristea, *Analytical Letters,* **2013**, *46(3)*, 498.
[19]. K. Slinkard, V.L. Singleton, *American Journal of Enolology and Viticulture,* **1977**, *28*, 49.
[20]. J.D. Marshall, J.R. Brooks, K. Lajtha. "*Sources of variation in the stable isotopic composition of plants*". R. Michener and K. Lajtha (eds.) in „*Stable Isotopes in Ecology and Environmental Science",* Blackwell Publishing, Oxford, **2007**.
[21]. Shtangeeva, *Water Air Soil Pollution*, **2014**, *225*, 1964.
[22]. P. Babula, V. Adam, R. Opatrilova, J. Zehnalek, L. Havel, R. Kizek, *Environmental Chemistry Letters*, **2008**, *6*, 189.
[23]. D. Liu, X. Wang, Y. Lin, Z. Chen, H. Xu, L. Wang, *Environmental Science and Pollution Research*, **2012a**, *19*, 3282.

THE EFFECT OF A NATURAL EXTRACT-BASED EXPERIMENTAL BLEACHING GEL UPON THE COLOUR AND SURFACE ROUGHNESS OF A COMPOSITE RESIN - AN IN VITRO STUDY

**DIANA CARLA MADA[a]*, CRISTINA GASPARIK[a],
MARIOARA MOLDOVAN[b], CRISTINA STEFANA MIRON-BORZAN[c],
ALEXANDRA IULIA IRIMIE[a], DANIELA CORNEA[a], DIANA DUDEA[a],
RADU SEPTIMIU CAMPIAN[a]**

ABSTRACT. *Objective:* To evaluate the bleaching effect and the changing in the surface roughness of one experimental natural-based bleaching gel and of three commercial bleaching gels, namely: Opalescence PF 16%, Ultradent, Opalescence Quick PF 45%, Ultradent (based on carbamide peroxide CP) and Philips Zoom DayWhite 6% HP light activated (based on hydrogen peroxide HP) upon A3 body shade Filtek Supreme, 3M Espe nanocomposite. *Material and methods*: Thirty disks of the A3 body shade Filtek Supreme, 3M Espe, were immersed in a coffee solution and further divided into 6 groups: group 1 was kept as control, while groups 2-6 underwent a certain bleaching protocol, with different materials and exposure time, as follows: group 2: experimental gel, five sessions, 6 hours each; group 3: Opalescence PF 16 % (Ultradent), five sessions 6 hours each; group 4: Opalescence Quick PF 45% (Ultradent), 2 sessions, 30 min each; group 5: Opalescence Quick PF 45% - 2 applications/30 min and Opalescence PF 16% - 5 applications/6h and group 6 was bleached using an in office gel containing HP 6% (Philips Zoom DayWhite 6% HP light-activated 2 applications/30min).

CIE L*a*b* parameters and surface roughness were recorded before and after bleaching. Data were analyzed using one-way repeated measures ANOVA, and multiple comparisons were adjusted using the Bonferroni method ($p<0.05$). Results: The average colour differences at the end of the bleaching protocols were as follows: 1:ΔE^*=1.40, 2:ΔE^*=3.76, 3:ΔE^*=5.13, 4:ΔE^*=4.79, 5:ΔE^*=5.44, and 6:ΔE^*=6.83. Overall, a significant statistical difference was found between the groups ($p<0.05$). However, multiple comparisons showed

[a] *Iuliu Hatieganu University of Medicine and Pharmacy, 8 Babeş Str., RO-400012, Cluj-Napoca, Romania*
[b] *Raluca Ripan Institute of Chemistry Research, 30 Fantanele Str., RO-400294, Cluj-Napoca, Romania*
[c] *Technical University of Cluj-Napoca, 128-130, 21 Decembrie 1989 Blvd., RO-400604, Cluj-Napoca, Romania*
* *Corresponding author: mada.diana@umfcluj.ro; dianacarla.mada@gmail.com*

D.C. MADA, C. GASPARIK, M. MOLDOVAN, C.S. MIRON-BORZAN, A.I. IRIMIE, D. CORNEA,
D. DUDEA, R.S. CAMPIAN

no significant difference among the groups based on carbamide peroxide (CP) (3, 4, and 5) (p>0.05). The results of the statistical test indicated a significant effect of the bleaching gels only for groups 5 and 6 (p<0.05). For these groups, surface roughness significantly decreased after the bleaching protocol. For the experimental group, no significant modifications of the surface were observed. Conclusions: The most effective protocol was the "in office" bleaching method based on hydrogen peroxide (HP) with light activation. The natural extract-based gel was less efficient than CP and HP groups; however, ΔE* was above the acceptability threshold. The natural extract-based experimental bleaching gel showed no significant change upon surface roughness.

Keywords: *nanocomposite, colour stability, bleaching, surface roughness, natural extract*

INTRODUCTION

Photo activated resin composites remain even today the dental restorative materials most frequently used in the treatment of both anterior and posterior teeth. Nowadays, patients seek better colour matching restorations and composite resins to satisfy their needs [1].

Discolouration is a significant aesthetic problem for direct tooth-coloured restorations. However, restoration longevity and the aesthetic appearance greatly depend on the quality of the finishing and polishing techniques employed [2-3]. An unacceptable colour match is a major reason for composite restoration replacement. Intrinsic factors - due to changes in the filler, matrix, or silane coating - or extrinsic factors - such as stain absorption - may cause the discolouration of the aesthetic materials [2]. Experimental studies have shown that the colouring effect also depends on the staining solutions used [4].

Tooth bleaching has gained considerable acceptance among dentists and patients, as it is a simple, effective and safe procedure to lighten discoloured teeth. Since its introduction by Haywood and Heymann in 1989 [5] tooth whitening has become one of the most popular aesthetic procedures offered by dentists.

There are several types of bleaching methods, all of them based on the principle of peroxide degradation into hydrogen peroxide (HP) or its compounds - carbamide peroxide (CP), unstable free radicals, which are further decomposed into large pigmented molecules - either through oxidation or through a reduction reaction [6]. The bleaching methods are: the so called "in office bleaching" based on 16%, 35%, 40%, 45% of either HP or CP, for 30 to 45 minutes, with or without light or laser activation, or the "at home bleaching", under the supervision of the dentist, with lower concentrations of HP or CP, applied with strips or custom trays.

Considerable research has been carried out in order to find out the effects bleaching has on tooth surface and on the dental restorative materials. In as far as the dental surface is concerned, the effects included alterations in the morphology, as well as in the chemical and physical properties [7]. Scanning electron microscope findings have shown microscopic changes in the tooth structure, namely: an increased porosity, depression and surface irregularities [8], an increased surface roughness (SR) [9], a decrease in hardness [10] as well as in fracture resistance [7]. SR suffered alterations during or after treatment, depending on the HP concentration [11]. Researchers believe that SR leads to an increased susceptibility to bacterial adhesion and staining [10,12,13]. After bleaching, pigments adhere to the rough surface, especially to that of the enamel, far easier than to the original tooth surface, which causes more discolouration [14,15].

Many studies have examined the changes induced by bleaching in the characteristics of composite resins, such as colour, surface hardness and roughness, staining susceptibility, microleakage and elution [16]. Using a spectrophotometer, Li et al. [17] found significant changes in the colour of nanohybrid and packable composite resins after bleaching with 15% CP. Another study [18] showed that this difference was especially noticeable when a high peroxide concentration (35% HP) was used on low-density resins, such as microfilled composite resins. The authors associated these results with the resin matrix volume and the filler type. Both studies reported that the colour change was clinically acceptable. A recent study by Wattanapayungkul et al. [19] demonstrated that the treatment of composite resins with a low peroxide concentration significantly increased surface roughness.

A few studies assessed the influence of bleaching gels upon glass ionomer cements. A recent *in situ* study by Li et al. [16] showed a significant difference in the colour of a conventional glass ionomer cement restoration after four weeks of bleaching with 15% CP, when compared to that noted before the treatment. However, two weeks after the completion of the whitening treatment, the colour returned to that recorded before the treatment, which means that the bleaching did not alter the colour of the glass ionomer cement.

Moreover, scanning electron microscopy (SEM) revealed a slight surface dissolution. Similarly, another study [20] found alterations, such as cracks and pits, in the surface of the glass ionomer cement, which were explained by the capacity of the bleaching agent to alter the surface properties of the material. The authors also found that bleached glass ionomer restorations were more susceptible to different staining solutions with a pH from 3.73 to 6.25, such as red wine, herbal tea, Coca-Cola and coffee [20].

These conflicting reports encourage further investigation into the effects bleaching agents have on composite resin colour and SR.

Our study aims to analyze: a). the bleaching effect of an experimental bleaching gel based on natural extracts in comparison with that of commercial bleaching agents based on CP or HP used in different protocols (simulating

D.C. MADA, C. GASPARIK, M. MOLDOVAN, C.S. MIRON-BORZAN, A.I. IRIMIE, D. CORNEA,
D. DUDEA, R.S. CAMPIAN

"at home" and "in office" applications); and b). the effect of the same bleaching agents on the surface roughness of the A3 body shade Filtek Supreme, 3M Espe nanocomposite.

The null hypothesis is that both surface roughness and the colour of the A3 body shade Filtek Supreme, 3M Espe nanocomposite do not change after the application of the bleaching gels.

RESULTS AND DISCUSSION

CIE L*a*b* parameters were recorded as follows: at the beginning of the bleaching protocol (Baseline), at the end of the bleaching protocol (Final), and at intermediate phases, after each bleaching session, depending on the protocol used. Colour difference (ΔE_{ab}* *) was calculated using the equation [21]:

$$\Delta E_{ab}* = [(\Delta L*)^2 + (\Delta a*)^2 + (\Delta b*)^2]^{1/2}$$

where $\Delta L*=L_2*- L_1*$, $\Delta a*=a_2*- a_1*$, $\Delta b*=b_2*- b_1*$; L_1*, a_1*, b_1* correspond to the colour parameters before bleaching and L_2*, a_2*, b_2* are the colour parameters of the specimens at the end of each bleaching session, depending on the protocol used.

At the end of the bleaching protocol, colour variation - expressed as colour difference (Final ΔE_{ab}*) calculated for the commercial and the experimental bleaching materials used in the different protocols - was, as follows: Group 1 : $\Delta E_{ab}*=1.40$, Group 2: $\Delta E_{ab}*=3.76$, Group 3: $\Delta E_{ab}*=5.13$, Group 4: $\Delta E_{ab}*=4.76$, Group 5: $\Delta E_{ab}*=5.44$, and Group 6: $\Delta E_{ab}*=6.83$, as shown in Table 1. Overall, a significant statistical difference was found between the groups ($p < 0.05$). However, multiple comparisons showed no significant difference between the groups based on CP (3, 4, and 5) ($p > 0.05$).

Univariate ANOVA was conducted to test the null hypothesis that surface roughness of composite resins does not change after the application of the bleaching gels for none of the tested products. The results of the statistical test indicated a significant effect of the bleaching gels only for groups 5 and 6 ($p < 0.05$), which provided enough evidence to reject the null hypothesis. For these groups, surface roughness significantly decreased after the bleaching protocol, while no significant difference was observed in the experimental group.

Choosing the bleaching agent can be a challenge, since best whitening results, with lack of side-effects are desired.

In the case of restorative materials, the aim is to have a bleaching result that is similar to the one gained for the teeth, as well as to prevent any changes in the surface texture and composition following the bleaching.

Our study has focused on both effects on dental composites – namely: colour change and the preservation of the initial structure. We have used the A3 body shade Filtek Supreme, 3M Espe, which is a light activated composite, for both anterior and posterior teeth.

Table 1. ΔE^{*}_{ab} values calculated for each group at different intervals
(N/A- not applicable- where the protocols involved a limited number of measurements)

Groups	ΔE_{ab}* 1	ΔE_{ab}* 2	ΔE_{ab}* 3	ΔE_{ab}* 4	Final ΔE_{ab}*
1. Control	0.95	1.13	1.07	1.35	1.40
2. Experimental	1.44	3.04	3.59	3.80	3.76
3. Opalescence 16%	4.17	4.48	4.90	4.90	5.13
4. Opalescence 45%	3.79	N/A	N/A	N/A	4.76
5. Opalescence 45%+16%	4.46	4.77	5.15	5.27	5.44
6. Zoom	6.41	N/A	N/A	N/A	6.83

Table 2. Mean surface roughness values and standard
deviations recorded for each group

Time	Group	Mean surface roughness (Ra)	Std. Deviation (+/-)
Before bleaching	Control	0.452	0.063
	Experimental	0.412	0.054
	Opalescence 16%	0.406	0.034
	Opalescence 45%	0.372	0.028
	Opalescence 16%+45%	0.429	0.041
	HP 35% light activated (Zoom)	0.417	0.024
After bleaching	Control	0.430	0.033
	Experimental	0.407	0.029
	Opalescence 16%	0.413	0.026
	Opalescence 45%	0.384	0.024
	Opalescence 16%+45%	0.397	0.045
	HP 35% light activated (Zoom)	0.371	0.032

D.C. MADA, C. GASPARIK, M. MOLDOVAN, C.S. MIRON-BORZAN, A.I. IRIMIE, D. CORNEA,
D. DUDEA, R.S. CAMPIAN

In as far as discolouration is concerned, the null hypothesis was rejected, since different degrees of colour variation were obtained following the bleaching protocols: five times bleaching for 6 hours, with colour measurements between the various bleaching sessions, for groups 1, 2, 3, and 5; and two times bleaching for 30 minutes for groups 4 and 6 with colour measurements between the various bleaching sessions.

Bleaching, either "at home" or "in-office", is one of the most popular treatments, appealing to both patients and dentists, as it is considered to be a simple and effective way of lightening discoloured teeth. Bleaching agents may result in a colour change of a restoration different from the one gained for the teeth, a situation that may not be accepted by the patient. If a restorative composite had a perfect colour match before the bleaching treatment, this may no longer be the case after bleaching.

Within the limits of this study, it has been noticed that even a low concentration of bleaching agent had an effect on the colour of the restorative materials.

The results of our study showed that a significant colour difference was obtained for group five, that was bleached with Opalescence 45%+16%, and group six, bleached with HP 35% light activated (Zoom), whereas the colour of the composite resin was least affected when the experimental natural-based bleaching gel was used.

In our study, colour differences were calculated using the CIE L*a*b* colour space. CIE (Commission Internationale de L' Eclairage) L*a*b* colour parameters are used to quantify the optical properties of natural dental structures and dental materials [21]. In order to quantify the differences between two coloured samples, colour difference thresholds have been introduced in dentistry. Paravina et al. conducted a multicenter study upon visual thresholds in dentistry; they have reported that values smaller than $\Delta E_{ab}^* = 1.2$ are not perceptible, while values greater than $\Delta E_{ab}^* = 2.7$ [22] are considered to be clinically unacceptable. In our study, at the end of the bleaching protocol, all test groups showed colour difference values above the acceptability threshold, thus suggesting that the bleaching effect was significant and visually noticeable.

The second effect we observed was that of the modifications in surface roughness.

According to Paravina et al., the apparent colour difference is related to the surfaces, which are a result of the polishing techniques of the composites [23]. Polishing the composite up to Grit-1200 greatly helps to stimulate the clinical circumstances.

A large number of previous studies have demonstrated that bleaching agents affect the restorative materials by modifying hardness, roughness, colour and surface morphology [24]. The active ingredients of the most commonly used bleaching materials in different bleaching methods are carbamide peroxide and hydrogen peroxide. Carbamide peroxide degrades into approximately one-third

of hydrogen peroxide and two-thirds of urea [25]. The free radicals that are formed eventually combine to form molecular oxygen and water. Some aspects of this chemical process might accelerate the hydrolytic degradation of the restorative materials, as described by Soderholm et al. [26]. Chemical softening of the restorative materials might also occur if the bleaching products have a high concentration of hydrogen peroxide [27].

It is known that nanoresin composites followed by microhybrid and hybrid composites showed least surface roughness (Ra) and colour change when exposed to different staining solutions [28]. Roman et al. [29] reported that unpolished composites presented higher Ra values than those that were polished.

The results of our study indicated a significant effect of the bleaching gels only in the case of groups 5 and 6 ($p<0.05$). For these groups, surface roughness significantly decreased after the bleaching protocol. No significant difference was found in the experimental group.

CONCLUSIONS

1. Both the commercial and the natural-based extract bleaching gels induced noticeable colour changes upon the tested composite resin; however, the most important colour change was noticed in the case of the HP 35% light activated Zoom bleaching gel.

2. The natural extract based gel was less efficient than the CP and HP groups; however, ΔE* was above the acceptability threshold.

3. The surface roughness of the tested composite resin was significantly altered only when high concentrations of CP or HP were used.

4. The natural extract-based experimental bleaching gel showed no significant changes in the surface roughness.

EXPERIMENTAL SECTION

1. Disk preparation, staining and bleaching protocols

Thirty nanocomposite resin disks (n=30) were fabricated (A3 body shade Filtek Supreme, 3M Espe). The composition of the resin matrices and fillers of this composite resin is listed in Table 3.

The specimens were polished to a uniform thickness using abrasive sandpaper (2mm thickness, 10mm diameter) and were eventually immersed into a coffee solution (5g/100ml, Jacobs Kronung, Kraft Foods, Germany) for 8 hours/day on three consecutive days.

During the staining process, the specimens were stored in distilled water at 37°C. The specimens were further divided into 6 groups: one control group, and 5 test groups.

Group 2 underwent a bleaching protocol using an experimental gel based on natural extracts (5 applications/6h).

For test groups 3 and 4 two commercial gels were used, one for "at home" use (Opalescence CP16%, Ultradent – 5 applications/6h) and one for "in office" use respectively (Opalescence Quick CP45%, Ultradent – 2 applications/ 30 min).

Group 5 underwent a combined bleaching protocol (CP45% - 2 applications/ 30 min and CP16% - 5 applications/6h).

Group 6 was bleached using an "in office" gel containing HP 6% (Philips Zoom DayWhite 6% HP light-activated 2 applications/30min.

Table 3. Composition of the resin matrices and fillers of the composite resin

Material	Shade	Description	Composition	The resin system
Filtek™ Ultimate 3M™ ESPE™	A3B (Body)	Universal restorative material	The filler is a combination of a non-agglomerated/non-aggregated, 20nm nanosilica filler, and loosely bound agglomerated zirconia/silica nanocluster, consisting of agglomerates of primary zirconia/silica particles with size of 5-20 nm fillers. The cluster particle size range is 0.6 to 1.4 microns. The filler loading is 78.5% by weight.	BIS-GMA, BIS-EMA (6), UDMA with small amounts of TEGDMA.

2. Colour evaluation

Measurements were performed using a dental spectrophotometer (VITA Easyshade® Advance 4.0., VITA, Bad Sackingen, Germany) according to the CIE L*a*b* colour system. L* refers to lightness; its value ranges from 0 (black) to 100 (white), while a* and b* are measures of greens or redness and respectively blueness or yellowness of an object. The a* and b* chromaticity coordinates reach 0 for neutral colours and increase in magnitude for saturated or intense colours [30]. Five measurements were taken for each sample at a time.

CIE L*a*b* parameters were recorded as follows: at the beginning of the bleaching protocol (Baseline), at the end of the bleaching protocol (Final), and at intermediate phases, after each bleaching session, depending on the protocol used. Colour difference ($\Delta E_{ab}*$) was calculated using the equation [21]:

$$\Delta E_{ab}* = [(\Delta L^*)^2 + (\Delta a^*)^2 + (\Delta b^*)^2]^{1/2}$$

where $\Delta L^* = L_2^* - L_1^*$, $\Delta a^* = a_2^* - a_1^*$, $\Delta b^* = b_2^* - b_1^*$; L_1^*, a_1^*, b_1^* correspond to the colour parameters before bleaching and L_2^*, a_2^*, b_2^* are the colour parameters of the specimens at different intervals of the bleaching protocol.

In order to measure the same colour during the staining and bleaching process, a thermoformed plastic positioning device was used, perforated according to the probe tip of the VITA EasyShade. Between the sessions the disks were stored in distilled water at room temperature.

Data were analyzed using one-way repeated measures ANOVA was and multiple comparisons were adjusted using the Bonferroni method ($p < 0.05$).

3. Surface roughness

Surface changes were identified by surface roughness measurements, using the Mitutoyo SJ 210 Surftest. Mean arithmetic deviation of the profile (Ra) was measured in 5 points of each sample, at the beginning and at the end of each bleaching protocol, for each group. Measurements were made with the profile method using a standard stylus device. The measuring speed, pin diameter, and pin top angle of the tool were 0.25mm/s, 5 µm, and 90°, respectively. The measuring force of the scanning arm on the surfaces was 4 mN, which did not cause any significant damage to the surface according to Mitutoyo Surftest SJ-201 user manual. Measurements were performed at room temperature, and the pin was calibrated before the tests. Surface roughness was evaluated for each specimen at the beginning and at the end of each bleaching protocol. The recorded data were statistically analyzed using Univariate ANOVA ($\alpha = 0.05$).

ACKNOWLEDGMENTS

CONFLICTS OF INTEREST

There are no conflicts of interests

R E F E R E N C E S

[1]. T.M. Roberson, H.O. Heymann, E.J. Jr. Swift, et al., *Journal of Dentistry,* **2001**, *29*(1):1-6;

[2]. F. Reis, M. Giannini, J.R. Lovadino, G.M. Ambrosano, *Dental Materials*, **2003**, *19*, p. 8-12;

[3]. M. Baseren, *Journal of Biomaterials Applications*, **2004**, *19*(2), 121-34;

[4]. D.A. Prodan, C. Gasparik, D.C. Mada, V. Miclaus, M. Baciut, D. Dudea, *Clinical Oral Investigations*, **2015**, *19* (4): 87, IF: 2,285;

[5]. V.B. Haywood, H.O. Heymann, *Quintessence International*, **1989**, *20*(3), 173-6;

[6]. S.X.S. Costa, A.B. Becker, A.N. de Souza Rastelli, L. de Castro Monteiro Loffredo, M.F. de Andrade, V.S. Bagnato, *International Journal of Dentistry*, **2009**, 7. doi: 10.1155, 313845;

[7]. T. Attin, C. Hannig, A. Wiegand, R. Attin, *Dental Materials*, **2004**, *20*, 852-86;

[8]. S. Sda Ferreira, J.L. Araujo, O.N. Morhy, C.M. Tapety, M.N. Youssef, M.A. Sobral, "The effect of fluoride therapies on the morphology of bleached human dental enamel", *Microscopy Research and Technique*, **2011**, *74*:512-6;

[9]. J.M. Martin, J.B. de Almeida, E.A. Rosa, P. Soares, V. Torno, R.N. Rached et al., *Quintessence International*, **2010**, 41:71-8;

[10]. R.D. Singh, S.M. Ram, O. Shetty, P. Chand, R. Yadav, *Journal of Conservative Dentistry*, **2010**, 13:76-9;

[11]. D.R. DE Abreu, R.T. Sasaki, F.L. Amaral, F.M. Florio, R.T. Basting, *Journal of Esthetic and Restorative Dentistry*, **2011**, 23:159-68;

[12]. J. Mathias, S. Kavitha, S. Mahalaxmi, *Journal of Conservative Dentistry*, **2009**; 12:22-5;

[13]. L. Mei, H.J. Busscher, H.C. van der Mei, Y. Ren, *Dental Materials*, **2011**, 27:770-8;

[14]. Y.S. Kim, H.K. Kwon, B.I. Kim, *Journal of Dentistry*, **2011**, 39:636-42;

[15]. Watts, M. Addy, *Journal of Dentistry* **2001**, 190-309-16 [PubMed];

[16]. J. El-Murr, D. Ruel, A.J. St-Georges, *Journal Canadian Dental Association*, **2011**, 71:b59;

[17]. Q. Li, H. Yu, Y. Wang, *Journal of Dentistry*, **2009**, 37(5):348-56, Pub 2009 Feb 8;

[18]. I. Hubbezoglu, B. Akaoglu, A. Dogan, S. Keskin, G. Blair, S. Ozcelik, et al., *Dental Materials*, **2008**, 27(1):105-16;

[19]. P. Wattanapayungkul, A.U.J. Yap, K.W. Chooi, M.F.L. A. Lee, R.S. Selma, R.D. Zhou, *Operative Dentistry*, **2004**, 29(4):398-403;

[20]. H. Yu, X. Pan, Y. Lin, Q. Li, M. Hussain, Y. Wang, *Operative Dentistry*, **2009**, 34(1):72-82;

[21]. W.M. Johnston, *Journal of Dentistry*, **2009**, 37(Suppl 1):e2-6;

[22]. R.D. Paravina, R. Ghinea, J.J. Herrera, A.D. Bona, C. Igiel, M. Linninger, M. Sakai, H. Takahashi, E. Tashkandi E., M. Perez Mdel, *Journal of Esthetic and Restorative Dentistry*, **2015**;

[23]. R.D. Paravina, *Journal of Esthetic and Restorative Dentistry*, **2009**, 21(2):133-9;

[24]. D. Dietschi, G. Campanile, J. Holz, J. M. Meyer, *Dental Materials*, **1994**, 10, 353-362;

[25]. H. Yu, Q. Li, M. Hussain, Y. Wang, *Journal of Dentistry*, **2008**, 36(4), 261-7;

[26]. J. Soderholm, *Scand J Dent Res*, **1986**, Aug, 94(4):364-9;

[27]. L. Landuyt, J. Snauwaert, J. De Munck, M. Peumans, Y. Yoshida, A. Poitevin, E. Coutinho, K. Suzuki, P. Lambrechts, B. Van Meerbek, *Biomaterials*, **2007**, 28, 3757-85;

[28]. P.S. Reddy, K.L. Tejaswi, S. Shetty, B.M. Annapoorna, S.C. Pujari, H.M. Thippeswamy, *The Journal of Contemporary Dental Practice*, **2013**, 14(4):718-23;

[29]. C.C. Alandia-Roman, D.R. Cruvinel, A.B. Sousa, F.C. Pires-de-Souza, H. Panzeri, *Journal of Dentistry*, **2013**, 41 Suppl 3:e73-9;

[30]. R.D. Paravina, M. Kimura, J.M. Powers, *Journal of Esthetic and Restorative Dentistry*, **2005**, 17:102-8.

HPLC ANALYSIS, ANTIMICROBIAL AND ANTIFUNGAL ACTIVITY OF AN EXPERIMENTAL PLANT BASED GEL, FOR ENDODONTIC USAGE

ANDRADA TONEA[a]*, LIVIU OANA[b], MINDRA BADEA[a], SORINA SAVA[a], CORINA VOINA[a], FLORICA RANGA[b], DAN VODNAR[b]

ABSTRACT. The aim of this study is to investigate the active compounds of an experimental gel and to evaluate its antimicrobial and antifungal effects. This gel consists of a mix extract of *Arctium lappa* L. root powder and *Aloe vera* (L.) Burm.f. gel and is used in endodontic procedures. With the help of HPLC/ESI(+)-MS method, various active compounds were identified in the experimental extract. For the evaluation of the antimicrobial and antifungal activity, microorganisms commonly found in endodontic infections were used. The agar-diffusion method was performed for each plant formula and the microdilution method was used to obtain the minimum inhibitory concentration and also the minimum bactericidal concentration. Clear inhibition zones around discs indicated the presence of antimicrobial and antifungal activity for the disc diffusion assay. The minimum inhibitory and bactericidal concentration obtained were compared to the antibiotics or antifungals, specific for each microorganism.

Keywords: antimicrobial, antifungal, HPLC/ESI(+)-MS, agar-diffusion, microdilution, Arctium lappa, Aloe vera

INTRODUCTION

Arctium lappa L., also known as burdock, is a plant belonging to the Compositae (Asteraceae) family, commonly found in Europe, North America and Asia [1]. In traditional medicine, burdock is famous for a wide variety of benefits. It has the capacity to reduce the amount of fluids in the organism, to treat skin diseases, for example eczema, acne or psoriasis, and to purify blood [2][3]. In Europe the plant is wide spread, except for the extreme northern regions of the continent [4].

[a] *"Iuliu Haţieganu" University of Medicine and Pharmacy Cluj-Napoca, 15 Babes Street, Cluj-Napoca 400012, Romania*
[b] *"University of Agricultural Sciences and Veterinary Medicine", 3-5 Mănăştur Street, Cluj-Napoca 400372, Romania*
* *Corresponding author: andrada.tonea@umfcluj.ro*

Previous studies linked *Arctium lappa* to multiple therapeutic activities. It has a stronger antioxidant effect than other vegetables or fruits [5]. Chemical reactions with free-radical terminations and oxygen inhibitory compounds found in *Arctium lappa* are accounting for supressing biochemical processes promoted by oxygen [6].

Studies regarding the antidiabetic properties of burdock roots demonstrated that phenolic compounds control the glycemic and lipidic level and are helpful in avoiding complications of the disease. Burdock roots can be used in food and beverages, as additional products to classic antidiabetic drugs [7].

Continuous development of anticancer medications, with minimum side effects, led to investigations of plant based products. On account of the antiproliferative effects of burdock, the plant extracts are able to exhibit selective antitumoral activity against leukaemia, kidney and mammary human cancer cell lines [8].

An important antimicrobial effect was also assigned to *Arctium lappa*. Research showed that the root of burdock possesses antimicrobial properties against food-related microorganisms, like *Staphylococcus aureus, Streptococcus pneumoniae, Bacillus subtilis, Escherichia coli, Shigella dysenteriae* and *Salmonella typhimurium* [9].

Aloe vera **(L.) Burm.f.,** is a plant belonging to the ample genus *Aloe,* of which many species are cultivated all over the world. It is used in a diversity of fields, from a therapeutic agent, due to its anti-inflammatory, antimicrobial and antifungal properties, to a decoration plant in the Mediterranean regions [10].

Products obtained from *Aloe vera* have global applications, ranging from the food industry to the pharmaceutical and cosmetic industry [11].

In the food industry the plant is used in numerous products, especially for the preparation of diets with a content of biologically-active compounds [12]. Tonic syrups and other refreshment drinks are obtained from the gel of this plant [13].

Aloe vera extracts are as well used in the pharmaceutical and cosmetic fields. Studies on hairless mice proved that oral administration of *Aloe vera* gel powder can prevent the loss of skin suppleness and can postpone the aging of the dermis caused by exposure to ultraviolet B radiations [14] Skin dehydration is as well avoided with the help of polysaccharide-rich elements of the plant, which are responsible for increasing the content in water of the stratum corneum [15].

Medicinal tablets with particular roles were produced. Pills containing *Aloe vera* were conceived for enhancing the absorption of vitamins C and E [16] and tablets coated with *Aloe vera* gel were used for the controlled release of active substances [17].

Extracts of this plant can be valuable treatments for burn injuries, by minimizing the healing time [18][19] and maintaining the collagen content in the primary phase of dermal healing [20].

Antimicrobial and antifungal properties of *Aloe vera* were likewise explored. *Aloe vera* products can be used as agents against *Helicobacter pylori* strains [21], against *Enterococcus bovis, Staphylococcus aureus, Escherichia coli, Proteus vulgaris, Proteus mirabilis, Pseudomonas aeruginosa, Morganella morganii* and *Klebsiella pneumoniae* [22] but also against fungal pathogens, like *Candida albicans* [23]. Moreover, antidiabetic [24], anticancer [25] and antiviral effects [26] of the plant encourage researchers to explore the development of its curative capacities.

Plants have high applicability not only in general medicine, but also in dental medicine. Antimicrobial effects of *Arctuim lappa* in dentistry, against oral microorganisms, were investigated and proven during several studies. Burdock extracts are effective against bacteria commonly found in the oral cavity, like S*taphylococcus aureus*, S*taphylococcus epidermidis*, *Streptococcus mutans*, *Candida albicans*, *Candida tropicalis* and *Candida glabrata* [27].

Aloe vera can be used as an oral dentifrice [28] or as a mouthwash, due to its capacity to diminish dental plaque. Equally, it prevents lesions of the oral mucosa, produced by anticancer radiation therapy [29]. Other uses in the field of periodontology are as local drugs in periodontal pockets [30] or as acemannan sponges, to prevent damage of the alveolar bone, cementum and periodontal ligament [31].

Particularly in endodontics, the necessity of plant based therapeutic agents appeared due to the side effects of the frequently used irrigants and local medicaments. Situations when sodium hypochlorite reaches the periapical tissues, beyond the apical foramen, are undesirable for every endodontist, since they can produce severe reactions. Patients can suffer pain episodes, hematoma and in rare cases even necrosis of the subcutaneous tissues [32]. Similar research showed that the chemical reaction sodium hypochlorite and chlorhexidine can produce para-chloroaniline, an organochlorine compound which exhibits a potentially carcinogenic effect [33][34].

A variety of plants, like *Caryophyllus aromaticus* L., *Glycyrrhiza glabra* L., *Camellia sinensis* (L.) Kuntze, *Apium graveolens* L., were studied as natural alternatives to the classic root canal disinfecting substances [35]. In relation to the antimicrobial effect of *Arctium lappa* and *Aloe vera* against root canal specific microorganisms, extended investigations opened new areas of interest for researchers and practicians. Inhibitory effects were reported against bacteria like *Enterococcus faecalis, Staphylococcus aureus, Pseudomonas aeruginosa* or *Bacillus subtilis* and as well against yeasts*, like Candida albicans* [36][37][38][39].

RESULTS AND DISCUSSION

HPLC/ESI(+)-MS analysis of the extracts revealed a total of 12 phenolic compounds, 11 for *Arctium lappa* root extract and 1 for *Aloe vera* extract. (Fig.1) (Fig.2).
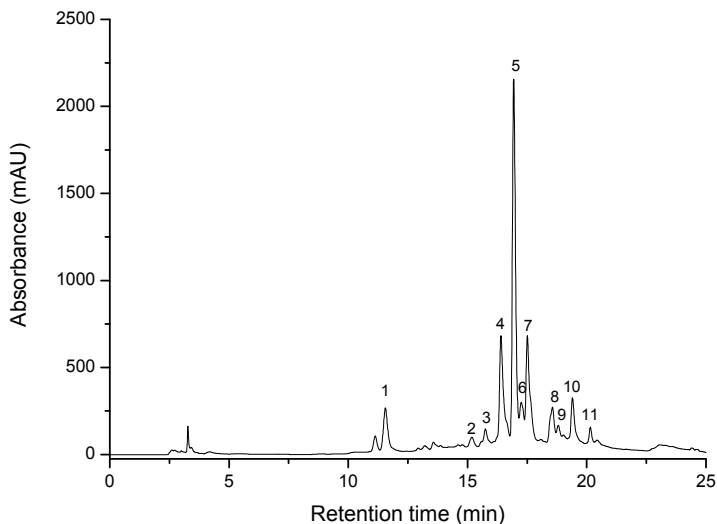
Figure 1. Chromatogram determined by HPLC /ESI(+)-MS analysis of phenolic compounds present in *Arctium lappa* root extract. For peak assignment see Table 1
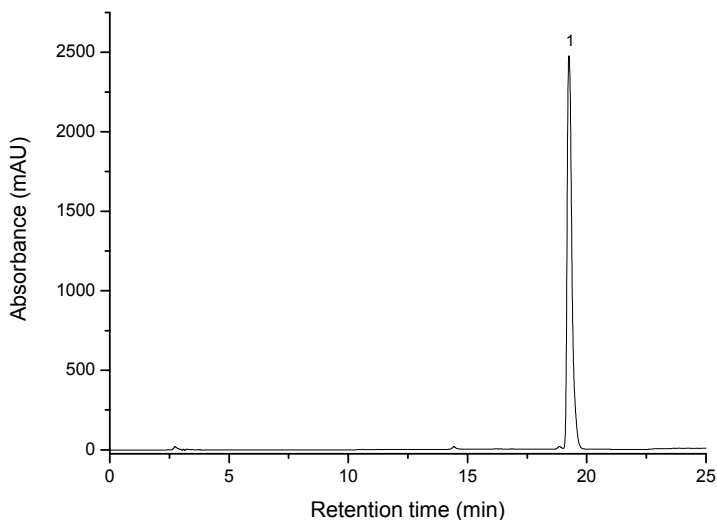
Figure 2. Chromatogram determined by HPLC /ESI(+)-MS analysis of phenolic compounds present in *Aloe vera* extract. For peak assignment see Table 2

For *Arctium lappa* root extract we identified peak 1 as chlorogenic acid (5-caffeoylquinic acid), with a [M + H]+ ion at 355 m/z. Peaks 2 and 3 had [M + H]+ ion at 517m/z and were identified as isomers of the caffeoylquinic acid. Chlorogenic acids are esters of the quinic acid and *trans*-cinnamic acids, such as caffeic acid*, p*-coumaric acid or ferulic acid [40]. They are studied and used for their antioxidant and antiinflammatory properties [41][42]. Antibacterial and antifungal activity of chlorogenic acids were as well reported in different studies. Attached to the external membrane of the bacteria, chlorogenic acid is able to break it and to induce cell destruction [43][44].

In endodontics, the cleaning effect of chlorogenic acid was previously observed. As an example, chamomile is able to exhibit antimicrobial activity trough the properties of chlorogenic acid and trough the properties of other phenolic components [45]. *Passiflora Edulis* is also effective in the removal of the smear layer from the root canal walls, due to its content in chlorogenic acid and other bioactive substances [46].

Peaks 4 and 5 had the same cvasimolecular ion at 537 m/z and were identified as lappaol A and isolappaol A. Lappaol F was identified at peak 7, with [M + H]+ ion at 713 m/z. Peak 6 and 11, with [M + H]+ ion at 373 m/z, were identified as arctiin and arctigenin. Arctignan E and Arctignan D were identified at peaks 8 and 10, with [M + H]+ ion at 733 m/z, while at peak 9 we identified matairesinol, with [M + H]+ ion at 359 m/z.

The major compound identified in *Arctium lappa* was arctiin and its derivatives, artignan and arctigenin. Arctiin, artignan, arctigenin and matairesinol are defined as lignan compounds, a group of phenylpropane derivatives [47] Likewise defined as lignans are lappaol A, isolappaol A and lappaol F. They are also known as sesquilignans.

Arctium lappa produces lignans as secondary metabolites, with various pharmacological properties. The antioxidant and the recent discovered anticancer effect make lignans the starting point for new drugs discovery [48][49]. Recent studies showed that lignans identified in *Arctium lappa* possess the ability to reverse multidrug resistance and even to amplify the efficacy of some drugs, while decreasing the dose needed to reach cell toxicity [50]. Lignans, and especially arctiin and its derivatives, are known for their antiinflammatory effect on macrophages, by diminishing the quantity of nitric oxide and pro-inflammatory cytokines, like TNF-α and IL6 [51][52].

The compound we identified in *Aloe vera* extract was *aloe-emodin*. It belongs to the class of anthraquinones, a group of natural phenolic substances. It is active against biofilms, especially against *Streptococcus mutans* [53], and against different Gram-positive and Gram-negative bacteria [54][55][56]. Its important activity against *methicillin-resistant Staphylococcus aureus* (MRSA) [57] and its antifungal activity against *Candida albicans* [58] were also confirmed.

Aloe-emodin was as well described as an anticancerous agent against neuroectodermal tumors [59], lung carcinoma cells [60] and hepatic cancer cell lines [61].

Table 1. Phenolics compounds in A*rctium lappa*

Peak No.	Compounds	m/z value	R$_t$ (min)	Concentration (mg/100g)
1	Chlorogenic acid (5-caffeoylquinic acid)	355	11.55	114.529
2	Caffeoylquinic acid isomer	517	15.19	84.062
3	Caffeoylquinic acid isomer	517	15.74	95.942
4	Lappaol A	537	16.40	186.706
5	Arctiin	535, *373*	16.93	323.886
6	isoLappaol A	537	17.25	104.601
7	Lappaol F	713	17.51	181.077
8	Arctignan E	733	18.56	111.676
9	Matairesinol	359	18.98	85.165
10	Arctignan D	733	19.40	133.115
11	Arctigenin	373	20.15	87.042

Table 2. Antraquinone in *Aloe barbadensis* Miller

Peak No.	Compounds	m/z value	Rt (min)	Concentration (mg/100g)
1	Aloe-emodin	271	19.25	131.728

The agar-diffusion method was used to determine the antimicrobial and antifungal activity of the microorganisms, commonly found in endodontic infections. The results were expressed in millimetres, representing the average inhibition diameters around the discs.

Arctium lappa root formula exhibited the largest zone of inhibition for *Candida albicans (ATCC10231)*, with an average diameter of 11.65 mm, followed by 3.69 mm for *Enterococcus faecalis (ATCC29212).* A smaller zone of inhibition to this formula exhibited *Pseudomonas aeruginosa (ATCC27853)*, with an average diameter of 2.63 mm, *Parvinomas micra (ATCC33270)*, 0.65 mm, *Peptostreptococcus anaerobius (ATCC27337),* 0.56 mm and *Fusobacterium nucleatum (ATCC25586),* 0.14 mm (Table 3).

Aloe vera gel formula exhibited the largest zone of inhibition for *Candida albicans (ATCC10231)*, 11.35 mm, followed by 6.24 mm for *Enterococcus faecalis (ATCC29212).* A medium sensitivity to this formula exhibited *Fusobacterium nucleatum (ATCC25586),* 3.65 mm, *Pseudomonas aeruginosa (ATCC27853),* 3.61 mm, *Peptostreptococcus anaerobius (ATCC27337),* 2.61 mm and *Parvimonas micra (ATCC33270),* 1.56 mm (Table 3).

The experimental mix of *Arctium lappa* root and *Aloe vera* gel exhibited the largest zone of inhibition for *Candida Albicans (ATCC10231)*, with an average diameter of 11.62 mm, followed by 5.69 mm for *Enterococcus faecalis (ATCC29212)*. A medium sensitivity to this formula exhibited *Pseudomonas aeruginosa (ATCC27853),* with an average diameter of 3.45 mm, *Peptostreptococcus anaerobius (ATCC27337)*, 2.02 mm, *Fusobacterium nucleatum (ATCC25586),* 1.89 mm and *Parvinomas micra (ATCC33270),* 1.01 mm (Table 3).

In order to compare specific antibiotics and antifungals, corresponding to the *Clinical and Laboratory Standards Institute*, inhibition zones for Amoxicillin and Clavulanic acid, Metronidazole, Ciprofloxacine and Fluconazole were determined (Table 4).

Table 3. Inhibition zones for plant extracts (mm.)

Samples	*P. aeruginosa (ATCC 27853)*	*E. faecalis (ATCC 29212)*	*P. micra (ATCC 33270)*	*P. anaerobius (ATCC 27337)*	*F. nucleatum (ATCC 25586)*	*C. albicans (ATCC 10231)*
Arctium lappa root extract (mg/ml)	2.63	3.69	0.65	0.56	0.14	11.65
Aloe barbadensis Miller gel extract (mg/ml)	3.61	6.24	1.56	2.61	3.65	11.35
Mix (mg/ml)	3.45	5.69	1.01	2.02	1.89	11.62

Table 4. Inhibition zones for standard CLSI medications (mm.)

Samples	*P. aeruginosa (ATCC 27853)*	*E. faecalis (ATCC 29212)*	*P. micra (ATCC 33270)*	*P. anaerobius (ATCC 27337)*	*F. nucleatum (ATCC 25586)*	*C. albicans (ATCC 10231)*
Amoxicillin and Clavulanic acid (10 µg/ml)		13.66	16.31	11.22		
Metronidazole (10 µg/ml)					9.15	
Ciprofloxacine (5µg/ml)	11.25					
Fluconazole (10 µg/ml)						12.68

Arctium lappa root formula showed the minimum inhibitory concentration (MIC) at 6.25 mg/ml for *Enterococcus Faecalis (ATCC29212), Pseudomonas aeruginosa (ATCC27853)* and *Candida albicans (ATCC10231)*. (Table 5).

Aloe vera gel showed the minimum inhibitory concentration (MIC) at 25 mg/ml for *Peptostreptococcus anaerobius (ATCC27337)* and *Fusobacterium nucleatum (ATCC25586)*, 12.5 mg/ml for *Parvinomas micra (ATCC33270)*, 6.25 mg/ml *for Pseudomonas aeruginosa (ATCC27853)* and *Candida albicans (ATCC10231)*, 3.125 mg/ml for *Enterococcus faecalis (ATCC29212)*. (Table 5)

Mix formula of *Arctium lappa* root powder and *Aloe vera* gel showed the minimum inhibitory concentration (MIC) 25 mg/ml for *Peptostreptococcus anaerobius (ATCC27337), Fusobacterium nucleatum (ATCC25586)* and *Parvimonas micra (ATCC33270)*, 6.25 mg/ml for *Candida albicans (ATCC10231)* and *Pseudomonas aeruginosa (ATCC27853)*, 3.125 mg/ml for *Enterococcus faecalis (ATCC29212)* (Table 5).

The lowest value of the minimum inhibitory concentration in case of the mix formula was found for *Enterococcus faecalis (ATCC29212)* (Table 5).

In order to compare specific antibiotics and antifungals, corresponding to the Clinical and Laboratory Standards Institute, minimum inhibitory concentrations for Amoxicillin and Clavulanic acid, Metronidazole, Ciprofloxacine and Fluconazole were determined (Table 6).

Table 5. Minimum Inhibitory Concentration (MIC) for plant extracts (mg/ml.)

Samples	*P. aeruginosa (ATCC 27853)*	*E. faecalis (ATCC 29212)*	*P. micra (ATCC 33270)*	*P. anaerobius (ATCC 27337)*	*F. nucleatum (ATCC 25586)*	*C. albicans (ATCC 10231)*
Arctium lappa Root extract (mg/ml)	6.25	6.25	100	100	100	6.25
Aloe barbadensis Miller gel extract (mg/ml)	6.25	3.125	12.5	25	25	6.25
Mix (mg/ml)	6.25	3.125	25	25	25	6.25

Table 6. Minimum Inhibitory Concentration (MIC) for standard CLSI medications (mg/ml.)

Samples	*P. aeruginosa (ATCC 27853)*	*E. faecalis (ATCC 29212)*	*P. micra (ATCC 33270)*	*P. anaerobius (ATCC 27337)*	*F. nucleatum (ATCC 25586)*	*C. albicans (ATCC 10231)*
Amoxicillin and Clavulanic acid (µg/ml)		1.56	3.125	3.125		
Metronidazole (µg/ml)					6.25	
Ciprofloxacine (µg/ml)	0.19					
Fluconazole (mg/ml)						12.5

Arctium lappa root formula showed the minimum bactericidal concentration (MBC) at 12.5 mg/ml for *Enterococcus Faecalis (ATCC29212), Pseudomonas Aeruginosa (ATCC27853)* and *Candida Albicans (ATCC10231)* (Table 7).

Aloe vera gel showed the minimum bactericidal concentration (MBC) at 6.25 mg/ml *for Enterococcus faecalis (ATCC29212),* 12.5 mg/ml for *Pseudomonas aeruginosa (ATCC27853)* and *Candida albicans (ATCC10231),* 50 mg/ml for *Peptostreptococcus anaerobius (ATCC27337)* and *Fusobacterium nucleatum (ATCC25586)* and 25 mg/ml for *Parvinomas micra (ATCC33270)* (Table 7).

Mix formula of *Arctium lappa* root powder and *Aloe vera* gel showed the minimum bactericidal concentration (MBC) 6.25 mg/ml for *Enterococcus faecalis (ATCC29212),* 12.5 mg/ml for *Candida albicans (ATCC10231)* and *Pseudomonas aeruginosa (ATCC27853),* and 50 mg/ml for *Parvinomas micra (ATCC33270), Peptostreptococcus anaerobius (ATCC27337)* and *Fusobacterium nucleatum (ATCC25586)* (Table 7).

The lowest value of the minimum bactericidal concentration (MBC) in case of the mix formula was found for *Enterococcus faecalis (ATCC29212)* (Table 7).

Table 7. Minimum bactericidal concentration (MBC) for plant extracts (mg/ml.)

Samples	*P. aeruginosa (ATCC 27853)*	*E. faecalis (ATCC 29212)*	*P. micra (ATCC 33270)*	*P. anaerobius (ATCC 27337)*	*F. nucleatum (ATCC 25586)*	*C. albicans (ATCC 10231)*
Arctium lappa root extract (mg/ml)	12.5	12.5	100	100	100	12.5
Aloe barbadensis Miller gel extract (mg/ml)	12.5	6.25	25	50	50	12.5
Mix (mg/ml)	12.5	6.25	50	50	50	12.5

For the comparison with specific antibiotics and antifungals, corresponding to the Clinical and Laboratory Standards Institute, minimum bactericidal concentrations for Amoxicillin and Clavulanic acid, Metronidazole, Ciprofloxacine and Fluconazole were determined (Table 8).

The working protocol for the root canal therapy follows different steps, all of them converging to a fundamental goal, the complete removal of the whole population of microorganisms. Some bacteria, like *Enterococcus faecalis*, or yeasts, *like Candida albicans* are resistant to the cleaning and shaping of the root canal and also to different intracanalar medications. Given these shortcomings, plant-based alternatives are being increasingly studied.

Table 8. Minimum bactericidal concentration (MBC) for standard CLSI medications (mg/ml.)

Samples	P. aeruginosa (ATCC 27853)	E. faecalis (ATCC 29212)	P. micra (ATCC 33270)	P. anaerobius (ATCC 27337)	F. nucleatum (ATCC 25586)	C. albicans (ATCC 10231)
Amoxicillin and Clavulanic acid (10µg/ml)		3.125	6.25	6.25		
Metronidazole (µg/ml)					12.5	
Ciprofloxacine (µg/ml)	0.38					
Fluconazole (mg/ml)						12.5

Although the culture and growth of anaerobic endodontic microorganisms represents a challenge for every researcher, the study of a number of six different bacterial strains adds value to the previously conducted studies [62].

The endodontic environment is a selective system, with preferences for certain species of microorganisms compared to others. Most bacteria are anaerobic or facultative anaerobic microorganisms and their sensitivity to the presence of oxygen varies by species. Progress in microbiological techniques allowed a series of microorganisms associated with endodontic to be identified.

Representative endodontic microorganisms such *as Enterococcus faecalis, Fusobacterium nucleatum, Peptostreptococcus anaerobius, Parvinomas micra, Pseudomonas aeruginosa* and *Candida albicans* were used for the antimicrobial and antifungal assay.

The mix extract of *Arctium lappa* root powder and *Aloe vera* gel demonstrated its highest efficiency against *Candida Albicans,* followed by *Enterococcus faecalis.*

Candida albicans is the predominant yeast identified and isolated from the infected root canal. It can adapt to different environments and can adhere to many types of surfaces. It can manifest a strong virulence expression and different morphologic varieties [63]. Research proved that *Candida albicans* is present in a higher percentage in reinfected or retreated root canals, compared to primary endodontic infections and can therefore play a role in the etiology of periapical disease [64]. This study demonstrates a very high efficiency of the mix extract of *Arctium lappa* root powder and *Aloe vera* gel against *Candida albicans.* The inhibition zone of the mix extract (11.62mm) is very close to the inhibition zone of Fluconazole (12.68mm), the specific antifungal medication given by the Clinical and Laboratory Standards Institute in 2015.

Enterococcus faecalis is known as the most rebel endodontic microorganism and is often resistant to intracanalar medication [65]. It is frequently the only bacterial species recovered from the previously treated root canals and is able to survive in the root canal on its own, as a single microorganism [66][67][68].

This study showed a good efficiency of the mix extract of *Arctium lappa* root powder and *Aloe vera* gel against *Enterococcus faecalis,* given that it is used in the correct dosage and at the correct minimal inhibitory and bactericidal concentration. The inhibition zone of the mix extract is 5.69 mm, compared to 12.68mm, corresponding to the inhibition zone of Amoxicillin and Clavulanic acid, the specific medication given by the Clinical and Laboratory Standards Institute in 2015.

A medium sensitivity to this formula exhibited *Pseudomonas aeruginosa*, *Parvinomas micra, Peptostreptococcus anaerobius* and *Fusobacterium nucleatum.*

Fusobacterium nucleatum and Pseudomonas aeruginosa are common microorganisms found in the roots of teeth with periapical radiolucency [69]. Previous studies indicated that *Fusobacterium nucleatum* is responsible for the inflammatory and painful episodes between treatment sessions, when the tooth is left open for drainage [70].

Peptostreptococcus anaerobiusis and *Parvinomas micra* are Gram-positive anaerobic cocci. The organisms are found in the commensal human flora but also in various infections, like endocarditis or infections of the gastrointestinal and genitourinary tracts [71] [72]. They are known for their implication in the root canal infections but also for the difficulty of their culture and growth [73].

The use of the mix gel at its correct inhibitory and bactericidal concentration diminishes the differences between the inhibition zones of the mix extract, compared to the specific antibiotics or antifungals, corresponding to the Clinical and Laboratory Standards Institute for each microorganism.

The valuable aspects brought by the minimal inhibitory concentration (MIC) and the minimal bactericidal concentration (MBC) validate the antimicrobial and antifungal effects of the mix extract of *Arctium lappa* root powder and *Aloe vera* gel.

CONCLUSIONS

In the present study we investigated an experimental substance, based on *Arctium lappa* root powder extract and *Aloe vera* gel, in relation with its content in bioactive compounds and its antibacterial and antifungal activity. Regarding the antimicrobial assay, the plant extract presented the highest activity against *Candida albicans*, followed by *Enterococcus faecalis*, the most resistant microorganisms in the root canal system. Our results, correlated with previous studies, show that bioactive compounds like chlorogenic acid, for *Arctium lappa* and aloe-emodin for *Aloe vera* are responsible for the efficiency of the extract against aerobic and anaerobic bacteria and as well against yeasts. The mix extract is also efficient against a series of other endodontic microorganisms, like *Pseudomonas aeruginosa*, *Parvimonas micra*, *Peptostreptococcus anaerobius* and *Fusobacterium nucleatum.* The use of a plant based gel as an auxiliary

method or even as an alternative to the classic root canal disinfection protocol is a step forward in the continuous attempt of the practitioners to obtain a sterilised root canal. Obviously, further and extended studies are needed, in order to define the mechanisms of in vivo antibacterial and antifungal activity .

EXPERIMENTAL SECTION

HPLC/ESI(+)-MS assay

Sample preparation for the injection in the HPLC system. The extraction of the phenolic compounds from the root of *Arctium lappa* was carried out as follows: 2 g of the sample were placed in a round bottom flask, along with 15 ml of 70% ethanol. The extraction was performed in reflux conditions, at 90° C for 2 hours. The solvent was filtered and the residue was extracted a further two times. The extract was combined and evaporated under reduced pressure, to a total volume of 15 ml, in order to obtain the necessary concentration. The sample was filtered through 0,45 μm nylon filter, followed by the injection in the HPLC system.

Aloe vera gel was extracted in 70% ethanol, at a rate of 1/1 (v / v). The sample was filtered through 0,45 μm nylon filter and followed by the injection in the HPLC system.

HPLC/ESI(+)-MS method. For this procedure we used the Agilent 1200 Series HPLC system. The model was equipped with a quaternary pump delivery system, a solvent degasser, an autosampler and a UV-Vis detector, supplied with photodiode and coupled with a singlequadrupole mass detector (MS), Agilent 6110 model (Agilent Technologies, Chelmsford, MA, USA).

We carried out the separation of the phenolic compounds on an Eclipse XDB C18 column, dimensions 4.6 x 150 mm, 5 μm, from Agilent Technologies. The mobile phases consisted in: A- water + 0.1 % acetic acid and B- acetonitrile + 0.1 % acetic acid, with the following gradient evolution: min. 0-2: solvent B 5%, min. 2-18: solvent B 40 %, min. 18-20: solvent B 90 %, min 20-24: solvent B 90 %, min. 24-25: solvent B 5%. The process was carried out for 30 minutes at a temperature of 25° C and a rate of 0.5 ml / min.

We monitored the chromatograms at 280 and 340 nm. We identified the compounds based on their retention times and UV-VIS spectra and performed comparisons with the chlorogenic acid, as a single external standard, purchased from Sigma-Aldrich, Darmstadt (Germany) and with previous published data. Accordingly, the samples were analysed by HPLC/ESI (+)-MS.

We obtained the mass spectrometric data by using the positive ionization mode. For the measurements we used following parameters: ion spray voltage of 3000V, capillary temperature of 300°C, nitrogen flow rate 8 l min., m/z:100-1000, full-scan. Data acquisition and interpretation of results was done using ChemStation software, Agilent Technologies, Chelmsford, MA, USA.

Antibacterial and antifungal activity. For the bioassay we used five bacterial strains and a yeast: one aerobic bacteria (*Pseudomonas aeruginosa-ATCC27853),* one aerotolerant anaerobic bacteria (*Enterococcus faecalis-ATCC29212*), three anaerobic bacteria (*Parvinomas micra-ATCC33270, Peptostreptococcus* anaerobius-*ATCC27337, Fusobacterium nucleatum-ATCC25586*) and a yeast, *Candida albicans (ATCC10231).* The microbial strains were purchased from Microbiologics, Saint Cloud, Minnesota, USA. All tested microorganisms were at the fourth passage from the American Type Culture Collection, as described in their Quality Control certificates. We cultured the bacteria on Muller-Hinton Agar (BioMerieux, Lyon, France) for aerobic microorganisms, on Columbia Agar (BioMerieux, Lyon, France) for anaerobic microorganisms and on Sabouraud Agar (BioMerieux, Lyon, France) for yeast. Cultures were stored at 4°C and subcultured once a month.

For the disc diffusion assay, we used the following plant extracts: 100 mg of *Arctium lappa* root powder, suspended in 1 ml distilled water, mixed for 8 hours and filtered by 0.45 µm Millipore filter, 100 ml of *Aloe vera* gel extract and 1:1 *Arctium lappa* root extract and *Aloe vera* gel mixture. We carried out the primary antimicrobial test screening by disc diffusion, using 100 µl of suspension containing 10^8 CFU/ml of bacteria and 10^6 CFU/ml of *Candida albicans,* spread evenly on the surface of the Muller–Hinton Agar, Columbia Agar, respectively Sabouraud Agar plates. Sterile 6 mm discs were used and processed, in triplicates, to contain 20 µl of the extract; these discs were then placed on the inoculated agar. For each studied microorganism we used specific antibiotics as following: *Amoxicillin and Clavulanic acid* for *Enterococcus faecalis*, *Peptostreptococcus anaerobius* and *Parvimonas micra*, *Metronidazole* for *Fusobacterium nucleatum*, *Ciprofloxacin* for *Pseudomonas aeruginosa* and *Fluconazole* for *Candida albicans*. For aerobic bacteria, the inoculated plates were incubated for 24 h at 37°C, for anaerobic bacteria for 48 h at 37°C in CO_2 gas bags (BioMerieux, Lyon, France) and for *Candida albicans* the inoculated plates were incubated for 2-3 days at 30°C. Clear inhibition zones around discs indicated the presence of antimicrobial activity. For high fidelity of the results, each assay was repeated three times.

Microdilution method. We used the modified microdilution technique to evaluate the antimicrobial and antifungal activity. We cultured the bacterial species overnight, at 37°C in Muller-Hinton Broth (BioMerieux, Lyon, France) for aerobics and yeast and on Thioglycollate Broth with Resazurin (BioMerieux, Lyon, France) for anaerobics. We adjusted the bacterial cell suspensions with sterile saline solution, to a concentration of approximately 3X 10^5 CFU/ml in a final volume of 100 µl per well. We stored the inoculum at +4°C for further use. We cultured dilutions of the inoculum on solid Muller–Hinton Agar (BioMerieux, Lyon, France), and Columbia Agar (BioMerieux, Lyon, France) for bacteria, to verify the absence of contamination and to check the validity of the inoculum. We determined the minimum inhibitory concentrations (MICs) by a serial dilution technique, using 96-well microtitre plates. Different solvent dilutions of ethanol were carried out: methanol extracts were carried out over the wells containing 100 µl of Muller-Hinton Broth or Thioglycollate broth

with Resazurin and afterwards, 10 µl of inoculum was added to all the wells. The microplates were incubated for 24-48 h at 37°C. We detected the minimum inhibitory concentration of the samples following the addition of 20 µl (0.2 mg/ml) of Resazurin solution to each well, and we incubated the plates for 2 h at 37°C. In general, a change from blue to pink indicates reduction of Resazurin and therefore bacterial growth. The minimum inhibitory concentration was defined as the lowest drug concentration that prevented this colour change.

We determined the minimum bactericidal concentrations (MBCs) by serial subcultivation of a 2 µl into microtitre plates, containing 100 µl of broth per well and further incubation for 48 h at 37°C. The lowest concentration with no visible growth was defined as minimum bactericidal concentration, indicating 99.5% killing of the original inoculum. As a positive control for bacterial growth we used Streptomycin (Sigma P 7794), 0.05–3 mg/ml.

ACKNOWLEDGMENTS

R E F E R E N C E S

[1]. Y.S. Chan, L.N. Cheng, J.H. Wu, E. Chan, Y.W. Kwan, S.M. Yuen Lee, G.P Heng Leung, P. Hoi-Fu Yu, S. W. Chan, *Inflammopharmacology,* **2011**, *19,* 245

[2]. S.E. Edwards, I. da Costa Rocha, E.M. Williamson, M. Heinrich, "Burdock, in Phytopharmacy: An Evidence-Based Guide to Herbal Medical Products", John Wiley & Sons, Ltd, Chichester, **2015**, chapter 17

[3]. A. Miglani, R. K. Manchanda, *Homeopathy*, **2014**, *103*, 203

[4]. T.G. Tutin, V.H. Heywood, N.A. Burges, D.M. Moore, D.H. Valentine, S.M. Walters, D.A. Webb, "Flora Europaea: Plantaginaceae to Compositae (and Rubiaceae)", Cambridge University Press, Cambridge, **2010**, 215

[5]. J. Liu, Y.Z. Cai, R.N.S. Wong, C. Kai-Fai Lee, S. Chi Wai Tang, S. Cho Wing Sze, Y. Tong, Y. Zhang, *Journal of Agricultural and Food Chemistry,* **2012**, *60*, 4067

[6]. P. Duh, *Journal of the American Oil Chemists' Society,* **1998**, *75*, 455

[7]. J. Cao, C. Li, P. Zhang, X. Cao, T. Huang, B. Yungui, C. Kaoshan, *African Journal of Biotechnology*, **2012**, *11*, 9079

[8]. F.S. Predes, A. Ruiz, J.E. Carvalho, M.A. Foglio, H. Dolder, *BMC Complementary and Alternative Medicine,* **2011,** *11*, 1

[9]. Z. Lou, H. Wang, W. Lv, C. Ma, Z. Wang, S. Chen, *Food Control,* **2010**, *21***,** 1272

[10]. T.G. Tutin, V.H. Heywood, N.A. Burges, D.M. Moore, D.H. Valentine, S.M. Walters, D.A. Webb, "Flora Europaea: Alismataceae to Orchidceae (Monocotyledones)", Cambridge University Press, Cambridge, 2005, 19

[11]. K. Eshun, Q He, *Critical reviews in food science and nutrition*, **2004**, *44*, 91

[12]. C.T. Ramachandra, P.S. Rao, *American Journal of Agricultural and Biological Sciences*, **2008**, *3*, 502

[13]. Jo. H. Hamman, *Molecules* **2008**, *13*, 1599
[14]. M. Saito, M. Tanaka, E. Misawa, R. Yao, K. Nabeshima, K. Yamauchi, F. Abe, Y. Yamamoto, F. Furukawa, *Bioscience, Biotechnology, and Biochemistry*, **2016**, *80*, 1416
[15]. S.E. Dal'Belo, L.R. Gaspar, M. Campos, *Skin Research and Technology*, **2006**, *12*, 241
[16]. J.A. Vinson, H.A. Kharrat, L. Andreoli, *Phytomedicine,* **2005***, 12,* 760
[17]. A. Hindustan, A. Chandrashekar, B. Anil Kumar, B. Reddy B.V. Ravindra, V.S Lakshmi, *International Journal of PharmTech Research,* **2010***, 2,* 1018
[18]. M.R. Akhoondinasab, M. Akhoondinasab, M. Saberi, *World Journal of Plastic Surgery,* **2014***, 3,* 29
[19]. M. Tarameshloo, M. Norouzian, S. Zarein-Dolab, M. Dadpay, J.Mohsenifar, R. Gazor, *Anatomy and Cell Biology*, **2012***, 45*, 170
[20]. M.R. Tabandeh, A. O'ryan, A. Mohammad Valipour, *International Journal of Biological Macromolecules,* **2014**, *65*, 424
[21]. L Cellini, S Di Bartolomeo, E Di Campli, S. Genovese, M. Locatelli, M Di Giulio, *Letters in Applied Microbioogy,* **2014***, 59,* 43
[22]. R. Pandey, A Mishra, *Applied Biochemistry and Biotechnology,* **2010***, 160,* 1356
[23]. Bernardes, M. P.F. Rodrigues, G.K. Bacelli, E. Munin, L.P. Alves, M.S. Costa, *Mycoses,* **2012***, 55*, 257
[24]. V. Singh, S.P. Singh, M. Singh, A.K. Gupta, A. Kumar, *Applied Biochemistry and Biotechnology,* **2015***, 175,* 2542
[25]. M.R. Saini, P.K. Goyal, G. Chaudhary, *Journal of Environmental Pathology, Toxicology and Oncology*, **2010**, *29*, 127
[26]. W. Lowther, K. Lorick, S.D. Lawrence, W.S. Yeow, *Transgenic Research*, **2012**, *21*, 1349
[27]. J.R. de Oliveira, R.B.de Aguiar Almeida, P. das Graças Figueiredo Vilela,' F.E. de Oliveira, R.F. da Rocha, A.O.C. Jorge, L.D. de Oliveira, *Archives of Oral Biology*, **2014**, *59*, 808
[28]. R. Pradeep, E. Agarwal, S.B. Naik, *Journal of Periodontology*, **2012**; *83,* 797
[29]. A. Ahmadi, *Chinese Journal of Integrative Medicine,* **2012***, 18,* 635
[30]. G. Bhat, P. Kudva, V. Dodwad*, Journal of Indian Society of Periodontology,* **2011***, 15,* 205
[31]. P. Chantarawaratit, P. Sangvanich, W. Banlunara, K. Soontornvipart, P. Thunyakitpisal, *Journal of Periodontal Research***, 2014***, 49,* 164
[32]. A. Gatot, J. Arbelle, A. Leiberman, I. Yanai-Inbar*, Journal of Endodontics,* **1991**, *17*, 573
[33]. R.S.Chhabra, J.E. Huff, J.K. Haseman, M.R. Elwell, A.C. Peters**,** *Food and Chemical Toxicology,* **1991**, *29,*119
[34]. B.P.F.A. Gomes, M.E. Vianna, A.A. Zaia, J.F.A. Almeida, F.J. Souza-Filho, C.C.C. Ferraz, *Brazilian Dental Journal,* **2013**, *24,* 89
[35]. B.B. Jyoti, *Journal of Conservative Dentistry*, **2005**, *8,* 31
[36]. J.V. Pereira, D.C. Baldoqui Bergamo, J.O. Pereira, S. de Castro França, R.C. Linhares Rodrigues Pietro, Y.T.C. Silva-Sousa*, Brazilian Dental Journal,* **2005,** *16,* 192
[37]. M. Pujar, S.D. Makandar, *International Journal of Contemporary Dentistry*, **2011**, *2,* 34
[38]. A. Abbaszadegan, S. Sahebi, A. Gholami, *Journal of Investigative and Clinical Dentistry*, **2016**, *7,* 93
[39]. O.R.Casian, M. Parvu, L. Vlase, M. Tamas, *Fitoterapia*, **2007**, *78,* 219
[40]. M.N. Clifford, *Journal of the science of Food and Agriculture*, **2000**, *80,* 1033
[41]. Farah, M. Monteiro, C.M. Donangelo, S. Lafay, *The Journal of Nutrition*, **2008**, *138,* 2309

[42]. R. Ferracane, G. Graziani, M. Gallo, V. Fogliano, A. Ritieni, *Journal of Pharmaceutical and Biomedical Analysis,* **2010***, 51,* 399
[43]. Z. Lou, H. Wang, S. Zhu, C. Ma, Z. Wang, *Journal of Food Science*, **2011***, 76*, M398
[44]. C.M. Ma, M. Kully, J.K. Khan, M. Hattori, M. Daneshtalab, *Bioorganic & Medicinal Chemistry*, **2007**, *15*, 6830
[45]. N. Venkateshbabu, S. Anand, M. Abarajithan, S.O. Sheriff, P.S. Jacob, N. Sonia, *The Open Dentistry Journal*, **2016**, *10*, 214
[46]. N. Lourith, M. Kanlayavattanakul, *Journal of Oleo Science*, **2013***, 62,* 235
[47]. J. Zhang, J. Chen, Z. Liang, C. Zhao, *Chemistry & Biodiversity*, **2014**, *11,* 1
[48]. Y. Cai, Q. Luo, M. Sun, H. Corke, *Life Sciences,* **2004***, 74,* 2157
[49]. S. Su, X. Cheng, M. Wink, *Journal of Pharmacy and Pharmacology,* **2015***, 67,* 1316
[50]. S. Su, *X.* Cheng, M. Wink, *Phytomedicine,* **2015,** *22,* 301
[51]. F. Zhao, L. Wang, K. Liu - *Journal of Ethnopharmacology*, **2009**, *122,* 457
[52]. S. Lee, S, Shin, H. Kim, S. Han, K. Kim, J. Kwon, J. Kwak, C. Lee, N. Ha, D. Yim, K. Kim, *Journal of Inflammation,* **2011***, 8*, 1
[53]. J.E. Kim, H.J. Kim, S. Pandit, K.W. Chang, J.G. Jeon, *Fitoterapia*, **2011***, 82*, 352
[54]. V. Cataldi, S. Di Bartolomeo, E. Di Campli, A. Nostro, L. Cellini, M. Di Giulio, *International Journal of Immunopathology & Pharmacology,* **2015**, *28*, 595
[55]. E. Cook, *The Internet Journal of Microbiology*, **2008***; 4*, 1
[56]. S. Alemdar, S. Agaoglu, *Journal of Animal and Veterinary Advances,* **2009***, 8,* 99
[57]. T. Hatano, M. Kusuda, K. Inada, T. Ogawa, S. Shiota, T. Tsuchiya, T. Yoshida, *Phytochemistry*, **2005**, *66*, 2047
[58]. S.K. Agarwal, S.S. Singh, S. Verma, S. Kumar, *Journal of Ethnopharmacology,* **2000***, 72,* 43
[59]. T. Pecere, M.V. Gazzola, C. Mucignat, C. Parolin, A. Cavaggioni, G. Basso, A. Diaspro, B. Salvato, M. Carli, G. Palu, *Cancer Research*, **2000**, *60*, 2800
[60]. H.Z. Lee, *British Journal of Pharmacology*, **2001**, *134,* 1093
[61]. P.L. Kuo, T.C. Lin, C.C. Lin, *Life Sciences*, **2002,** *71*, 1879
[62]. M.M. Menezes, M.C.Valera, A.O.C Jorge, C.Y.Coga-Ito, C.H.R Camargo, M.N.G Mancini, *International Endodontic Journal*, **2004**, *37,* 311
[63]. P. Sudbery, N. Gow, J. Berman, *Trends in Microbiology*, **2004**, *12*, 317
[64]. J.F. Siqueira Jr., B. H. Sen, *Oral Surgery, Oral Medicine, Oral Pathology, Oral Radiology, and Endodontology,* **2004**, *5,* 632
[65]. M. Evans J.K. Davies, G. Sundqvist, D. Figdor, *International Endodontic Journal,* **2002**, *35*, 221
[66]. H.H. Hancock III, A. Sigurdsson, M. Trope, J. Moiseiwitsch, *Oral Surgery, Oral Medicine, Oral Pathology, Oral Radiology, and Endodontology*, **2001**, *91*, 579
[67]. N. Vivacqua-Gomes, E.D. Gurgel-Filho, B.P.F.A. Gomes, C.C.R. Ferraz, A.A. Zaia, F.J. Souza-Filho, *International Endodontic Journal*, **2005**, *38*, 697
[68]. I.N. Rôças, J.F. Siqueira, *Journal of Clinical Microbiology*, **2012**, *50*, 1721
[69]. F.C.S. Chu, C.S.P. Tsang, T.W. Chow, L.P. Samaranayake, *Journal of Endodontics*, **2005**, *31*, 424
[70]. L.E.C. de Paz Villanueva, *Oral Surgery, Oral Medicine, Oral Pathology, Oral Radiology, and Endodontology*, 2002*, 93*, 179
[71]. M.P. Riggio, A. Lennon, *Journal of Medical Microbiology*, **2002**, *51*, 1097
[72]. A. Gomez, D. A. Gerber, E. Zambrano, N. Banaei, *Anaerobe,* **2015**, *36*, 53
[73]. A.M.T. Öncül, E. Uzunoğlu, Z.C. Karahan, A.M. Aksoy, R. Kişnişci, Ö. Karaahmetoğlu, *Journal of Oral and Maxillofacial Surgery*, **2015**, *73,* 259

4-AMINOPIPERIDINE BASED NEW AMINO-*s*-TRIAZINES AS POTENTIAL DENDRITIC BUILIDING-BLOCKS

ANA-MARIA ŢICALĂ[a], DAN PORUMB[a], CARMEN SĂCĂLIŞ[a]* AND MIRCEA DARABANTU[a]*

ABSTRACT. Starting from commercial 4-aminopiperidine, three new amino-*s*-triazines, seen as potential dendritic building-blocks, were synthesised by chemoselective S_N2-Ar amination of cyanuric chloride. A three steps synthetic sequence, (i) Boc-chemoselective *N*-protection of 4-aminopiperidine → (ii) amination of cyanuric chloride → (iii) deprotection, yielded a novel potential dendritic central unit, 2,4,6-tris[(piperidin-4-yl)amino]-*s*-triazine.

***Keywords:** 4-aminopiperidine, S_N2-Ar amination, dendritic cores, melamines*

INTRODUCTION

N,N'N''-substituted melamines are well-known building-blocks in the construction of dendritic systems [1] as early as 2000 [1a] when Simanek and co-workers reported the access to the first dendrimer, encompassing *s*-triazine rings as branch-cells and cores, obtained by iterative chemoselective S_N2-Ar amination of cyanuric chloride. During elaboration of these arborescent architectures, the need of *meta*-trivalent and C_3 symmetric central building-blocks, such as 2,4,6-tris(piperazin-1-yl)-*s*-triazine **1** (Scheme 1) was revealed [2]. Melamine **1** can be easily prepared by amination of cyanuric chloride with commercial *N*-(*tert*-butoxy- carbonyl)piperazine, followed by the removal of Boc protecting groups [2a].

In continuation of our efforts in a similar direction, we previously reported the synthesis and stereodynamic behaviour of a new potential dendritic building-block, 2,4,6-tris(4-oxopiperidin-1-yl)-*s*-triazine **2** (Scheme 1) [3]. Compound **2** is readily available by amination in of cyanuric chloride with the use of the ethylene ketal of 4-piperidone and final acidolysis of the 1,3-dioxolane rings.

---

[a] *Babeş-Bolyai University, Faculty of Chemistry and Chemical Engineering, Department of Chemistry 11 Arany Jànos st., RO-400028, Cluj-Napoca, Romania*

* *Corresponding authors: cbatiu@chem.ubbcluj.ro, darab@chem.ubbcluj.ro*

ANA-MARIA ŢICALĂ, DAN PORUMB, CARMEN SĂCĂLIŞ, MIRCEA DARABANTU
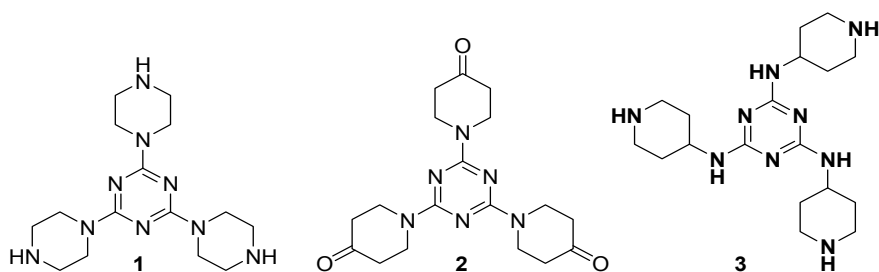
Scheme 1

Subsequent to the above findings, the aim of the present work is to account on the first synthesis of an identically *N,N',N"*-substituted melamine built from 4-aminopiperidine through its primary amino group, namely 2,4,6-tris[(piperidin-4-yl)amino]-*s*-triazine **3** (Scheme 1), together with that of its main precursors. Last but not least, it is worth mentioning that, recently, series of 4-aminopiperidine-linked amino-*s*-triazines were described as well and evaluated for *in vitro* anti-HIV activity with very promising results [4].

RESULTS AND DISCUSSION

1. Structural premises

Previously reported *N,N',N"*-substituted melamines **1** and **2** are statistically C_3-symmetric owing to the chair ⇆ chair flipping of piperazine or 4-piperidone rings (Scheme 2). On the other hand, due to the p(N-exocyclic)→π(*s*-triazine) extended conjugation, the well-documented partial double bond character of the C(*s*-triazine)-N(exocyclic) linkages [5] promotes, at room temperature, hindered rotation about these connexions [3b, 3c]. In terms of DNMR, this feature is defined as "slow exchange status between (un)equally populated sites" [6], i.e., in the case of melamines **1** and **2**, a slow topomerisation. Upon heating up to 80-90 °C, these C_3-symmetric melamines reach a fast freely rotating status about all bonds C(*s*-triazine)-N(exocyclic) (single mediated structures) in a rapid topomerisation [3b].

In the target melamine **3** (Scheme 2), since the anchorage of the 4-aminopiperidine units to the *s*-triazine ring is realised *via* the primary amino group, the abovementioned stereodynamism implies, in a topological idealized model, the existence of two interchangeable rotational diastereomers, **3**-*propeller* and **3**-*asymmetric* [5i] from which only the first one is C_3-symmetric. Conversely, in both rotamers, the piperidine rings should be anancomeric* due to the presence

---

* According to the definition from Ref. [6b] "Fixed in a single conformation either by geometric constraints or because of an overwhelmingly on-sided conformational equilibrium"

in position C-4-eq of a bulky (*s*-triazin-2, -4, -6-triyl)amino ligand. Finally, as a result of the same p(N-exocyclic)→π(*s*-triazine) extended delocalisation, pyramidal inversion and proton interchange should involve, primarily, the piperidine nitrogen.
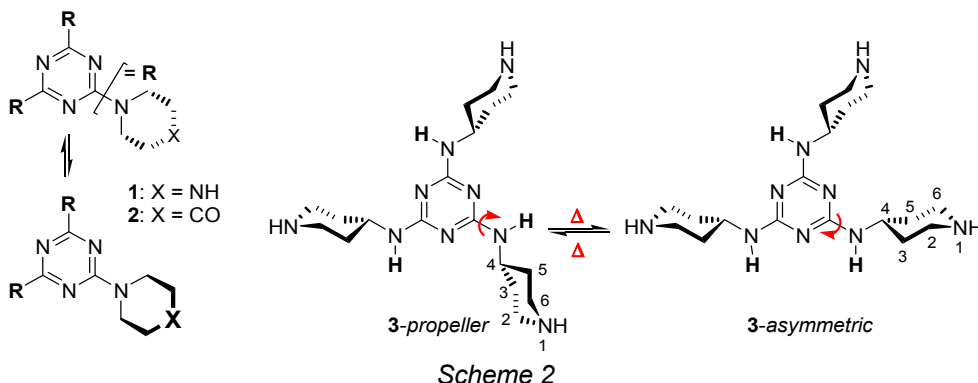
Scheme 2

2. Synthesis

With the above premises in mind, we have obtained melamine **3** in three steps **I**-**III** (Scheme 3). Though 1-Boc-4-aminopiperidine **4** is commercial (CAS Number 87120-72-7, GC purity $\geq$ 96.5%) [7], we decided to prepare this compound by applying a patented [8] simple methodology (**I**). While the

5a (68%*): R^2 = Cl
5b (21%): R^1 = R^2
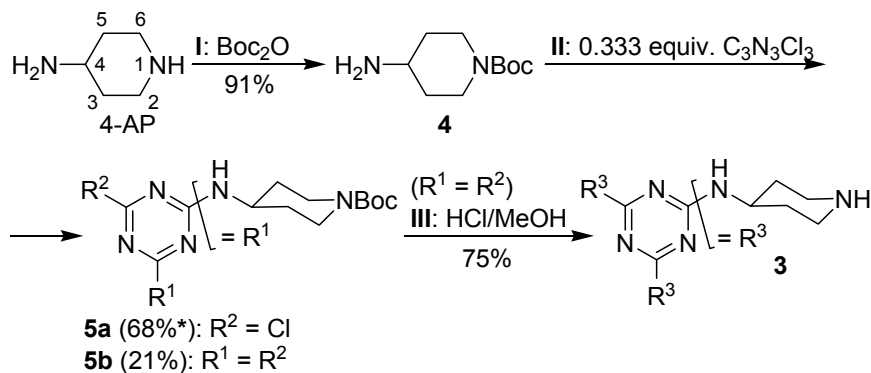
*Partial conversions of cyanuric chloride into the depicted compounds, based on the effective amounts of material isolated after column chromatography

Key

I: 1.020 equiv. Boc_2O, 1.005 equiv. TEA, H_2O : 1,4-dioxane (9:5 v/v) / 2-4 ^{o}C (1 h) / r.t. (12 h) / N_2
II: 0.333 equiv. cyanuric chloride, 0.333 equiv. K_2CO_3, 1,4-dioxane / r.t. (24 h) / reflux (88 h) / N_2
III: 20.328 equiv. HCl (aq. 6 N HCl), MeOH / 0-1 ^{o}C (70 min) / 0 ^{o}C (2 h) / r.t. (3 h) / 40 ^{o}C (15 h) / N_2 / aq. NaOH 10%, 0 ^{o}C, pH = 14

Scheme 3

synthetic protocol was reproducible, our work-up to isolate crude product **4** had to be different with respect to the cited literature. In our hands, the extraction of the organic material with ethyl acetate followed by concentration under mild conditions and predicted slow crystallisation [8], afforded a mixture of compounds with a GC-MS composition as 66.5% **4** (1-Boc-4-NH$_2$ derivative) and 33.5% an additionally *N*-acetylated analogue of **4**, 1-Boc-4-NH-Ac (transamidation product, not depicted in Scheme 3).

Replacement by us of ethyl acetate with chloroform provided crude compound **4** only ($\geq$ 97% GC-MS purity).

Concerning the utility of this preliminary chemoselective *N*-protection step, we note that the previous use of 4-aminopiperidine in melamine dendritic chemistry, playing the role of linker, is already documented [1b, 9c]. However, this role refers to the free diamine only. Thus, by exploiting the higher basicity and nucleophilicity of the secondary amino group against the primary one, two distinct chloro-diamino-*s*-triazine dendrons can be attached to 4-aminopiperidine. This strategy was based on Simanek and co-workers' "relative reactivity maps" [9a, 9b, 9d, 9e] of several (aza)alicyclic (di)amines against cyanuric chloride. In the case of 4-aminopiperidine, one can approximate the pK_b of the primary amino-group as being comparable with that of isopropyl amine (3.37) and that of the secondary amino-group similar with that of piperidine itself (2.78) [10].

Furthermore (**II**), amination of cyanuric chloride with three molar equivalents of **4** afforded, constantly, the mixture of two compounds, chloro-diamino-*s*-triazine **5a** (major) and melamine **5b** (minor), separable by column chromatography. In spite of various conditions used (solvent: 1,4-dioxane, THF or toluene; proton scavenger: K$_2$CO$_3$ or DIPEA), neither global conversion of cyanuric chloride ($\sim$85%) nor chemoselectivity (**5a**:**5b** $\sim$3:1) could be improved. One reason for these results consists of the conformational nature of our amino-nucleophile, a real rigid "back-bone" which did not allow an appropriate steric arrangement, mandatory to the S$_N$2-Ar process◆ (see later discussion in Section 3). No similar examples were reported so far (including as well the case of simple but flipping cyclohexylamine [11] in reaction with cyanuric chloride [12]), except our previous data concerning other saturated six-membered and anancomeric amino-heterocycles, e.g. amino-1,3-dioxanes [13a-c] and 4,4'-bipiperidine [3c, 13d].

Final deprotection (**III**) of **5a** in a 6N HCl aq. / MeOH medium gave the expected *N,N',N''*-substituted melamine **3** (Scheme 3) with a good yield. In this purpose, we followed, with minor modifications, the previously published procedure of Simanek and co-workers [2a]. As other piperidine ring systems, earlier reported by us [3, 13c, 13d], melamine **3** required storage under inert atmosphere in order to avoid its carbonation.

◆ Indeed, the same total amination of cyanuric chloride performed with flipping 1-Boc-piperazine, provides the corresponding melamine in high yield (90-93%), during 20 h in refluxing THF [2a].

3. *Structural investigations based on (VT) ^{1}H-NMR*

The identity of all compounds under consideration was fully confirmed by routine analysis (see EXPERIMENTAL SECTION). In such doing, we were particularly interested in the moderate reactivity of our amino-nucleophile **4** supported by the experimental conditions, depicted in Scheme 3. Next, since (VT) NMR is, by far, the optimal option in order to investigate the specific stereodynamism of amino-*s*-triazines [3, 5, 9b, 13], we adopted as well this technique for the present discussion (Table 1).

The (VT) ^{1}H-NMR data in are mandatory to several comments:

a) The anancomeric nature of compounds **4**, **5a**, **5b** and **3** was supported by important ^{1}H geminal anisochronies at piperidine positions C-2(6) and C-3(5), expressed as $\Delta\delta_H = \delta_{H\text{-eq}} - \delta_{H\text{-ax}} > 0$ values. Regardless the NMR solvent (CDCl$_3$ or DMSO-d_6) and temperature (r.t. or 353 K), in compounds **4**, **5a**, and **5b** geminal anisochrony was much higher in positions C-2(6), α-located against the carbamate group (around 1 ppm!), than in positions C-3(5) (0.32-0.66 ppm) [14]. Upon heating at 353 K, no reached flexibility of the piperidine ring skeleton, as δ_H mediating $\delta_{H\text{-eq}} \leftrightarrows \delta_{H\text{-ax}}$ values, was observed.

Table 1. Relevant (VT) ^{1}H-NMR δ_H values of compounds **4**, **5a**, **5b** and **3** on 400 MHz time scale

No.	Solvent	T (K)	H-3, -5 (ax)	H-3, -5 (eq)	H-2, -6 (ax)	H-2, -6 (eq)	H-4 (ax)	NH[b]
					δ_H (ppm)[a]			
4	CDCl$_3$	298	1.29	1.75	1.89	2.78	2.72	3.98
	DMSO-d_6	298	1.22	1.66	2.72	3.82	3.04	3.39
	DMSO-d_6	353	1.30	1.69	2.82	3.81	2.50	3.43
5a	CDCl$_3$	298	1.27	1.93	2.88	4.00	3.88	5.31 5.53 5.65 6.11
	DMSO-d_6	298	1.30	1.76	2.82	3.87	3.87	7.45 7.77 7.79 7.91
	DMSO-d_6	353	1.40	1.80	2.87	3.90	3.87	7.44 7.55

No.	Solvent	δ_H (ppm)[a]						
		T (K)	H-3, -5 (ax)	H-3, -5 (eq)	H-2, -6 (ax)	H-2, -6 (eq)	H-4 (ax)	NH[b]
5b	CDCl$_3$	298	1.32	1.93	2.86	3.98	3.88	4.84 4.95
	DMSO-d_6	298	1.30	1.71	2.75	3.91	3.88	6.27 6.41 6.51 6.70
	DMSO-d_6	353	1.36	1.80	2.82	3.91		6.13
3[c]	D$_2$O+DCl	298	-0.31	0.02	0.91 1.02	1.25	1.85 2.15	-

[a] Labelling of topological equivalent positions as (') and (") was omitted for reasons of simplicity.
[b] When multiple δ_H values are collected, they refer to detection of different stereoisomeric species issued from the rotational diastereomerism about C(s-triazine)-N(exocyclic) partial double bond (see discussion).
[c] As protonated form; the D$_2$O resonance (at 4.79 ppm) was taken as reference signal.

Particularly, the ^{1}H-NMR spectra of our amino-nucleophile **4** at room temperature not only that fully confirmed all above but also allowed the assignment, based on the stereospecific homocoupling ($^nJ_{H,H}$) patterns in the sequence C-2(6)-C-3(5)-C-4, of the equatorial position of the amino-group (Figure 1).

b) The presence of the carbamate group (>N-CO-O^{t}Bu), with a well-documented magnetic anisotropy [15], had two major consequences:

(i) the occurrence, at room temperature, of a slow rotational motion about the partial double-bond in the amide sequence >N-(C=O)- $\leftrightarrow$ >N$^+$=(C-O$^-$)-, unable, however, to induce any chemical non-equivalence between proximal protons H-2-eq vs. H-6-eq or carbons C-2 vs.C-6. That is, the electronic effect of the O^{t}Bu fragment, acting as EDG (or ERG), was concurrent against the effective existence of the above partial-double bond.

(ii) the carbamate group was responsible for the observed geminal $\Delta\delta_H$ anisochrony, and, in tandem with the s-triazinylamino unit equatorial location (compounds **5a** and **5b**), determined the rigidity of the piperidine rings.

c) At room temperature, compound **5a** displayed an expected three terms frozen rotational equilibrium of type $a(nti) \leftrightarrows s(yn)$ about the partial double bonds C(s-triazine)-N(exocyclic) (Chart 1). Discrimination between rotameric species was made founded on the different proximity of the best separated ("indicative") protons, NH, with respect to the dipole moment of the bond C-2(s-triazine)-Cl, i.e. this link was considered a strong deshielding factor ("dipole rule" [3, 13, 16], Table 1). The rotameric occurrence was non statistic♥ but dependent on the ability of the solvent to act as a hydrogen bond acceptor [5i],

---

♥ (%)**5a** (a-a) = **5a** (s-s) = 25, (%)**5a** (a-s) = 50 [the (a-s) arrangement is, statistically, twice favored]
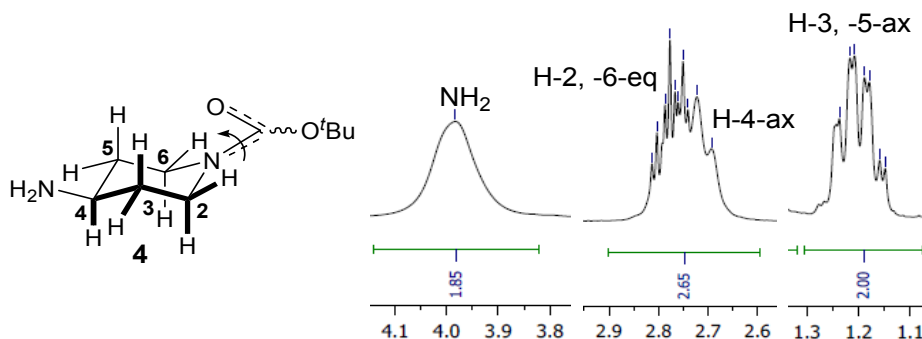
Figure 1. Details from the ^{1}H-NMR spectrum (400 MHz, CDCl$_3$, 298 K) of compound **4** (crude product): 3.98 (2H, br s, NH$_2$), 2.78 (2H, ddd, $^2J_{gem}$~8.9 Hz, $^3J_{cis\text{-}eq\text{-}ax}$~$^3J_{trans\text{-}eq\text{-}eq}$=4.3 Hz, H-2, -6-eq), 2.72 (1H, br dd app. br t, $^3J_{trans\text{-}ax\text{-}ax}$=11.6 Hz, H-4-ax), 1.19 (2H, dddd, $^2J_{gem}$~$^3J_{trans\text{-}ax\text{-}ax}$~$^3J_{trans\text{-}ax\text{-}ax}$=11.7 Hz, $^3J_{cis\text{-}ax\text{-}eq}$=3.8 Hz, H-3, -5-ax) ppm.

	Occurrence (%)		
Rotamer	CDCl$_3$	DMSO-d_6	TG (ppb/K)[a]
(*a-a*)	12	36	-7.45
(*a-s*)	48	57	-5.27, -4.91
(*s-s*)	40	7	-0.91

[a]Calculated as [($\delta_H^{298\ K}$ - $\delta_H^{353\ K}$)/(298 K - 353 K)]×10^3<0 (δ_H values taken from Table 1)

*1-*tert*-butoxycarbonylpiperidin-4-yl unit

Chlorine atom and the *N*-ligand **R as references for descriptors *a*(*nti*) and *s*(*yn*) [3, 5i, 13]
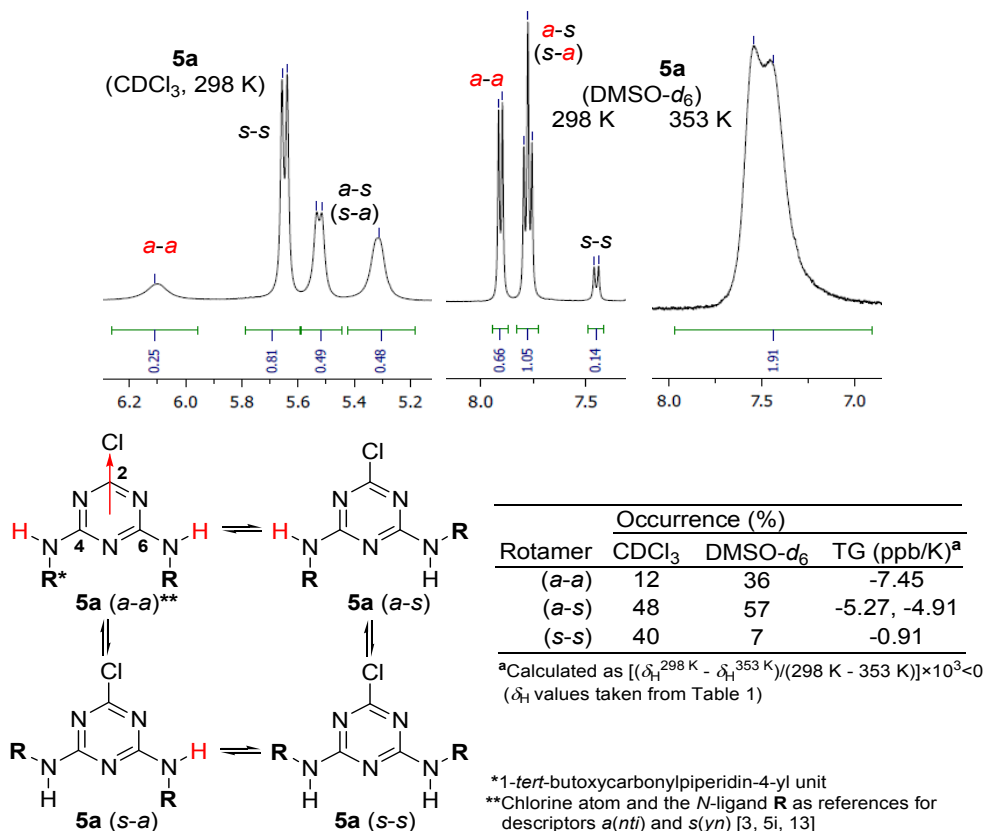
Chart 1

DMSO (ε = 46.7) against chloroform (ε = 4.81). In order to better evaluate this behaviour, we used Temperature Gradients (TGs) of the "indicative" NH protons. Though the use of this parameter is suitable for amide $-N(H)-C(=O)- \leftrightarrow -N^+(H)=C(-O^-)-$ protons of peptides and proteins [17] in D_2O, it can also be applied to amino-s-triazines, $-N(H)-C(=N-)- \leftrightarrow -N^+(H)=C(-N^--)-$ as recommended by Simanek and Moreno [9c]. Following this extrapolation, if TG values of "amidine-like" protons in amino-s-triazines are more negative than -4 ppb/K in strong hydrogen bond acceptor solvents, such as DMSO-d_6 [5i], the NH groups are exposed to the solvent rather than forming intramolecular hydrogen bonds. Conversely, a TG value less negative than -4 ppb/K discloses that the NH group preferentially forms intramolecular hydrogen bonds at room temperature. As one can see (Chart 1), besides the normal aptitude for binding of the carbamate units of **5a**, the contribution to solvation of NH groups, $Me_2S=O…H…N<$, was also significant. Indeed, 95% of the rotameric species of **5a** had TGs more negative than -4 ppb/K in conjunction with the adopted *anti-anti* and *anti-syn* arrangements of the *N*-Boc piperidine arms. Upon heating at 353 K, compound **5a** could be near totally deblocked (Chart 1) with respect to the connexions C(s-triazine)-N(exocyclic), however not, as already mentioned, concerning the rigidity of the piperidine ring (Table 1).

d) Similar concepts applied in the case of melamine **5b** (Chart 2). At room temperature, both the expected rotational diastereomers, **5b**-*propeller* (C_3-symmetric) and **5b**-*asymmetric* could be ^1H detected in a ratio completely different than statistics (25% *propeller* against 75% *asymmetric*) in DMSO-d_6 only. Except for one arm of the *asymmetric* rotamer (TG -2.55 ppb/K, Chart 2), all other arrangements exhibited TGs (much) less negative than -4 ppb/K. Upon heating, melamine **5b** reached the almost free rotational status in the region C(s-triazine)-N (exocyclic).

CONCLUSIONS

Starting from 4-aminopiperidine, we have developed the synthesis of a new *N,N',N"*-substituted melamine possessing piperidin-4-yl units as *N*-ligands, together with its foremost precursors. Indeed, the 1-Boc-piperidin-4-yl unit *N,N'*-substituting a chloro-diamino-s-triazine, can be seen as an useful building-block in dendritic melamines construction. The synthetic feasibility of these compounds is crucially influenced, mainly in the third amination step, by the rigid conformation and significant solvation of the reaction partners, namely 1-Boc-4-NH_2 piperidine and *C*-substituted s-triazines with 1-Boc-piperidin-4-ylamino units. The inherent occurrence of the rotational diastereomerism about the partial double bonds C(s-triazine)-N(exocyclic) revealed a non-statistic content of frozen or slowly exchangeable rotamers, hence a new opening route towards structural diversity.

Chart 2

	Occurrence (%)		
Rotamer	CDCl$_3$	DMSO-d_6	TG (ppb/K)[a]
propeller	-	47	-6.90
asymmetric	-	53	-2.55, -5.10, -10.36

[a]Calculated as $[(\delta_H^{298\,K} - \delta_H^{353\,K})/(298\,K - 353\,K)]\times10^3 < 0$
(δ_H values taken from Table 1)

*1-*tert*-butoxycarbonylpiperidin-4-yl unit
**Terminology adopted from Ref. [5i]
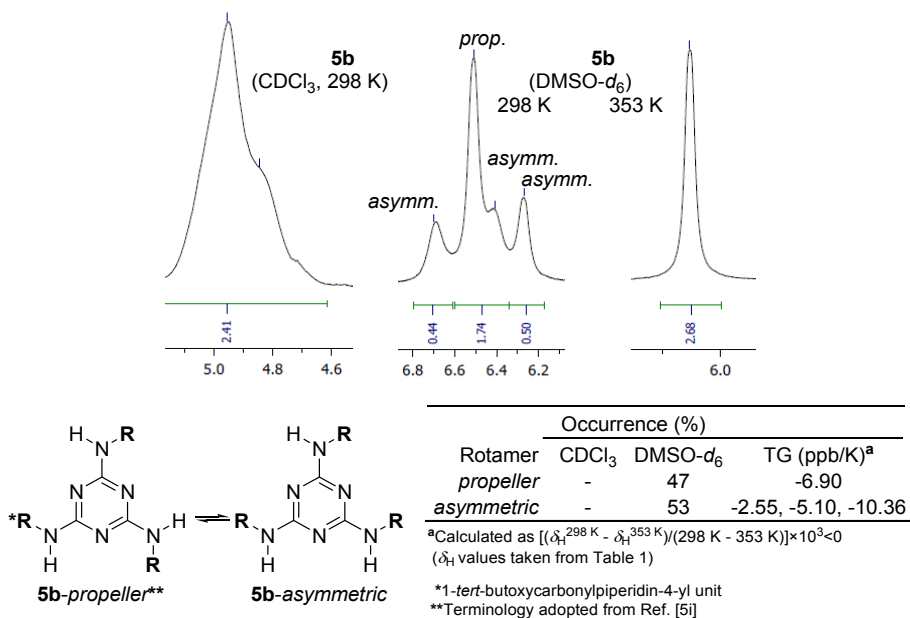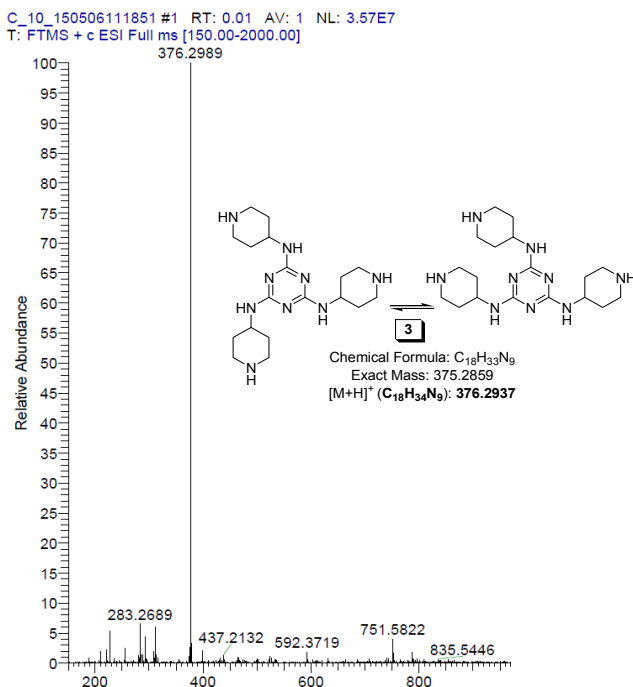
Figure 2. HRMS spectrum (ESI) of compound **3**
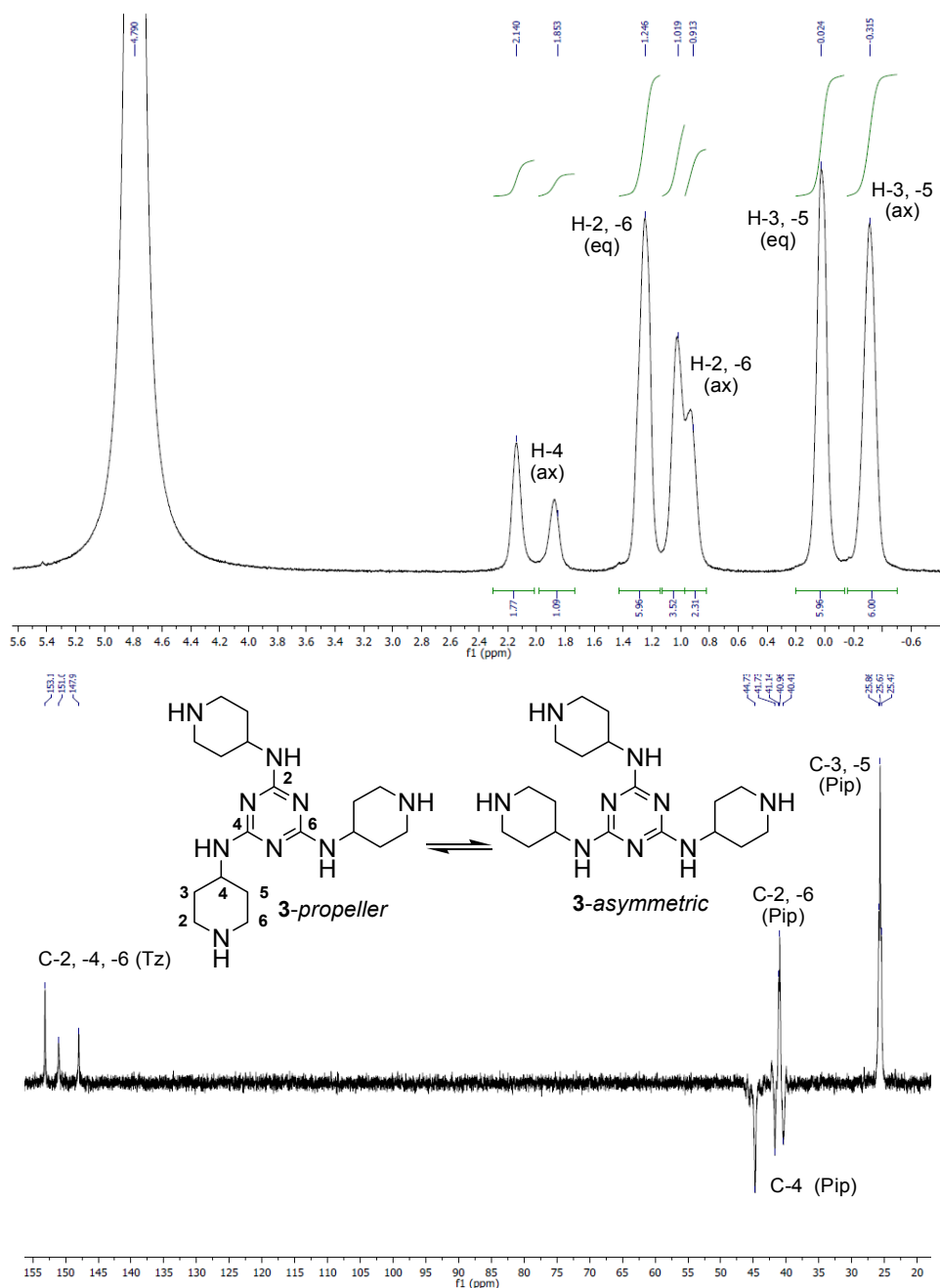
Figure 3. ^{1}H-and ^{13}C-J_{mod}-NMR spectra (400 MHz, D_2O+DCl, pH = 0.5-1, 298 K) of compound **3**. The protonated forms of **3** should be deduced implicitly.

EXPERIMENTAL SECTION

General. All reagents and solvents were of commercial quality and required no purification prior to use. Melting points were carried out on an ELECTROTHERMAL® instrument and were not corrected. TLC monitoring was performed by using aluminium sheets with silica gel 60 F$_{254}$ (Merck®) (visualisation in UV at λ=254 nm except compound **4**, in I$_2$ bath). Column chromatography was conducted on Silica gel Si 60 (0.063-0.200 mm, Merck®). IR spectra were recorded on a JASCO® FT-IR 6100 Spectrometer. Only relevant absorption maxima are listed, throughout, in cm^{-1}: s (strong), m (medium) and w (weak). NMR spectra were recorded on Bruker® AM 400 instruments operating at 400 and 100 MHz for ^{1}H and ^{13}C nuclei, respectively. All chemical shifts (δ values) are given in parts per million (ppm); all homocoupling patterns ($^nJ_{H,H}$ values) are given in Hertz. No TMS was added, chemical shifts were measured against the solvent residual peak. In the NMR descriptions, some specific abbreviations were used: "br s" (broad singlet), "br d" (broad doublet), "br m" (broad multiplet), "br dd app. br t" (broad doublet of doublets appearance as broad triplet), Pip (Piperidine) and Tz (*s*-Triazine). GC-MS spectra were recorded on a Gas Chromatograph with Mass Spectrometer Shimadzu® QP 2010 PLUS. Mass spectra were carried out on a LTQ ORBITRAP® XL (Thermo Scientific) instrument which was externally calibrated using the manufacturer's ESI(+) calibration mix. The samples were introduced into the spectrometer by direct infusion.

Preparation of 4-amino-1-tert-butoxycarbonylpiperidine **4** (crude product). Under inert atmosphere, to a cooled (0 °C) dioxane / water (5 : 9 v/v) solution, 4-aminopiperidine (1.526 g, 1.60 mL, 14.93 mmol) was added with vigorous stirring at 0 °C. A cooled (0 °C) solution obtained by dissolving di-*tert*-butyldicarbonate (Boc$_2$O) (3.431 g, 15.24 mmol) and trimethylamine (TEA) (1.504 g, 2.06 mL, 15.01 mmol) in 1,4-dioxane (4 mL) was then added dropwise over 1 h at max. 2-4 °C. Next, the reaction mixture was let to reach the room temperature and left to stir for additional 12 h. 1,4-Dioxane was gently removed under reduced pressure and the remaining aqueous phase was extracted with chloroform (6 x 30 mL). The combined organic solution was dried over Na$_2$SO$_4$, filtered off and then evaporated in vacuum to dryness. The resulted oily residue slowly solidified in time (48-72 h) to provide crude compound **4** (2.721 g, with 97% GC purity, 91% yield with respect to 4-aminopiperidine). White solid. M.p. 50-52 °C (lit. [8] 47-52 °C). R_f (isopropanole : 25% aq. NH$_3$ = 9 : 1 v/v) = 0.64. IR (KBr) ν_{max} 3351 (w), 2979 (m), 2935 (m), 2862 (m), 2680 (w), 2576 (w), 2220 (w), 1694 (s), 1562 (m), 1531 (m), 1423 (s), 1392 (m), 1366 (m), 1284 (m), 1150 (s), 1043 (w) cm^{-1}. ^{1}H- and 2D-^{1}H,^{1}H-COSY-NMR (400 MHz, CDCl$_3$, 298 K) δ_H 1.19 (2H, dddd, $^2J_{H,H}$~$^3J_{H,H}$~$^3J_{H,H}$=11.7 Hz, $^3J_{H,H}$=3.8 Hz, H-3, -5-ax), 1.40 (s, 9H, ^{t}Bu), 1.75

(2H, d, $^2J_{H,H}$=12.4 Hz, H-3, -5-eq), 1.89 (2H, s, H-2, -6-ax), 2.72 (1H, br dd app. br t, $^3J_{H,H}$=11.6 Hz, Hz, H-4-ax), 2.78 (2H, ddd, $^2J_{H,H}$=8.9 Hz, $^3J_{H,H}$=4.3 Hz, H-2, -6-eq), 3.98 (2H, br s, NH$_2$) ppm. ^{13}C-J_{mod}-NMR (100 MHz, CDCl$_3$, 298 K) δ_C 28.5 (Me), 32.4 (C-3, -5), 35.4 (C-2, -6), 48.9 (C-4), 79.6 [C(Me)$_3$], 154.9 (C=O) ppm. ^{1}H-RMN (400 MHz, DMSO-d_6, 298 K) δ_H 1.07, 1.22 (2H: br ddd, $^2J_{H,H}$~$^3J_{H,H}$~$^3J_{H,H}$=11.1 Hz; br dd, $^2J_{H,H}$~$^3J_{H,H}$=9.8 Hz, H-3, -5-ax), 1.38 (9H, s, ^{t}Bu), 1.66 (2H, d, $^2J_{H,H}$=12.0 Hz, H-3, -5-eq), 2.72 (2H, br d, $J_{H,H}$=10.0 Hz, H-2, -6-ax), 3.04 (2H, br s, H-4-ax), 3.39 (2H, br s, NH$_2$), 3.82 (2H, br d, $^2J_{H,H}$=10.8 Hz, H-2, -6-eq) ppm. ^{1}H-RMN (400 MHz, DMSO-d_6, 353 K) δ_H 1.13, 1.30 (2H: br ddd, $^2J_{H,H}$~$^3J_{H,H}$~$^3J_{H,H}$=10.9, Hz; br dd, $^2J_{H,H}$~$^3J_{H,H}$=11.2 Hz, H-3, -5-ax), 1.41 (9H, s, ^{t}Bu), 1.69 (2H, d, $^2J_{H,H}$=12.8 Hz, H-3, -5-eq), 2.50 (2H, br s, H-4-ax), 2.82 (2H, br dd app. br t, $J_{H,H}$=12.0 Hz, H-2, -6-ax), 3.43 (2H, br s, NH$_2$), 3.81 (2H, br d, $^2J_{H,H}$=12.0 Hz, H-2, -6-eq) ppm. HRMS-ESI(+) (rel. int. %) m/z: 201.1591 (7) [M+H]$^+$. [M+H]$^+$ calcd. for C$_{10}$H$_{20}$N$_2$O$_2$, 201.1525.

Preparation of compounds **5a** *and* **5b.** At room temperature and under inert atmosphere, into a 1,4-dioxane (10 mL) solution containing cyanuric chloride (0.455 g, 2.47 mmol), anhyd. K$_2$CO$_3$ (1.047 g, 7.53 mmol) was suspended with vigorous stirring. A 1,4-dioxane (30 mL) solution containing 4-amino-1-*tert*-butoxycarbonylpiperidi-ne **4** (1.538 g as 97 % GC-MS purity, 1.492 g 100%, 7.49 mmol) was added dropwise over 1 h. After additional 24 h of stirring at room temperature, TLC monitoring (eluent acetone : ligroin : chloroform = 2:1:3 v/v/v) indicated the incomplete consumption of cyanuric chloride and formation of compounds **5a** (major) and **5b** (minor). Therefore, the reaction mixture was refluxed for 88 h, i.e., until TLC monitoring indicated no more evolution of the amination process. The reaction mixture was evaporated to dryness under reduced pressure and the solid residue was taken with distilled water (30 mL) with stirring, at room temperature. The resulted suspension was filtered off and well washed with distilled water to the complete removal of minerals. After drying at room temperature, the crude material (1.738 g) was purified by column chromatography on silica gel (eluent acetone : ligroin : chloroform= 2:1:3 v/v/v) to give 0.853 g pure compound **5a** (68% partial conversion of cyanuric chloride) as the first fraction. Next elution afforded 0.355 g compound **5b** (21% partial conversion of cyanuric chloride).

2-Chloro-4,6-bis(1-tert-butoxycarbonylpiperidin-4-ylamino)-s-triazine **5a.** White solid. M.p. 177-179 °C. R_f (acetone : ligroin : chloroform = 2:1:3 v/v/v) = 0.75. IR (KBr) ν_{max} 3357 (m), 3256 (m), 2976 (m), 2931 (m), 2846 (w), 1698 (s), 1678 (s), 1576 (s), 1534 (s), 1425 (s), 1365 (s), 1240 (m), 1175 (s), 1143 (s), 969 (w), 806 (w) cm^{-1}. ^{1}H- and 2D-^{1}H,^{1}H-COSY-NMR (400 MHz, CDCl$_3$, 298 K) δ_H 1.27-1.43 (22H, br m, 2×^{t}Bu, H-3, -3', -5, -5'-ax), 1.93 (4H, br s, H-3, -3', -5, -5'-eq), 2.88 (4H, d, $J_{H,H}$=10.8 Hz, H-2, -2', -6, -6'-ax), 3.87 (2H, br m, H-4,

-4'-ax), 4.00 (4H, br s, H-2, -2', -6, -6'-eq), 5.31, 5.52, 5.65, 6.11 (0.48H, br s; 0.49H, d, $^3J_{H,H}$=6.8 Hz; 0.81H, $^3J_{H,H}$=7.6 Hz; 0.25H, br s; NH) ppm. ^{13}C-J_{mod}-NMR (100 MHz, CDCl$_3$, 298 K) δ_C 28.5 (Me), 31.6, 31.7, 32.0, 32.2 (C-3, -3', -5, -5', Pip), 42.6 (C-2, -2', -6, -6', Pip), 48.0, 48.1, 48.2, 48.5 (C-4, -4', Pip), 79.8, 79.9 [C(Me)$_3$], 154.7, 154.8 (C=O), 164.4, 165.0, 165.2 (C-4, -6, Tz), 168.6, 169.5 (C-2, Tz) ppm. ^{1}H-NMR (400 MHz, DMSO-d_6, 298 K) δ_H 1.30 (4H, br dd app. br t, $^2J_{H,H}$~$^3J_{H,H}$=11.6 Hz, H-3, -3', -5, -5'-ax), 1.39 (18H, s, 2×^{t}Bu), 1.76 (4H, br dd app. br q, $^2J_{H,H}$=10.1 Hz, H-3, -3', -5, -5'-eq), 2.82 (4H, br s, H-2, -2', -6, -6'-ax), 3.87 (6H, br s, H-4, -4'-ax, H-2, -2', -6, -6'-eq), 7.45, 7.77, 7.79, 7.91 (0.14H, d, $^3J_{H,H}$=8.0 Hz; 0.52H, $^3J_{H,H}$=7.6 Hz; 0.52H, $^3J_{H,H}$=7.6 Hz; 0.66H, $^3J_{H,H}$=7.2 Hz; NH) ppm. ^{1}H- and 2D-^{1}H,^{1}H-COSY-NMR (400 MHz, DMSO-d_6, 353 K) δ_H 1.40 (4H, br t, $^2J_{H,H}$~$^3J_{H,H}$=12.8 Hz, H-3, -3', -5, -5'-ax), 1.42 (18H, s, 2×^{t}Bu), 1.80 (4H, br d, $^2J_{H,H}$=10.4 Hz, Hz, H-3, -3', -5, -5'-eq), 2.87 (4H, br dd app. br t, $^2J_{H,H}$~$^3J_{H,H}$=11.6 Hz, H-2, -2', -6, -6'-ax), 3.87 (2H, br s, H-4, -4'-ax), 3.90 (4H, br s, H-2, -2', -6, -6'-eq), 7.44, 7.55 (2H, 2×br s, NH) ppm. HRMS-ESI(+) (rel. int. %) *m*/*z*: 512.2767 (100) [M+H]$^+$. [M+H]$^+$ calcd. for C$_{23}$H$_{39}$ClN$_7$O$_4$, 512.2752.

2,4,6-Tris(1-tert-butoxycarbonylpiperidin-4-ylamino)-s-triazine **5b**. White solid. M.p. 182-184 °C. R_f (acetone : ligroin : chloroform = 2:1:3 v/v/v) = 0.45. IR (KBr) ν$_{max}$ 3340 (w), 2977 (m), 2930 (m), 2853 (w), 1704 (s), 1577 (m), 1504 (s), 1423 (s), 1365 (m), 1238 (m), 1161 (s), 870 (w), 813 (w), 769 (w) cm^{-1}. ^{1}H-NMR (400 MHz, CDCl$_3$, 298 K) δ_H 1.32 (6H, br s, H-3, -3', -3'', -5, -5', -5''-ax), 1.43 (27H, s, 3×^{t}Bu), 1.93 (6H, br s, H-3, -3', -3'', -5, -5', -5''-eq), 2.86 (6H, br s, H-2, -2', -2'', -6, -6', -6''-ax), 3.88 (3H, br s, H-4, -4', -4''-ax), 3.98 (6H, br s, H-2, -2', -2'', -6, -6', -6''-eq), 4.84, 4.95 (3H, 2×br s, NH) ppm. ^{13}C-J_{mod}-NMR (100 MHz, CDCl$_3$, 298 K) δ_C 28.5 (Me), 32.3 (C-3, -3', -3'', -5, -5', -5'', Pip), 47.3, 47.4, 48.1 (C-4, -4', -4'', Pip), 79.7 [C(Me)$_3$], 154.9 (C=O) ppm. ^{1}H-NMR (400 MHz, DMSO-d_6, 298 K) δ_H 1.30 (6H, br s, H-3, -3', -3'', -5, -5', -5''-ax), 1.39 (27H, s, 3×^{t}Bu), 1.71 (6H, br d, $^2J_{H,H}$=10.0 Hz, H-3, -3', -3'', -5, -5', -5''-eq), 2.75 (6H, br s, H-2, -2', -2'', -6, -6', -6''-ax), 3.88 (3H, br s, H-4, -4', -4''-ax), 3.91 (6H, br s, H-2, -2', -2'', -6, -6', -6''-eq), 6.27, 6.41, 6.51, 6.70 (3H, 4×br s, NH) ppm. ^{1}H- and 2D-^{1}H,^{1}H-COSY-NMR (400 MHZ, DMSO-d_6, 353 K) δ_H 1.37 (6H, dddd, $^2J_{H,H}$~$^3J_{H,H}$~$^3J_{H,H}$=12.0 Hz, $^3J_{H,H}$=3.2 Hz, H-3, -3', -3'', -5, -5', -5''-ax), 1.42 (27H, s 3×^{t}Bu), 1.80 (6H, dd, $^2J_{H,H}$=10.0 Hz, $^3J_{H,H}$=2.4 Hz, H-3, -3', -3'', -5, -5', -5''-eq), 2.83 (6H, dd app. t, $^2J_{H,H}$~$^3J_{H,H}$=11.4 Hz, H-2, -2', -2'', -6, -6', -6''-ax), 3.88 (3H, br s, H-4, -4', -4''-ax), 3.91 (6H, br s, H-2, -2', -2'', -6, -6', -6''-eq), 6.13 (3H, br s, NH) ppm. HRMS-ESI(+) (rel. int. %) *m*/*z*: 676.4528 (100) [M+H]$^+$, 620.3900. (9) [M+H-C$_4$H$_8$]$^+$. [M+H]$^+$ calcd. for C$_{33}$H$_{58}$N$_9$O$_6$, 676.4510. [M+H-C$_4$H$_8$]$^+$ calcd. for C$_{29}$H$_{50}$N$_9$O$_6$, 620.3884.

ANA-MARIA ŢICALĂ, DAN PORUMB, CARMEN SĂCĂLIŞ, MIRCEA DARABANTU

Preparation of 2,4,6-tris(piperidin-4-ylamino)-s-triazine **3.** Under inert atmosphere and vigorous stirring, to a suspension of 2,4,6-tris(1-*tert*-butoxycarbonylpiperidin-4-ylamino)-*s*-triazine **5b** (0.350 g, 0.518 mmol) in cooled (0 °C) methanol (5 mL), a 6N HCl solution (1.8 mL, 10.53 mmol pure HCl) was added dropwise over 70 min. keeping the temperature at 0-1 °C. The resulted slurry was stirred at 0 °C for 2 h and then allowed to reach the room temperature over 3 h. The reaction mixture was slowly heated at 40 °C for 15 h. After this period, TLC monitoring (eluent : acetone : ligroin : chloroform = 2:1:3 v/v/v) indicated the complete consumption of **5b** and formation of the desired compound **3** (eluent EtOH : 25% aq. NH_3 = 1:9 v/v**)** as a single spot. The reaction mixture was evaporated under reduced pressure to the complete removal of methanol. The remaining solution was diluted with distilled water (2 mL), cooled at 0 °C for 1 h then carefully made alkaline with a 10% NaOH aq. soln. to pH = 14. The resulted suspension was cooled at 0 °C for 24 h then filtered off. The organic solid was well-washed with cooled (0 °C) and distilled water to the complete removal of minerals and dried in vacuum at room temperature to yield 0.145 g compound **3** (75% yield with respect to **5b**). White solid. M.p. 340-342 °C. R_f (EtOH : 25% aq. NH_3 = 1:9 v/v) = 0.15. IR (KBr) ν_{max} 3278 (m), 2947 (w), 2914 (w), 2813 (w), 2739 (w), 1588 (m), 1517 (s), 1385 (m), 1353 (m), 1178 (w), 860 (w), 811 (m) cm^{-1}. ^{1}H- and 2D-^{1}H,^{1}H-COSY-NMR (400 MHz, D_2O+DCl, 298 K) -0.33 (6H, br s, H-3, -3', -3", -5, -5', -5"-ax), 0.02 (6H, br s, H-3, -3', -3", -5, -5', -5"-eq), 0.91, 1.02 (6H, 2×br s, H-2, -2', -2", -6', -6', -6"-ax), 1.25 (6H, br s, H-2, -2', -2", -6, -6', -6"-eq), 1.85, 2.14 (3H, 2×br s, H-4, -4', -4"-ax) ppm. ^{13}C-J_{mod}-NMR (100 MHz, D_2O+DCl, 298 K) δ_C 25.5, 25.7, 25.9 (C-3, -3', -3", -5, -5', -5", Pip), 40.4, 41.7, 43.7 (C-4, -4', -4", Pip), 40.96, 41.14 (C-2, -2', -2", -6, -6', -6", Pip), 148.0, 151, 153.1 (C-2, -4, -6, Tz) ppm. HRMS-ESI(+) (rel. int. %) *m/z*: 376.2989 (100) [M+H]$^+$. [M+H]$^+$ calcd. for $C_{18}H_{34}N_9$, 376.2937.

ACKNOWLEDGMENTS

REFERENCES AND NOTES

[1]. a) W. Zhang, E.E. Simanek, *Org. Lett.*, **2000**, *2*, 843; b) M. B. Steffensen, E.E. Simanek, *Angew. Chem. Int. Ed.*, **2004**, *43*, 5178; c) E. Hollink, E.E. Simanek, *Org. Lett.*, **2006**, *8*, 2293; d) H. Crampton, E. Hollink, L.M. Perez, E.E. Simanek, *New J. Chem.*, **2007**, *31*, 1283; e) A. Chouai, E.E. Simanek, *J. Org. Chem.*, **2008**, *73*, 2357; f) J. Lim, E.E. Simanek, *Org. Lett.*, **2008**, *10*, 201; g) A.E. Enciso, F. Ramirez-Crescencio, M. Zeiser, R. Redón, E.E. Simanek, *Polym. Chem.*, **2015**, *6*, 5219; h) R.S. Sreeperumbuduru, Z.M. Abid, K.M. Claunch, H.-H. Chen, S.M. McGillivray, E.E. Simanek, *RSC Adv.*, **2016**, *6*, 8806.

[2]. a) A. Chouai, V.J. Venditto, E.E. Simanek, *Org. Synth.*, **2009**, *86*, 141; b) A. Chouai, V.J. Venditto, E.E. Simanek, *Org. Synth.*, **2009**, *86*, 151.

[3]. a) F. Popa, I. Simioanca, M. Pintea, M. Fazekas, L. Gratecap, C. Berghian, C. Batiu, M. Darabantu, *Studia UBB Chemia*, **2008**, *LIII(4)*, 5; b) F. Popa, P. Lameiras, E. Henon, O. Moldovan, A. Martinez, C. Batiu, Y. Ramondenc, M. Darabantu, *Can. J. Chem.*, **2011**, *89*, 1207; c) F. Popa, P. Lameiras, O. Moldovan, M. Tomoaia-Cotisel, E. Henon, A. Martinez, C. Sacalis, A. Mocanu, Y. Ramondenc, M. Darabantu, *Tetrahedron*, **2012**, *68*, 8945; d) O. Moldovan, P. Lameiras, I. Nagy, T. Opruta, F. Popa, C. Antheaume, Y. Ramondenc, M. Darabantu, *Tetrahedron*, **2013**, *69*, 2199.

[4]. a) X. Chen, P. Zhan, C. Pannecouque, J. Balzarini, E. De Clercq, X. Liu, *Eur. J. Med. Chem.*, **2012**, *51*, 60; b) X. Chen, P. Zhan, Z. Cheng, C. Meng, S. Shao, C. Pannecouque, E. De Clercq, X. Liu, *Bioorg. and Med. Chem.*, **2012**, *20*, 3856.

[5]. a) T. Drakenberg, S. Forsen, *Chem. Commun.*, **1971**, *21*, 1404; b) S.S. Mirvish, P. Gannett, D.M. Babcook, D. Williamson, S.C. Chen, D.D. Weisenburger, *J. Agric. Food Chem.*, **1991**, *39*, 1205; c) I. Willner, J. Rosengaus, Y. J. Eichen, *Phys. Org. Chem.*, **1993**, *6*, 29; d) A.R. Katritzky, I. Ghiviriga, D.C. Oniciu, A. Barkock, *J. Chem. Soc., Perkin Trans. 2*, **1995**, *4*, 785; e) A.R. Katritzky, I. Ghiviriga, P.G. Steel, D.C. Oniciu, *J. Chem. Soc., Perkin Trans. 2*, **1996**, *3*, 443; f) P. Amm, N. Platzer, J. Guilhem, J.P. Bouchet, J.P. Volland, *Magn. Reson. Chem.*, **1998**, *36*, 587; g) H.E. Birkett, R.K. Harris, P. Hodgkinson, K. Carr, M.H. Charlton, J.C. Cherryman, A.M. Chippendale, R.P. Glover, *Magn. Reson. Chem.*, **2000**, *38*, 504; h) M. Amm, N. Platzer, J.P. Bouchet, J.P. Volland, *Magn. Reson. Chem.*, **2001**, *39*, 77; i) I. Ghiviriga, D.C. Oniciu, *Chem. Commun.*, **2002**, *22*, 2718; j) H.E. Birkett, J.C. Cherryman, A.M. Chippendale, J.O.S. Evans, R.K. Harris, M. James, I.J. King, G. Mc Pherson, *Magn. Reson. Chem.*, **2003**, *41*, 324.

[6]. a) F. Friebolin, *Basic one- and two dimensional NMR spectroscopy*, VCH Verlagsgesellschaft: Weinheim, New York, **1991**, p. 93, 263-291; b) E.L. Eliel, H.S. Wilen, *Stereochemistry of the Organic Compounds*, John Wiley & Sons, New York, **1994**, p. 642, 1191

[7]. http://www.sigmaaldrich.com/Graphics/COfAInfo/SigmaSAPQM/SPEC/64/6400 42/640042-BULK_____ALDRICH__.pdf.

[8]. a) F. Himmelsbach, G. Dahmann, T. von Ruden, T. Metz (Dr. Karl Thomas GmbH) **1998**, *US Pat. US5821240A1*, Mar.5, **1997** / Oct.13, **1998**, App. No. US 08/811,907; b) F. Himmelsbach, G. Dahmann, T. von Ruden, T. Metz (Dr. Karl Thomas GmbH) **1999**, *US Pat. US5977102A1*, Mar.5, **1997** / Nov.2, **1999**, App. No. US 08/812,002; c) D. Xiao, Y. Zhu, Y. Hu, H. Wang, Y. Liu, J. Li, D. Sun, Z. Wang, Y. Wei, Z. Wang, G. Tang, L. Jing (Centaurus Biopharma Co.,Ltd.) **2012**, *WO2012/103806A1*, Jan.31, **2012**/Aug.9, 2012. App. No. PCT/CN2012/070800.

[9]. a) M.B. Steffensen, E.E. Simanek, *Org. Lett.*, **2003**, *5*, 2359; b) K.X. Moreno, E.E. Simanek, *Tetrahedron Lett.*, **2008**, *49*, 1152; c) X.K. Moreno, E.E. Simanek, *Macromolecules*, **2008**, *41*, 4108; d) M.A. Mintzer, L.M. Perez, E.E. Simanek, *Tetrahedron Lett.*, **2010**, *51*, 1631; e) E.E. Simanek, H. Abdou, S. Lalwani, J. Lim, M. Mintzer, V.J. Venditto, B. Vittur, *Proc. R. Soc. A.*, **2010**, *466*, 1445.

[10]. H.K. Hall, *J. Am. Chem. Soc.*, **1957**, *79*, 5441.

[11]. For the conformational analysis of cyclohexylamine (aminocyclohexane) by means of (VT) ^{1}H-, ^{13}C- or ^{15}N-NMR and computational methods see a) H. Booth, M. L. Jozefowicz, *J. Chem. Soc. Perkin 2*, **1976**, 895; b) H. –J. Schneider, V. Hoppen, *J. Org. Chem.*, **1978**, *43*, 3866; c) G. W. Buchanan, V.L. Webb, *Tetrahedron Lett.*, **1983**, *24*, 4519.

[12]. *See for example* a) J.T. Thurston, J.R. Dudley, D.W. Kaiser, I. Hechenbleikner, F.C. Schaefer, D. Holm-Hansen, *J. Am. Chem. Soc.*, **1951**, *73*, 2981; b) K.N. Sarmah, N.K. Sarmah, K.B. Kurmi, T.V. Patel, *Adv. Appl. Sci. Res.*, **2012**, *3*, 459.

[13]. a) M. Fazekas, M. Pintea, P. Lameiras, A. Lesur, C. Berghian, I. Silaghi-Dumitrescu, N. Plé, M. Darabantu, *Eur. J. Org. Chem.*, **2008**, *14*, 2473; b) O. Moldovan, P. Lameiras, E. Hénon, F. Popa, A. Martinez, D. Harakat, C. Sacalis, Y. Ramondenc, M. Darabantu, *Centr. Eur. J. Chem.*, **2012**, *10*, 1119; c) O. Moldovan, I. Nagy, P. Lameiras, C. Antheaume, C. Sacalis, M. Darabantu, *Tetrahedron: Asymmetry*, **2015**, *26*, 683; d) C. Morar, G. Turdean, A. Bende, P. Lameiras, C. Antheaume, L. M. Muresan, M. Darabantu, *Compt. Rend. Chim.*, **2016**, http://dx.doi.org/10.1016/j.crci.2016.07.002.

[14]. For the relevance of this α-geminal anisochrony versus a carbamate group in anancomeric 1-Boc-4-NH$_2$ piperidine, see the ^{1}H-NMR analysis of flipping non-symmetrically N-substituted-N-Boc piperazines in J. Lim, G.M. Pavan, O. Annunziata, E.E. Simanek, *J. Am. Chem.Soc.*, **2012**, *134*, 1942.

[15]. W.E. Stewart, T.H. Siddall, *Chem. Rev.*, **1970**, *70*, 517.

[16]. a) J. Lim, E.E. Simanek, *Mol. Pharm.*, **2005**, *2*, 273; b) M. Pintea, M. Fazekas, P. Lameiras, I. Cadis, C. Berghian, I. Silaghi-Dumitrescu, F. Popa, C. Bele, N. Plé, M. Darabantu, *Tetrahedron*, **2008**, *64*, 8851.

[17]. H. Kessler, *Angew. Chem., Int. Ed. Engl.*, **1982**, *21*, 512.

ANTIRADICAL ACTIVITY OF L-GLUTAMINE, L-ASPARAGINE AND L-ASPARTIC ACID DERIVED REDUCED SCHIFF BASE COPPER(II) COMPLEXES

LUCIA LINTNEROVÁ[a]*, JINDRA VALENTOVÁ[a], FERDINAND DEVÍNSKY[a]

ABSTRACT. Superoxide dismutases (SOD) are a group of metallo-enzymes, containing one or two coordinated metals, and their main role in the organism is protection against superoxide radicals, one of the reactive oxygen species (ROS). Among these Cu(II)-Zn(II) SOD is present in cytoplasm and acts as a scavenger of superoxide radicals. Cu(II)-complexes may act as low-molecule analogue of Cu-Zn SOD and therefore are being studied as antiradical agents. In this study a series of Cu(II) complexes were synthesizes, containing ligands prepared from salicyl aldehyde and amino acids: L-asparagine, L-glutamine and L-aspartic acid. Complexes prepared from L-asparagine and L-glutamine are novel and were compared with the already reported complex Cu(HSal-L-Asp) hydrate (**6e**). An assay based on the ability to inhibit reduction of iodonitrotetrazolium dye (INT) by superoxide anion-radicals was used to determine antiradical activity of these complex. The prepared complexes - Cu(HSal-L-Asn) acetate (**6a**), Cu(HSal-L-Asn) hydrate (**6b**) and Cu(HSal-L-Gln) acetate (**6c**) proved to be good antiradical agents compared to complex **6e**. The IC_{50} values of the radical transport were 19.2 ± 1.2 µM for **6a**, 53.9 ± 9.4 µM for **6b** and 4.11 ± 0.37 mM for **6c**.

Keywords: copper complexes, reduced Schiff bases, antiradical activity, SOD mimetics, INT method, amino acid derived ligands

INTRODUCTION

Superoxide radicals and other reactive oxygen species (ROS) are produced by normal cell metabolism and their overproduction may damage proteins, saccharides, cell membrane lipids and nucleic bases. This process

[a] *Department of Chemical Theory of Drugs, Faculty of Pharmacy, Comenius University in Bratislava, 8 Kalinčiakova Str, 83232 Bratislava, Slovakia*
* *Corresponding author: lintnerova@fpharm.uniba.sk*

is also called oxidative stress [1] and it's connected to many diseases (infertility, cardiovascular diseases, diabetes, neoplasia, ischaemia and reperfusion, asthma etc.) [2-5]. In the last 20-30 years, plant extracts or compounds isolated from plants, mostly flavonoids and polyphenolic acids, were studied as antiradical agents [6-8]. Also, new synthetic compounds including Schiff bases of various benzaldehydes and amines or amino acids [8-15] were studied mostly *in vitro* by various methods for their antiradical and/or anti-inflammatory activity [16]. Main used methods used for radical scavenging are the DPPH method (using 2,2-diphenyl-1-picrylhydrazyl) or ABTS method (using 2,2'-azino-bis(3-ethylbenzothiazoline-6-sulphonic acid) [17,18].

Metal complexes (Cu(II), Fe(III), Zn(II), Mn(II), Co(II) etc.) containing these antiradical agents as ligands were reported to yield even better antiradical activities [19], but also act as compounds with cytostatic [20], antidiabetic [21] or anti-inflammatory compounds [22]. The idea of using metal complexes as potential agents in therapy of oxidative stress was inspired by the enzyme group of Superoxide dismutases (SOD), which contain one or two different metal ions (Fe^{3+}, Mn^{2+}, Cu^{2+}-Zn^{2+}) in their active center. SOD enzymes act as protectors against oxidative stress, because they catalyze the dismutation reaction of free superoxide anion-radicals to oxygen molecules and peroxide anions [23]. For radical scavenging models, the copper(II) and zinc(II) containing SOD1 enzyme is most interesting, since it's present in the cell cytoplasm [24]. Metal complexes of small molecule ligands with radical scavenging ability are often called SOD mimetics (or mimics). A lot of attention was given to flavonoid metal complexes, especially highly active copper(II) complexes [25].

But Schiff bases, being good chelating agents of Cu(II), Ni(II), Fe(III), Zn(II), Co(II) and other ions, also became popular ligands for antiradical or antioxidant complexes [19,26,27]. In Schiff bases two moieties can be combined – an aldehyde, usually a benzaldehyde derived from phenolic acid derivatives, for example salicylic or gallic acid, and an amine with chelating groups in the structure for binding to the central ion of the complex. These chelating groups can be nitrogen in heterocycles [28,29] or with carboxylic (amino acids) and other groups [10,16,25,30]. Besides antiradical activity, some of these Schiff base complexes showed also antimicrobial [31], cytotoxic [32], antifungal [33], DNA-binding [30] or catecholase activity [34]. Vančo et al. studied the SOD mimetic abilities of Schiff base ligands derived from L-alanine, β-alanine and γ-aminobutyric acid with activities 28.2 – 68.8% inhibition at $1.43.10^{-3}$ M using the INT method [21]. Another structural variation of the Schiff base ligands is the reduction of the C=N bond to form secondary amines or so called reduced Schiff bases, which are more stable and easier to isolate then the Schiff bases themselves, especially in aqueous systems. This reduction causes significant changes in the chelating abilities of the ligand, which also affects the antiradical, catecholase mimetic or other activities [35,36,37].

In this research, we synthesized five copper(II) complexes of reduced Schiff base ligands (Figure 1) prepared from salicyl aldehyde (**3**) and the amino acids L-asparagine (**1a**) and L-glutamine (**1b**), which contain both an amide group at the end of their side chain, but differ in the number of carbons in the chain. There is just little information about the two compounds **5a** and **5b**, which we used as ligands, in literature. We found only two complexes of the **5a** containing Ni(II) with only studied structure [38], and a large heptametric La(III) complex able to bind to DNA[39]. There is practically no data available of the L-glutamine derived ligand and its complexes. Therefore, we wanted to prepare this novel complexes and compare the antiradical activities of their copper(II) complexes also with the copper(II) complex of the L-aspartic acid derived ligand (**5c**). This complex was already reported in literature, its structure was studied and it's known to form stable copper(II) complexes, however, its antiradical activity was not yet studied [38,40].

RESULTS AND DISCUSSION

The synthesis (Scheme 1) of the target ligands started from L-asparagine, L-glutamine and L-aspartic acid, which were first turned into methyl ester hydrochlorides (**2**) using thionyl chloride in methanol. This step was necessary to achieve higher purity of the synthesis intermediates and final ligands. Due to esterification, the polarity of the compounds decreased and this allowed a much easier and more reliable separation of the compounds from inorganic material which was present in the second synthesis step. In this second step the methyl esters reacted with salicyl aldehyde (**3**). The use of sodium hydroxide served for neutralization of the hydrochloride salt. The condensation reaction lead to the Schiff base (imine) formation, which was not isolated because of possible decomposition. A reduction reaction with $NaBH_4$ followed the condensation as a one-pot synthesis. This process produced a stable secondary amine (4), a reduced Schiff base. Last step of the ligand synthesis was a mild hydrolysis of the methyl ester under basic conditions and after neutralization with 10% HCl we obtained the ligands **5a-c** as white powders. All the intermediates and the ligands of the synthesis were characterized by spectroscopy methods (IR, ^{1}H and ^{13}C NMR) and elemental analysis was measured from all ligands **5a-c** (see in exp. section).

For complexation reactions, we used either method A with copper(II) acetate monohydrate or method B with copper(II) nitrate trihydrate for L-asparagine and L- glutamine derived ligands (5a and 5b) and in case of the L-aspartic acid derived ligand **5c** only method B was used. Complexes **6a-e** were isolated as fine green or blue powders, where L was either an acetic acid molecule (in

case of method A) or water molecule (in case of method B). The presence of acetic acid or water was determined by elemental analysis and they are either coordinated directly to copper(II) or adsorbed on the ligand by electrostatic interactions or hydrogen bond. Green powders were obtained from all 5 complexation reactions and they were characterized by IR spectra and elemental analysis. However, the product of complexation of HSal-L-Gln (**5b**) and copper(II) nitrate trihydrate yielded a powder of insufficient elemental analysis result and for this reason could not be used in the antiradical activity assays.
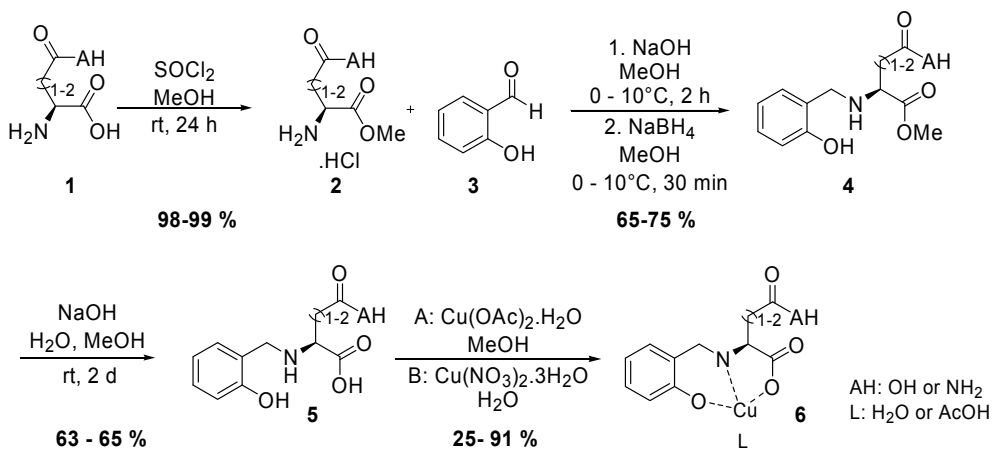
Scheme 1

The other four complexes with good elemental analysis were used in antiradical activity determination assays. The method used in the assay is a spectrophotometric detection of single electron transfer from KO_2, which served as a radical source, to 2-(4-Iodophenyl)-3-(4-nitrophenyl)-5-phenyl-2*H*-tetrazolium chloride (iodonitrotetrazolium dye, INT). The electron transfer leads to formation of blue formazan, which is detected as absorbance at 500 nm. The decline of the INT-formazan concentration is expressed as % of inhibition and it is linearly proportional to antiradical (SOD-mimic) activity of the measured compound.

The solubility often is an issue in case of copper(II) complexes. Good solubility of the complexes in the initial solutions provides also reliable data of the measured % of inhibition. In our case, all measured complexes were soluble in the initial solution with concentration 1.10^{-2} M. Solutions of this concentrations were used in preliminary antiradical assays, which served to select complexes with higher activity. Complexes with good % of inhibition were **6b** with 98.24 ± 0.23% at $1.43.10^{-3}$M and **6a** with 100.33 ± 0.37% at half concentration compared

to **6b**, at $5.71.10^{-4}$M (Table 1). Less active was complex **6c** with only 42.16 ± 3.30% and the least active was the complex **6e** prepared from L-aspartic acid derived ligand displayed only 16.81 ± 0.63 % activity, which is even lower than the inhibition % reported for their complexes reported by Vančo et al. [21]. Therefore, complex **6e** could not be used in further assays. Two carboxylic groups present in the molecule **5c** provide for be better chelating abilities of the ligand compared to the amide containing **5a** and **5b**. High stability of complex **6e** seems to be the reason for rather low antiradical activity, rending the complex unable to interact with free radicals in the solution. The other three complexes proved to be much better antiradical agents already in these preliminary assays.

Table 1. % of inhibition in initial antiradical activity measurements

complex	% of inhibition	concentration [M]
6a	100.33 ± 0.37	$5.71.10^{-4}$
6b	98.24 ± 0.23	$1.43.10^{-3}$
6c	42.16 ± 3.30	$1.43.10^{-3}$
6e	16.81 ± 0.63	$1.43.10^{-3}$

For the IC_{50} determination a series of sample solutions was prepared with concentrations decreasing from the initial value to 4.10^{-4} M for **6b** and **6c**. The concentrations range of **6a** had to be broaden to 4.10^{-5} M to obtain also inhibition values below 50%. The measured concentrations were obtained by addition of INT and KO_2 solutions and DMSO (see in exp. section). Complex **6a** and **6b** are rather active as can be seen in the Figure 1, but the **6b** complex was achieving lower % of inhibition at all concentrations. The % of inhibition had a linear trend depending on the measured concentration and for each complex a linear trend function was proposed (Figure 1). IC_{50} values were calculated from these functions as complex concentration at 50% of inhibition (Table 2). The best value was calculated for HSal-L-Asn Cu(II) acetate (**6a**) with 19.2 ± 1.2 μM, followed by HSal-L-Asn Cu(II) hydrate (**6b**) with 53.9 ± 9.4μM. HSal-L-Gln Cu(II) acetate (**6c**) exhibited much lower activity with IC_{50} equal to 4.11 ± 0.37 mM. This decrease of activity of complex **6c** derived from L-glutamine could have two explanations, again one could be the stability of the complex. But the precipitation of the complex during the preparation took a longer time compared to **6a** and **6b** and the yield of the complexation of **6c** is also the lowest of all. It is more probable that the radical transfer to

copper central ion is disturbed in **6c** by the longer side chain. As standard for scavenging of superoxide anion-radicals served cystamine with IC_{50} = 1.7 ± 0.1 mM.

Table 2. IC_{50} values of prepared complexes

complex	**6a**	**6b**	**6c**
IC_{50}	19.2 ± 1.2 µM	53.9 ± 9.4 µM	4.11 ± 0.37 mM
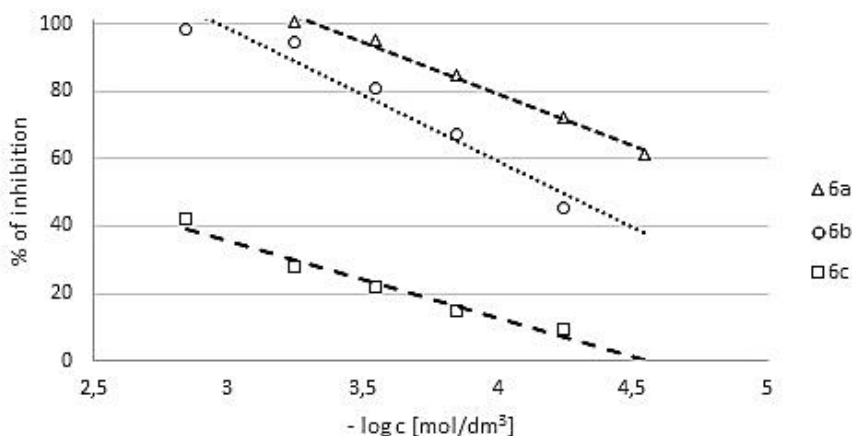
Figure 1. The linear relation between % of inhibition and negative logarithm of measured concentration of the complexes **6a-c**. The linear trend line function was used in IC_{50} value calculation.

CONCLUSIONS

In a three-step synthesis three ligands derived from L-asparagine, L-glutamine and L-aspartic acid were prepared. These ligands were used in complex formation reactions with copper(II) acetate hydrate in methanol and/or copper(II) nitrate trihydrate. From these complexation reactions four complexes with good elemental analysis were obtained and used in an antiradical activity assay using INT spectrophotometric method. The complex **6e** prepared from L-aspartic acid derived ligand had too low activity to be used in IC_{50} determination. The IC_{50} values for the novel complexes were in µM range for complexes **6a** and **6b**, both prepared from L-asparagine, and in mM range in case of complex **6c**, with the L-glutamine derivative as ligand. Complex **6c** also less active then cystamine used as a standard.

ACKNOWLEDGMENTS

EXPERIMENTAL SECTION

All chemicals for syntheses were reagent grade and were used as they received (Sigma-Aldrich), with exception of methanol which was dried using pre-drying with calcium oxide, reflux with magnesium activated with iodine and distillation.

All NMR spectra were measured on a Varian Gemini 2000 spectrometer at working frequencies 300 MHz for ^{1}H NMR and 75 MHz for ^{13}C NMR. Spectra were measured in DMSO-d_6 or D_2O, using TMS as internal standard. For the NMR signal assigning the numbering on aromatic ring starts from the position of the main chain. Infrared spectra were recorded on Nicolet 6700 FT-IR spectrophotometer in range 500 – 4000 cm^{-1} and the samples were in solid state. Elemental analysis was measured by Flash 2000 CHNS-O Analyser (Thermo Scientific).

Antiradical activity measurements were done on Synergy HT BioTek spectrophotometer. DMSO(analytical reagent grade) was used as solvent, 2-(4-Iodophenyl)-3-(4-nitrophenyl)-5-phenyl-2H-tetrazolium chloride (INT) and KO_2 were bought from Alfa-Aesar. INT initial solution was prepared in a sodium tetrahydridoborate buffer solution with pH adjusted to 7.1 with HCl.

General procedure for preparation of methyl ester hydrochlorides of amino acids (2a-c). To a solution of the amino acid **1** (22.45 mmol, 1 mol equiv) in 15 ml (20 ml in case of L-aspartic acid reaction) of dry methanol in a two-neck flask thionyl chloride (2.3 ml, 31.43 mmol, 1.4 mol equiv in case of L-Asn and L-Gln and 3.5 ml, 47.83 mmol, 2.1 mol equiv in case of L-Asp) was added drop-wise over 5 – 10 minutes. Because of the exothermic reaction, the vapors had to be cooled by reflux condenser. After the addition was complete, the temperature was left to decrease to room temperature and the mixture was stirred for 24 hours. After the reaction was complete, the solvent was removed by evaporation (RVE). The white or light yellow solid was washed with n-hexane (twice 50 ml), and evaporated with another portion of n-hexane. The product was dried at low pressure.

Methyl-L-asparagine hydrochloride (2a). Was isolated as light yellow solid in 4.06 g (99 % yield). M.p. 122-126°C.^{1}H NMR (300 MHz, D_2O, ppm) δ: 4.37 (dd, 1H, J = 4.8 and 6.0 Hz, CH), 3.71 (s, 3H, CH_3), 3.02 – 3.06 (m, 2H, CH_2). ^{13}C NMR (75 MHz, D_2O, ppm) δ: 171.5 and 169.2 (2x COO), 53.3 (CH_3), 49.0 (CH), 33.5 (CH_2). IR (solid, cm[-1]): 3420 (m, N-H), 3126 (s), 3041 (s), 2826 (m), 1739 (s, C=O), 1623 (w), 1506 (w), 1399 (s), 1254 (m), 1151 (w), 1072 (w), 955 (w), 886 (w).

Methyl-L-glutamine hydrochloride (2b). Was isolated as light yellow solid in 4.30 g (98 % yield). M.p. 141-144°C.^{1}H NMR (300 MHz, D_2O, ppm) δ: 4.06 (dd, 1H, J = 6.6 and 7.2 Hz, CH), 3.68 (s, 3H, CH_3), 2.46 – 2.52 (m, 2H, CH$\underline{CH_2}$), 2.05- 2.15 (m, 2H, $\underline{CH_2}CONH_2$). ^{13}C NMR (75 MHz, D_2O, ppm) δ: 174.8 and 170.1 (2x CO), 53.5 (CH_3), 48.8 (CH), 29.2 ($\underline{CH_2}CONH_2$), 24.7 (CH$\underline{CH_2}$). IR (solid, cm[-1]): 3412 (m, N-H), 3127 (s), 3040 (s), 2858 (m), 2722 (w), 1721 (s, C=O), 1671 (s, C=O), 1611 (w), 1058 (m), 1425 (w), 1399 (s), 1274 (m), 1253 (m), 1213 (s), 1147 (w), 1081 (w), 1000 (w), 862 (w), 823 (m), 676 (w), 635 (w).

Dimethyl-L-aspartate hydrochloride (2c). Was isolated as white powder in 4.04 g (98 % yield). M.p. 112-114°C.^{1}H NMR (300 MHz, D_2O, ppm) δ: 4.52 (dd, 1H, J = 6.3 Hz and 5.1 Hz, CH), 3.85 (s, 3H, CH_3), 3.76 (s, 3H, CH_3), 3.19 (m, 2H, CH_2).^{13}C NMR (75 MHz, D_2O, ppm) δ: 174.5 and 172.3 (2x $\underline{C}OOCH_3$), 56.8 and 55.9 (2x COO$\underline{CH_3}$), 52.1 (CH), 36.6 (CH_2). IR (solid, cm[-1]): 3399 (s, OH), 3212 (m), 2959 (s), 1743 (s), 1621 (m), 1515 (m), 1442 (s), 1410 (w), 1379 (m), 1249 (s), 1216 (s), 1155 (m), 1078 (m), 1016 (m), 951 (w), 888 (w), 843 (w), 798 (w), 667 (m), 641 (m), 621 (m).

General procedure for preparation of *N*-(2-Hydroxy-benzyl)-amino acid methyl esters (4a-c). To a solution of the amino acid methyl ester hydrochloride **2** (12.45 mmol, 1.3 mol equiv) in 20 ml of dry methanol sodium hydroxide (0.50 g, 12.45 mmol, 1.3 mol equiv) was added at room temperature and the mixture was stirred until the hydroxide was consumed completely. During this reaction sodium chloride is formed, which can be observed as white powder-like precipitate. After 15-30 minutes of stirring, the mixture was cooled down using an ice bath to 0 – 10 °C and a solution of salicyl aldehyde (**3**) (1.00ml, 9.58 mmol, 1 mol equiv) in 5 ml of dry methanol was added drop-wise over 5-10 minutes. A color change from almost colorless to yellow was observed. The mixture was stirred at 0 – 10°C until the reaction was complete – about 1 - 2 hours (TLC control: n-hexane : ethyl acetate = 8 : 1). Afterwards, solid $NaBH_4$ (440 mg, 11.50 mmol, 1.2 mol equiv) was added portion-wise and the solution was stirred until the yellow color disappeared (15 – 30 min). Solvent was removed by evaporation to dryness. The product was obtained from the solid by washing the solid with diethyl ether and evaporation. The product was further dried at low pressure.

N-(2-Hydroxy-benzyl)-L-asparagine methyl ester (4a). Was isolated as an oil in 1.81 g (75 %). ^{1}H NMR (300 MHz, DMSO-d_6, ppm) δ: 7.04 – 7.13 (m, 2H, C4-H and C6-H), 6.73 – 6.76 (m, 2H, C3-H and C5-H), 3.78 (d, 2H, J(H,H´) = 14.7 Hz, Ar-CH̲H), 3.62 – 3.68 (m, 2H, Ar-CHH and NHC̲H̲), 3.59 (s, 3H, COOC̲H̲$_3$), 2.56 – 2.77 (m, 2H, CHC̲H̲$_2$). ^{13}C NMR (75 MHz, DMSO-d_6, ppm) δ: 173.2 and 170.9 (2x CO), 156.1 (C2), 128.9 and 127.9 (C4 and C6), 124.9 (C1), 118.7 (C5), 115.1(C3), 56.5 (CH), 51.8 (COOC̲H̲$_3$), 47.3 (Ar-C̲H̲$_2$), 36.9 (CHC̲H̲$_2$). IR (solid, cm^{-1}): 3430 (w, N-H), 3094 (w), 2954 (m), 2818 (m), 2754 (w), 1733 (s, C=O), 1603 (w), 1589 (s), 1490 (m), 1459 (m), 1438 (m), 1375 (s), 1253 (s), 1207 (s), 1178 (m), 1114 (w), 1039 (w), 1004 (m), 846 (m), 757 (s), 659 (w).

N-(2-Hydroxy-benzyl)-L-glutamine methyl ester (4b). Was isolated as an oil in 1.66 g (65 %). ^{1}H NMR (300 MHz, DMSO-d_6, ppm) δ: 7.01 – 7.12 (m, 2H, C4-H and C6-H), 6.72 – 6.82 (m, 2H, C3-H and C5-H), 4.62 (d, 1H, J(H,H´) = 14.7 Hz, Ar-CH̲H), 4.07 – 4.11 (m, 1H, CH), 4.01 (d, 1H, J(H,H´) = 14.7 Hz, Ar-CHH̲), 3.63 (s, 3H, COOC̲H̲$_3$), 2.25 – 2.32 (m, 2H, CHC̲H̲$_2$), 1.91 – 1.96 (m, 2H, C̲H̲$_2$CONH$_2$). ^{13}C NMR (75 MHz, DMSO-d_6, ppm) δ: 174.5 and 172.4 (2x CO), 155.5 (C2), 129.7 and 128.7 (C4 and C6), 122.1 (C1), 119.0 (C5), 115.1(C3), 58.7 (CH), 52.1 (COOC̲H̲$_3$), 40.3 (Ar-C̲H̲$_2$), 28.9 (CHC̲H̲$_2$), 22.3 (C̲H̲$_2$CONH$_2$). IR (solid, cm^{-1}): 3420 (m, N-H), 3097 (m), 2954 (m), 2741 (w), 1746 (s, C=O), 1659 (s, C=O), 1607 (w), 1598 (w), 1488 (w), 1457 (s), 1436 (w), 1382 (w), 1357 (w), 1331 (w), 1279 (m), 1245 (s), 1207 (s), 1174 (s), 1109 (m), 1036 (w), 999 (w), 868 (w), 763 (s), 677 (w).

N-(2-Hydroxy-benzyl)-L-aspartate dimethyl ester (4c). Was isolated as a colorless oil in 2.30 g (95 %). 1H NMR (300 MHz, DMSO-d_6, ppm) δ: 7.03 – 7.12 (m, 2H, C4-H and C6-H), 6.69 – 6.75 (m, 2H, C3-H and C5-H), 3.77 and 3.65 (d, 1H and 1H, J(H,H´) = 13.5 Hz, Ar-C̲H̲$_2$), 3.62 and 3.58 (s, 6H, 2x COOC̲H̲$_3$), 3.61 (m, 1H, CH), 2.69 (m, 2H, CHC̲H̲$_2$). 13C NMR (75 MHz, DMSO-d_6, ppm) δ: 173.1 and 170.9 (2x C̲O̲OCH$_3$), 156.1 (C2), 128.9 and 127.9 (C4 and C6), 124.9(C1), 118.7(C5), 115.1(C3), 56.5(CH), 51.8 and 51.5 (2x COOC̲H̲$_3$), 47.2(Ar-C̲H̲$_2$), 36.9(CHC̲H̲$_2$). IR (solid, cm^{-1}): 3309(m, NH), 2954(m), 1734(s, C=O), 1616(w), 1588(m), 1490(m), 1456(w), 1437(m), 1369(m), 1252(s), 1203(s), 1171(s), 1104(w), 1036(w), 1001(m), 935(w), 844(w), 756(s), 722(w), 647(w), 639(w), 622(w).

General procedure for preparation of N-(2-Hydroxy-benzyl)-amino acid ligands (5a-c). To a stirred solution of the methyl ester **4**(4.51 mmol, 1 mol equiv) in 12 ml of methanol and 3 ml of water sodium hydroxide (0.42 g, 10.55 mmol, 2.1 mol equiv) was added and left to stir for 2 – 3 days. The pH of the reaction mixture was altered to 5 – 6 using 10% hydrochloric acid. All solvents

were removed by evaporation. The solid was washed with water (to remove inorganic salts), acetone and diethyl ether. The product was obtained as a powder after drying.

N-(2-Hydroxy-benzyl)-L-asparagine (5a). Yield 698 mg (65 %). M.p. 204-207°C.Elemental analysis calculated for $C_{11}H_{14}N_2O_4$ (MW = 238.24) C 55.46; H 5.92; N 11.76, measured C 55.39; H 6.01; N 11.61. ^{1}H NMR (300 MHz, D_2O, ppm) δ: 7.19 – 7.26 (m, 2H, C4-H and C6-H), 6.83 – 6.88 (m, 2H, C3-H and C5-H), 4.11 – 4.21 (m, 2H, J(H,H′) = 17.1 Hz, Ar-$\underline{CH_2}$), 3.64 (dd, 1H, J = 4.2 Hz and 9.0 Hz, CH), 2.68 (dd, 1H, J= 4.2 Hz and 17.7 Hz, CHC$\underline{H}$H), 2.56 (dd, 1H, J = 9.0 Hz and 17.7 Hz, CHCH$\underline{H}$). ^{13}C NMR (75 MHz, D_2O, ppm) δ: 173.1 and 173.0 (2x CO), 156.7 (C2), 129.7 and 128.7 (C4 and C6), 127.3 (C1), 118.6 (C5), 115.4 (C3), 56.6 (CH), 46.8 (Ar-$\underline{CH_2}$), 28.0 (CH$\underline{CH_2}$). IR (solid, cm^{-1}): 3450 (m, N-H), 3151 (m), 2754 (w), 2573 (w), 1593 (s, C=O), 1508 (w), 1464 (m), 1393 (s), 1373 (s), 1333 (m), 1278 (m), 1258 (m), 1203 (w), 1113 (w), 1040 (w), 1017 (w), 861 (w), 758 (s), 664 (m).

N-(2-Hydroxy-benzyl)-L-glutamine (5b). Yield 716 mg (63 %). M.p. 215-219°C. Elemental analysis calculated for $C_{12}H_{15}N_2O_4$ (MW = 252.27) C 57.13; H 6.39; N 11.10, measured C 57.02; H 6.30; N 10.95. 1H NMR (300 MHz, DMSO-d_6, ppm) δ: 7.13 (ddd, ^{1}H, J(3,4 or 4,5) = 9 Hz, J (3,4 or 4,5) = 7.8 Hz, J(4,6) = 1.5 Hz, C4-H), 7.00 (dd, 1H, J(5,6) = 6 Hz, J(4,6) = 1.5 Hz, C6-H), 6.77 – 6.83 (m, 2H, C3-H and C5-H), 4.72 (d, 1H, J(H,H') = 14.7 Hz, Ar-C$\underline{H}$H), 3.97 (d, 1H, J(H,H′) = 14.7 Hz, Ar-CHH), 3.83 (dd, 1H, J = 4.5 Hz and 9.3 Hz, CH), 2.16 – 2.45 (m, 4H, CH$\underline{CH_2CH_2}$). ^{13}C NMR (75 MHz, DMSO-d_6, ppm) δ: 174.5 and 173.7 (2x CO), 155.8 (C2), 129.5 and 128.4 (C4 and C6), 122.8 (C1), 118.8 (C5), 115.6 (C3), 59.9 (CH), 40.3 (Ar-$\underline{CH_2}$), 29.4 (CH$\underline{CH_2}$), 25.5 ($\underline{CH_2}CONH_2$). IR (solid, cm^{-1}): 3458 (w, N-H), 3183 (m, O-H), 2957 (m), 2736 (w), 1659 (s, C=O), 1596 (s, C=O), 1505 (w), 1489 (w), 1457 (s), 1418 (s), 1357 (w), 1277 (m), 1240 (s), 1183 (w), 1154 (w), 1107 (m), 1041 (w), 957 (w), 850 (w), 756 (s), 665 (w).

N-(2-Hydroxy-benzyl)-L-aspartic acid (5c). Yield 576 mg (76 %). M.p. 218-220°C. Elemental analysis calculated for $C_{11}H_{13}NO_5$ (MW = 239.23) C 55.23; H 5.48; N 5.86, measured C 54.99; H 5.33; N 6.06. 1H NMR (300 MHz, D_2O, ppm) δ: 7.16 – 7.21 (m, 2H, C6-H and C4-H), 6.81 – 6.85 (m, 2H, C3-H and C5-H), 4.16 (d, 1H, J(H,H′) = 13.0 Hz, Ar-C$\underline{H}$H), 4.10 (d, 1H, J(H,H′) = 13.0 Hz, Ar-CH$\underline{H}$), 3.60 (dd, 1H, J = 9.3 Hz and 3.9 Hz, CH), 2.63 (dd, 1H, J = 15.6 Hz and 3.9 Hz, CHC$\underline{H}$H), 2.53(1H, dd, J = 15.6 Hz and 9.3 Hz, CHCH$\underline{H}$). 13C NMR (75 MHz, D_2O, ppm) δ: 177.3 and 173.2 (2x $\underline{C}$OOH), 155.1 (C2), 131.6 and 131.3 (C4 and C6), 120.4 (C5), 117.6 (C1), 115.4 (C3), 58.7(CH) 46.5(Ar-$\underline{CH_2}$), 35.4(CH$\underline{CH_2}$). IR (solid, cm^{-1}): 3215(m), 3046(m), 2591(m), 2359(w), 1625(s), 1600(s), 1489(w), 1463(m), 1410(s), 1387(s), 1371(s), 1313(m),

1273(w), 1259(m), 1243(m), 1208(w), 1113(w), 1074(w), 1041(m), 978(w), 946(w), 915(w), 884(m), 833(w), 801(w), 786(w), 751(s), 753(s), 714(w), 668(m), 645(w), 616(w).

General procedure for preparation of Cu(II) complexes.

Method A. To a stirred and to reflux heated solution of Cu(OAc)$_2$.H$_2$O (168 mg, 0.84 mmol, 1.00 mol equiv) in methanol (10 ml), a solution of the amino acid ligand **5** (0.84 mmol, 1.00 mol equiv) in 10 ml methanol was added. A color change from blue to green is usually observed. The mixture is stirred with heating for 30 minutes and then left to cool without stirring. The cooled solution was allowed to concentrate by slight evaporation.

Method B. To a stirred and heated solution of the amino acid ligand **5** (0.84 mmol, 1.00 mol equiv) and NaOH (34 mg, 0.84 mmol, 1.00 mol equiv) in 10 ml of distilled water a solution of Cu(NO$_3$)$_3$.3H$_2$O (203 mg, 0.84 mmol, 1.00 mol equiv) in 2 ml of distilled water was added. A color change was observed from blue to green. The mixture is left to cool without stirring. The cooled solution was allowed to concentrate by slight evaporation.

HSal-L-Asn Cu(II) acetate complex (6a). Method A provided Cu(HSal-L-Asn) acetate as a green powder in 274 mg (91 %). Elemental analysis calculated for C$_{13}$H$_{17}$CuN$_2$O$_6$ (MW = 359.82) C 43.39; H 4.48; N 7.79, measured C 43.11; H 4.35; N 7.84. IR (solid, cm^{-1}): 3386 (m, N-H), 3250 (m, N-H), 2957 (w), 2784 (w), 1603 (m, N-H), 1582 (s, C=O), 1487 (w), 1456 (m), 1413 (s), 1285 (m), 1244 (m), 1185 (w), 1153 (w), 1108 (w), 1043 (w), 959 (w), 899(w), 852 (w), 757 (m), 676 (s).

HSal-L-Asn Cu(II) hydrate complex (6b). Method B provided Cu(HSal-L-Asn) hydrate as a green powder in 77 mg (29 %). Elemental analysis calculated for C$_{13}$H$_{17}$CuN$_2$O$_6$ (MW = 317.79) C 41.51; H 4.44; N 8.82, measured C 41.21; H 4.67; N 8.60. IR (solid, cm^{-1}): 3452 (m, N-H), 3220 (m, N-H), 2986 (m), 2768 (w), 1581 (s, C=O), 1482 (w), 1435 (m), 1403 (m), 1335 (s), 1291 (s), 1159 (w), 1096 (m), 1040 (w), 1017 (w), 893 (w), 827 (w), 759 (w), 667 (w).

HSal-L-Gln Cu(II) acetate complex (6c). Method A provided Cu(HSal-L-Gln) acetate as a green powder in 80 mg (25 %). Elemental analysis calculated for C$_{14}$H$_{19}$CuN$_2$O$_6$ (MW = 373.85) C 44.98; H 4.85; N 7.49, measured C 44.84; H 4.96; N 7.62. IR (solid, cm^{-1}): 3392 (m, N-H), 3266 (m, N-H), 2950 (w), 2802 (w), 1600 (m), 1583 (s, C=O), 1488 (w), 1456 (m), 1416 (s), 1286 (m), 1243 (m), 1185 (w), 1153 (w), 1108 (w), 1044 (w), 957 (w), 900(w), 848 (w), 757 (m), 677 (s).

HSal-L-Asp Cu(II) hydrate complex (6e). Method B provided Cu(HSal-L-Asp) hydrate as a blue powder in 112 mg (42 %). Elemental analysis calculated for $C_{11}H_{13}CuNO_6$ (MW = 318.77) C 41.45; H 4.39; N 4.11, measured C 41.06; H 4.38; N 4.04. IR (solid, cm^{-1}): 3514 (w), 3280 (m), 3120 (s), 2966 (s), 1645 (s), 1612 (w), 1574 (s), 1505 (m), 1429 (m), 1448 (w), 1429 (m), 1406 (s), 1383 (w), 1353 (s) 1330 (w), 1317 (s), 1294 (w), 1271 (s), 1232 (m), 1191 (m), 1158 (w), 1109 (m), 1081 (w), 1047 (w), 1013 (m), 987 (w), 952 (w), 896 (w), 872 (w), 852 (m), 828 (w), 777 (s), 766 (s), 732 (w), 660 (s), 645 (w).

Antiradical activity assay. The used method is based on competitive equilibrium between transition of electrons/radicals from KO_2 to 2-(4-Iodophenyl)-3-(4-nitrophenyl)-5-phenyl-2*H*-tetrazolium chloride (INT) and transition of electrons/radicals to the measured compound. Transition of electrons to INT leads to formation of formazan. Active compounds are, in this fashion, able to inhibit the formation of the blue formazan, detected as light absorption at 500 nm.

For each measurement, an initial solution of the sample of a specific concentration was prepared ($1.10^{-2} – 1.10^{-5}$ M) in DMSO, also initial solutions of INT (4 M) in borate buffer (pH = 7.1) and a saturated solution of KO_2 in DMSO. From these a set of diluted solutions of volume 3.5 ml was made: 1. blank solution containing only INT dye (0.5 ml of INT solution and 3 ml of DMSO), 2. 3-5 control solutions containing INT dye and KO_2 (0.5 ml of INT solution, 0.5 ml of KO_2 solution and 2.5 ml of DMSO), 3. 3 sample solutions containing all three compounds - the complex, INT dye and KO_2 (0.5 ml of INT solution, 0.5 ml of initial complex solution of concentration $1.10^{-2} – 1.10^{-5}$ M, 0.5 ml of KO_2 solution and 2 ml of DMSO) and 4. sample control solution containing the complex and KO_2 (0.5 ml of complex solution of concentration $1.10^{-2} – 1.10^{-5}$ M, 0.5 ml of KO_2 solution and 2.5 ml of DMSO). In sample solutions and sample control solution (3. and 4.) the concentration of the sample was diluted 7-times, since each solution contained only 1/7 of the original initial solution. 200 µl of the solutions was moved into a micro-titration plate and the absorbance at 500 nm was measured in parallel in all four types of solutions. The resulting inhibition percent was calculated according the formula: 100 – [(sample absorbance – sample control absorbance) / average absorbance of control solutions] x 100. Result of each measurement was the average value from the 3 sample solutions with a standard deviation [21].

For IC_{50} determination a series of measurements with decreasing sample concentration was evaluated. With decreasing concentration, the % of inhibition was also decreasing in linear trend. A diagram of this linear relationship was created and a linear trend function was calculated. The IC_{50} value was calculated as the concentration with 50% inhibition of INT-formazan formation from the resulting diagram.

R E F E R E N C E S

[1]. H. Sies, *Experimental Physiology*, **1997**, *82*, 291.
[2]. I. Ghoneim, A.B. Abdel-Naim, A.E. Khalifa, E.S. El-Denshary, *Pharmacological Research*, **2002**, *46*, 273.
[3]. S. Tozokumi, *Free Radical Biology and Medicine*, **1996**, *34*, 93.
[4]. S. Noguchi, *Free Radical Biology and Medicine*, **2002**, *1588*, 159.
[5]. B. Halliwell, *Journal of Laboratory and Clinical Medicine*, **1992**, *119*, 598.
[6]. D. Heimler, L. Isolani, P. Vignolini, A. Romani, *Food Chemistry*, **2009**, *114*, 765.
[7]. V. Mancebo-Campos, M. Desamparados Salvador, G. Fregapane, *Food Chemistry*, **2014**, *150*, 374.
[8]. D. Ravishankar, A.K. Rajora, F. Greco, H.M.I. Osborn, *International Journal of Biochemistry & Cell Biology*, **2013**, *45*, 2821.
[9]. C.-T. Yang, M. Vetrichelvan, X. Yang, B. Moubaraki, K.S. Murray, J.J. Vittal, *Dalton Transactions*, **2004**, *1*, 113.
[10]. L.A. Tavadyan, H.G. Tonikyan, S.H. Minasyan, L.A. Harutyunyan, F.T. Greenaway, S. Williams, R.A. Gray-Kaufman, J.R.J. Sorenson, *Inorganica Chimica Acta*, **2002**, *328*, 1.
[11]. M.S. Islas, T. Rojo, L. Lezama, M.G. Merino, M.A. Cortes, M.R. Puyol, E.G. Ferrer, P. A. M. Williams, *Journal of Inorganic Biochemistry*, **2013**, *123*, 23.
[12]. A. Klanicová, Z. Trávníček, J. Vančo, I. Popa, Z. Šindelář, *Polyhedron*, **2010**, *29*, 2582.
[13]. C.A. Kaştaş, G. Kaştaş, A. Güder, M. Gür, H. Muğlu, O. Büyükgüngör, *Journal of Molecular Structure*, **2016**, in press.
[14]. N.S. Ilkevych, G. Schroeder, V.I. Rybachenko, K.Y. Chotiy, R.A. Makarova, *Spectrochimica Acta Part A: Molecular and Biomolecular Spectroscopy*, **2012**, *86*, 821.
[15]. K. Wajda-Hermanowicz, D. Pieniążczak, R. Wróbel, A. Zatajska, Z. Ciunik, S. Berski, *Journal of Molecular Structure*, **2016**, *1114*, 108.
[16]. I.B. Afanas'ev, E.A. Ostrakhovitch, E.V. Mikhal'chik, G.A. Ibragimova, L.G. Korkina, *Biochemical Pharmacology*, **2001**, *61*, 677.
[17]. H.M. Ali, W. Almagribi, M.N. Al-Rashidi, *Food Chemistry*, **2016**, *194*, 1275.
[18]. K.M. Schaich, X. Tian, J. Xie, *Journal of Functional Foods*, **2015**, *18*, 782.
[19]. J. Vančo, J. Marek, Z. Trávníček, E. Račanská, J. Muselík, O. Švajlenová, *Journal of Inorganic Biochemistry*, **2008**, *102*, 595.
[20]. M.V. Nikolić, M.Ž. Mijajlović, V.V. Jevtić, Z.R. Ratković, S.B. Novaković, G.A. Bogdanović, J. Milovanović, A. Arsenijević, B. Stojanović, S.R. Trifunović, G.P. Radić, *Journal of Molecular Structure*, **2016**, *1116*, 264.
[21]. J. Vančo, O. Švajlenová, E. Račanská, J. Muselík, J. Valentová, *Journal of Trace Elements in Medicine and Biology*, **2004**, *18*, 155.
[22]. R.S. Hoonur, B.R. Patil, D.S. Badiger, R.S. Vadavi, K.B. Gudasi, P.R. Dandawate, M.M. Ghaisas, S.B. Padhye, M. Nethaji, *European Journal of Medicinal Chemistry*, **2010**, *45*, 2277.

[23]. P. Mishra, A. Dixit, M. Ray, S. C. Sabat, *Biochimie*, **2014**, *97*, 181.

[24]. F.O. Dimayuga, C. Wang, J.M. Clark, E.R. Dimayuga, V.M. Dimayuga, A.J. Bruce-Keller, *Journal of Neuroimmunology*, **2007**, *182*, 89.

[25]. V.A. Kostyuk, A.I. Potapovich, E.N. Strigunova, T.V. Kostyuk, I.B. Afanas'ev, *Archives of Biochemistry and Biophysics*, **2004**, *428*, 204.

[26]. Y. Ünver, K.K. Sancak, F. Çelik, E. Birinci, M. Küçük, S. Soylu, N.A. Burnaz, *European Journal of Medicinal Chemistry,* **2014**, 84, 639.

[27]. M. Selvaganapathy, N. Pravin, K. Pothiraj, N. Raman, *Journal of Photochemistry and Photobiology B: Biology*, **2014**, *138*, 256.

[28]. S. Demir, A. Güder, T.K. Yazıcılar, S. Cağlar, O. Büyükgüngör, *Spectrochimica Acta Part A: Molecular and Biomolecular Spectroscopy*, **2015**, *150*, 821.

[29]. E. Pontiki, D. Hadjipavlou-Litina, A.T. Chaviara, C.A. Bolos, *Bioorganic & Medicinal Chemistry Letters*, **2006**, *16*, 2234.

[30]. L.H. Abdel-Rahman, A.M. Abu-Dief, M. Ismael, M.A.A. Mohamed, N.A. Hashem, *Journal of Molecular Structure*, **2016**, *1103*, 232.

[31]. J. Vančo, Z. Trávniček, J. Marek, R. Herchel, *Inorganica Chimica Acta*, **2010**, *363*, 3887.

[32]. A. García-Raso, J.J. Fiol, A. López-Zafra, J.A. Castro, A. Cabrero, I. Mata, E. Molins, *Polyhedron,* **2003**, *22*, 403.

[33]. L.H. Abdel-Rahman, R.M. El-Khatib, L.A.E. Nassr, A.M. Abu-Dief, M. Ismael, A.A. Seleem, *Spectrochimica Acta Part A: Molecular and Biomolecular Spectroscopy*, **2014**, *117*, 366.

[34]. S. Mondal, B. Pakhira, A.J. Blake, M.G.B. Drew, S.K. Chattopadhyay, *Polyhedron*, **2016**, *117*, 327.

[35]. I. Yousuf, F. Arjmand, *Journal of Photochemistry and Photobiology B: Biology*, **2016**, *164*, 83.

[36]. B. Sreenivasulu, *Australian Journal of Chemistry*, **2009**, *62*, 968.

[37]. L. Jia, P. Jiang, J. Xu, Z. Hao, X. Xu, L. Chen, J. Wu, N. Tang, Q. Wang, J.J. Vittal, *Inorganica Chimica Acta*, **2010**, *363*, 855.

[38]. B. Sreenivasulu, J.J. Vittal, *Inorganica Chimica Acta*, **2009**, *362*, 2735.

[39]. F. Bao, X. Xu, W. Zhou, C. Pang, Z. Li, Z. Gu, *Journal of Inorganic Biochemistry*, **2014**, *138*, 73.

[40]. L. Jia, N. Tang, J. J. Vittal, *Inorganica Chimica Acta*, **2009**, *362,* 2525.

PREDICTING CHROMATOGRAPHIC BEHAVIOR OF SEVERAL CHIRAL β-BLOCKERS FROM MOLECULAR STRUCTURE BY QSPR ANALYSIS

MONA-MARIA TALMACIU[a], EDE BODOKI[a*], JAMES PLATTS[b], RADU OPREAN[a]

ABSTRACT. The chiral HPLC separation parameters of a series of fourteen β-blockers previously performed on four polysaccharide-based chiral stationary phases (CSPs) was evaluated through computational techniques, using a set of 340 molecular descriptors (MD), calculated with the Molecular Operating Environment (MOE) software. Several semi-empirical mathematical models were built and refined by PLS, O2PLS multivariate data analysis and by PLS-Tree® clustering, correlating chromatographic data with the descriptors. The resulting models revealed the importance of certain analyze descriptors shaping chromatographic behaviour of the studied enantiomers. The chiral selector backbone as well as the presence of halogen atom(s) in the structure of the used stationary phase appears to exert an influence on the type of descriptors that significantly contribute either positively or negatively on the prediction power of the developed models. The influence of additive on the predictive power of models was also briefly analysed. This QSPR study generated models with a good predictive power. However, these results could be substantially improved in the future by including the descriptors for the chiral selectors and additives in the model and by performing docking studies.

Keywords: Molecular descriptors, MOE, β-blockers, clustering, chiral HPLC

INTRODUCTION

The development of methods for the separation of enantiomers is of significant importance in analytical chemistry, because of the identical nature of their physico-chemical properties and, at the same time, the highly stereospecific interaction behaviour with other chiral molecules, in specific conditions. In clinical

---

[a] *"Iuliu Haţieganu" University of Medicine and Pharmacy, Faculty of Pharmacy, Department of Analytical Chemistry and Instrumental Analysis, Louis Pasteur St. 400349 Cluj-Napoca, Romania*
[b] *Cardiff University, School of Chemistry, Computational Chemistry Department, Cardiff CF10 3XQ, Wales, UK*
* *Corresponding author: bodokie@umfcluj.ro*

practice it translates in differences in terms of biological activity, potency, toxicity. In analytical chemistry research, more specifically in direct chromatographic separations, it leads to the formation of distinct diastereomeric complexes between the chiral selector and each of the optical isomers. Researchers working on enantiomeric separations using chiral stationary phases (CSPs) are faced with the challenge of having to screen and select the most appropriate chiral selectors and understand whether the chiral discrimination can be indeed achievable. This is generally done by trial and error, resulting in a time consuming and expensive strategy [1]. In order to reduce costs and time, experiments have started to be coupled with attempts at rationalizing enantiospecific recognition by a chiral selector at a molecular level. In its review on separation mechanisms in stereoselective chromatographic and electromigration techniques, Scriba notes several factors that might be involved in the stereoselective interactions between enantiomers and chiral selectors: H-bonds and π–π interactions, fit or non-fit of the solute in a cavity or cleft of the selector, conformational changes of the selector during complex formation with the solute (induced-fit) [2].

A deeper understanding of the manner in which the solute and selector features correlate with the experimental outcomes can be achieved by building interaction and prediction models. A detailed discussion of the models of chiral separations can be found in the review by Lämmerhofer [3].

The approaches having been used so far to build such models are quantitative structure-property relationships (QSPR), quantitative structure-retention relationships (QSRR) and quantitative structure-activity relationships (QSAR). The idea of these computerized statistical chemometric techniques is to find a correlation between dependent variables, like chromatographic parameters and independent variables, which are various analyte or/and selector descriptors. These have been applied to predict retention for a new analyte and to identify unknown analytes, to investigate the molecular mechanism of separation in a chromatographic system and predicting retention factors [4-6], separation factors [7, 8] and resolution [9] or by performing docking studies [10]. Also, such models were used to quantitatively compare separation properties of different types of chromatographic columns, to evaluate properties like lipophilicity and dissociation constants, to estimate relative bioactivities within sets of drugs.

Aside from the mentioned applications, these chemometric techniques can be used for optimizing HPLC chiral separations by offering the possibility of rationalizing the selection of a chiral column with characteristics that can be provided by QSRR. Many papers are focused on the use of chirality descriptors in QSAR [11-13], some results being selected to be discussed in the following rows. Aires-de-Sousa and Gasteiger developed two different kinds of chirality codes named "conformation-independent chirality code" (CICC) and "conformation-dependent chirality code" (CDCC) to distinguish between enantiomers [14, 15], but when investigating further the efficiency along a more straightforward statistical technique [16], they did not satisfy. In order to generate more interpretable

results, Zhang et al. [17] introduced the Physicochemical Atomic Stereodescriptors (PAS) based on twenty-one physicochemical properties of the ligands attached to a chiral centre. Later, total and atom-level molecular descriptors relevant to QSAR/QSPR studies and 'rational' drug design were developed to define quadratic chiral indices for a molecule from its pseudograph considering either atom (vertex) adjacency [18-20] or bond (edge) adjacency [21]. Their drawback was caused by the use of 2D molecular information for their calculation. Their application was subsequently extended to consider 3D features of small to medium-sized molecules based on the trigonometric-3D-chirality-correction factor approach, using a new vector called the chirality molecular vector [22]. However, these descriptors and codes were not broadly used because of the complicated computational methods. Because of the vast number of molecular descriptors available, but which were not able to discriminate between enantiomers several research groups [23-27] developed chirality indices by applying correction factors to the topological indexes already existent.

A new class of chirality descriptors called Relative Chirality Index (RCI), calculated based on valence connectivity, the formula weights of the groups and the electrotopological state of the various atoms and groups in the four substituents at the asymmetric carbon were studied by Natarajan et al. [28]. They were found that RCI are not being applicable to large molecules. In 2012, five quantum chemical descriptors were applied in a study of Rasulev: HLG (gap between E_{HOMO} and E_{LUMO}), hardness (η, $\eta = E_{HOMO} - E_{LUMO} = HLG$), softness ($\sigma$, $\sigma = 1/\eta$), electronegativity (χ, $\chi = (E_{HOMO} + E_{LUMO}) / 2$), total energy ($E_{total}$) [29].

Nowadays, thousands of descriptors encoding the molecular structure features of analytes or selectors can be calculated by various software like Gaussian, Marvin Suite [30], DRAGON, CORINA, ADRIANA. Code, MOPAC, VolSurf, Molecular Operating Environment (MOE) [4, 8], PaDEL and many others.

Statistical analysis has been the most commonly used tool for interpreting correlations between experimental parameters and molecular descriptors. The most widely used model-building technique is multivariate data analysis. Aside from being most reported in the literature, multivariate statistical analysis and building semi-empirical models for prediction could contribute to the elucidation of the most significant chiral descriptors contributing to the separation of enantiomers. Various methods for data analysis exist today. Partial Least Square regression, also known as Projections to Latent Structures (PLS) has been used for over three decades. Several improvements have been introduced during this period of time; first, orthogonal PLS- OPLS [31] and then O2PLS [32, 33] were formulated, which are able to filter out variation that is not directly related to the response in various data analytical objectives related to classification, discrimination, regression or prediction. In contrast to PLS and OPLS, O2PLS is bidirectional and it is able to map how different types of variation in two datasets are connected, as well as to identify the unique information in each

dataset. The blocks X (chemical descriptors) and Y (chromatographic responses) represent two data matrices to be compared. X can be used to predict Y (as with PLS and OPLS), but at the same time Y can be used to predict X (unlike PLS and OPLS) [34]. With O2PLS one can model: the joint X-Y covariation, the Y-orthogonal variation in X and the X-orthogonal variation in Y.

To our knowledge there is no study already conducted on the entire set of β-blockers employed in the current analysis, dedicated to find correlations between their 3D structures derived molecular descriptors and the experimentally obtained chromatographic parameters. The present study aims to highlight some structural features, derived from significant molecular descriptors that are likely to be responsible for the observed enantio-selectivity and could possibly contribute to understanding the molecular characteristics that are involved in the chiral separation mechanism.

RESULTS AND DISCUSSIONS

Statistical analysis

MOE calculates 340 descriptors from three classes - 2D descriptors, i3D and x3D, internal and external 3D descriptors [35]. After the screening process and the calculation of molecular descriptors, the available data was compiled and analysed statistically.

Data analysis of MD and chromatographic parameters by PCA and OPLS/O2PLS

The available X- and Y-block variables, described above, were subjected to O2PLS analysis.

Multivariate data analysis began on the entire data set (all observations recorded on 4 columns with 3 additives, N= 336) with a principal component analysis (PCA). Standard scaling and mean-centering (centred and scaled to unit variance) was performed in the data pre-treatment step. Pre-treatment using PCA of the X-data gave an eighteen-component model, which explained 96.4% of the variation (R2X=0.964).The score scatter plot of the PCA-X model (data not shown), as in the case of the subsequent PLS models, indicated significant structural and chromatographic differences between R- and S- carvedilol and the rest of the enantiomers. As an additional exploratory data analysis hierarchical cluster analysis (HCA) and PLS-Tree®[33] was also performed for identifying more subtle clustering within the set of variables (X-data block) or observations (both X- and Y-block) that eventually might offer better models for parts of the data. As a next step multivariate regression analysis by PLS modelling on the entire mean centred and scaled data set has been carried out. Both, PLS

and O2PLS regression on the entire data set provided models with relatively modest predictive ability (PLS - Q2cum = 0.435; O2PLS - Q2cum = 0.454), where one of the possible reasons might be the absence of molecular descriptors related to the four different CSPs in the chemometric model. Therefore, the observations were grouped in four classes, according to the nature of the CSP. The corresponding O2PLS models presented significantly improved prediction abilities, where the cross-validated variances were Q2(cum) = 0.606 for column IA, Q2(cum) = 0.61 for column IB, Q2(cum) = 0.837 for column IC, Q2(cum)= 0.851 for column ID.
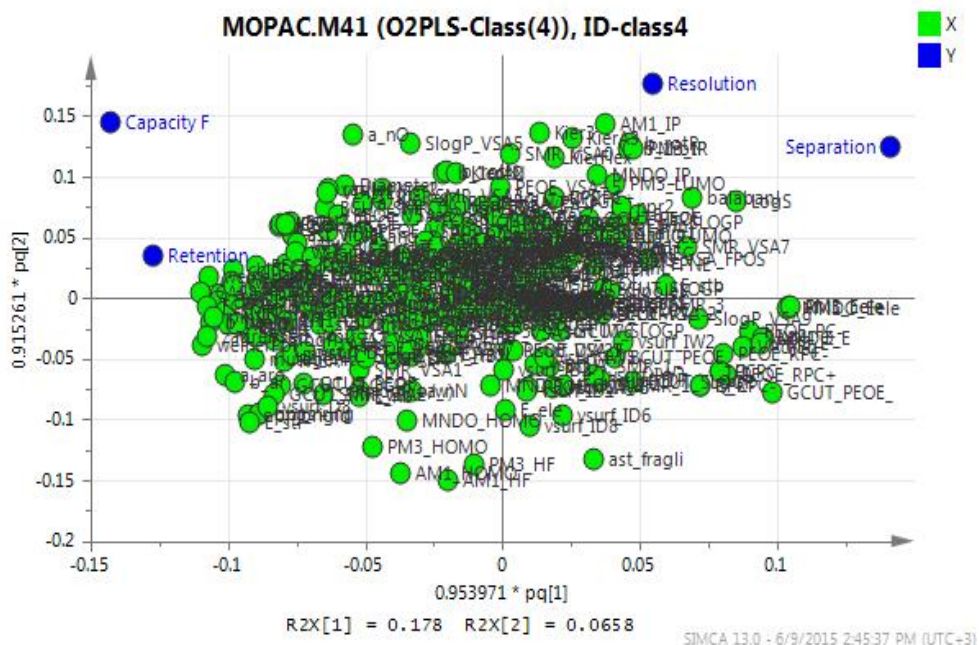
Figure 1. 2D loading scatter plot in function of the first two principal components of the O2PLS model (separated on ID column)

The loading scatter plot (Figure 1) indicates the relationship between all factors (X) and responses (Y), and how molecular descriptors correlate to each of the responses of interest (chromatographic parameters). Interpreting a model with so many components based on the scatter plots may be cumbersome; therefore a more appropriate approach was the examination of the Variable Importance in the Projection (VIP) plot, that summarizes the importance of the variables both to explain X and to correlate to Y. Usually VIP values larger than 1 indicate significant X-variables and values below 0.5 are considered to lack significance. Additionally, to correct for data skewness and to improve the efficiency of data analysis, further pre-processing (i.e. log-transformation)

of the Y-data (α, k', t_R) was performed. In order to conveniently compare the performance in terms of predictive power amongst the generated models, the Root Mean Square Error from cross-validation (RMSEcv) was calculated (data not shown). It should be noted that, with and without data pre-processing, the best predictive power is obtained in case of the separation factor, whereas the retention time seems to be modelled the poorest. Nevertheless, log-transformation of α, k' and t_R does offer improvements in the case of columns IA and IB, with a slight increase of the cross-validation residuals in the case of columns IC and ID. Because of the improvements offered by logarithmic transformation of chromatographic parameters, only data obtained with log-transform will be further considered.

Model improvement through external validation approach

External validation approach was also tested, dividing the observations into two sub-sets, where the training set represented the initial set of observations out of which every 5th observation was removed. The arbitrary sampling of the validation set was meant to additionally prove the reliability of the O2PLS model, where in principle from the systematic variability the part uncorrelated (orthogonal) to Y has already been removed. The resulting set of complementary observations (N = 5-6), grouped by the type of additive and used column, represented the validation set on which predictions of the chromatographic data were performed.

The measure of predictive ability, expressed as the Root Mean Square Error of Prediction (RMSEP), representing the fitted residuals for the observations from the validation set (Table 1), may serve for the comparison between the predictive powers of the models generated from the training sets, as well as for the validation of the entire dataset. Satisfactory predictive capability, which has been obtained in almost every case of the orthogonal PLS modelling, was further improved by the log-transformation of three of the chromatographic parameters (α, k' and t_R).By comparing the individual measure of predictive power (either RMSEcv or RMSEP) for a given model, one can observe that the lowest values, thus the best predictive ability, is obtained in case of the separation (α) and capacity (k') factors.

New OPLS models have been developed for each type of CSP and additive, subjecting them to an external validation procedure using the same validation set mentioned above (every 5th analysis of the entire dataset). The quality and improved predictive ability of the resulting models, as well as the ruggedness and validity of the dataset, was proven by the calculated statistical parameters (i.e. R^2Y, Q^2Y, and RMSEP) as well as by the predicted values of retention time for the enantiomers of the validation set.

In spite of the relatively limited number of observations in the calibration set the predicted retention time values in many cases are quite close to the observed ones. Nevertheless, in some cases relatively high bias between the two values is recorded, indicating the need for further improvement.

Table 1. Measure of predictive power related to the validation set of the generated O2PLS models from the training sets with pre-processing of Y-variables

Column	Additive	RMSEP			
		A	k'	t_R	R_S
IA	EA	0.0562	0.6310	1.4545	0.7216
	EDA	0.1055	0.6664	2.1430	0.8403
	DEA	1213.31	0.8300	3.5738	10.719
IB	EA	0.1189	0.7266	1.9881	0.6274
	EDA	0.2126	1.8689	6.4567	1.9854
	DEA	0.0823	1.6827	2.1845	0.5373
IC	EA	0.1848	0.6197	2.0120	2.4205
	EDA	0.7623	1.3828	3.1781	510.571
	DEA	0.1158	1.0064	2.5615	1.7668
ID	EA	0.2559	0.4868	4.8475	1.1110
	EDA	0.1156	0.6293	1.7575	0.8572
	DEA	0.4250	0.5786	6.1821	2.8185

Model improvement by cluster analysis

Because the above chemometric models do not include molecular descriptors weighing the structural and physicochemical particularities of the CSPs, and neither of the tested basic additives, additional exploratory data analysis has been performed on the available data set for the identification of a more subtle data clustering that might have been overlooked by PCA and which would enable the generation of daughter training sets that eventually could lead to an improved modelling of the chromatographic behaviour.

Among the two available clustering tools HCA (bottom-up approach) and PLS-Tree® (top-down approach), the later was preferred, since it accounts also for the Y-variables (chromatographic parameters) and offers cleaner dendrograms (classification trees). As algorithm parameters in the assessment of score value split points A = 0.1 and B = 0.3 were selected, with a maximum depth of 4 of the PLS-Tree. Running the PLS-Tree clustering on either the entire data set (all 4 columns and all 4 additives) or only on data sub-sets defined by the afore mentioned qualitative variables (type of column, type of basic additive) two main clusters of β-blockers (Figure 2) could be distinguished: group 1) containing oxprenolol, metoprolol, alprenolol, propranolol, pindolol and group 2) the remaining β-blocker representatives. When working on the IB and IC data subsets, esmolol, betaxolol and carazolol were also assigned into the first group. Due to its particular structure carvedilol represents a moderate outlier in several models; however, to build a predictive model that applies to the entire class of β-blocker drugs, it has been kept within the observations.
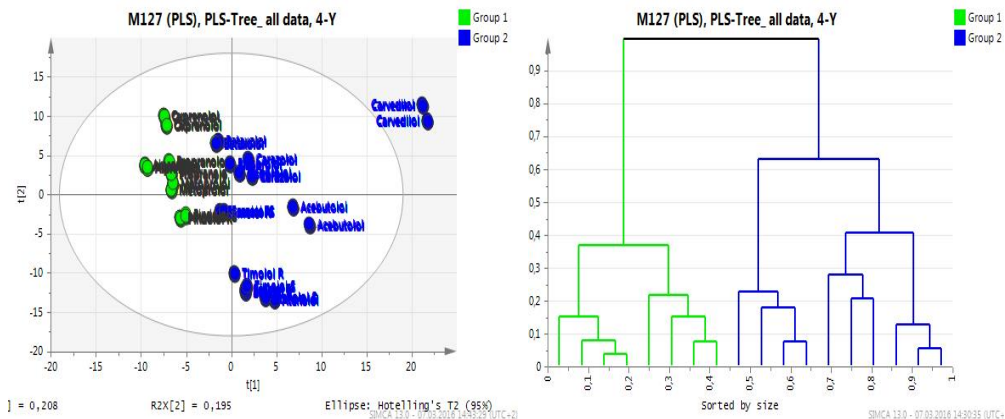
Figure 2. The two main clusters of b-blockers (left) and the corresponding dendrogram (right) by PLS-Tree® clustering on the entire data set

The two main observed clusters were used to create O2PLS class models for each individual column. As it turned out, the predictive ability (Q2cum) and RMSEP values (Table I and II) of the resulting models were far superior to those obtained before clustering of observations (β-blockers), therefore once again for each cluster a validation set has been assigned (every 5th observation), based on which retention time values predictions were performed. If in the case of columns IA and IB no consistent improvements in the prediction of retention time is observed (data not shown), in the case of IC and ID columns the prediction errors are significantly lower. In the case of IC and ID columns the influence of the mobile phase additives (EA, DEA, EDA) on the enantioseparation is almost negligible (around 62% on IC and 69% on ID of the 14 studied herein β-blockers were baseline or partially separated in the case of all the three basic additives employed), in comparison with their influence of the enantioselectivity using columns IA and IB (out of the 14 β-blockers 56% using EA, 25% using DEA, 50% using EDA on the IA column, and 56% using EA, 56% using DEA, 44% using EDA on the IB column, respectively were baseline or partially separated) The experimental results are taken from the study of Moldovan et al. [36].

For each column, the clustered data set was once again split according to the employed basic additive and O2PLS class models were once again generated. The overall predictive power (mean value of Q2Y and RMSEcv) for each pair of column - basic additive is significantly improved in comparison with the models obtained on the data sets that were not subjected to PLS-Tree® clustering (data not shown).

Table 2. Measure of predictive power related to the validation set
of the generated PLS models upon PLS-Tree clustering

Column	Cluster	RMSEP			
		A	k'	t_R	R_S
IA	1(OXP, PRN et.)	0.1152	0.2816	0.8125	0.9989
	2	0.0883	1.0001	2.7539	1.3652
IB	1	0.2021	0.5987	1.9030	2.0035
	2	0.0361	2.5970	3.7774	0.3508
IC	1	0.0356	0.0932	0.2843	0.6766
	2	0.0127	0.3511	0.9316	0.2059
ID	1	0.1399	0.0375	0.1344	0.9984
	2	0.1108	0.3817	3.6494	0.8716

Unfortunately, a further splitting of the data sets into validation sets significantly reduces the number of observations making up the training sets in many cases less than 5 observations, which is not able to further provide any real improvements in their prediction ability. However, as mentioned earlier, extending the range of accounted variables with molecular descriptors of the employed CSPs and mobile phase modifiers, a stronger correlation structure between the nature of selector and selectand (ligand) may be identified, able to account for more intimate structural complementarities and particularities.

Relationship between retention times and significant MDs

The loading scatter plots convey information about the descriptors that are influential in the modelling of chromatographic parameters on columns IA, IB, IC and ID and how they are correlated. Among the descriptors showing a significant contribution to every predictive model are to be mentioned the surface area, volume and shape descriptors, number of heavy atoms, the sum of hydrogen bond donors and acceptors, the number of O and N atoms in the molecule, the entropy of element distribution, the van der Waals surface area and volume, molecular weight, molecular refractivity and polarizability, total polar surface area.

Columns IA and ID are based on amylose, while IB and IC are based on cellulose derivatives. Moreover, column IA and IB only differ on the polysaccharide type backbone, but the substituent is the same, 3,5-dimethylphenylcarbamate. The particularities induced by the increasing number of halogen atoms on the substituents of Columns IC and ID (3,5-diclorophenylcarbamate on IC and

3-cloropehnylcarbamate on ID) may also be revealed. Without considering whether the correlation is positive or negative, two classes of descriptors exhibit by far the strongest contributions: the class of 3D descriptors that depend on surface area, volume and shape and the class of 2D partial charge descriptors. The first one registered contribution scores of 21.08% on Chiralpak IA, 32.62% on Chiralpak IB, 30.68% on Chiralpak IC and 23.51% on Chiralpak ID. Correlating this information with the structures of chiral selectors, strong similarities in the percentage of contribution scores and the nature of polymeric backbone is to be identified (~20% on amylose and ~30% on cellulose based CSP, respectively). The second class of descriptors showed a greater contribution for columns IA and IC and slightly lower, but still significant for IB and ID. Medium contributions were observed for the classes of adjacency and distance matrix and atom count descriptors.

Partial charge descriptors and surface area, volume and shape descriptors were the two classes of MD that exhibited the highest positive correlation to the chromatographic parameters. However, in case of the partial charge type, contribution can be seen only in case of columns IA and IB, while for IC and ID there is no visible contribution to the model. Columns IA and IB have distinct polymer backbone, but the same substituent, which could be accountable for the behaviour.

A preferential behaviour of descriptors is also observed in case of MOPAC MDs, which for columns with cellulose-based polymer backbone correlate positively with the chromatographic parameters, while for amylose-based columns the correlation is insignificant. From the distribution of contribution scores on each of the two cellulose-based columns, it results that on IC the heat of formation and total potential energy, which have values of over 1,5, are highly significant for the prediction model. For IB column, the highest contribution is exhibited by MNDO_dipole (~1). The difference between the two columns is the presence on column IC of two halogen atoms, suggesting that these could be responsible for the particular behaviour. While in case of column IC the total potential energy is a descriptor that significantly correlates in a positive way, the same descriptor, for the other columns, correlates negatively with the chromatographic parameters, registering values of contribution scores of over 2, rendering it extremely significant for the predictive model. In case of column IC the MOPAC descriptors that contribute negatively are the dipole moment and ionization potential. In case of columns IA, IB and ID the class of molecular descriptors with the strongest negative correlation with the chromatographic parameters was the partial charge descriptors, which contribute to the model 9.9%, for IA, 15.26% for IB and 17.53% for ID. For column IC the contribution is significant, 22.99%, but its highest contribution is exhibited by the class of surface area, shape and volume 3D descriptors, with 30.68% of the entire model, compared to the other three columns which register values between 3% and 7%. The surface area, shape and volume descriptors depend on structure connectivity and conformation. Our study revealed a particular behaviour in terms of the negative correlation with chromatographic parameters for column

108

IC, with regard to most classes of molecular descriptors. The only occurrence of lower negative correlation compared to the other three columns was seen for connectivity index descriptors, where column ID registered a percentage of 5.97, while for column IC it was 1.87 and the other two 0%.

CONCLUSIONS

Several approaches were tested in order to obtain useful information from the data obtained after descriptor calculation with MOE. The models obtained were tested and further refined by splitting the observations into calibration and validation sets. In the case of the external validation set, relatively close values of predicted retention times were obtained compared to the experimental ones. After PLS-Tree®, two main clusters of b-blockers were distinguished: the 1st containing oxprenolol, metoprolol, alprenolol, propranolol, pindolol and the 2nd group containing the remaining β-blocker representatives. Two classes of descriptors exhibit by far the strongest contributions: the class of 3D descriptors that depend on surface area, volume and shape and the class of 2D partial charge descriptors.A preferential behaviour of descriptors is also observed in case of MOPAC MDs, which for columns with cellulose-based polymer backbone correlate positively with the chromatographic parameters, while for amylose-based columns the correlation is insignificant.

Descriptors that exhibited significant contributions to the models, either positive or negative were H-bond donor and acceptor atoms, total potential energy, heat of formation, ionization potential, van der Waals surface area and volume, molecular weight, molecular refractivity and polarizability, total polar surface area.

It is estimated that the predictive power of the models could be further improved by expanding the number of observations on the entire range of existing β-blockers as well as by feeding into the model 3D molecular descriptors derived from the used CSPs. Developing models able to correlate molecular descriptors of CSPs and of various chiral molecules of interest with their corresponding chromatographic parameters could rationalize the selection procedure of CSP during method development as well as further contribute towards the elucidation of the molecular interactions responsible for chiral separation.

EXPERIMENTAL SECTION

HPLC experiments

All HPLC experiments were performed as described by Moldovan et al. [36]. The chromatographic behaviour (retention times, separation factors, capacity factors, resolutions) of the racemic mixtures of 14 β- blockers was studied by

gradient elution HPLC [36], with a mobile phase made up of 2-Propanol/n-Hexane with their ratio varying from 80/20 to 50/50 (v/v)) with 0.1% (v/v) additive (EA, DEA, EDA) added to 2-Propanol.

Molecular Modeling and Geometry Optimization

The 2D chemical structures of the β- blockers (14 molecules with one stereogenic centre) were downloaded from ChemicalBook, the chemistry of the structures was verified and then they were cleaned in 3D, using MarvinView Chemaxon). The chirality at the stereogenic centres was verified by applying the Cahn-Ingold-Prelog priority rules. Then the structures were preoptimized using MOPAC2012, by PM6 method. The resulting geometries were further refined by means of low mode dynamics (LMD) conformational search using the standard settings in MOE and MMFF94x force field to enforce low energy conformations of the molecules. The lowest energy conformer of all the compounds was transferred to database viewer and different classes of 2D and 3D descriptors were calculated.

Generation of Descriptors

A total of 340 2D and 3D descriptors were calculated for each conformation of each enantiomer with MOE and then the values corresponding to the conformation with the lowest energy were chosen. Calculations were performed with MOE (Molecular Operating Environment, v. 2014.09 on an Intel ® Core(TM) i3-4005U CPU @ 1.7 GHz personal computer with 12 GB of RAM running under Microsoft Windows 8.1). These data served as a basis for a further statistical analysis.

Statistical Analysis

The obtained chromatographic data and the calculated molecular descriptors were subjected to orthogonal partial least-squares (O2PLS) multivariate analysis using Simca-p+ v.13 software (MKS Data Analytics Solution, Sweden). The variables (K=340) building the X-block of data represented the molecular descriptors generated by MOE, derived from MOPAC calculation output and 2 qualitative variables/class identifiers (nature of column and type of additive), whereas the Y-block of data was made up by the chromatographic parameters (separation factor (α), retention time (t_r), capacity factor (k') and resolution (R_s)).

R E F E R E N C E S

[1]. K. Boronová, J. Lehotay, K. Hroboňová, D. Armstrong. *Journal of Chromatography A*. **2013**, *1301,* 38.
[2]. G. Scriba. *Chromatographia*. **2012**, *75*, 815.
[3]. M. Lammerhofer. *Journal of Chromatography A*. **2010**, *1217*, 814.
[4]. J. Gregor, N. Garrett, B. Gilpin, C. Randall, D. Saunders. *New Zealand Journal of Marine and Freshwater Research*. **2002**, *36(2)*, 387.
[5]. J. Kuebler, A. Russell, A. Hakami, A. Clappier, H. van den Bergh. *Atmospheric Environment*. **2002**, *36(17*), 2817.
[6]. R. Marshall. *Journal of Clinical Epidemiology*. **2001**, *54(6)*, 603.
[7]. D. Dabić, M. Natić, Z. Džambaski, R. Marković, D. Milojković-Opsenica, Ž. Tešić. *Journal of Separation Science*. **2011**, *34(18),* 2397.
[8]. M. Szaleniec, A. Dudzik, M. Pawul, B. Kozik. *Journal of Chromatography A*. **2009**, *1216(34*), 6224.
[9]. L. Asensi-Bernardi, L. Escuder-Gilabert, Y. Martín-Biosca, M. Medina-Hernández, S. Sagrado. *Journal of Chromatography A*. **2013**, *1308,* 152.
[10]. M. Szaleniec, A. Dudzik, M. Pawul, B. Kozik. *Journal of Chromatography A*. **2009**, *1216(34),* 6224.
[11]. G.M. Crippen. *Current Computer-Aided Drug Design*. **2008**, *4*, 259.
[12]. R. Natarajan, S.C. Basak. *Current Computer-Aided Drug Design*. **2009**, *5*, 1.
[13]. R. Natarajan, S.C. Basak. *Current Topics in Medicinal Chemistry.* **2011**, *11*, 771.
[14]. J. Aires-de-Sousa, J. Gasteiger. *Journal of Chemical Information and Computer Sciences.* **2001**, *41*, 369.
[15]. J. Aires-de-Sousa, J. Gasteiger, I. Gutman, D.I. Vidovic. *Journal of Chemical Information and Computer Sciences*. **2004**, *44*, 831.
[16]. S. Caetano, J. Aires-de-Sousa, M. Daszykowski, Y. Heyden. *Analytica Chimica Acta.* **2005***, 544(1-2),* 315.
[17]. Q.-Y. Zhang, J. Aires-de-Sousa. *Journal of Chemical Information and Modeling*. **2006**, *46*, 2278.
[18]. Y.M. Ponce, A. Huesca-Guillen, F. Ibarra-Velarde. *Journal of Molecular Structure*. **2005**, *717*, 67.
[19]. Y.M. Ponce. *Journal of Chemical Information and Computer Sciences.* **2004**, *44*, 2010.
[20]. Y.M. Ponce. *Molecules*. **2003**, *8*, 687
[21]. J.A. Castillo-Garit, Y.M. Ponce, F. Torrens, R. García-Domenech, J.E. Rodríguez-Borges. *QSAR & Combinatorial Science*. **2009**, *28*, 1465.
[22]. Y.M. Ponce, A. Huesca-Guillen, F. Ibarra-Velarde. *Journal of Molecular Structure*. **2005**, *717*, 67.
[23]. J.V. de Julian-Ortiz, C.G. de Alapont, I. Rios-Santamarina, R. Garcia-Domenech, J. Galvez. *Journal of Molecular Graphics and Modeling.* **1998**, *16*, 14.
[24]. A. Golbraikh, A. Tropsha. *Journal of Chemical Information and Computer Sciences*. **2003**, *43,* 144.
[25]. I. Lukovits, W. Linert. *Journal of Chemical Information and Computer Sciences*. **2001**, *41*, 1517.

[26]. H.P. Schultz, E.B. Schultz, T.P. Schultz. *Journal of Chemical Information and Computer Sciences*. **1995**, *35*, 864.

[27]. C. Yang, C. Zhong. *QSAR & Combinatorial Science.* **2005**, *24*, 1047.

[28]. R. Natarajan, S.C. Basak. *Current Topics in Medicinal Chemistry*. **2011**, *11*, 771.

[29]. B. Rasulev, M. Turabekova, M. Gorska, K. Kulig, A. Bielejewska, J. Lipkowski, J. Leszczynski. *Chirality*. **2012**, *24*, 72.

[30]. M. Fresqui, M. Ferreira, M. Trsic. *Analytica Chimica Acta*. **2013**, *759*, 43-52

[31]. J. Trygg. *Journal of Chemometrics*. **2002**, *16(6),* 283.

[32]. L. Eriksson, J. Rosén, E. Johansson, J. Trygg. *Molecular Informatics*. **2012**, *31(6-7)*, 414.

[33]. L. Eriksson, J. Trygg, S. Wold. *Journal of Chemometrics*. **2009**, *23(11)*, 569.

[34]. Y.M. Ponce, J.A. Castillo-Garit. *Journal of Computer-Aided Molecular Design.* **2005**, *19*, 369.

[35]. Chemcomp.com. MOE - Cheminformatics and QSAR [Internet]. **2015** https://www.chemcomp.com/MOE-Cheminformatics_and_QSAR.htm

[36]. R. Moldovan, G. Dascăl, V. Mirel, E. Bodoki, R. Oprean. *Farmacia*. **2015**, *63(6)*, 909.

MOLECULAR MODELING STUDY OF TERNARY COMPLEXES OF HYDROXYPROPYL-β-CYCLODEXTRIN WITH NONSTEROIDAL ANTI-INFLAMMATORY DRUGS

PÁLMA BUCUR[a], MIRCEA DUMITRU CROITORU[b*], IBOLYA FÜLÖP[b]

ABSTRACT. In this study, ternary complexes of four nonsteroidal anti-inflammatory drugs (ibuprofen, ketoprofen, flufenamic acid and mefenamic acid) with hydroxypropyl-β-cyclodextrin were studied using a molecular modeling technique. As third component in the complexes, different types of small molecules were chosen – regarding the acid-base character, molecular volume, etc. The binding energy, surface area contraction and volume contraction of these binary and ternary complexes were calculated. The results show that, by adding auxiliary substance to the active ingredient-cyclodextrin binary system, more stable complexes are formed. The ternary complexes are stabilised by hydrogen bonds and van der Waals interactions.

Keywords: cyclodextrin, ternary complex, molecular modeling, NSAID

INTRODUCTION

Cyclodextrins (CD) are cyclic oligosaccharides, consisting of 6-8 glucopyranose units (α-, β-, and γ-CD). They are amphiphilic molecules, shaped like a truncated cone, with a hydrophilic exterior and a hydrophobic interior surface. Cyclodextrin complexes are often used in the pharmaceutical industry to optimize biopharmaceutical properties, especially to increase aqueous solubility of poorly water-soluble drugs [1,2].

The most common are the binary, so-called 'host-guest complexes', when the drug molecule is inserted into the cyclodextrin cavity. Guest molecules are usually drugs with low solubility and molecular size that allow integral or partial fitting in the cavity of cyclodextrin. These complexes have better solubility than the original drug molecule [1,3,4].

---

[a] *Spital Sovata-Niraj, 156 Principala str. RO-545500, Sovata, Romania*
[b] *Department of Toxicology and Biopharmacy, University of Medicine and Pharmacy Tîrgu Mureș, 38 Gh. Marinescu str., RO-540139, Tîrgu Mureș, Romania*
* *Corresponding Author: croitoru.mircea@umftgm.ro*

By adding a third auxiliary substance, a ternary complex is formed with a higher complexation efficiency associated with a better water solubility compared to the binary complex. The most commonly used third molecules are polymers (polyvinylpyrrolidone, hydroxypropyl methylcellulose, polyethylene glycols) and small molecules (amino acids, lecithin, carboxylic acids, ethanol, Fe ions, Mg ions, etc) [5–8]. The aim of this study was to investigate the geometry and structure of some ternary complexes in order to assess the variations in the complexation efficiency in the presence of a third component using molecular modeling technique. Four non-steroidal anti-inflammatory drugs (NSAIDs) were chosen as model guest molecules, because their binary cyclodextrin complexes are widely studied due to their low water solubility and gastro-intestinal adverse effects.

The examples reported in the scientific literature show that association of an organic acid or base as third component to the cyclodextrin-guest molecule complex has positive influence on complexation energy, regardless of the acid-base character of the guest molecule. Therefore, seven auxiliary substances were used as third component: three low molecular weight organic acids (citric acid, CA; malic acid, MA and fumaric acid, FA), two amino acids (glutamic acid, Glu and thyrosine, Tyr) and two organic amines (diethanolamine, DEA and triethanolamine, TEA). As host molecule, a modified cyclodextrin (hydroxypropyl-β-cyclodextrin, HP-β-CD (DS = 3)) was used.

RESULTS AND DISCUSSION

In this study, the energy difference between the minimum energy before and after complexation (named binding energy, BE), and some QSAR properties (logP, volume and the van der Waals or solvent-accessible surface area) of the binary and ternary complexes of the HP-β-CD were investigated. The most stable complexes indicated by the highest negative values of the BE and the energy with the highest contribution to the BE (the van de Waals energies, E_{vdW}), are shown in the Table 1.

As can be seen, by adding a third component to the binary system, the binding energy increases in all cases (the lowest BE value corresponds to the most stable complex), meaning that the auxiliary substances stabilise the guest-host interaction. By analysing the partial energies of the BE (bond energy, angle energy, dihedral energy, stretch-bond energy and the energy from van der Waals interactions), it was observed that the van der Waals forces have the largest contribution. The positive value of the dihedral energy (resulting in a higher value of de E_{vdW} compared to the BE value) in the case of the ternary complexes show a dihedral "freezing" when complex is formed. Beside van der Waals forces, in some cases, hydrogen bonds also play a part in stabilizing the complexes (Table 2).

Table 1. The binding energy of the binary and ternary complexes

Binding Energy (kJ/mol)

IBU	binary	ternary						
		CA	MA	FA	GLU	TYR	DEA	TEA
BE	-113.5	-163.7	-156.3	-148.1	-148.1	*-194.5*	-141.3	-153.8
E_{vdW}	-117.6	-162.6	-152.5	-147.7	-154.8	-193.3	-144.7	-141.1
KETO	**binary**	ternary						
		CA	MA	FA	GLU	TYR	DEA	TEA
BE	-129.0	-180.4	-179.4	-166.4	-173.2	*-190.7*	-158.8	-158.7
E_{vdW}	-117.9	-163.4	-174.8	-177.8	-182.0	-178.9	-176.2	-154.2
FLU	**binary**	ternary						
		CA	MA	FA	GLU	TYR	DEA	TEA
BE	-122.4	-169.4	-157.4	-156.9	-164.1	*-183.7*	-154.2	-159.1
E_{vdW}	-111.5	-183.5	-174.7	-164.1	-147.3	-190.6	-159.3	-159.1
MEF	**binary**	ternary						
		CA	MA	FA	GLU	TYR	DEA	TEA
BE	-114.7	-160.7	-149.7	-152.6	-159.8	*-192.8*	-155.3	-154.2
E_{vdW}	-110.0	-150.8	-145.4	-138.7	-160.7	-185.5	-142.3	-148.3

Abbreviations: IBU - ibuprofen, KETO - ketoprofen, FLU - flufenamic acid, MEF - mefenamic acid, CA - citric acid, MA - malic acid, FA - fumaric acid, GLU - glutamic acid, Tyr - thyrosine, DEA - diethanolamine, TEA - triethanolamine

Table 2. The presence of hydrogen bonds in the complexes

	binary	ternary						
		CA	MA	FA	GLU	TYR	DEA	TEA
IBU	+	+	-	+	-	+	-	+
KETO	-	-	+	+	+	-	-	-
FLU	-	+	+	-	-	-	+	**+**
MEF	-	+	-	+	-	-	+	-

A statistically significant difference between the sum of the minimum energies of the components and the energies of the optimized system exists in all cases ($p < 0.05$; Kruskal-Wallis one-way test). In the case of the binary systems, the KETO forms the most stable complex with HP-β-CD. The Tyr-containing complexes are the most thermodynamically stable in all four cases, followed by the CA-containing complexes, which can be explained by the fact that, due to their lesser volume they fit better between the CD and the active ingredient.

The formation of inclusion complexes can manifest by the contraction of the surface area (BSA, binding surface area) and, to a lesser extent, the volume (BV, binding volume) of the system. The highest BSAs and highest BVs are presented in Table 3 and Table 4, respectively.

Table 3. The binding surface area ($Å^2$) of the binary and the ternary complexes

	binary	ternary						
		CA	MA	FA	GLU	TYR	DEA	TEA
IBU	-476.0	-757.0	-729.2	-715.2	-745.9	*-778.7*	-744.4	-762.2
KETO	-546.3	-846.5	-784.5	-789.7	-780.7	*-893.6*	-796.5	-804.8
FLU	-478.2	-788.5	-761.2	-769.6	-809.9	-808.9	-763.1	*-827.4*
MEF	-484.9	-772.0	-742.3	-726.7	-764.1	*-803.3*	-757.1	-786.6

Table 4. The binding volume ($Å^3$) of the binary and the ternary complexes

	binary	ternary						
		CA	MA	FA	GLU	TYR	DEA	TEA
IBU	-458.3	*-701.2*	-669.9	-676.6	-676.3	-700.3	-674.7	-688.3
KETO	-513.3	-746.0	-730.9	-724.4	-703.6	*-803.2*	-767.8	-732.0
FLU	-445.8	-709.9	-688.8	-712.4	-729.4	-751.8	-722.5	*-758.9*
MEF	-347.9	*-707.4*	-574.8	-539.3	-658.4	-543.7	-587.3	-640.8

The surface area decreased by 32.14 ± 0.61%, 33.86 ± 0.39%, 33.43 ± 0.29% and 32.87 ± 0.72% in the case of ternary complexes of IBU, KETO, FLU and MEF, respectively. In the case of the binary complexes, the average surface area decreased by 24 ± 0.93%, the difference being statistically significant ($p < 0.05$, Wilcoxon Signed-Rank test). The decrease of the solvent-accessible surface area in the case of the ternary systems can be explained by the formation of the re-entrant surfaces.

The volume of the ternary complexes of IBU, KETO, FLU and MEF decreased by 14.56 ± 0.29%, 15.46 ± 0.14%, 15.35 ± 0.13% and 15.10 ± 0.31%, respectively. In the case of the binary complexes the average surface area decreased by 10.95 ± 0.52%. The difference between the BV of the binary complexes and BV of the ternary complexes is statistically significant ($p < 0.05$, Wilcoxon Signed-Rank test). These surface area and volume contractions were evaluated by comparing the sum of the individual values to the geometrically optimized complexes.

Each ternary complex has a distinct molecular geometry; the difference is attributed to the extent to which the studied NSAIDs and the auxiliary substances are inserted into the CD cavity.

The topology of the binary complexes was similar to that observed in our previous work: all active ingredients enter the cavity of CD [9]. Regarding the ternary complexes, in the case of the most stable KETO-complex, the whole molecule enters in the cyclodextrin's cavity and the auxiliary component is situated between the secondary hydroxyl groups of the HP-β-CD and the benzoyl group of the KETO (Figure 1a and 1b, hydrogen depleted structure).

a   *b*
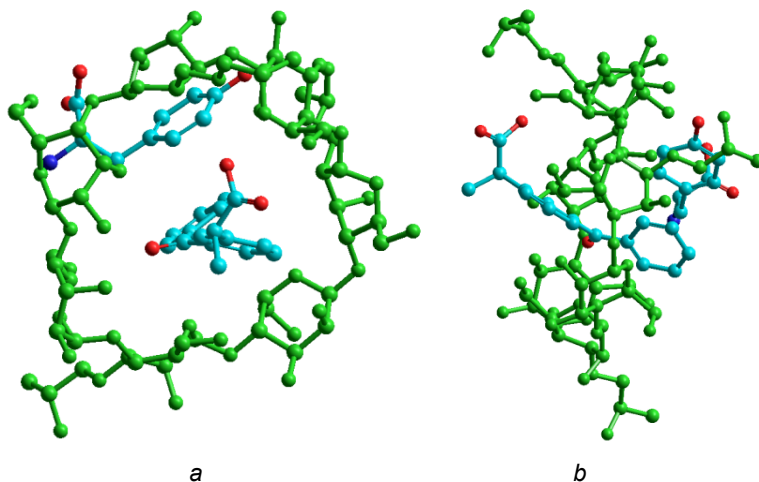
Figure 1. The 3D structure of the HP-β-CD:KETO:Tyr complex
(*a* top view; *b* side view)

In the case of the most stable HP-β-CD:IBU:Tyr complex, the active ingredient is fully included inside the CD's cavity and the Tyr is situated close to the isobutyl moiety of the IBU. The IBU complexes, those with MA, FA and GLU content, have similar molecular geometry to the Tyr containing complex. In the case of those complexes in which the third component is the MA, DEA and TEA, both the active ingredient and the third component are situated bound to one of the edges of the CD.

Regarding the conformation of the ternary complexes of the FLU, the active ingredient is totally inserted into the CD's cavity in the case of the CA-, MA-, Tyr-, DEA-, TEA-complexes; the third component is situated close to the trifluoromethyl moiety of the FLU, oriented to the secondary hydroxyls of the CD.

In the case of the HP-β-CD:MEF:MA/Glu/TEA complexes, both substances are located on the edges of the CD. In the other cases the MEF is included in the cavity of the CD and the auxiliary substance is located on the wider edge of the CD.

In the cases of MEF and FLU, the FA containing complexes have a different topology, compared to the others; the auxiliary substance is included in the cavity of the CD, and the active ingredient is situated at the edge of secondary hydroxyl groups.

Regarding the correlation between the average values of BSA and BV parameters, the positive association between the two variables is statistically significant ($p < 0.01$, Spearman correlation, two-tailed) in all four cases. Between the BE and BSA a statistically significant, positive correlation exists in the case of the KETO and MEF ($p < 0.05$, Spearman correlation, two-tailed).

The molecular dynamics simulation results show that the entropy (TS) of the ternary complexes is slightly increased (7.3-14%) compared to the binary complexes in all four cases; similarly to the calculated Helmholtz free energy.

The change in free energy (ΔF) and the entropy change (TΔS) of the complexes are presented in Table 5.

Table 5. Changes in the free energy (ΔF, kJ/mol) and entropy (TΔS, kJ/mol) of the complexes

IBU	binary	ternary						
		CA	MA	FA	GLU	TYR	DEA	TEA
ΔF	-85.4	-88.0	-59.6	-89.3	-88.7	*-139.7*	-40.8	-73.8
TΔS	-69.7	-106.1	-106.2	-92.8	-132.9	-92.1	-116.9	-99.3

KETO	binary	ternary						
		CA	MA	FA	GLU	TYR	DEA	TEA
ΔF	-92.4	-129.9	-88.0	-122.6	-139.6	-131.7	-61.9	*-155.3*
TΔS	-44.7	-101.0	-126.4	-111.0	-125.7	-141.9	-98.4	-110.9

FLU	binary	ternary						
		CA	MA	FA	GLU	TYR	DEA	TEA
ΔF	-56.0	-117.9	-112.1	*-143.4*	-143.4	-104.5	-103.6	-106.3
TΔS	-101.0	-138.9	-150.4	-130.0	-144.0	-146.8	-229.1	153.9

MEF	binary	ternary						
		CA	MA	FA	GLU	TYR	DEA	TEA
ΔF	-73.0	-71.2	-170.7	-114.1	-85.3	*-132.2*	-118.6	-80.8
TΔS	-88.2	-158.4	-192.4	-104.4	-126.7	-138.2	-127.5	-117.3

CONCLUSIONS

Our results show that the ternary complexes of the studied active ingredients have higher binding energy compared to the binary complexes: therefore, by adding a third component to the system, higher stability constants can be achieved. The surface area and volume contraction, observed in the case of the ternary complexes, suggest that the auxiliary substances significantly increase the active ingredient affinity for HP-β-CD, compared to the binary complex. The mechanism of which the third components help the complexation of the active ingredient is complex: one can assume that they favour the formation of the van der Waals bonds between the CD and the guest molecule.

In the case of IBU, FLU and MEF exists a positive correlation ($p < 0.05$, Spearman correlation, two-tailed) between the molecular mass of the third component and the binding energy. Other parameters (pKa, logP, number of H donating and accepting groups) do not show correlation with the binding energies.

In this "in vacuum" model, the volume and surface contraction of the complexes suggest an entropy decrease, supported by the molecular dynamics simulation results. The results show that adding a second guest molecule to the binary complex the process is accompanied by a large loss of entropy. The negative value of the ΔF demonstrates the spontaneity of the complexation process, which could be explained by the enthalpy-entropy compensation; the complexation process is a mainly enthalpy driven mechanism: therefore, the van der Waals forces have a major role in stabilising the complex. This interpretation agrees with the scientific literature data [10].

In the case of the ternary complexes, additional mechanisms help the complexation process (e.g. salt formation, pH adjustment, etc.) In aqueous medium the role of the water molecules is important; the release of the water from the cyclodextrin cavity can result in a positive entropy change, favouring the reduction of the free energy.

Zhang et al. got similar result: -85.91 kJ/mol as the binding energy of the binary complexes of the doxycycline with HP-β-CD [11]. In a research made by Huang et al. [12], the interval of the binding energy of the binary complexes of the βCD with salsolinol, N-methyl-salsolinol and 1-benzyl-tetrahydroisoquinoline is between -57.64 and -108.72 kJ/mol, which is similar to our result. Tan et al. also measured a similar value: -86.14 kJ/mol as the binding energy of the binary complex of the β-CD with rifaldazine [13]. The findings of Mendez et al. are close to our results, they show that amino acids can enhance the affinity of the benzoic acid for β-CD [14].

In 2014 Barbosa et al. made a research in which the binary and the ternary complexes of the βCD were examined, they got -81.62 kJ/mol as the binding energy of the binary complex and -135.75 kJ/mol as the binding energy of the ternary complex with TEA; results which are close to our findings [15].

EXPERIMENTAL SECTION

Energy minimisation

In this study the formation energy, the volume and the surface area of the binary (1:1 molar ratio) and ternary (1:1:1 molar ratio) inclusion complexes of HP-β-CD with four NSAIDs (IBU, KETO, FLU, MEF) and seven auxiliary

substances (CA, MA, FA, Glu, Tyr, DEA, TEA) were measured. In the first step, the structures of the NSAIDs, auxiliary substances and the HP-β-CD were geometrically optimised using the molecular mechanics method with MM+ force in HyperChem Professional software, version 8.0 [16]. The NSAIDs were manually inserted in the HP-β-CD's cavity, and then the auxiliary substances were placed between the active ingredient and the edge of the cyclodextrin. The adduct structures were optimized using the Polak-Ribiere algorithm until 0,01 RMS gradient was achieved. Optimization of the complexes was repeated forty times, starting with forty different layouts (n=40). The calculations were performed in vacuum phase.

The binding energy (BE) of the binary and the ternary complexes was calculated by the following formula:

$$BE = E_{binary} - (E_{CD} + E_{NSAID})$$
$$BE = E_{ternary} - (E_{CD} + E_{NSAID} + E_{III})$$

E_{binary}, $E_{ternary}$ represent the average minimum energy of the binary complexes and ternary complexes; E_{CD}, E_{NSAID} and E_{III} represent the minimum energy of HP-β-CD, NSAIDs and the third auxiliary component, respectively. Negative formation energy shows a thermodynamically favoured complex.

The binding surface area (BSA) and the binding volume (BV) of the binary and the ternary complexes were calculated using the formulas:

$$BSA = SA_{binary} - (SA_{CD} + SA_{NSAID})$$
$$BSA = SA_{ternary} - (SA_{CD} + SA_{NSAID} + SA_{III})$$

SA_{binary}, $SA_{ternary}$, SA_{CD}, SA_{NSAID} and SA_{III} represent the surface area of the binary complex, ternary complex, HP-β-CD, NSAIDs and the third component, respectively.

$$BV = V_{binary} - (V_{CD} + V_{NSAID})$$
$$BV = V_{ternary} - (V_{CD} + V_{NSAID} + V_{III})$$

V_{binary}, $V_{ternary}$, V_{CD}, V_{NSAID} and V_{III} represent the volume of the binary complex, ternary complex, cyclodextrin, NSAID and the third component, respectively.

In all cases forty conformations were tested; the results were statistically analysed using Kruskal-Wallis one-way test, Wilcoxon Signed-Rank tests and Spearman rank correlation test.

Molecular dynamics

Molecular dynamics simulations of the most stable complexes were performed at constant temperature of 298.15 K for 10 ps, with a time step of 0.001 ps, using the HyperChem Professional software, version 8.0 [16].

ACKNOWLEDGMENTS

R E F E R E N C E S

[1]. T. Loftsson, D. Duchêne, *International Journal of Pharmaceutics*, **2007**, *329*, 1.

[2]. J. Zhang, P.X. Ma, *Advanced Drug Delivery Reviews*, **2013**, *65*, 1215.

[3]. C. Scarpignato, *Current Medicinal Chemistry*, **2013**, *20*, 2415.

[4]. I.A. Alsarra, M.O. Ahmed, F.K. Alanazi, K.E.H. Eltahir, A.M. Alsheikh, S.H. Neau, *Interantional Journal of Medical Sciences*, **2010**, *7*, 232.

[5]. J.C. de Miranda, T.E.A. Martins, F. Veiga, H.G. Ferraz, *Brazilian Journal of Pharmaceutical Sciences*, **2011**, *47*, 665.

[6]. M. Valero, C. Carrillo, L.J. Rodríguez, *International Journal of Pharmaceutics*, **2003**, *265*, 141.

[7]. H. Yang, C. Bohne, *The Journal of Physical Chemistry*, **1996**, *100*, 14533.

[8]. W. Zheng, M. Tarr, *Journal of physical chemistry B*, **2004**, *108*, 10172.

[9]. I. Fülöp, Á. Gyéresi, E. Laczkó, M.D. Croitoru, *Acta Medica Marisiensis*, **2011**, *57*, 463.

[10]. H. Dodziuk (ed.), "Cyclodextrins and Their Complexes", Wiley-VCH, Weinheim, **2006**, chapter 8.

[11]. Z. Wang, Z. He, L. Zhang, H. Zhang, M. Zhang, X. Wen, G. Quan, X. Huang, X. Pan, C. Wu, *Acta Pharmaceutica Sinica B*, **2013**, *3*, 130.

[12]. M.J. Huang, Z. Quan, Y.M. Liu, *International Journal of Quantum Chemistry*, **2009**, *109*, 81.

[13]. Q. Tan, D. He, L. Yang, Y. Ren, J. Liu, J. Zhang, *International Journal of Nanomedicine*, **2013**, *8*, 477.

[14]. S.G. Méndez, F.J. Otero Espinar, A.L. Alvarez, M.R. Longhi, M.A. Quevedo, A. Zoppi, *Journal of Inclusion Phenomena and Macrocyclic Chemistry*, **2016**, *85*, 33.

[15]. J.A.A. Barbosa, A. Zoppi, M.A. Quevedo, P.N. de Melo, A.S.A. de Medeiros, L. Streck, A.R. de Oliveira, M.F. Fernandes-Pedrosa, M.R. Longhi, A.A. da Silva-Junior, *International Journal of Molecular Sciences*, **2014**, *15*, 17077.

[16]. HyperChem (TM) Professional 8.0, Hypercube, Inc., 1115 NW 4th Street, Gainesville, Florida 32601, USA.

STUDY OF GEOMETRICAL SHAPING OF LINEAR CHAINED POLYMERS STABILIZED AS HELIXES

LORENTZ JÄNTSCHI[a,b] AND SORANA D. BOLBOACĂ[c*]

ABSTRACT. The hypothesis of the study was that linear chained polymers have a natural chance to stabilize as a helix. Ten linear chained polymers, poly(ethylene glycol), polyethyleneimine, poly(lactic acid), poly(N-vinyl-pyrrolidone), poly(trans-1-butenylene), poly(1-chloro-trans-1-butenylene), poly(1-methyl-trans-1-butenylene), poly(1,4,4-trifluoro-trans-1-butenylene), polyacrylonitrile, polychlorotrifluoroethylene, were investigated. The structure of polymers was drawn and then optimized at Hartree-Fock, 6-31G* level of theory. The helix parameter was extracted from the optimized geometries using a home-made program. Seven out of ten polymers are likely to have a helical structure; the polymers with oxygen shown the highest residual error. The helix coefficient and rotation step per monomer were also calculated. The top three polymers according to rotation step per monomer behaved same as the one according to the helix coefficient. The top three non-increasing order was: polychlorotrifluoroethylene-Cl, polyacrylonitrile-N, and poly(lactic acid)-C-methyl. The smallest rotation step per monomer was associated with the smallest value of the helix coefficient (this being linearly related to rotation step per monomer). The highest helix radius was identified for poly(1-chloro-trans-1-butenylene), followed by poly(1-methyl-trans-1-butenylene) and poly(1,4,4-trifluoro-trans-1-butenylene).

Keywords: linear chained polymer, helix radius, computational study

INTRODUCTION

The polymer term is derived from Greek poly- 'many' & -mer 'parts' and identifies a molecule constructed by many repeated subunits [1] (Table 1).

[a] *Technical University of Cluj-Napoca, Department of Physics and Chemistry, 103-105 Muncii Blvd., RO-400641, Cluj-Napoca, Romania*
[b] *Babeş-Bolyai University, Institute for Doctoral Studies, 1 Kogălniceanu Str., RO-400084, Cluj-Napoca, Romania*
[c] *Iuliu Haţieganu University of Medicine and Pharmacy, Department of Medical Informatics and Biostatistics, 6 Louis Pasteur Str., RO-400349, Cluj-Napoca, Romania*
* *Corresponding author: sbolboaca@umfcluj.ro*

Polymer based materials have different properties, such as resistive memory [2], physical and electronic properties [3], and a variety of uses (see Table 2 [4,5]).

Table 1. Basic structure of polymers

Monomer			Polymer	
Structure	**Name**	**CID**	**Repeating unit**	**Name**
$CH_2=CH_2$	Ethene	6325	$(-CH-CH-)_n$	Polyethylene
$CH_2=CHCl$	Chloroethene	6338	$(-CH_2-CH(Cl)-)_n$	Polyvinyl chloride
$F_2C=CF_2$	Tetrafluoroethene	8301	$(-F_2C-CF_2-)_n$	Polytetrafluoroethylene

Table 2. Applications of polymers

	Polymer	**Monomer unit**	**Uses**
1	polypeptides	$-NH-CO-$ (amino acids)	proteins, wool, silk, steric stabilizers, colloidal additives
2	polyvinyls	$-CH_2-CH(X)-$	plastics
3	polyesters	$-CO-O-$	clothing, containers
4	polysiloxanes, silicones	$-Si-O-$	lubricants, rubbers, paints
5	polyamide	$-NH-CO-$	nylon, fabrics, auto parts
6	polyurethanes	$-NH-CO-O-$	adhesives, flexible furniture
7	cellulose	$-C-O-$	paper, photographic film
8	polycarbonates	$-O-CO-O-$	optical equipment, CDs
9	polyethylene oxide (PEO, PEG)	$-CH_2-O-CH_2-$	detergents, cosmetics
10	polyacrylamide (PAA)	$-CH_2-CH(CONH_2)-$	plastics, textiles, diapers
11	polyvinyl alcohol (PVA)	$-CH_2-CH(OH)-$	fibers, adhesives, textiles
12	polyethylene (PE)	$-CH_2-CH_2-$	coating, containers, films
13	polystyrene (PS)	$-CH_2-CH(C_6H_5)-$	packing (fast-food containers), housewares
14	polybutadiene (PBD)	$-CH_2=CH-CH=CH_2-$	latex paints, rubbers
15	polydimethylsiloxane (PDMS)	$-Si(CH_3)_2-O-$	silicone oil, lubricants
16	polypropylene (PP)	$-CH_2-CH(CH_3)-$	carpets, bottles, wrap films, microwaveable containers
17	polymethylmethacrylate (PMMA)	$-CH_2-CCH_3(CO_2CH_3)-$	transparent windows, plexiglass, perpex
18	polytetrafluoroethylene (PTFE)	$-CF_2-CF_2-$	teflon
19	polyvinyl chloride (PVC)	$-CH_2-CH(Cl)-$	plastic sheet, insulation, pipes

Classification of polymers is done according to vary criteria, such as synthesis method, molecular structure (linear or branched), chemical family (organic or inorganic), etc. [6].

According to their structure, polymers are classified as [7]:

• Linear: a single continuous chain of repeated unit (such as acrylics, nylons, polyethylene, polyvinyl chloride).
• Branched: side chains of repeated unit connecting into the main chain of repeated unit (such as polyethylene). A linear polymer may show branching points and side chains (parts out of the linear chain, like branches off the trunk of a tree).
• Cross-linked: interconnections between chains (such as rubbers)
• Network: many interconnections between chains such that the entire sample is a single molecule (such as epoxies, phenolics)
• Configuration: 3D structure of polymer based on orientations that can be changed just by breaking the bonds

Linear polymers may include different atoms in the main chain and may or may not have rings (cyclolinear polymers):

• Just carbon atoms (C) in the main chain: saturated main chain (polyethylene, polypropylene), unsaturation of the main chain (natural rubber, polyacetylene), or polar side groups (PVC, PMMA, Teflon)
• Oxygen (O) in the main chain: polyformaldehyde (acetal), epoxy polymers (PEO, PPO), polyesters, polycarbonates
• N in the main chain: polyamines, polyamides (polypeptides), polyurethanes
• Other atoms in the main chain: polysulfones, polysiloxanes (silicones), polyphosphazenes
• Rings in the main chain: poly(p-phenylene), polyaniline, cellulose

After a while, linear constructions of polymers (such is a hose) have the natural tendency to bend. The expose of hoses to biodiesel, for example, led to decrease of its tensile strength [8], while the sterilization of surgical silicone hose led to modification of the structure of polymer [9]. The main question is in which degree this tendency to bend is a natural tendency?

A series of studies shown that some synthetic polymers (m-terphenyl-based π-conjugated polymer [10], poly(ethylene glycol) (PEG) [11-13], poly(ethylene imine) (PEI) [14], squaraine polymers [15]) or natural polymer-like compounds (functional polymers like DNA [16], RNA [17], globular proteins [18]) have the tendency to form a helix. Of course, the most important case is the helix of DNA, but the question about the tendency of other polymers to form helix even if was investigated [19-22] it still needs more attention. The present study takes into account a series of polymers, from both biological and synthetic groups having as the subject of investigation the tendency of polymers to form a helix.

RESULTS AND DISCUSSION

The residual errors obtained by applying (3) varied from 0.0016 to 0.4428 with highest residuals for oxygen atom in any position (even, odd, or all – polymer #4, Table 3). Systematically, the polymers with oxygen had highest values of residuals, followed by the polymers with C-methyl group. The highest value of residual errors is thus observed in the polymer that tend to form a double helix and all investigated structures of #4 proved to have outliers. Furthermore, the sample size after removal of the outliers (if any) proved inversed linearly related to residual errors (Pearson's correlation coefficient R = -0.8969, p-value = 7.68e-5). Accordingly, with some exceptions (see #4 O-all, Table 3), when the sample size increases, the residual error decreases.

Table 3. Residual errors for investigated polymers likely to have a helical structure

Polymer	Atom	n	n'	Residual error (SS)	Remarks
#3	C-methyl	17	15	0.0393	SS 100 times higher with the ends ➔ the ends are outliers (2)
#4	O-even	11	9	0.3123	SS 46 times higher with the ends ➔ the ends are outliers (2)
	O-odd	12	10	0.4428	SS 66 times higher with the ends ➔ the ends are outliers (2)
	O-all	21	17	0.1255	SS 100 times higher with the ends ➔ the ends are outliers (4)
#6	Cl	18	18	0.0127	Ends are not outliers
#7	C-methyl	18	18	0.0684	Ends are not outliers
#8	C-1	18	18	0.0033	Ends are not outliers
	C-2	18	18	0.0016	Ends are not outliers
	C-3	18	18	0.0019	Ends are not outliers
	C-4	18	18	0.0016	Ends are not outliers
#9	N	18	16	0.0285	SS 4 times higher with the ends ➔ the ends are outliers (2)
#10	Cl	18	16	0.0047	SS 37 times higher with the ends ➔ the ends these are outliers (2)

n = sample size; n' = sample size after removal of the outliers

The rotation step (coefficient c_0 in (2)) and the rotation step/monomer were obtained for each investigated polymer and are given in Table 4. All other calculated coefficients of the helix of the investigated polymers are given in Table 5.

Table 4. The coefficient of the helix and rotation step

Polymer (atom type)	Helix coefficient (c_0)	Rotation step (/monomer) (°)
#3 (- C-methyl)	2.972e-1	107
#4 (- O-even)	9.288e-2	33.4
#4 (- O-odd)	9.193e-2	33.1
#4 (- O-all)	9.183e-2	33.1
	1.233e-1	44.4 (odd/even)
#6 (- Cl)	2.148e-2	7.73
#7 (- C-methyl)	3.085e-2	11.1
#8 (- C-1)		
#8 (- C-2)		
#8 (- C-3)	2.743e-2	9.87
#8 (- C-4)		
#9 (- N)	3.347e-1	120.5
#10 (- Cl)	3.609e-1	129.9

Table 5. Helix coefficients – see (2)

Polymer (atom type)	Helix coefficients for axial projection					
		x axis		y axis		z axis
#3	c_1	3.9983e-2	c_5	3.2314e0	c_9	3.2505e+0
	c_2	-2.2040e+0	c_6	-6.7020e-1	c_{10}	9.0419e-1
	c_3	-1.7105e+0	c_7	5.3824e-3	c_{11}	-3.0941e-2
	c_4	1.5932e+1	c_8	-1.2359e-1	c_{12}	2.1275e-1
#4 (even)	c_1	3.257e+0	c_5	2.088e0	c_9	4.026e+0
	c_2	-1.807e+0	c_6	-1.724e0	c_{10}	-3.349e+0
	c_3	1.345e+0	c_7	-2.036e0	c_{11}	-1.073e-1
	c_4	-1.640e+1	c_8	2.487e+1	c_{12}	1.270+0
#4 (odd)	c_1	2.584e+0	c_5	1.555e+0	c_9	2.906e+0
	c_2	-3.290e+0	c_6	-3.228e+0	c_{10}	-4.865e+0
	c_3	1.306e+0	c_7	-2.039e+0	c_{11}	-9.570e-2
	c_4	-1.525e+1	c_8	2.358e+1	c_{12}	1.162e+0
#4 (all)	c_1	2.9031e+0	c_5	1.8583e+0	c_9	3.4290e+0
	c_2	-2.5169e+0	c_6	-2.4382e+0	c_{10}	-4.0614e+0
	c_3	1.3204e+0	c_7	-2.0466e+0	c_{11}	-1.0094e-1
	c_4	-1.5757e+1	c_8	2.4304e+1	c_{12}	1.2071e+0
	c_{13}	4.1484e-1	c_{14}	2.5537e-1	c_{15}	5.3846e-1
	c_{16}	-4.0826e-1	c_{17}	6.6823e-1	c_{18}	2.4509e-2
# (6)	c_1	2.48427e1	c_5	3.19611e+1	c_9	1.79865e+1
	c_2	-2.88747e0	c_6	-1.34873e+0	c_{10}	1.64965e-1
	c_3	1.74459e0	c_7	-1.01784e-1	c_{11}	1.90010e+0
	c_4	-1.68632e1	c_8	-2.24718e+1	c_{12}	-1.90634e+1
# (7)	c_1	1.82640e1	c_5	2.33646e+1	c_9	1.41794e+1
	c_2	2.93375e0	c_6	1.33951e+0	c_{10}	-1.99841e-1
	c_3	1.57034e0	c_7	6.32800e-2	c_{11}	1.93730e+0
	c_4	-1.46022e1	c_8	1.16876e+1	c_{12}	-1.77684e+1

127

Table 5. (Continued)

Polymer (atom type)		Helix coefficients for axial projection				
		x axis		y axis		z axis
#8 (-C1)	c_1	-9.14110e+0	c_5	1.51182e+1	c_9	1.70206e+1
	c_2	-1.46653e-1	c_6	-6.30651e-1	c_{10}	1.07360e+0
	c_3	3.29307e+0	c_7	1.82544e+0	c_{11}	7.95252e-1
	c_4	-3.25477e+1	c_8	-2.22678e+1	c_{12}	2.49521e+0
#8 (-C2)	c_1	-9.46739e+0	c_5	1.57384e+1	c_9	1.76728e+1
	c_2	-9.44889e-2	c_6	-5.76774e-1	c_{10}	1.12318e+0
	c_3	3.29773e+0	c_7	1.83040e+0	c_{11}	8.01570e-1
	c_4	-3.20550e+1	c_8	-2.20244e+1	c_{12}	2.53498e+0
#8 (-C3)	c_1	-9.40050e+0	c_5	1.56074e+1	c_9	1.75550e+1
	c_2	-7.59906e-2	c_6	-5.58858e-1	c_{10}	1.13939e+0
	c_3	3.29710e+0	c_7	1.82896e+0	c_{11}	8.05768e-1
	c_4	-3.07980e+1	c_8	-2.12904e+1	c_{12}	2.81228e+0
#8 (-C4)	c_1	-9.18430e+0	c_5	1.53022e+1	c_9	1.71931e+1
	c_2	6.26188e-3	c_6	-4.76742e-1	c_{10}	1.22481e+0
	c_3	3.30040e+0	c_7	1.82834e+0	c_{11}	8.03362e-1
	c_4	-3.06020e+1	c_8	-2.12218e+1	c_{12}	2.87783e+0
#9 (-N)	c_1	-3.21292e+0	c_5	1.08286e-2	c_9	3.22894e+0
	c_2	-2.35726e+0	c_6	-2.48275e+0	c_{10}	2.35661e+0
	c_3	3.07394e-3	c_7	2.21476e+0	c_{11}	7.50670e-4
	c_4	-2.71106e-2	c_8	-1.96284e+1	c_{12}	1.54767e-3
#10 (-Cl)	c_1	2.42189e+0	c_5	-3.60496e-2	c_9	-2.41754e+0
	c_2	-7.72781e-1	c_6	-7.46450e-1	c_{10}	-2.34239e+0
	c_3	2.90532e-2	c_7	2.32023e+0	c_{11}	3.25795e-3
	c_4	-2.59285e-1	c_8	-2.07402e+1	c_{12}	1.17230e-2

The smallest coefficient of the helix was observed on polymers with highest size (n=18, see Table 4); and without outliers while the highest coefficient of the helix was observed in polymers #3, #9 and #10. As expected, the smallest rotation step per monomer was associated with the smallest value of the helix coefficient, which is linearly related to the rotation step per monomer (R = 0.9999, p-value = 8.55e-25).

Several coefficients, such as c_4, c_8, c_{12} (and c_{16}, c_{17}, c_{18} for the double helix) are not of interest since represent the position of the helix relative to the origin of the coordinates system, position which is arbitrary. The rest of coefficients represent the projection of the helix on a coordinate system rotated relatively to the convenient direction of the helix propagation.

Three coefficients (among those provided in Table 5) are of interest: c_1, c_5 and c_9 since they allow computing the approximation of the helix radius, by formula:

$$helix\,radius = \frac{\sqrt{c_1^2 + c_5^2 + c_9^2}}{\sqrt{2}} \qquad (5)$$

The smallest helix radius was evaluated for #10 (internal helix), followed by #4odd (double helix), and #3 (internal helix) (see Table 6). The highest value was estimated for the polymer #6, followed by #7 and #8, all polymers being with sample size of 18 and without any outlier.

Starting from the values obtained in this research, the coefficients of the 'classical' helix equation (0) could be obtained. Furthermore, the results obtained here could be used to investigate other polymers likely to form helixes.

CONCLUSIONS

Seven out of ten investigated polymers are likely to form helixes (internal and double helix). The polymer with the highest coefficient of the helix and highest rotation step per monomer was a polymer with internal helix, polychlorotrifluoroethylene-Cl. The coefficient of the helix proved to be linearly related to the rotation step per monomer (p-value < 0.0001).

Table 6. Radius of the helix approximated by (5)

Polymer (atom type)	Radius (Angs)
#3	3.24
#4 (even)	3.95
#4 (odd)	2.96
#4 (all)	3.44
#6	31.32
#7	23.24
#8 (-C1)	17.35
#8 (-C2)	18.02
#8 (-C3)	17.89
#8 (-C4)	17.52
#9 (-N)	3.22
#10 (-Cl)	2.42

The highest helix radius was identified for poly(1-chloro-trans-1-butenylene) while the smallest helix radius was calculated for polychlorotrifluoroethylene-Cl.

EXPERIMENTAL SECTION

Hypothesis: Linear chained polymers have a good chance to stabilize as a helix. A series of linear polymers were included into this study. Not all of them have enough steric constraints to provide a 'regular irregularity', the essential ingredient of the helix form. Table 7 gives the series of investigated polymers, along with this first level of approximation revealed for instance by a simple geometry built at any level of theory.

Table 7. Structural characteristics and use of the investigated linear polymers

	Name	Structure	Remarks	Likely to provide helix
1	poly(ethylene glycol)		PEG - biological interest (laxative [23], improvement of action potential after spinal cord injury [24], drug delivery [25])	[NO] purely linear
2	polyethyleneimine		PEI - biological interest (gene delivery [26], drug carrier [27])	[NO] purely linear
3	poly(lactic acid)		PLA - biological interest [28] (tissue engineering [29], suture materials [30], delivery systems [31])	[YES], internal helix (see Fig. 2)
4	poly(N-vinyl-pyrrolidone)		PVP - other interest (beverages, disinfectant, in complexation with of iodine, film forming agents [32,33])	[YES] double helix (see Fig. 3)
5	poly(trans-1-butenylene)		other interest (glass transition temperature [34])	[YES]
6	poly(1-chloro-trans-1-butenylene)		other interest (glass transition temperature [34])	[YES]
7	poly(1-methyl-trans-1-butenylene)		other interest (glass transition temperature [34])	[YES]
8	poly(1,4,4-trifluoro-trans-1-butenylene)		other interest (glass transition temperature [34])	[YES]
9	polyacrylonitrile		PAN - other interest (nanofibers [35,36], treatment of metals [36])	[YES] internal helix (see Fig. 4)
10	Polychlorotrifluoro-ethylene		PCTFE or PTFCE - other interest (chemical industry, manufacturing, electronics, architecture, energy, health and domestic sectors [37])	[YES] internal helix (see Fig. 5)

Spartan optimized geometries are shown in Figure 1.
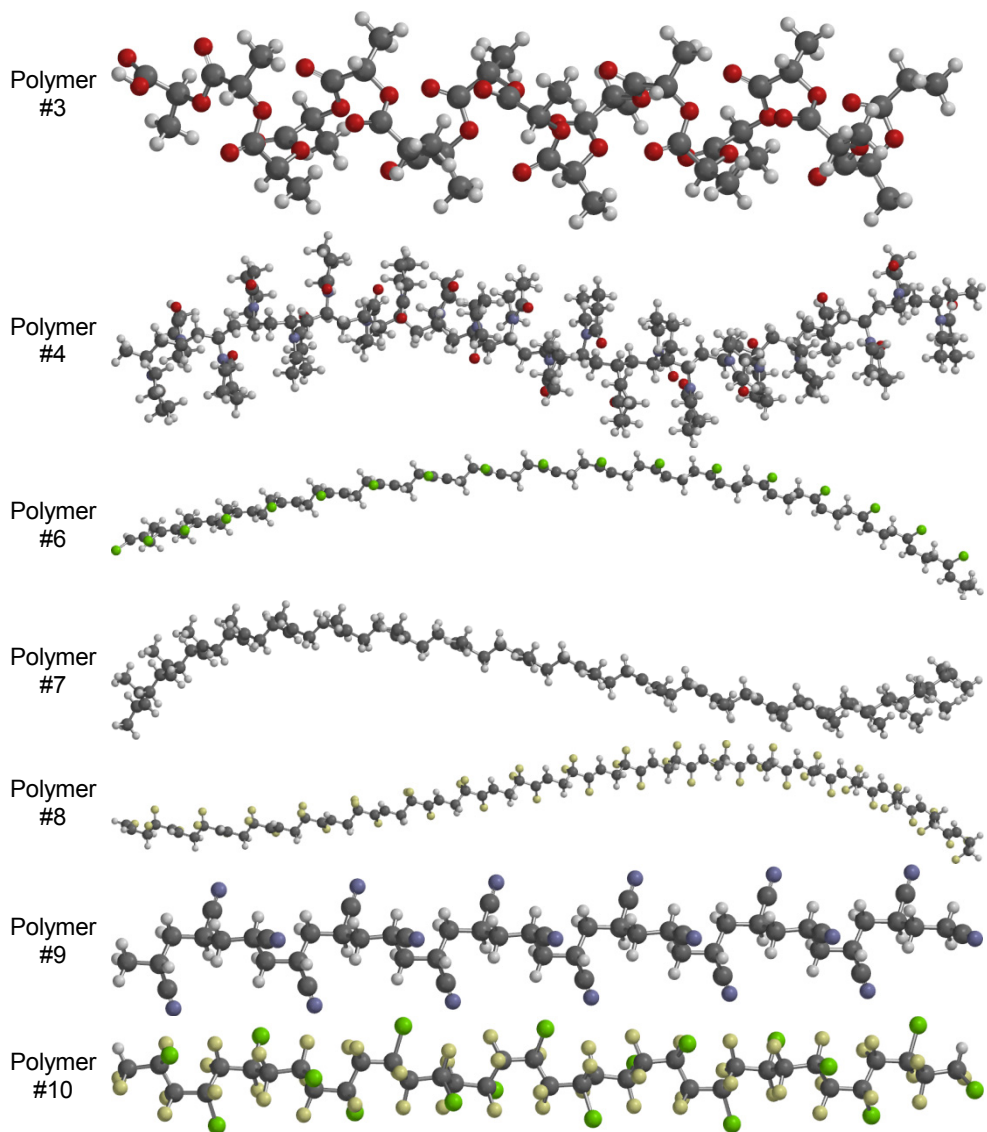
Figure 1. Spartan images of the studied polymers with optimized geometry
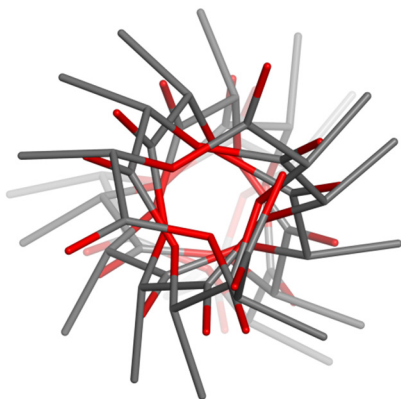
Figure 2. Internal helix of poly(lactic acid) (O atoms, red)
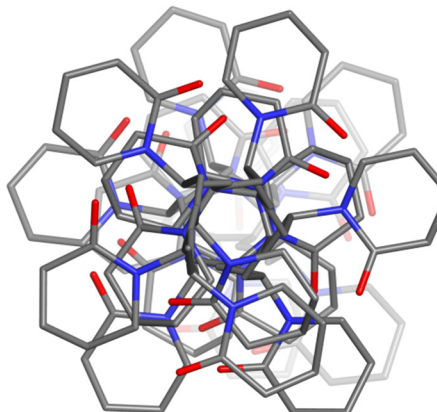
Figure 3. Double helix of poly(N-vinyl-pyrrolidone) (N atoms, blue; O atoms, red)
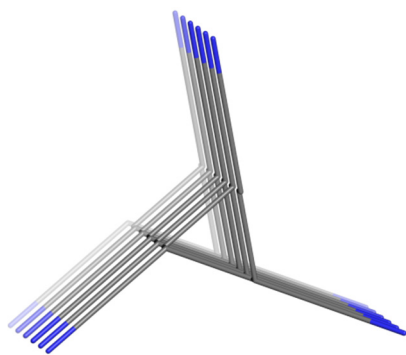
Figure 4. Internal helix of polyacrylonitrile (N atoms, blue)
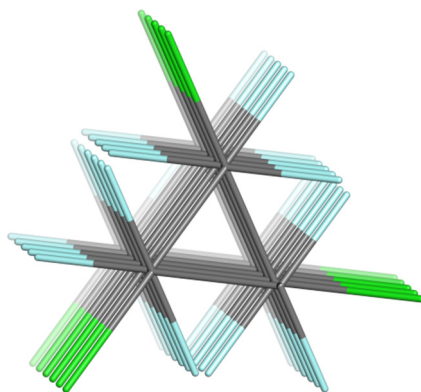
Figure 5. Internal helix of polychlorotrifluoroethylene (chlorine atoms, green, fluorine atoms, cyan)

The 10 polymers of interest were drawn by HyperChem and the geometry of each polymer was optimized. The optimization was done by Spartan software, at Hartree-Fock (HF [38]) level of theory (6-31G* [39]). A home-made program, that extracts from the optimized geometry the parameters of the helix.

Recall that a helix is defined as in Eq 0:

$$x = a_1 + a_2 \cdot \sin(a_0 \cdot t)$$
$$y = a_3 + a_4 \cdot \cos(a_0 \cdot t) \tag{0}$$
$$z = a_5 + a_6 \cdot t$$

where x, y, and z are the axial projections of the helix, and a_i ($0 \leq i \leq 6$) are unknown coefficients (a_1, a_3 and a_5 expressing a translation of the reference system relative to the helix, by keeping the direction of the axis the same; a_0, a_2, a_4 and a_6 are helix parameters; for circular-based helixes $a_2 = a_4$); t defines the evolution of the helix.

Equation 0 is theoretically important, but in practice there is no way to align the helix on the z-axis without the identification of the unknown coefficients (a_0..a_6); actually the equations of the helix are hidden behind a transformation of the system coordinates. Therefore, the equations maximizing the agreement between the model and the observation may be as follows:

$$x = b_1 \cdot \sin(b_0 \cdot t) + b_2 \cdot \cos(b_0 \cdot t) + b_3 \cdot t + b_4$$
$$y = b_5 \cdot \sin(b_0 \cdot t) + b_6 \cdot \cos(b_0 \cdot t) + b_7 \cdot t + b_8 \tag{1}$$
$$z = b_9 \cdot \sin(b_0 \cdot t) + b_{10} \cdot \cos(b_0 \cdot t) + b_{11} \cdot t + b_{12}$$

where b_i ($0 \leq i \leq 12$) are unknown coefficients (to be determined), and t is as above.

Some unknown coefficients may be incorporated inside of the periodic functions, providing a more convenient expression for the helix:

$$x = c_1 \cdot \cos(c_0 \cdot 2\pi \cdot t + 2\pi \cdot c_2) + c_3 \cdot t + c_4$$
$$y = c_5 \cdot \cos(c_0 \cdot 2\pi \cdot t + 2\pi \cdot c_6) + c_7 \cdot t + c_8 \qquad (2)$$
$$z = c_9 \cdot \cos(c_0 \cdot 2\pi \cdot t + 2\pi \cdot c_{10}) + c_{11} \cdot t + c_{12}$$

where again c_i ($0 \le i \le 12$) are unknown coefficients, and 2π coefficient is introduced for convenient interpretation of the c_0 and c_2, c_6 and c_{10} coefficients.

The maximization of the agreement was achieved by minimizing the squared residual sum:

$$S^2 = S_{x,i}^2 + S_{y,i}^2 + S_{y,i}^2 \rightarrow \min.$$

$$S_{x,i}^2 = \sum_{i=1}^{n} (x_i - c_1 \cdot \cos(c_0 \cdot t + c_2) - c_3 \cdot t - c_4)^2$$

$$S_{y,i}^2 = \sum_{i=1}^{n} (y_i - c_5 \cdot \cos(c_0 \cdot t + c_6) - c_7 \cdot t - c_8)^2 \qquad (3)$$

$$S_{z,i}^2 = \sum_{i=1}^{n} (x_i - c_9 \cdot \cos(c_0 \cdot t + c_{10}) - c_{11} \cdot t - c_{12})^2$$

where n is the number of observations (grid points in the supposed helix-like structure).

A simple look on (3) gives the minimal number of observations (n) to obtain a statistically significant result: $n \ge 3 \times 12/3$ (three coordinates - e.g. x, y, z - 12 unknowns, 3 observations per unknown). Therefore, no less than 12 monomers should be in the polymer in order to obtain statistical significant coefficients.

For a double helix, one follows equations:

$$x = (c_1 + (-1)^t \cdot c_{13}) \cdot \cos(c_0 \cdot 2\pi \cdot t + c_2 + 2\pi \cdot (-1)^t \cdot c_{19}) + c_3 \cdot t + c_4 + (-1)^t \cdot c_{16}$$
$$y = (c_5 + (-1)^t \cdot c_{14}) \cdot \cos(c_0 \cdot 2\pi \cdot t + c_6 + 2\pi \cdot (-1)^t \cdot c_{19}) + c_7 \cdot t + c_8 + (-1)^t \cdot c_{17} \qquad (4)$$
$$z = (c_9 + (-1)^t \cdot c_{15}) \cdot \cos(c_0 \cdot 2\pi \cdot t + c_{10} + 2\pi \cdot (-1)^t \cdot c_{19}) + c_{11} \cdot t + c_{12} + (-1)^t \cdot c_{18}$$

As can be observed, for the double helix, a series of new unknown coefficients appeared; c_{19} parameterizes a possible shift between the appearance of the helixes, while c_{16}, c_{17} and c_{18} account for the differences among the origin points of the helixes, and finally c_{13}, c_{14} and c_{15} parameterizes the differences in amplitude.

ACKNOWLEDGMENTS

R E F E R E N C E S

[1]. "Macromolecule (polymer molecule)". "IUPAC. Compendium of Chemical Terminology, 2nd ed. (the "Gold Book"). Compiled by A. D. McNaught and A. Wilkinson. Blackwell Scientific Publications, Oxford (**1997**). XML on-line corrected version: http://goldbook.iupac.org (2006-) created by M. Nic, J. Jirat, B. Kosata; updates compiled by A. Jenkins [Last update: 2014-02-24; version: 2.3.3] [cited August 24, 2015]. ISBN 0-9678550-9-8. doi:10.1351/goldbook. DOI of macromolecule: doi:10.1351/goldbook.M03667

[2]. W.P. Lin, S.J. Liu, T. Gong, Q. Zhao, W. Huang, *Advanced Materials*, **2014**, *26(4)*, 570.

[3]. C. Tan, Z. Liu, W. Huang, H. Zhang, *Chemical Society Reviews*, **2015**, *44(9)*, 2615.

[4]. S. Kalpakjian, S.R. Schmid, "Manufacturing Processes for Engineering Materials", 5th ed. **2008**. Available from: http://www3.nd.edu/~manufact/MPEM_pdf_files/Ch10.pdf

[5]. J.R. Fried, "Polymer Science and Technology", 3rd Ed. Prentice Hall, Massachusetts, USA, **2014**.

[6]. B.S. Mitchell, "An introduction to materials engineering and science for chemical and materials engineers", John Wiley & Sons, Inc., New Jersey, **2004**.

[7]. C.M. Agrawal, J.L. Ong, M.R. Appleford, G. Mani, "Introduction to Biomaterials: Basic Theory with Engineering Applications", Cambridge University Press, New York, **2014**.

[8]. M. Coronado, G. Montero, B. Valdez, M. Stoytcheva, A. Eliezer, C. García, H. Campbell, A. Pérez, *Energy*, **2014**, *68*, 364.

[9]. S.T. Montoya, P.A.P. Alzate, Y.M. Goez, C.E.E. Cuartas, P.G. Giraldo, "Evaluating the properties of silicone hoses for aesthetic surgery subjected to cycles of reuse," 8th Pan American Health Care Exchanges Conference, PAHCE 2013; Medellin; Colombia; 29 April 2013 through 4 May 2013. Pan American Health Care Exchanges, PAHCE 2013: Article number 6568271.

[10]. W. Makiguchi, S. Kobayashi, K. Furukawa, H. Iida, Y. Furusho, E. Yashima, *Journal of Polymer Science Part A: Polymer Chemistry*, **2015**, *53(8)*, 990.

[11]. Y. Takahashi, H. Tadokoro, *Macromolecules*, **1973**, 6(5), 672.

[12]. R. Yang, X.R. Yang, D.F. Evans, W.A. Hendrickson, J. Baker, *The Journal of Physical Chemistry*, **1990**, *94(15)*, 6123.

[13]. H. Dong, J.Y. Shu, N. Dube, Y. Ma, M.V. Tirrell, K.H. Downing, T. Xu, *Journal of the American Chemical Society*, **2012**, *134(28)*, 11807.

[14]. Y. Chatani, T. Kobatake, H. Tadokoro, R. Tanaka, *Macromolecules*, **1982**, *15(1)*, 170.

[15]. C. Lambert, F. Koch, S.F. Völker, A. Schmiedel, M. Holzapfel, A. Humeniuk, M.I.S. Röhr, R. Mitric, T. Brixner, *Journal of the American Chemical Society*, **2015**, *137(24)*, 7851.

[16]. J.D. Watson, F.H.C. Crick, *Nature*, **1953**, *171*, 737.

[17]. N. Safaee, A.M. Noronha, D. Rodionov, G. Kozlov, C.J. Wilds, G.M. Sheldrick, K. Gehring, *Angewandte Chemie International Edition*, **2013**, *52(39)*, 10370.

[18]. J.W. Prothero, *Biophysical Journal*, **1966**, *6(3)*, 367.
[19]. R.D. Farahani, K. Chizari, D. Therriault, *Nanoscale*, **2014**, *6(18)*, 10470.
[20]. Y. Yang, Y. Zhang, Z. Wei, *Advanced Materials*, **2013**, *25(42)*, 6039.
[21]. F. Totsingan, V. Jain, M.M. Green, *Artificial DNA, PNA & XNA*, **2012**, *3(2)*, 31.
[22]. T. Nakano, Y. Okamoto, *Chemical Reviews*, **2001**, *101(12)*, 4013.
[23]. X. Ping, K. Jiang, S.-Y. Lee, J.-X. Cheng, X. Jin, *Journal of Neurotrauma*, **2014**, *31(13)*, 1172.
[24]. A. Kolate, D. Baradia, S. Patil, I. Vhora, G. Kore, A. Misra, *Journal of Controlled Release*, **2014**, *192*, 67.
[25]. X. Zhao, H. Cui, W. Chen, Y. Wang, B. Cui, C. Sun, Z. Meng, G. Liu, *PLoS ONE*, 2014, 9(6), Article number e98919.
[26]. K. Kim, B. Bae, Y.J. Kang, J.-M. Nam, S. Kang, J.-H. Ryu, *Biomacromolecules*, **2013**, *14(10)*, 3515.
[27]. M. Jamshidian, E.A. Tehrany, M. Imran, M. Jacquot, S. Desobry, *Comprehensive Reviews in Food Science and Food Safety*, **2010**, *9(5)*, 552.
[28]. P. Gentile, V. Chiono, I. Carmagnola, P.V. Hatton, *Journal of Molecular Sciences*, **2014**, *15(3)*, 3640.
[29]. R. Mehta, V. Kumar, H. Bhunia, S.N. Upadhyay, *Journal of Macromolecular Science Polymer Reviews*, **2005**, *45*, 325.
[30]. C. Chen, G. Lv, C. Pan, M. Song, C. Wu, D. Guo, X. Wang, B. Chen, Z. Gu, *Biomedical Materials*, **2007**, *2*, L1.
[31]. F. Haaf, A. Sanner, F. Straub, *Polymer Journal*, **1985**, *17*, 143.
[32]. X. Liu, Y. Xu, Z. Wu, H. Chen, *Macromolecular Bioscience*, **2013**, *13(2)*, 147.
[33]. R.B. Fox, "Glass transition temperature for selected polymers", In: Haynes, W.M. (Ed). "Handbook of Chemistry and Physics". CRC Press, USA, **2012**.
[34]. L. Zhang, A. Aboagye, A. Kelkar, C. Lai, H. Fong, *Journal of Materials Science*, **2014**, *49(2)*, 463.
[35]. D. Liu, H. Chen, P. Yin, N. Ji, G. Zong, R. Qu, *Journal of Polymer Science Part A: Polymer Chemistry*, **2011**, *49(13)*, 2916.
[36]. J. Gardiner, *Australian Journal of Chemistry*, **2015**, *68(1)*, 13.
[37]. J.C. Slater, *Reviews of Modern Physics*, **1963**, *35(3)*, 484.
[38]. R. Ditchfield, W.J. Hehre, J.A. Pople, *Journal of Chemical Physics*, **1971**, *54(2)*, 724.

DENSITY FUNCTIONAL STUDY OF BOND DISSOCIATION ENERGIES IN HIGHLY BROMINATED DIPHENYL ETHERS

DAN MAFTEI[a], MIHAI DUMITRAȘ[a], DRAGOȘ-LUCIAN ISAC[a,b], ALIN-CONSTANTIN DÎRȚU[a,*]

ABSTRACT. Bond dissociation enthalpies (DEs) relevant to thermal dissociation of brominated diphenyl ethers were investigated in a computational approach at the density functional theory (DFT) level. In a preliminary assessment of eight of the most popular exchange-correlation functionals (including B3P86, PBE1PBE, mPW1PW91, wB97xD and two of each of the M05 and M06 families) the M06 meta-hybrid is shown to perform the best in reproducing two experimental C-O and C-Br BDEs, with errors bellow 1 kcal/mol and less dependent on basis set. The M06/cc-pVDZ is chosen as a good compromise between cost and accuracy for computing DEs of seven brominated diphenyl ethers. In the case of decabromodiphenyl ether we report a DE of 68.7 kcal/mol for the homolysis of the ether group and 74 to 77 kcal/mol for bromine cleavage. Compared to the corresponding values of the fully brominated compound, in lower brominated congeners we predict a substantial increase of both DEs with the decrease of bromine content.

Keywords: *brominated flame retardants, decabromodiphenyl ether, density functional theory, bond dissociation energies*

INTRODUCTION

Flame retardants (FRs) are materials that inhibit or resist the spread of fire that are added to polymers which are used in consumer goods [1,2]. There is limited knowledge about the mechanisms via which these chemicals migrate into and behave in the indoor environment and finally influence the human exposure to such compounds [3]. The estimation of human exposure to brominated FRs is based on reported levels for such compounds in several

---

[a] *Department of Chemistry, "Alexandru Ioan Cuza" University of Iasi, Department of Chemistry, Carol I Blvd. No 11, 700506 Iasi, Romania*
[b] *"Petru Poni" Institute of Macromolecular Chemistry Iasi, Grigore Ghica Voda Al. No. 41A, 700487 Iasi, Romania*
* *Corresponding author: alin.dirtu@chem.uaic.ro*

matrices like food or indoor dust [4]. Since higher elution temperatures are needed when applying conventional chromatographic techniques for their determination, FRs might undergo thermal degradation and therefore errors occur in their analysis [5] especially when targeting the highly brominated FRs such as polybrominated diphenyl ethers (PBDEs) and decabromodiphenyl ether (BDE 209) in particular. By the use of theoretical computations, it is possible to evaluate the most probable degradation products as well as the degradation mechanisms of selected brominated FRs.

In spite of their great importance, to the best of our knowledge there are only few experimental studies concerning the degradation of PBDEs, generally focused on photodegradation or reductive debromination mechanisms [6–8]. In contrast to the scarcity of experimental thermochemical data, PBDEs have inspired a large amount of computational work, the molecular structure of several species [9] as well as their dehalogenation (either photochemical [10] or reductive) leading to lower brominated congeners being the subject of several studies performed at levels ranging from semiempirical [11] to *ab initio* and Density Functional Theory (DFT) [12,13]. In effect, a consistent dataset of thermochemical parameters computed for PBDEs can be compiled from the literature of the last decade [14]. However, the lack of accurate experimental or even theoretical references regarding the thermochemistry of PBDEs, assumptions on their relative stability or reactivity, based on results of either semiempirical or DFT calculations, strongly reflect the particular parametrization (i.e. AM1, PM3, etc.) or the composition of the exchange-correlation functional, respectively. Although compound theoretical methods exist, including all-electron multi-reference computations and perturbational corrections to provide accurate thermochemical quantities regardless the nature of the compound of interest, most of them can hardly be applied to PBDEs in general and to highly brominated congeners in particular. Therefore, if one relays on DFT as a scalable alternative, the chosen density functional should account for the effects of electron correlation in an implicit manner.

In line with the above considerations, our study focused on the use of the DFT to model the bond dissociation energies (DEs) relevant to thermal decomposition of PBDEs including the fully brominated decabromodiphenyl ether (BDE 209, structure given in Scheme 1) and eight of the most abundant lower brominated congeners reported by previous literature for indoor dust samples [3,4].
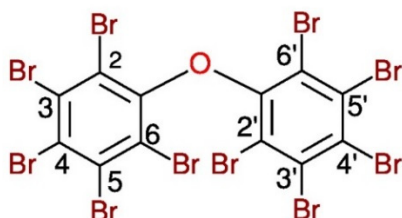
Scheme 1. Structure of decabromodiphenyl ether (BDE 209)

Unlike previous DFT works on PBDEs, we have selected the exchange-correlation density functional from six of the most popular for computational thermochemistry [15–17] including B3P86, wB97xD, PBE0 [18], mPW1PW91 [19] as well as M05 [20] and M06 [21] as well as their double exchange M05-2X [22] and M06-2X variants, based on the accuracy in reproducing two experimental C–O and C–Br bond DEs.

RESULTS AND DISCUSSION

DEs for relevant bonds in bromobenzene (C_6H_5–Br) and diphenyl ether (C_6H_5O–C_6H_5), computed with each of the considered functionals in conjunction with eight basis sets are collected in Tables 1 and 2, respectively. First, it could be noticed the strong variation of the computed values with the exchange-correlation functional, with up to 8-12 kcal/mol (10-15%) discrepancy between M05 values, the lowest overall, and the double exchange M05-2X counterparts. In addition, values computed with the same two functionals are in qualitative disagreement, the later (M05-2X) foreseeing a DE for the C_6H_5O–C_6H_5 bond at 3 kcal/mol below the corresponding value for the C_6H_5–Br, whereas the M05 functional reproduces the same quantities in the reverse order.

Table 1. C_6H_5–Br bond dissociation enthalpies (in kcal/mol, at 298.15K) computed at different DFT levels

Basis set	Exchange-correlation functional							
	M05	M05-2X	M06	M06-2X	B3P86	PBE0	mPW1PW91	wB97xD
6-311G(d)	74.1	85.6	79.6	86.1	79.0	78.9	77.0	81.6
6-311+G(d)	72.5	84.6	78.4	85.0	77.9	77.7	75.9	80.4
6-311+G(d,p)	72.7	84.7	78.6	85.0	78.1	77.9	76.0	80.5
6-311++G(d,p)	72.6	84.6	78.5	84.9	78.0	77.8	76.0	80.4
cc-pVDZ	75.6	86.7	80.6	87.7	80.2	80.0	78.1	82.7
cc-pVTZ	74.2	86.1	80.1	86.3	79.5	79.3	77.3	81.8
aug-cc-pVDZ	73.3	86.0	80.2	86.3	78.9	78.5	76.7	81.7
aug-cc-pVTZ	73.3	86.1	80.1	86.3	78.9	78.5	76.7	81.5

While the eight functionals considered generally disagree, even on the ordering of the two bond DEs, values computed with each of the functionals are almost independent on the basis set. In the case of the first four (Pople) basis sets, further addition of diffuse and/or polarization functions to the 6-311G(d)

Table 2. $C_6H_5O–C_6H_5$ bond dissociation enthalpies (in kcal/mol, at 298.15K) computed at different DFT levels

Basis set	Exchange-correlation functional							
	M05	M05-2X	M06	M06-2X	B3P86	PBE0	mPW1PW91	wB97xD
6-311G(d)	73.8	81.3	77.1	78.4	80.5	79.8	78.3	79.4
6-311+G(d)	73.6	81.2	76.9	78.2	80.4	79.7	78.2	79.3
6-311+G(d,p)	73.6	81.2	76.9	78.2	80.4	79.7	78.2	79.3
6-311++G(d,p)	73.6	81.2	76.9	78.2	80.4	79.7	78.2	79.3
cc-pVDZ	74.9	82.2	77.8	79.8	81.0	80.3	78.8	80.1
cc-pVTZ	75.1	82.6	77.9	79.1	81.3	80.6	79.0	80.2
aug-cc-pVDZ	74.9	82.6	78.0	80.1	81.2	80.5	79.0	80.3
aug-cc-pVTZ	74.9	82.7	77.8	79.1	81.3	80.5	79.0	80.2

yields C–Br DEs up to 1 kcal/mol lower and has essential no effect (-0.2 kcal/mol) on C–O DEs. Using correlation-consistent (cc, Dunning) basis sets result in even lower differences, DEs computed at DFT/aug-cc-pVTZ being less than 0.5 kcal/mol apart from the corresponding values computed using the cc-pVDZ basis set, the latter at a substantially reduced cost. Provided the methodology adopted in computing DEs (see Experimental Section, *Computational protocols*), prone to basis set incompleteness or superposition errors, ensuring that values computed are essentially converged values with respect to the basis set size is of particular importance. Therefore, from a methodological perspective, we emphasized that using either the cc-pVDZ or the aug-cc-pVDZ variant, the latter at a substantial cost when used on highly brominated systems, should provide converged DEs in conjunction with any of the above functionals.

Finally, to assess the accuracy of each density functional one needs to compare the computed DEs with the experimental values of either 80 kcal/mol [23] or 80.3 kcal/mol [24] reported for the corresponding C–Br bond and 77.8 kcal/mol [24] for C–O, respectively. Differences between computed and experimental DEs are graphically presented in Figure 1. For the C–Br bond we choose the recent value of 80.3 kcal/mol. One may note the sharp discrepancies of M05 and M05-2X values that underestimate and overestimate, respectively, the experimental quantities with up to 7-8 kcal/mol (10%). In addition, the M05, PBE0 and mPW1PW91 functionals reverse the order of the two bond DEs, B3P86 and M06-2X recover the two bond DEs values with different accuracy, whereas including dispersion corrections (as in wB97xD) improves marginally the computed DEs.
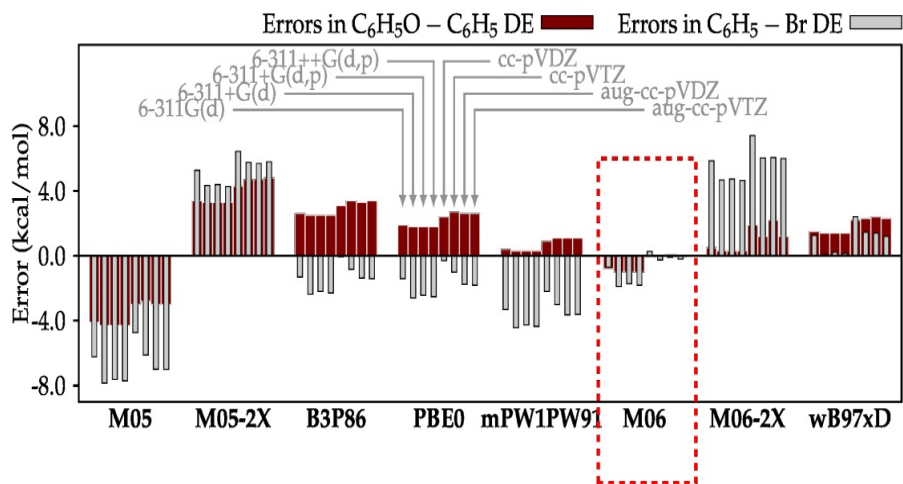
Figure 1. Differences (in kcal/mol) between computed C_6H_5–Br and C_6H_5O–C_6H_5 bond DEs and experimental counterparts

Among the selected functionals, the accuracy required in modeling the two bond DEs (2.5 kcal/mol apart) is achieved by M06 when used with any of the correlation-consistent cc-pVnZ basis sets. M06/cc-pVTZ values are within 0.1-0.2 kcal/mol of their experimental counterparts, but chemical accuracy (< 1 kcal/mol deviation) is achieved already at M06/cc-pVDZ, with a substantially reduced computational effort. Therefore we have further assumed comparable accuracy of the latter in modeling the C–O and C–Br bond energetics in PBDEs.

Table 3. Selected bond lengths (Å), valence and torsion angles (°) in BDE 209, computed at M06/cc-pVDZ level *vs.* experimental data

	Parameter	Computed	Experimental	
			Ref. [25]	Ref. [26]
Bond lengths	C_1-O	1.363	1.397	1.386
	C_2-Br	1.888	1.894	1.879
	C_3-Br	1.885	1.887	1.877
	C_4-Br	1.887	1.901	1.885
Valence angles	C_1-O-$C_{1'}$	125.0	120.9	120.7
	C_2-C_1-O	123.8	125.8	124.7
Torsion angle	C_2-C_1-O-$C_{1'}$	49.7	47.5	46.2

In Table 3 we compared a subset of internal coordinates from the geometry of BDE 209, optimized at M06/cc-pVDZ level in gas phase, with average experimental (XRD) values from selected references. Excepting the notable underestimation of the C–O bond (-0.2 to -0.3 Å), which may result in overestimated DE, and the 4° overestimation of the C–O–C angle, most of the remaining internal coordinates were reproduced within experimental uncertainties, in spite of the fact that M06 functional is not generally regarded as providing accurate geometries.

In a thermal decomposition scenario, degradation of highly brominated PBDEs may be initiated by either a debromination step, that explain the formation of nona-brominated congeners, the homolysis of C–O bond yielding brominated phenols or both. Energetics of the two pathways, as standard bond DEs computed at M06/cc-pVDZ level, is depicted in Figure 2. Compared to the DE computed for the corresponding bond in dyphenyl ether, our computations foresee a 9 kcal/mol weaker C–O bond in BDE 209. This may be rationalized on the basis of mutual repulsion between the bromine atoms in position adjacent to the ether group, but also considering the additional stabilization of the resulting brominated radicals compared to the unbrominated analogues [27]. In contrast, C–Br bonds are predicted at only 4-6 kcal/mol lower DEs in BDE 209 than in diphenylether. The computed 5-8 kcal/mol difference between the energetics of the C–Br and C–O bonds may be however underestimated, on the basis of an anticipated overestimation of the latter (see above). Hence, while most of the previous studies emphasize on debromination, photo-oxidation and subsequent intramolecular processes [27–29] in lower brominated PBDEs, results reported herein suggest that thermal decomposition toward polybrominated phenoxyl radicals and polybrominated phenyls is slightly favored in decabrominated diphenyl ether. However, the overall thermal decomposition mechanism may be influenced by several other factors, including radical stabilization or bimolecular steps not considered in our current approach.

Figure 3 depicts C–O and C–Br bonds DEs computed at the same M06/cc-pVDZ level of theory for six PBDE congeners: 2,2',3,3',4,4',6,6'-octabromodiphenyl ether (BDE 197), 2,2',3,4,4',5',6-heptabromodiphenyl ether (BDE 183), 2,2',4,4',5,5'-hexabromodiphenyl ether (BDE 153), 2,2',4,4',5,6'-hexabromodiphenyl ether (BDE 154), 2,2',4,4',5-pentabromodiphenyl ether (BDE 99), 2,2',4,4',6-pentabromo-diphenyl ether (BDE 100), 2,2',4,4'-tetrabromodiphenyl ether (BDE 47) and 2,4,4'-tribromodiphenyl ether (BDE 28). The above mentioned PBDE congeners were selected based on previous literature on their levels reported for indoor dust samples, one of the most important matrices when addressing human exposure to such compounds, while together with BDE 209 they generally consist of more than 95% of the total PBDEs measured in such samples [3,4].
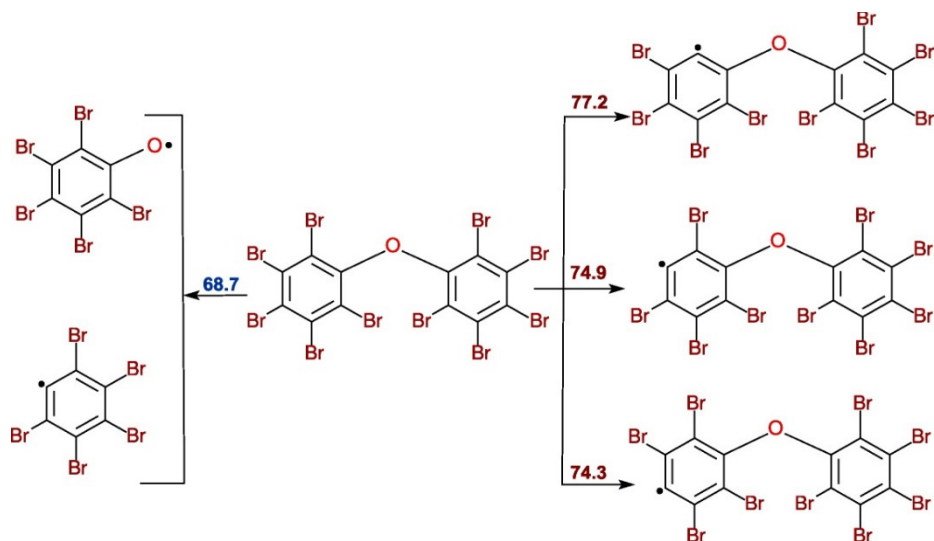
Figure 2. Differences (in kcal/mol) between computed C_6H_5–Br and C_6H_5O–C_6H_5 bond DEs and experimental counterparts

Values predicted for the C–O and C–Br bond DEs may be rationalized not only on the basis of bromine content, but also of the position of bromine atoms on the two rings. The overall trend shows that C–O bonds strengthens with the reduction of bromine content, from less than 70 kcal/mol in BDE 209 (see Figure 2) or about 70 kcal/mol in octa-brominated BDE 197 to more than 77 kcal/mol in the tri-brominated congener BDE 28. However, in asymmetric congeners the two C–O bonds do not follow the same trend. For instance, the homolytic cleavage of the C–O bond leading to 2,4,5-tribromo-phenyl radical is slightly favored to that leading to 2,4,5-tribromo-phenoxyl, the result being most likely related to a different stabilization energy of the two radicals. In the case of C–Br bonds, while the overall variation show a similar trend, the lower the number of bromine atoms, the higher the DE, mutual repulsion between bromine atoms in adjacent positions appears to weaken the corresponding C–Br bond with up to 6 kcal/mol when compared to the anticipated values. Given the smaller differences between C–Br and C–O bond DEs in congeners with lower bromine content it results in comparable strengths for the two bonds. However, regardless of the ordering of the two bond DEs, in deriving a kinetic model for the thermal decomposition of PBDEs one should account for the multiplicity of the C–Br bonds.
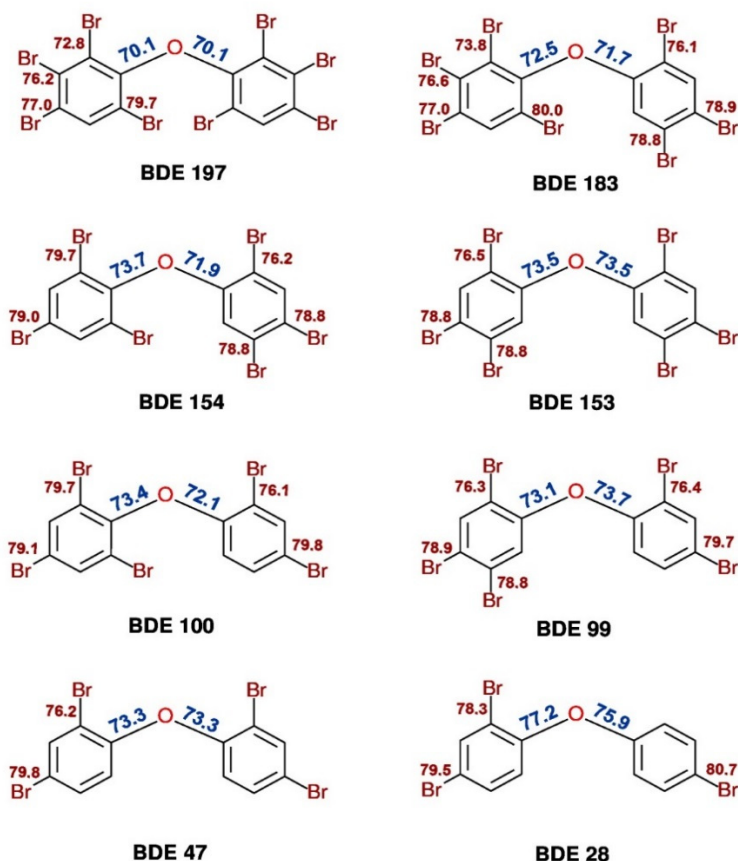
Figure 3. Bond DEs for C–O and C–Br (in kcal/mol) of selected PBDE congeners computed at M06/cc-PVDZ level in gas phase

CONCLUSIONS

Given the relatively low number of studies to report on the experimental thermochemical data concerning the PBDEs, we limit out conclusion to qualitative aspects derived from comparing the energetics of the two bond types, C–O and C–Br, of anticipated relevance for their thermal decomposition. We have shown that some of the most popular exchange-correlation density functionals, few of them used previously in computational works on PBDEs, show large deviations form experimental data on model compounds. Hence, some of the conclusions derived from absolute quantitative predictions at respective levels of theory, notoriously the M05 and M05-2X functionals, may

need to be reevaluated. Bond dissociation energies computed at the M06/cc-pVDZ level, recommended by our work for computational thermochemistry of PBDEs, suggest that thermal decomposition of highly brominated congeners may result in polibrominated phenols and polibrominated benzene, whereas the debromination is prefered in the case of lower brominated congeners. These findings represent valuable information for the environmental studies focusing on the human exposure sources to PBDEs, but also to their corresponding degradation products, when screening methods might be systematically adjusted based on information provided by combined theoretical studies and thermal degradation experiments performed on selected target molecules.

EXPERIMENTAL SECTION

Computational protocols

All electronic structure calculations were performed using Gaussian 09 rev. C01 [30] running on a local cluster. Equilibrium geometries of all species, including radicals, were computed in the Unrestricted Kohn-Sham (UKS) formalism of the Density Functional Theory (DFT) in gas phase. Unconstrained geometry optimizations were performed using standard "tight" convergence criteria in both self-consistent field and geometry cycles and "ultrafine" integration grids. Harmonic vibrational frequencies computations were run subsequent to each optimization, in order to confirm, on one hand, the nature of the located stationary point and to perform further calculation of thermochemical parameters, on the other. Frequencies used in evaluation of zero-point vibrational energy were unscaled. Unless noted otherwise, standard bond dissociation enthalpies were calculated by subtracting the enthalpy of the molecule of interest from the sum of enthalpies of the two fragments, each at the corresponding equilibrium geometry of the lowest-energy electronic state.

ACKNOWLEDGMENTS

R E F E R E N C E S

[1]. World Health Organization / International Classification for Patient Safety (WHO / ICPS). *Environmental Health Criteria 162:* Brominated Diphenyl Ethers. Geneva: World Health Organization, **1994**.

[2]. World Health Organization / International Classification for Patient Safety (WHO / ICPS). Environmental Health Criteria 192: Flame Retardants-General Introduction. Geneva: World Health Organization; **1997**.

[3]. A. Covaci, S. Harrad, M.A.E. Abdallah, N. Ali, R.J. Law, D. Herzke, C.A. de Wit, *Environment International*, **2011**, *37*, 532.

[4]. A.C. Dirtu, N. Ali, N. Van den Eede, H. Neels, A. Covaci, *Environment International*, **2012**, *49*, 1.

[5]. A.C. Dirtu, M.A.E. Abdallah, A. Covaci, *Trends in Analytical Chemistry*, **2013**, *43*, 189.

[6]. Y. Shih, C.K. Wang, *Journal of Hazardous Materials*, **2009**, *165*, 34.

[7]. Y. Pan, D.C.W. Tsang, Y. Wang, Y. Li, X. Yang, *Chemical Engineering Journal*, **2016**, *297*, 74.

[8]. G. Rotko, P.P. Romańczyk, S.S. Kurek, *Electrochemistry Communications*, **2013**, *37*, 64.

[9]. J. Hu, L. Eriksson, Å. Bergman, E. Kolehmainen, J. Knuutinen, R. Suontamo, X. Wei, *Chemosphere*, **2005**, *59*, 1033.

[10]. L. Pan, W. Bian, *ChemPhysChem*, **2013**, *14*, 1264.

[11]. Y. -Y. Zhao, F. -M. Tao, E.Y. Zeng, *Chemosphere*, **2008**, *70*, 901.

[12]. M. Grabda, S. Oleszek-Kudlak, E. Shibata, T. Nakamura, *Journal of Molecular Structure: THEOCHEM*, **2007**, *822*, 38.

[13]. J. Zhou, J. Chen, C.H. Liang, Q. Xie, Y.N. Wang, S. Zhang, X. Qiao, X. Li, *Environmental Science and Technology*, **2011**, *45*, 4839.

[14]. J. Luo, J. Hu, X. Wei, L. Fu, L. Li, *Chemosphere*, **2015**, *131*, 17.

[15]. Y.G. Lazarou, A.V. Prosmitis, V.C. Papadimitriou, P. Papagiannakopoulos, *Journal of Physical Chemistry A*, **2001**, *105*, 6729.

[16]. X. Q. Yao, X.J. Hou, H. Jiao, H.W. Xiang, Y.W. Li, *Journal of Physical Chemistry A*, **2003**, *107*, 9991.

[17]. G.A. DiLabio, D.A. Pratt, *The Journal of Physical Chemistry A*, **2000**, *104*, 1938.

[18]. C. Adamo, V. Barone, *The Journal of Chemical Physics*, **1999**, *110*, 6158.

[19]. C. Adamo, V. Barone, *The Journal of Chemical Physics*, **1998**, *108*, 664.

[20]. Y. Zhao, N.E. Schultz, D.G. Truhlar, *The Journal of Chemical Physics*, **2005**, *123*, 161103.

[21]. Y. Zhao, D.G. Truhlar, *Theoretical Chemistry Accounts*, **2008**, *120*, 215.

[22]. Y. Zhao, N.E. Schultz, D.G. Truhlar, *Journal of Chemical Theory and Computation*, **2006**, *2*, 364.

[23]. D.F. McMillen, D.M. Golden, *Annual Review of Physical Chemistry*, **1982**, *33*, 493.

[24]. "CRC Handbook of Chemistry and Physics". CRC Press: Boca Raton, **2007**.

[25]. J. Eriksson, L. Eriksson, E. Jakobsson, *Acta Crystallographica Section C Crystal Structure Communications*, **1999**, *55*, 2169.

[26]. A.A. Mrse, S.F. Watkins, F.R. Fronczek, *Acta Crystallographica Section C Crystal Structure Communications*, **2000**, *56*, e576.

[27]. G. Rotko, P.P. Romańczyk, G. Andryianau, S.S. Kurek, *Electrochemistry Communications*, **2014**, *43*, 117.

[28]. M. Altarawneh, B.Z. Dlugogorski, *The Journal of Physical Chemistry A*, **2014**, *118*, 9338.

[29]. M. Altarawneh, B.Z. Dlugogorski, *Environmental Science and Technology*, **2013**, *47*, 5118.

[30]. M.J. Frisch, G.W. Trucks, H.B. Schlegel *et al.*, *"Gaussian 09 Revision C.01"*, Wallingford CT, **2009**.

SYNTHESIS OF MAGNETIC IRON OXIDES FROM FERROUS SULFATE AND SUBSTITUTES AMINES

MARCELA STOIA[a], ANDRA TAMAȘ[a,*], GERLINDE RUSU[a], JEAN MOROȘANU[a]

ABSTRACT. In this paper, magnetic iron oxides were synthesized by using a modified Ueda method starting from ferrous sulfate as iron precursor and different substitued organic amines as precipitants. The evolution of the obtained iron oxides with the annealing temperatures was monitored by thermal analysis, FTIR spectroscopy and X-ray diffractometry. The magnetic powders obtained have been characterized by SEM microscopy and magnetic measurements.

Keywords: iron oxides, magnetic, substitutes amines, thermal analysis

INTRODUCTION

Magnetic nanoparticles of iron oxides (e.g Fe_3O_4, γ-Fe_2O_3) have attracted attention in biomedical applications like drug delivery systems, magnetic resonance imaging, and cancer therapy [1-4], but also as adsorbents in water purification due to their numerous advantages [5].

Many synthesis routes were developed for obtaining magnetite: coprecipitation of Fe(II) and Fe(III) hydroxides [6], precipitation of Fe(II) hydroxide and oxidation [7], spray pyrolysis [8], sol-gel [9], thermal decomposition of different precursors [10], combustion [11], hydrothermal [12], solvothermal [13], ball-milling [14] etc. However, magnetite nanoparticles are very much susceptible to air oxidation even at low temperatures [15,16]. The heating of magnetite nanoparticles in air at low temperatures leads to maghemite, while at higher temperatures maghemite is further oxidized to hematite [17]. Maghemite has the same crystalline structure as magnetite, namely spinel ferrite. Bulk magnetite

---

[a] *University Politehnica Timișoara, Faculty of Industrial Chemistry and Environmental Engineering, 6 Vasile Pârvan str., RO-300223,Timișoara, Romania*
* *Corresponding author: andra.tamas@upt.ro*

and maghemite possess ferrimagnetic properties at room temperature [18]. Many papers about nanostructured iron oxides do not clearly differentiate between both spinel-type iron oxides, since they are very similar. Moreover, particle size and particle size distribution (besides phase composition) are key factors that determine the specific loss power [19].

Due to this susceptibility to oxidation, it is very difficult to synthesize and stabilize pure magnetite; in most cases a mixture of magnetite and maghemite is obtained [20].

There are various coprecipitation routes for the preparation of magnetite nanoparticles, but in most cases synthesis is performed in an inert gas atmosphere, which is bubbling within the solvent to remove dissolved oxygen and to prevent oxidation of Fe(II) into Fe(III) [21]. In this method, Fe^{2+} and Fe^{3+} ions are generally precipitated in alkaline solutions, such as NH_4OH, KOH or NaOH. In most cases, the syntheses are performed at 70-80°C or higher temperatures [22].

Magnetite can be obtained only from Fe^{2+} in the presence of various types of amines: hydroxylamine sulfate [23], bispyridoxylidene hydrazine phthalazine [24], dodecylamine [25]. Only the precipitation of Fe^{2+}, followed by oxidation with H_2O_2 [26,27] or $NaNO_2$ [28] can be also used. Another method uses only Fe^{3+} for precipitation, followed by partially reducing of ferric to ferrous ion by Na_2SO_3 [29] in the precipitation product.

In this paper we report the synthesis of magnetic iron oxides using a modified Ueda method [30,31], starting from ferrous sulfate as iron precursor and different substituted organic amines (diethanolamine, triethanolamine, diethylamine and triethylamine) as precipitants. The evolution of the obtained iron oxides with the annealing temperatures was monitored by thermal analysis, FTIR spectroscopy and X-ray diffractometry. The magnetic powders obtained have been characterized by SEM microscopy and magnetic measurements.

RESULTS AND DISCUSSION

The powders synthesized by ethanolamines have been different from the ones obtained with ethylamines. Firstly, their colour is significantly different: the two powders obtained with ethanolamine (FeDEOA and FeTEOA) had a greenish-brown colour, while the powders obtained with ethylamine (FeDEA and FeTEA) were brown-black. Secondly, the powders FeDEOA and FeTEOA were almost nonmagnetic, while the powders FeDEA and FeTEA had strong magnetic properties. Thus, we concluded that in case of ethanolamines some iron (III) oxyhydroxides are formed, while in case of ethylamines magnetite might be the precipitation product.

All the initial powders have been characterized by TG/DSC thermal analysis in air and in nitrogen, in order to investigate their thermal evolution. The thermal behavior of the powders prepared with ethanolamines (Figure 1) is clearly different from the one of the powders obtained from alkylamines.

Thus, in the case of the samples synthesized with DEOA (Figure 1a) and TEOA (Figure 1b), there are three mass losses. The first mass loss, of about 6% for DEOA and 4% for TEOA, registered in the range 25-150°C, corresponds to the elimination of the adsorbed water, having an endothermic effect associated on DSC with a minimum around 60°C. The main mass loss of about 9% for DEOA and 5% TEOA, that takes place in the range 150-350°C, accompanied by an endothermal effect on DTA curve with minimum about 250°C, suggests a dehydration process of the possible precipitation of FeO(OH) to α-Fe$_2$O$_3$. This endothermic effect was reported in literature around 340°C [32] and was evidenced to be dependent on the goethite particle size, concluding that a small-sized goethite, with a high specific surface area, would generally feature a single peak transition, occurring at lower temperatures.
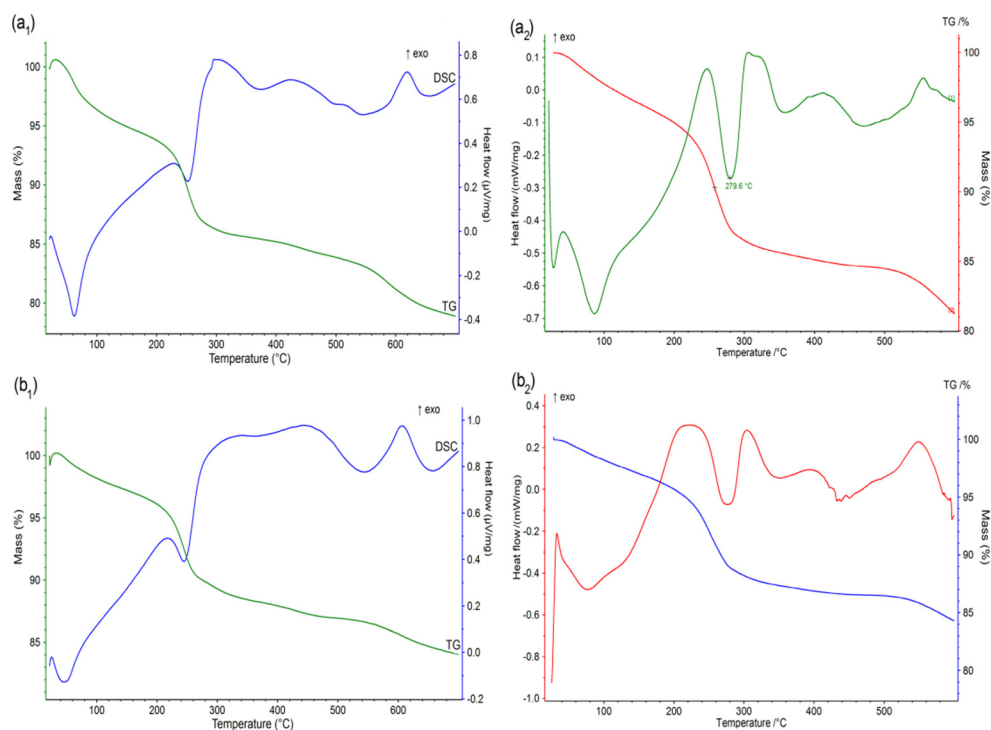
Figure 1. TG/DSC curves of the synthesized powders: (a) FeDEOA and (b) FeTEOA in nitrogen ($_1$) and in air ($_2$) atmosphere;

Comparing the experimental mass losses in this range with the theoretical one (10.1% corresponding to $2FeO(OH) => Fe_2O_3 + H_2O$) it results that, in our case, the powders are not formed from pure goethite, but there are probably other iron oxides formed during precipitation. In the range 400-500°C, a weak exothermic effect is registered during a small continuous mass loss. This effect may suggest a crystalline phase transition (possible maghemite to hematite) more visible when using air atmosphere (Figure 1a$_2$, b$_2$). The presence of this process in case of heating in nitrogen can only be due to the air contained in the pores of the analyzed powder.

The third small mass loss, correlated with an exothermic effect on DSC curve around 600°C, must be due to a final dehydroxylating step, overlapped with the crystallization of $\alpha\text{-}Fe_2O_3$ from the possible present maghemite that can results by dehydration of lepidocrocite [33].

By comparing the thermal curves registered in nitrogen (Figure 1a$_1$, b$_1$) with the ones registered in air (Figure 1a$_2$, b$_2$) one can see, that there is a great similarity. The thermal behavior exhibits the same decomposition steps, and the corresponding mass losses did not differ significantly.

In order to confirm the thermal evolution of the powders we have characterized, by FTIR spectroscopy, the powders FeDEOA and FeTEOA as synthesized and annealed at 150°C, 300°C and 450°C, in air, for 3 hours. The obtained FTIR spectra in the range 1200-400 cm^{-1} are shown in Figure 2. The evolution of the two samples is similar. The main difference between the spectra of the as synthesized sample and the one annealed at 150°C, is the significant decrease in intensity of the bands characteristic to the adsorbed water molecules: the large bands in the range 3500-3000 cm^{-1} and 1643 cm^{-1}, confirm the elimination of water in this range of temperature.

The band from the range 3500-4000 cm^{-1} presented two shoulders (two minima) around 3350 cm^{-1} and 3180 cm^{-1}: the shoulder at 3400 cm^{-1} was assigned in literature [34] to the stretching mode of H_2O molecules, whereas the shoulder at 3140 cm^{-1} can be assigned to the stretching mode of the OH group in a goethite structure. In Figure 2, we have illustrated only the range 1200-400 cm^{-1} for a better highlight of the bands characteristic to iron oxides. The bands located around 1130 cm^{-1}, which can be assigned to hydroxyl groups, decrease their intensities by raising the temperature to 150°C, showing that, in the range 25-150°C, a partial dehydroxylating also takes place.

The two central FTIR bands located at 887 cm^{-1} and 794 cm^{-1} can be assigned to Fe-O-H bending vibrations in $\alpha\text{-}FeOOH$, according to Music at al [35]. The broad bands located around 600 cm^{-1} and 450 cm^{-1} were assigned by the same authors to an amorphous iron(III) hydroxyde, or to ferrihydrite. The band located around 600 cm^{-1} increases in intensity, especially in the case of the FeTEOA powder, probably due to the formation of some magnetite by the

150

thermal decomposition of goethite, as it has been evidenced in literature [36]. The thermal treatment at 300°C leads to significant changes in the FTIR spectra. Thus, the bands characteristic to –OH vibrations from goethite are no longer present, proving the complete dehydration, with the formation of a magnetic phase, probably a mixture of hematite - confirmed by the pronounced bands located at 449 cm^{-1} and ~549 cm^{-1} [37], and maghemite- confirmed by the shoulder located at 630 cm^{-1} [38]. The other bands of maghemite overlapped with hematite bands.
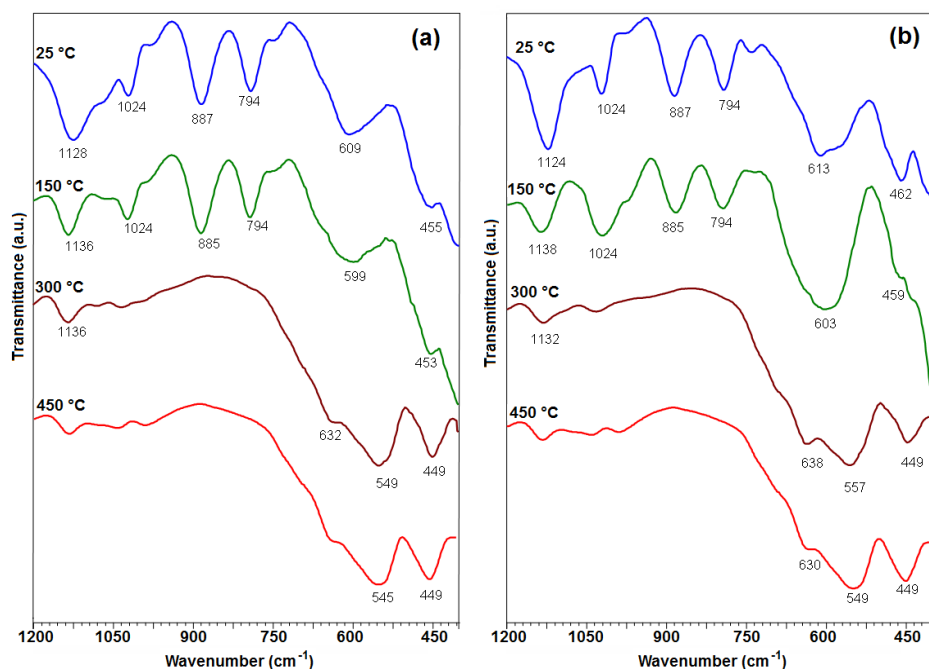
Figure 2. FTIR spectra of the powders FeDEOA (a) and FeTEOA (b) thermally treated

The increase of the annealing temperature at 450°C does not produce significant changes in the FTIR spectra, as also results from thermal behavior. The XRD patterns of the powders FeDEOA and FeTEOA, annealed at different temperatures, are shown in Figure 3 a,b. The evolution of the crystalline phases in the studied samples are similar.

Thus, the powders obtained at room temperature, without thermal treatment, contain a spinel phase, identified as magnetite (JCPDS card no. 01-080-6403) [39], and iron(III) oxyhydroxyde FeO(OH) as two crystalline phases:

goethite (JCPDS card no. 04-015-8332), and lepidocrocite (JCPDS card no. 00-044-1415). The thermal treatment at 150°C does not change the crystalline phase composition of the two powders. After annealing the powders at 300°C, both goethite and lepidocrocite dissapear, as a result of the dehydration evidenced through thermal analysis. According to literature, lepidocrocite (γ-FeOOH) thermally decomposes above 200°C to γ-Fe$_2$O$_3$, while goethite (α-FeOOH) decomposes to α-Fe$_2$O$_3$ [33]. The main crystalline phase is a spinel phase, identified as γ-Fe$_2$O$_3$ (JCPDS card no. 00-039-1346) instead of magnetite, as it is well known that magnetite is oxidized above 200°C, in air, to maghemite [40]. Also, a second low crystalline phase, identified as α-Fe$_2$O$_3$ (JCPDS card no. 04-002-7501) is present. One can notice from the XRD patterns of powders annealed at 450°C (Figure 3a,b) that in case of sample FeTEOA the content of hematite is significantly lower compared to FeDEOA, due to its initial lower content of goethite.
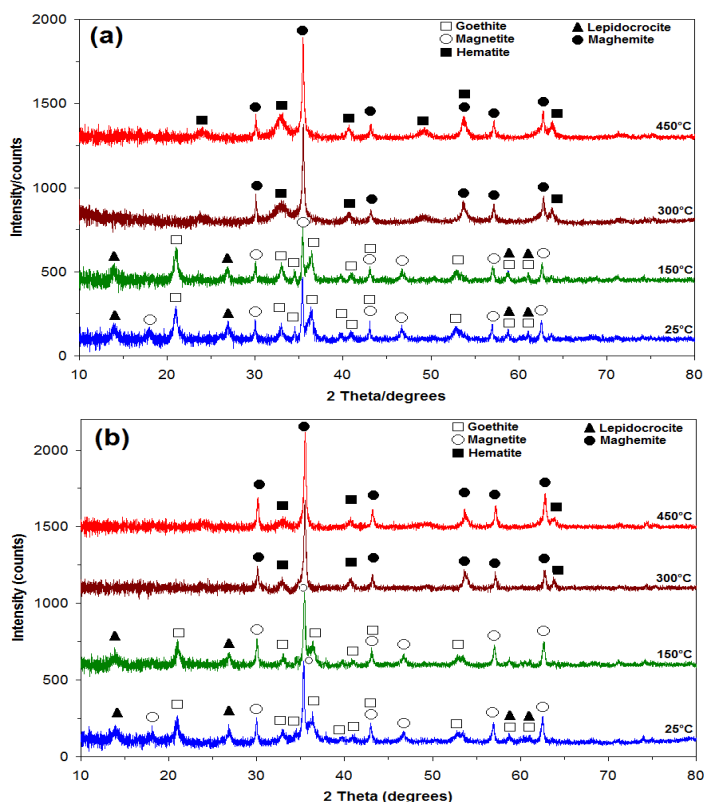
Figure 3. XRD pattern of the powders FeDEOA (a) and FeTEOA (b) thermally treated

We can conclude that in case of the powders synthesized with ethanolamine, the magnetic maghemite phase is stabilized up to 450°C, representing the predominant phase for the powder annealed at this temperature.

The powders FeDEA and FeTEA, as expected, showed a completely different thermal behavior compared to FeDEOA and FeTEOA. Figure 4 shows the TG/DSC curves for the as synthesized powders FeDEA and FeTEA.
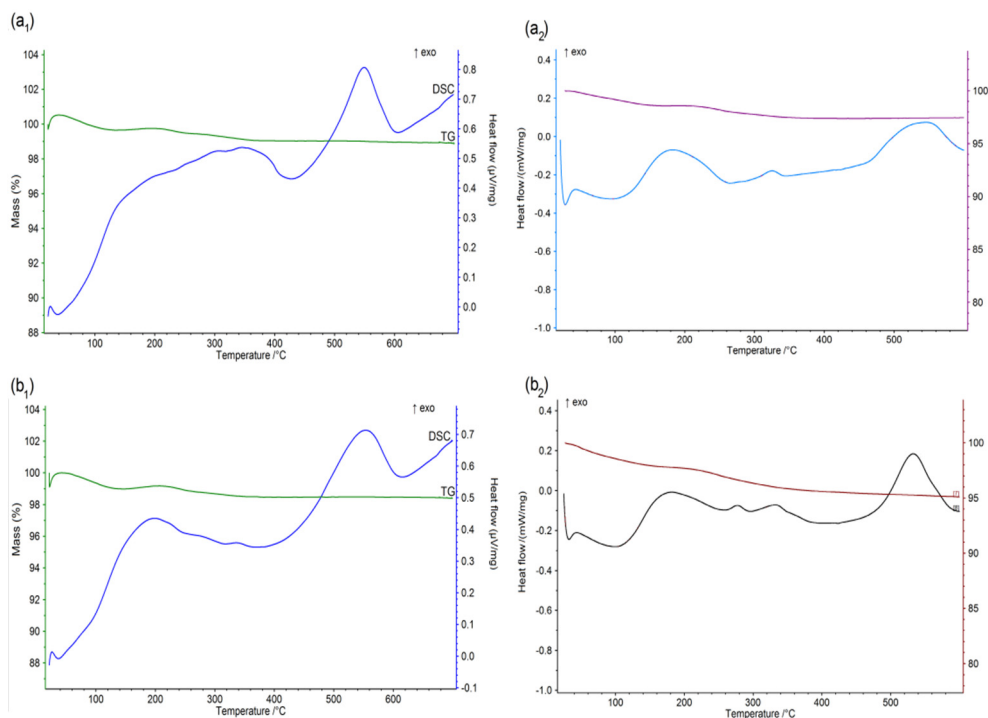
Figure 4. TG/DSC curves of the synthesized powders: (a) FeDEA and (b) FeTEA

One can notice from the TG curves that powder mass does not change significantly during heating up to 600°C, concluding that in this case the desired phase, namely magnetite, was obtained in the as synthesized samples. Even if the heating was performed in nitrogen atmosphere, a slight mass increase is registered in the range 150-220°C, characteristic to magnetite (Fe_3O_4) oxidation at maghemite [41], associated on DSC curve, especially in case of FeDEA (Figure 4a) by an exothermic effect. This can be explained by the presence of air within the powder pores. Above 220°C, the mass no longer changes, but on DSC curve

appears a pronounced exothermic effect with maximum around 550°C, which can be assigned to the transition of maghemite (γ-Fe$_2$O$_3$) to hematite (α-Fe$_2$O$_3$) [42]. The shape of TG curves in air atmosphere is similar. The mass change is small, but the exothermic effects registered around 200°C are better evidenced, due to the fact that in air, the oxidation process of magnetite to maghemite is more pronounced.

The FTIR spectra of FeDEA and FeTEA powders are shown in Figure 5.
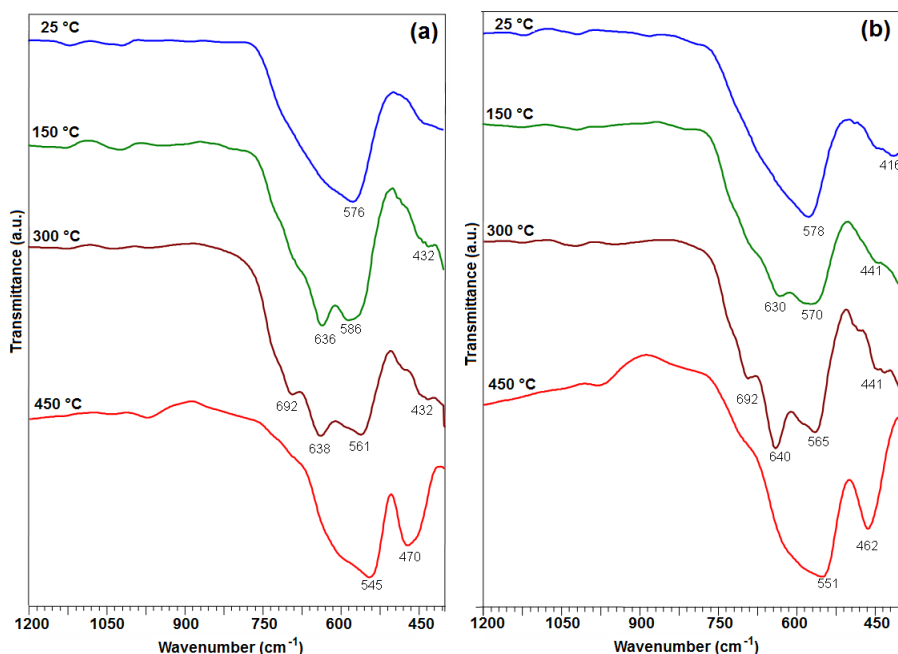
Figure 5. FTIR spectra of the powders FeDEA (a) and FeTEA (b) thermally treated

The single (large) band located in the region 400-600 cm^{-1}, with a maximum at 576cm^{-1} registered in the FT-IR spectra of the as synthesized powders FeDEA and FeTEA, evidenced the formation of magnetite as major phase. The asymetry of the band, suggests the presence of another phase with bands located in this range, most probably maghemite. This hypothesis is confirmed by the splitting of this band after the thermal treatment at 150°C, with appearance of a new band around 630 cm^{-1}, together with the band at 430°C characteristic to maghemite [38]. One can notice that the content of maghemite in the powder FeTEA annealed at 150°C is lower, compared to the powder FeDEA. After being annealed at 300°C, both powders contain only

maghemite, evidenced by the bands located at 692 cm^{-1}, 630 cm^{-1}, 560 cm^{-1}, 430 cm^{-1}. The annealing of these powders to 450°C leads to significant changes in their FTIR spectra. Thus, both spectra (Figure 5 a,b) evidence two strong bands located around 460 cm^{-1} and 550 cm^{-1}, characteristic to α-Fe$_2$O$_3$ phase [43]. The width and asymmetry of the band located around 550cm^{-1} may be due to the incomplete transition of maghemite to hematite.

The XRD patterns of powders FeDEA and FeTEA, annealed at different temperatures are shown in Figure 6 a,b.
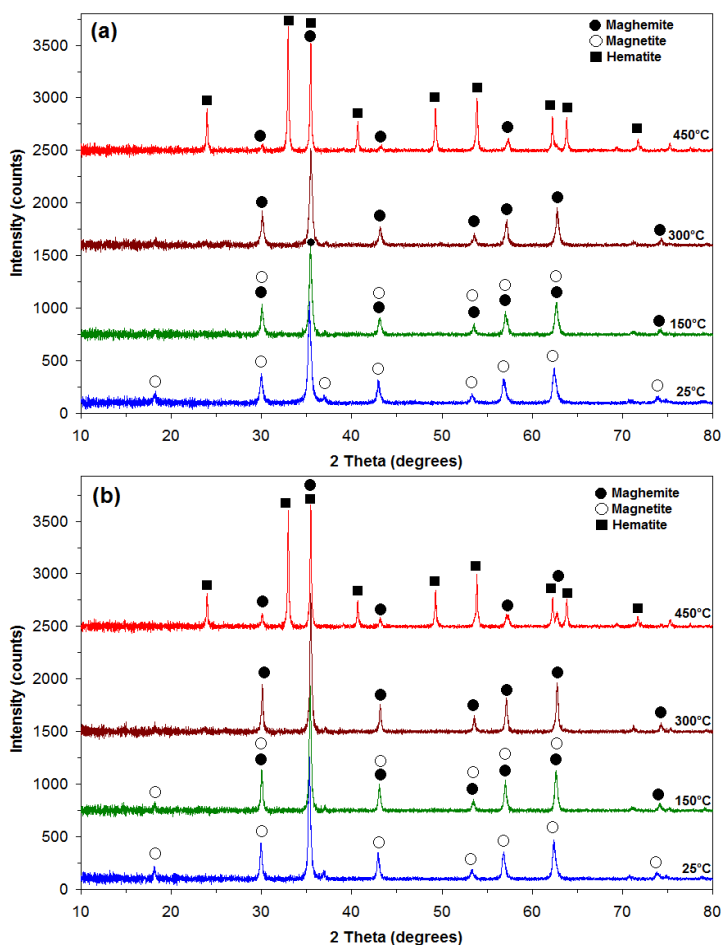
Figure 6. XRD pattern of the powders FeDEOA (a) and FeTEOA (b) thermally treated in air

One can see that the evolution of the crystalline phases with the annealing temperature is similar for the two powders. Starting with the room temperature and up to 300°C as annealing temperature, both powders present a single spinel crystalline phase, with magnetic properties (it gets magnetized under the field of a permanent magnet). This phase was assigned, in case of the as synthesized powders (room temperature) to magnetite (Fe_3O_4) while for the powders annealed at 300°C, it was assigned to maghemite (γ-Fe_2O_3), based on the thermal behavior and FT-IR study. This is in agreement with the literature [18,40]. A detail which sustains our assignment is also the slight but visible shift of the diffraction peaks (especially in case of (511) diffraction peak located around 62 degree) characteristic to the spinel phase to higher 2theta values, as reported before in literature [20]. In case of powders annealed at 150°C, we can consider that we have a mixture of magnetite and maghemite, the position of the diffraction peaks being intermediary between the ones at room temperatures and the ones at 300°C.

The evolution of the crystalline phases can be reflected by the magnetic behavior of the powders. Thus, all the powders obtained at room temperatures and the powders FeTEOA and FeTEA annealed at different temperatures have been characterized by magnetic measurements. The values of the saturation magnetization (M_s), coercive field (H_c) and saturation field (H_s) are listed in the Table 1.

Table 1. The values of magnetic parameters

Sample	Annealing temperature (°C)	M_s (emu g^{-1})	H_c (kA m^{-1})	H_s (kA m^{-1})
FeDEOA	25	8	38	382
FeTEOA	25	20	32	302
	150	20	33	363
	300	27	29	400
	450	18	29	412
FeDEA	25	54	38	383
FeTEA	25	55	37	470
	150	53	38	391
	300	57	35	385
	450	17	37	395

The evolution of the saturation magnetization with the annealing temperature, in case of FeDEA sample, suggests that the powder obtained at room temperature is composed mostly of maghemite, the value of 55 emu g^{-1} being a value characteristic to maghemite nanopowders (up to 60 nm [44]), not to magnetite nanopowders (above 65 emu g^{-1} [45,46]). The insignificant change of the saturation magnetization shows that the composition of the magnetic phase is almost constant up to 300°C. In case of the powder annealed at 450°C, the saturation magnetization suddenly drops, due to the partial transition of magnetic maghemite to nonmagnetic hematite, in agreement with the XRD and FTIR results.

In case of powder FeTEOA the magnetization values of the initial sample and the sample heated at 150°C, are identical due to the constant composition, in agreement with XRD data. The value of the saturation magnetization increases from 20 emu g^{-1} to 27 emu g^{-1} due to the transition of lepidocrocite to magnetic maghemite, while goethite turns into nonmagnetic hematite. The drop of saturation magnetization value to 18 emu g^{-1} after the annealing at 450°C is due to the partial transition of magnetic maghemite to nonmagnetic hematite.

The SEM images of the powders FeTEOA and FeTEA annealed at 150°C and 300°C are shown in Figure 7 and Figure 8.
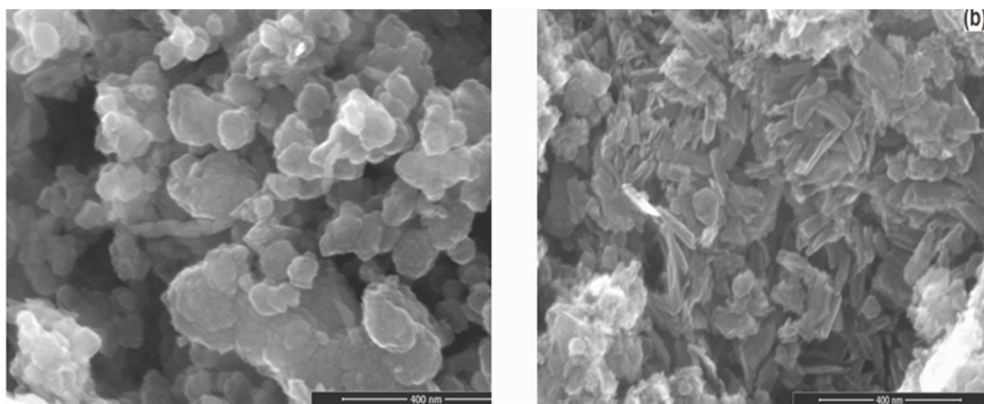
Figure 7. SEM images of powder FeTEOA annealed at 150°C and 300°C

According to the SEM images, both powders are formed from fine quasi-spherical nanoparticles aglomerated in structuress up to hundreds of nanometers, which form micrometrical aggregates. In case of FeTEOA powder, the structures formed by the nanoparticles are less homogenous, and change after the

annealing at 300°C, probably due to the change of crystalline phases. In the case of powder FeTEA, SEM image (Figure 8) evidences ball like structures of nanoparticles, with no significant changes from 150°C to 300°C.
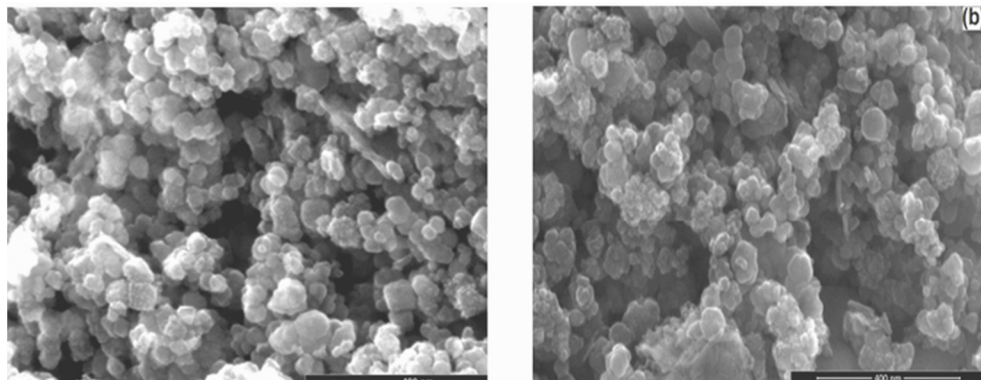
Figure 8. SEM images of powder FeTEA annealed at 150°C and 300°C

CONCLUSIONS

Magnetic iron oxides have been successfully synthesized by a one pot precipitation method starting from iron(II) sulfate and amines in aqueous solutions. TG/DSC simultaneous thermal analysis evidenced the difference in powder composition, the thermal behavior of the powders precipitated with ethanolamines being completely different from that of the powders with ethylamines. Ethanolamines were not able to insure the formation of magnetic iron oxides by precipitation. They led to a mixture of FeOOH and Fe_3O_4, as was evidenced by FTIR, XRD analysis and magnetic measurements. By annealing the obtained powders at 450°C, magnetic maghemite was obtained as the major crystalline phase, impurified with small quantities of hematite. In case of ethylamine, a mixture of magnetite and maghemite was obtained directly from synthesis. After being annealed at 300°C, the powders contain only maghemite. The thermal treatment of these powders at 450°C, led to nonmagnetic hematite as major crystalline phase. The magnetic properties of the powders annealed at different temperature are in agreament with RX results. The saturation magnetization of the powders FeTEOA and FeTEA annealed at 450°C were almost identical, 18 emu g^{-1} and 17 emu g^{-1}, respectively, evidencing the presence of a less crystalline nonmagnetic phase (hematite) in case of FeTEOA powder, and a less crystalline magnetic phase (maghemite) in case of FeTEA powder.

EXPERIMENTAL SECTION

Materials

The starting materials were: ferrous sulfate ($FeSO_4.7H_2O$), diethanolamine-DEOA ($C_4H_{11}O_2N$), triethanolamine-TEOA ($C_6H_{15}O_3N$), diethylamine-DEA ($C_4H_{11}N$), triethylamine-TEA ($C_6H_{15}N$), and sulfuric acid (H_2SO_4) and were all reagent grade, used without further purification.

Synthesis

In a typical synthesis, the quantity of $FeSO_4$ necessary for the synthesis of 0.01 mol of Fe_3O_4 was dissolved in 100 mL distilled water, under addition in drops of H_2SO_4 6M, until complete dissolution, in a 400 mL beaker. The obtained clear solution, was neutralized by addition of the corresponding amine, until the iron hydroxide starts to precipitate. At that moment, the calculated volume of amine (corresponding to an excess of 50% to the stoichiometric quantity necessary for the precipitation of ferrous hydroxide) was quickly added to the ferrous sulfate solution. During the addition of amine, the suspension temperature increases up to 50°C. A viscous, gelatinous precipitate was obtained, which was kept under magnetic stirring for 30 minutes. We have observed that the colours of the precipitates were different. When using DEA and TEA the precipitates were gray, while using DEOA and TEOA they were greenish-black. The beakers have been sealed with a plastic foil and kept in the darkness for 3 days.

Characterization techniques

Thermal behavior of the powders was studied using a NETZSCH STA 449F1 STA449F1A-0220-M, in nitrogen and in air atmosphere, at a flow rate of 20 mL min^{-1}. The TG/DSC curves were recorded in the range of 25-700°C with a heating rate of 10°C min^{-1}, using alumina crucibles. The phase composition of the samples was determined by XRD, using a Rigaku Ultima IV diffractometer (Cu$_{K\alpha}$ radiation). FTIR spectra were carried out using a Shimadzu Prestige-21 spectrometer in the range 400-4000 cm^{-1}, using KBr pellets and a resolution of 4 cm^{-1}. The morphology of the nanopowders was investigated by scanning electron microscopy (SEM), using a FEI Quanta FEG 250 microscope. The magnetic investigation of the final nanopowders was carried out at room temperature, on a Vibrating Sample Magnetometer (DMS VSM).

ACKNOWLEDGMENTS

R E F E R E N C E S

[1]. M. Wahajuddin, *International Journal of Nanomedicine,* **2012**, *7*, 3445.
[2]. X. M. Liu, J.K. Kim, *Materials Letters,* **2009**, *63*, 428.
[3]. Y.S. Li, J.S. Church, A.L. Woodhead, F. Moussa, *Spectrochimica Acta Part A*, **2010**, *76,* 484.
[4]. M.D. Shariful Islam, Y. Kusumoto, J. Kurawaki, M.D. Abdulla-al-Mamun, H.A. Manaka, *Bulletin of Materials Science,* **2012**, *35(7)*, 1047.
[5]. X. Jing-San, Z. Ying-Jie, *Journal of Colloid and Interfacial Science*, **2012**, *385*, 58.
[6]. L. Shen, Y. Qiao, Y. Guon, S. Meng, G. Yang, M. Wu, J. Zhao, *Ceramics International,* **2014**, *40*, 1519.
[7]. J.R. Correa, D. Canetti, R. Castillo, J.C. Llopiz, J. Dufou, *Materials Research Bulletin,* **2006**, *41*, 703.
[8]. R. Strobel, S.E. Pratsinis, *Advanced Powder Technology*, **2009**, *20*, 190.
[9]. O.M. Lemine, K. Omri, B. Zhang, L. El Mira, M. Sajieddine, A. Alyamani, M. Bououdina, *Superlattices and Microstructures,* **2012**,*52*, 793.
[10]. S.F. Chin, S.C. Pang, C.H. Tan, *Journal of Materials and Environmental Science,* **2011**, *2(3),* 299.
[11]. R. Ianoș, A. Tăculescu, C. Păcurariu, I. Lazău, *Journal of the American Ceramic Society,* **2012**, *95(7),* 2236.
[12]. C.Y. Hawa, F. Mohamed, C.H. Chia, S. Radiman, S. Zakaria, N. Huang, H. Lim, *Ceramics International,* **2010**, *36*, 1417.
[13]. X. Wang, J. Yu, G. Shi, G. Xu, Z. Zhang, *Journal of Materials Science,* **2014**, *49,* 6029.
[14]. M.M. Can, S. Ozcan, A. Ceylan, T. Firat, *Materials Science and Engineering: B,* **2010**, *172,* 72.
[15]. D. Maity, D.C. Agrawal, *Journal of Magnetism and Magnetic Materials,* **2007**, *308*, 46.
[16]. B.K. Szostko, U. Wykowska, D. Satula, P. Nordblad, *Beilstein Journal of Nanotechnology,* **2015**, *6*, 1385.
[17]. J.P. Sanders, P.K. Gallagher, *Journal of Thermal Analysis and Calorimetry,* **2003**, *72*, 777.

[18]. F. Fajaroh, H. Setyawan, A. Nur, I.W. Lenggoro, *Advanced Powder Technology*, **2013**, *24*, 507.

[19]. J. Murbe, A. Rechtenbach, J. Topfer, *Materials Chemistry and Physics,* **2008**, *110,* 426.

[20]. W. Kim, C.Y. Suh, S.W. Cho, K.M. Roh, H. Kwon, K. Song, I.J. Shon, *Talanta*, **2012**, *94,* 348.

[21]. A. Bandhu, S. Mukherjee, S. Acharya, S. Modak, S.K. Brahma, D. Das, P.K. Chakrabarti, *Solid State Communications,* **2009**, *149*, 1790.

[22]. M.C. Mascolo, Y. Pei, T.A. Ring, *Materials,* **2013**, *6(12),* 5549.

[23]. S. Ardizzone, L. Formaro, Mat. Chem.Phys., **1983**, *8*, 125.

[24]. S. Sarel, S. Avramovic, G. Risarn, E.R. Bauminger, I. Feiner, I. Nowik, R. Williams, N.P. Hughes, *Inorg. Chem.,* **1989**, *28*, 4187.

[25]. D. Hu, Y. Wang, Q. Song, *Particuology*, **2009**, *7*, 363.

[26]. Y. Mizukoshi, T. Shuto, N. Masahashi, S. Tanabe, *Ultrasonics Sonochemistry,* **2009**, *16*, 525.

[27]. M. Aslam, E.A. Schultz, T. Sun, T. Meade, V.P. Dravid, *Crystal Growth & Design*, **2007**, *7(3),* 471.

[28]. I. Nedkov, T. Merodiiska, L. Slavov, R.E. Vandenberghe, Y. Kusano, J. Takada, *Journal of Magnetism and Magnetic Materials,* **2006**, *300*, 358.

[29]. S. Qu, H. Yang, D. Ren, S. Kan, G. Zou, D. Li, M. Li, *Journal of Colloid and Interface Science,* **1999**, *215*, 190.

[30]. M. Ueda, S. Shimada, M. Inaga, *Journal of the European Ceramic Society,* **1996**, *16,* 685.

[31]. M.A. Legodi, D. Waal de, *Dyes and Pigments*, **2007**, *74*, 161.

[32]. S. Gialanella, F. Girardi, G. Ischia, I. Lonardelli, M. Mattarelli, M. Montagna, *Journal of Thermal Analysis and Calorimetry,* **2010**, *102(3),* 867.

[33]. V. Balek, J. Subrt, *Pure and Applied Chemistry,* **1995**, *67(11),* 1839.

[34]. M. Gotic, S. Music, S. Popovic, L. Sekovanic, *Croatica Chemica Acta,* **2008**, *81(4),* 569.

[35]. M. Zic, M. Ristic, S. Music, *Journal of Molecular Structure,* **2007**, *834-836,* 141.

[36]. O. Ozdemir, D.J. Dunlop, *Earth and Planetary Science Letters,* **2000**, *177,* 59.

[37]. Y. Wang, A. Muramatsu, T. Sugimoto, *Colloids and Surfaces A: Physicochemical and Engineering Aspects,* **1998**, *134(3),* 281.

[38]. A. Ercuta, M. Chirita, *Journal of Crystal Growth,* **2013**, *380,* 182.

[39]. ***, The Powder Diffraction File (PDF 4+) JCPDS – Joint Committee on Powder Diffraction Standards, ICC – International Center for Diffraction Data, **2012**.

[40]. J.P. Sanders, P.K. Gallagher, *Thermochimica Acta,* **2003**, *406*, 241.

[41]. R. Nayak, J.R. Rao, *Journal of Scientific and Industrial Research,* **2005**, *64*, 35.

[42]. S. Buathong, D. Ung, T.J. Daou, C. Ulhaq-Bouillet, G. Pourroy, D. Guillon, L. Ivanova, I. Bernhardt, S. Begin-Colin, B. Donnio, *The Journal of Physical Chemistry C,* **2009**, *113*, 12201.

[43]. Y.S. Li, J.S. Church, A.L. Woodhead, *Journal of Magnetism and Magnetic Materials,* **2012**, *324,* 1543.

[44]. J.A.R. Guivar, A.I. Martinez, A.O. Anaya, L. De Los Santos Valladares, L.L. Felix, A.B. Dominguez, *Advances in Nanoparticles,* **2014**, *3,* 114.

[45]. D. Maity, S.N. Kale, R. Kaul-Ghanekar, J-M. Xue, J. Ding, *Journal of Magnetism and Magnetic Materials,* **2009**, *321,* 2093.

[46]. T. Hosono, H. Takahashi, A. Fujita, R.J. Joseyphus, K. Tohji, B. Jeyadevan, *Journal of Magnetism and Magnetic Materials,* **2009**, *321,* 3019.

CHEMICAL-MINERALOGICAL CHARACTERISATION OF BELITES FROM EXPERIMENTAL SAB CLINKERS

EMILIA MOSONYI[a]*, JÓZSEF FAZAKAS[b,c], MARIA SPATARU[c], TIMEA HALMAGYI[c]

ABSTRACT. Guided by theoretical (sulphoaluminate belitic) SAB clinker chemical compositions, raw materials of known chemical composition (locally sourced from the Carpathian orocline), were mixed and tested by burning in laboratory conditions at different temperatures 1220, 1240 and 1260°C. The resulting materials were analyzed by optical transmission and reflection microscopy (using HF etching) and completed with XRD analyses. In this paper we describe chemical and mineralogical characterization of clinker belitic components manufactured in laboratory conditions. Belite nests and clusters with complex zoned structure are observed optically in interstitial material of the clinker that is composed of sulfoaluminate, ferrite and anhydrite. These structures display all three morphological types of belite, corresponding to the different polymorphs of belite, depending on the burning and quenching conditions of the clinker. The XRD patterns are interpreted to show that the appearance of β- and α'-belite and different α'→β transition forms are due to cooling to room temperatures and presence of the belite polymorph stabilizing ions SO_3, Al^{3+}, Fe^{3+} and alkali. The conclusions of the study were that belites were formed in various mixtures of raw materials treated at low burning temperatures, relatively slow cooling rates (resulting in different proportions of impurity absorption) and with some experiments run under reducing conditions during firing. Chemically, the lime saturation factor of clinkers is low (LSF= 0.74 - 0.84), such compositions favoring the clinker belite component; the silica ratio is low (SR < 1.5), which can improve the burnability of the clinker; the alumina ratio is medium (AR= 1.5 - 2.5), chemically restricting the solid solution of mineral phases, and the hydraulic modulus (HM) is under 1.7, enhancing resistance to chemical attack.

Keywords: SAB clinker, belite polymorphs, mineralogy, XRD

---

[a] *Babeş-Bolyai University, Faculty of Biology and Geology, Department of Geology, 1 Mihail Kogalniceanu str., RO-400082, Cluj-Napoca, Romania*
[b] *Babeş-Bolyai University, Faculty of Economical Sciences and Management, 58-60 Teodor Mihali str, Campus FSEGA, RO-400591, Cluj-Napoca, Romania*
[c] *C. VALDEK IMPEX SRL, str. 1 Decembrie 1918, Bl. 15, Sc. E, et. 3, ap. 9, Sfântu Gheorghe, Covasna, Romania*
* *Corresponding author: emilia.mosonyi@ubbcluj.ro*

EMILIA MOSONYI, JÓZSEF FAZAKAS, MARIA SPATARU, TIMEA HALMAGYI

INTRODUCTION

The subject of this study, the sulphoaluminate belitic clinkers, "the third cement series" [1] contain calcium sulphoaluminate, belite, ferrite and anhydrite as main mineral phases [2, 3, 4].

As a low energy type clinker, its recipe may comprise natural raw materials or natural materials mixed with industrial waste or mining dump materials which are sinterized at about 200°C lower than normal Portland cement [5, 6]. These types of clinkers are environmentally friendly due to lowering greenhouse gas (CO_2) emission by 20 - 30% compared with Portland cement clinker production [7].

Our purpose was to test by burning in laboratory conditions, at different temperatures (1220, 1240 and 1260°C) few raw mix recipes for theoretical (tentative) SAB clinker compositions. The recipes were counted by reverse Bogue method, using mainly local raw materials of known chemical compositions.

The components of our experimentally produced SAB clinkers comprise, beside limestone, clay, diatomite, volcanic tuff or basaltic scoria, red mud and gypsum. The latter component is a mineralizer [8], which stabilizes the reactive β-belite form in the clinker composition and lowers the sintering temperature (1200 - 1250°C).

The clinkers' main component, belite (theoretic formula C_2S), in the cement industry may present 5 polymorphs [9, 10]:

The transition temperatures for: α → α'$_H$ → α'$_L$ → β → γ, are 1425°C, 1160°C, 630- 680°C and <500°C respectively. The α polymorph is ditrigonal dipyramidal and optically is almost isotropic; α' is orthorhombic, having high refraction indexes (n_α= 1.719, n_γ = 1.732) β-belite is monoclinic and posses the highest hydraulic activity; the γ polymorph is orthorhombic, having n= 1.642 - 1.645 and splintery fracture. The γ-belite has the lowest density and hydraulic properties.

The α, α'$_H$, α'$_L$, β structures are parts of the same species family of glaserite ($K_3Na(SO_4)_2$) (Moore, 1973) [11], but the γ polymorph is similar to olivine $(Fe Mg)_2(SiO_4)$ [12, 13]. The α' and β polymorphs are generated from α structure form by progressive change of the lattice symmetry and density. The β → γ conversion implies a mechanical phenomenon, known as self-pulverization (dusting).

The higher temperature polymorphs on cooling to room temperature are stabilized by substituent ions. Such components could be Al^{3+}, Fe^{3+} and S^{6+} which can replaces via coupled substitution $2Al^{3+}+ S^{6+}$ for $3Si^{4+}$ [14] in the SiO_4^{4-} positions or Mg^{2+} replaces Ca^{2+} in the belite crystallochemical formula [15] or K, Na, P which can stabilize α'- polymorph [16].

In the case of the presence of fine grained belite (crystallites) the transformation to gamma form does not take place even if stabilizer ions are not present [17].

During α → β transitions, the lower-temperature polymorphs are less able to accommodate substitute ions and the exsolution of substituting ions progressively greater, filling the spaces between belite twin lamellae as different phases [18] or mechanical twinning results due to density transformations. Hence, the interpretations of belite composition data are only tentative mainly due to exsolution effects [19].

The positive correlation between SO_3 content of clinkers and belite component was outlined by Regourd et al. (1969) [20] who sinterized β-belites and studied their cell parameters and microstructures. The authors indicated that in higher temperature polymorphs there are more substitutions, but in the same time the XRD analyses evidenced lowering crystallinity and peak intensities of these belites.

Ono et al. (1969), Ono (1975) and Yamaguchi and Takagi (1969) [21-23] described the optical properties of belite from clinkers. From morphological point of view, the belite can be classified [24] as: type I, with rounded grains of 20 - 40 μm, possessing skeleton structure, consisting of α and β forms of belite (interpreted [22], having two twinning directions owing to the symmetry transformation during α→ α'$_H$ → α'$_L$ →β transitions, although this form is mainly monoclinic β-belite; type II represents grains with irregular forms and having only one parallel twin lamellae, owing to α'$_L$ → β transition; type III, formed at lower temperatures, is untwined, but can display exsolution spots.

RESULTS AND DISCUSSION

Taking into consideration the chemical compositions of the clinkers raw materials (see the experimental section) and a tentative theoretical clinker composition, using the Bogue counting's, a few SAB clinker recipes were selected for burning and selected cement parameters were counted. In CaO - Al_2O_3 - Fe_2O_3 - SiO_2 system, the Kühl modules [25-28]: Silica Ratio SR, Alumina Ratio AR, Lime Saturation Factor LSF, (modified [29, 30, 31], Hydraulic Modulus HM and belite sulphate content $S*_b$ [32] are shown in Table 1.

Chemically, the LSF of clinkers are relative low, hence it stabilizes the belite component, the SR is under 1.5, AR is medium and HM is under 1.7. Based on the raw materials mixing recipe (Table 2) the sinterized products were analysed.

Table 1. The tentative chemical compositions (wt%), main mineral phases (%) (Bogue countings) and Kühl chemical ratios of resulting clinkers (lime saturation factor LSF), silica ratio SR, alumina ratio AR, hydraulic modulus HM, SO_3 content (%) of belites S^*_b

sample	CaO	Fe_2O_3	SiO_2	Al_2O_3	SO_3	C_2S	$C_4A_3S^*$	C_4AF	CS^*	LSF	SR	AR	HM	S^*_b
2	54.13	3.94	18.84	9.03	14.06	54	13	12	21	0,84	1,45	2,29	1.71	17,6
3	55.15	7.23	19.53	10.63	7.46	56	12	22	10	0,87	1,07	1,47	1.54	9,5
8	51.38	7.56	15.00	18.86	7.20	43	28	23	6	0,76	0,67	2,49	1.56	9,1
11	53.11	4.93	17.44	12.17	12.36	50	18	15	17	0,74	1,02	2,47	1.24	15,5

Table 2. The composition of raw materials mixture (mixing recipe)

Sample	Raw materials mixture - %					
	Vârghiş Limestone	Oradea Red mud	Racoşul de Jos Basaltic scoria	Bodoc Clay	Racoşul de Sus Volcanic tuff	Nucşoara Gypsum
2	57.43	-	-	10.88	-	31.69
3	47.44	-	-	0.05	-	52,51
8	42.05	6.20	0.38	-	-	51.37
11	46.55	-	-		10.57	42.88

The thin section images of clinkers revealed calcium silicate particles (mainly belite C_2S) from few tens of micrometers up to 200-250 micrometers and dominantly olive- greenish to brownish interstitial material composed of sulphoaluminate, ferrite, anhydrite, amorphous glass material and circular to elliptical pores filled with alkali sulphates. The silicate particles are mainly belitic and they form nests and clusters of complex frequently zoned microstructure. In these structures, all three morphological belite types are developed with or without one or two directions of twin lamellae, presenting overgrowth zones or lamellar sometimes finger-like prolongations (ragged belite) or rough surfaces owing to the matrix corrosion effects. Not rare are situations in which belite rings developed around interstitial central pores. The belite grains present mainly rounded or irregular forms containing exsolutions or mechanical twin lamellae, sometimes spherulitic structures, the latter due to α'→β conversion [22]. The belite colors are pale yellow up to amber, the birefringence colors are first order yellow to orange (Δ= 0.017 - 0.018). The chemical compositions of belites could be only tentative, owing to many exsolution structures. The SO_3 content of belite is relatively high (Table 1, S*b= 9 - 18%) and was calculated in relation to the clinker SO_3 content. The S^{6+} enters the tetrahedral position replacing the Si^{4+} ions in the belite structure and stabilizes it at high temperature. Other stabilizing ions are Fe^{3+} and Al^{3+}, resulting the greenish yellow or pale yellow up to amber belite color.

The centre of nest structures may contain prismatic alite (C_3S) or periclase (M) relics. The belite has mainly rounded shapes, sometimes rough surfaces due to the matrix corrosion (reducing burning conditions) or finger- like overgrowths (ragged belite, owing to the slow cooling conditions). In other cases belite presents dot-like exsolutions. Some microscopic images and interpretations of belite properties are presented in Figures 1- 7.
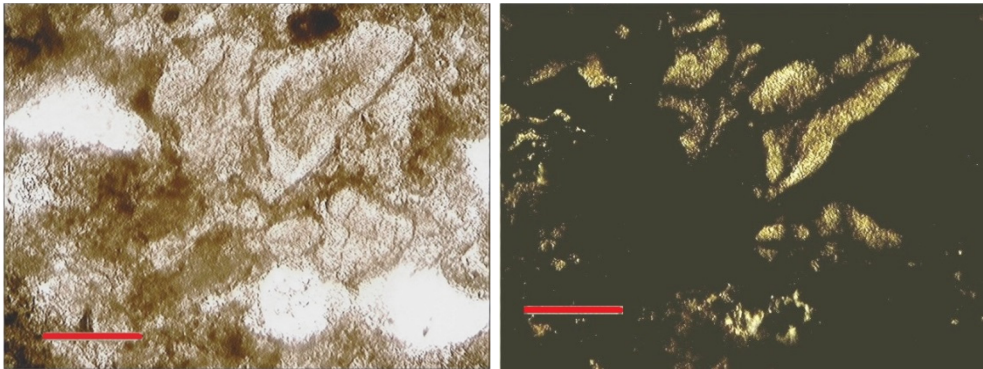
Figure 1. **a** (1N), **b**(N+). Sample 2 - raw mixture sinterized at 1220 °C: zoned belite spherulites (core zone brownish colored, overgrown by a light gray belitic ring with dot-like exsolutions- top center), corroded by matrix material. All these interpreted as formed under slow cooling conditions. Scale bar 50µm
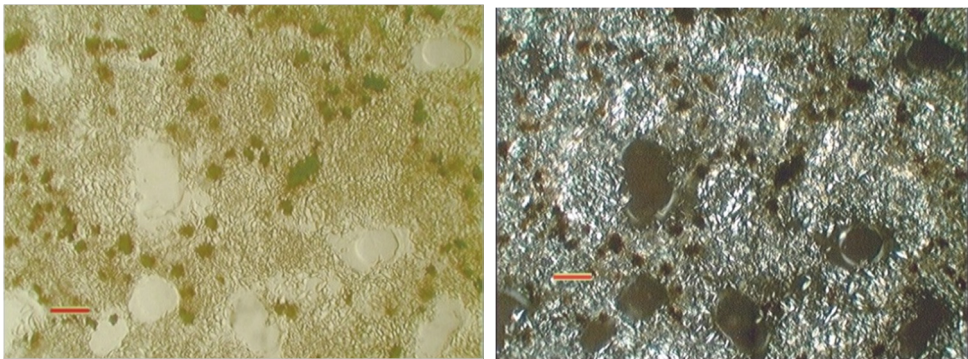
Figure 2. a (1N), b (N+). Sample 2A**,** burned at 1240 °C: pores filled with alkali sulphates (colorless, low relief), belite II (yellowish - white birefringence color and twin lamellae in one direction) chains and rings around pores; in the centre there is an alitic nest with belitic corona corroded by ferrite. Scale 50 µm
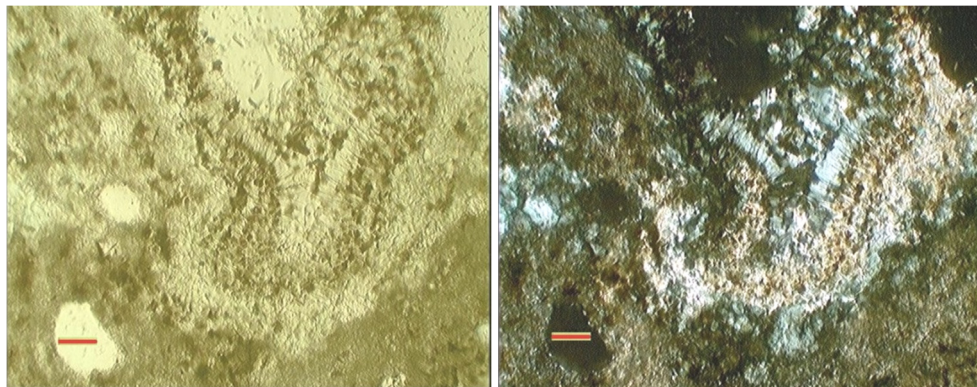
Figure 3. a (1N), **b** (N+) Sample 3, burned at 1220 °C: around the pore (top centre) was developed a ring with zonal structure: in the core - a radial lath - like alite ring overgrew by belite III with iron exsolutions and covered by belit I, the later being corroded by matrix phases (rough surface, due to reducing burning conditions). Scale bar 50 μm
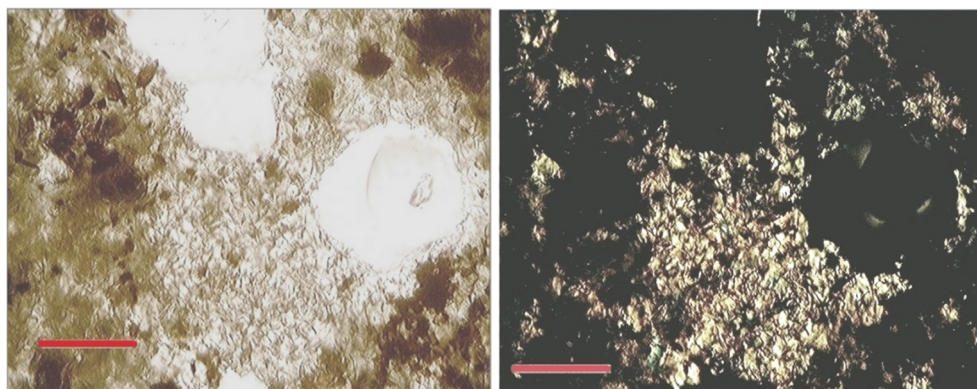
Figure 4. a(1N), **b** (N+). Sample 8A, burned at **1240** °**C**. External part of sample: around pores were crystallised alite and belite rings. In the centre of images is a complex belite cluster containing from core to rim: belite III with exsolution dots, belite I, belite II. The cluster has belite II satellite overgrowth and can contain alite prism relics (bottom of image). Scale 50μm
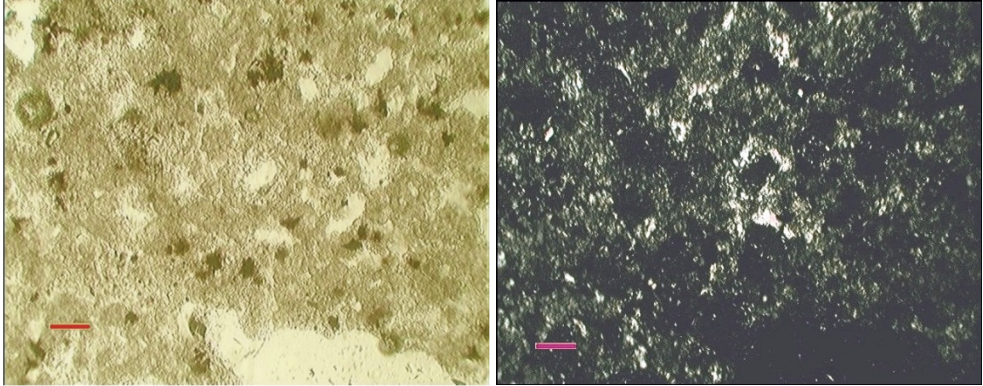
Figure 5. a (1N), b (N+). Sample 11A, burned at 1240°C: slightly differentiated interstitial material consists of yellowish green sulphoaluminate and ferrite; in the image centre there is a little pore with belite I ring overgrew by a belite II. Low cooling rate. Scale 50 µm
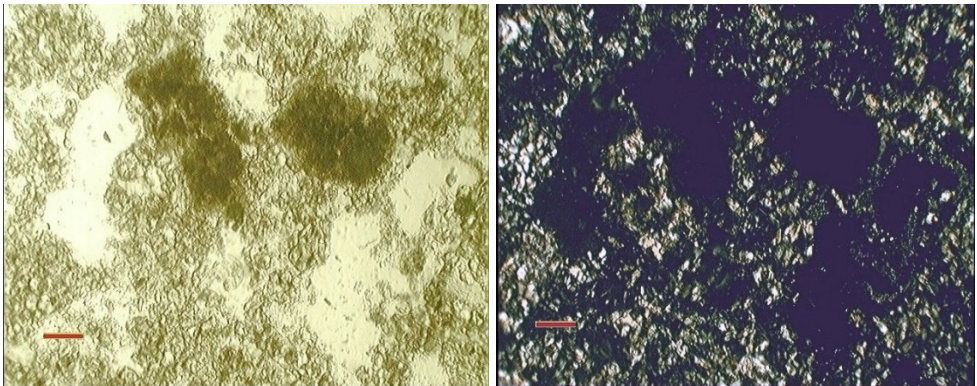
Figure 6. a (1N), **b** (N+). Sample 11B, fired at 1260°C: two drops of brownish olive interstitial material (isotropic sulphoaluminate in N+) between alitic (bottom left: polygonal grains) nests, belite I and belite III spherulites with rare alitic relics (dark grey birefringence). Scale bar 50 µm

The belite could be also evidenced in reflected plane polarized light on clinker surface etched with HF (method in [33]).The belite appears as bluish colored, mainly rounded grains, sometimes corroded by matrix phases, alite is brownish, the ferrite is white, other interstitial phases are grey, or not etched. (Figure 7).
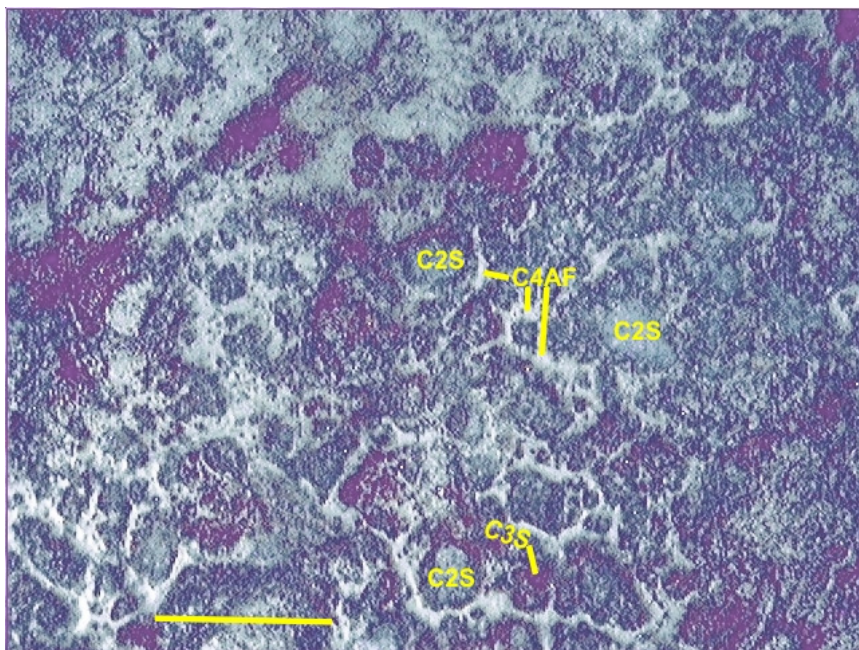
Figure 7. HF etched surface of sample 8, burned at 1220°C (in reflected plane polarised light). The belite I (C_2S) grains are rounded, bluish colored, frequently corroded by interstitial material, alite (C_3S) - brownish colored. The white colored phase = brownmillerite (C_4AF). Scale bar =50 µm

The interpretations of XRD pattern of all samples revealed the presence of main phases from SAB clinkers: belite (C_2S = B), sulphoaluminate ($C_4A_6S^*$= Sa), ferrite (brownmillerite C_4AF = Bw) and anhydrite (CS^* = Ah) (**Figures 8, 9**) beside low quantities of: alite (C_3S), ettringite ($C_6AS^*_3H_{32}$), gehlenite (C_2AS), limeite (C), periclase (M), Na- alunite ($N_{0.5}K_{0.42}A_3S^*H_{16}$), Na-sulphate ($N_2S^*$) etc.

The polymorphic structure of studied belites could be evidenced in the XRD pattern detail (2θ= 30- 35°) from Figure 9. The β-belite- is the most important polymorph and it is developed in all presented samples (2θ= 30.95°, 31.83°, 32.07°, 32.18°, 32.67°, 32.80°, 33.85°, 34.20°). The α'-belite peaks were revealed in samples 2A, 3, 8A, 11A (2θ= 30.6°, 31.2°, 31.8, 31.95°, 32.20°, 32.90°). The best fitting belite standard, for example sample 3 (Figure 10) has orthorhombic symmetry which reveals α'-polymorph.
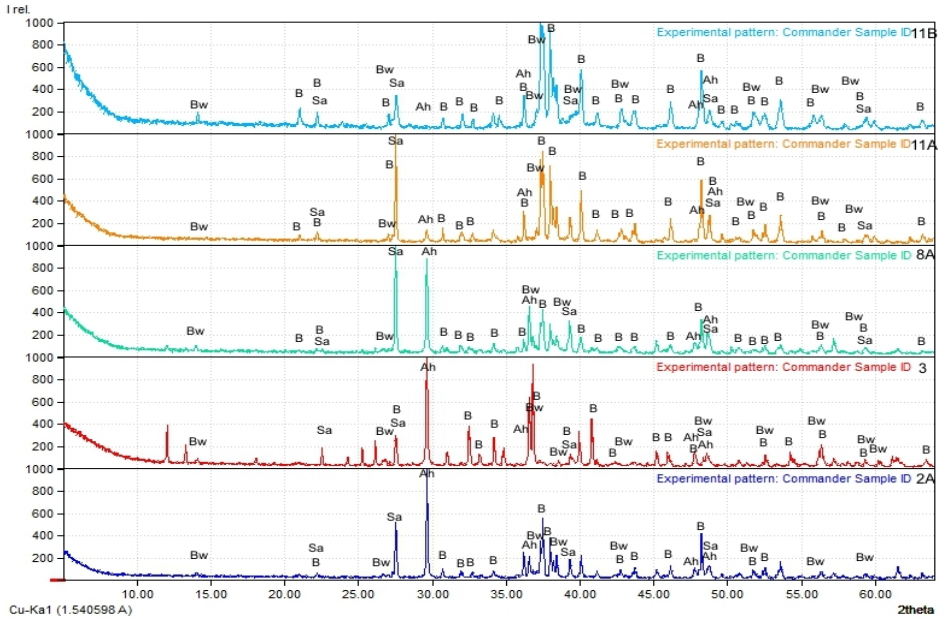
Figure 8. XRD pattern of few selected clinker samples (2A, 3, 8A, 11A, 11B). The sample 3 was fired at 1220°C, samples: 2A, 8A, 11A – at 1240°C and sample 11B - at 1260°C. (Reflections were recalculated for Cu-Kα1 for comparison with pdf2 database). C_2S = B = belite; CS^* = Ah = anhydrite; $C_4A_6S^*$ = Sa = sulphoaluminate; C_4AF = Bw = brownmillerite.
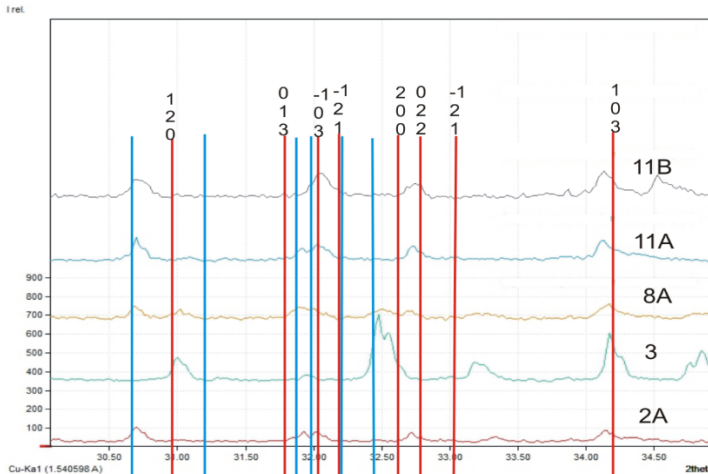
Figure 9. Detail of XRD patterns (2θ = 30 - 35° and reflections were recalculated for Cu-Kα1 for comparison with belite database) of samples 2A, 3, 8A, 11A, 11B. The reflexions of α'-belite and β- belite were marked with different colors. The Miller indexes of β-belite crystallographic faces are indicated.
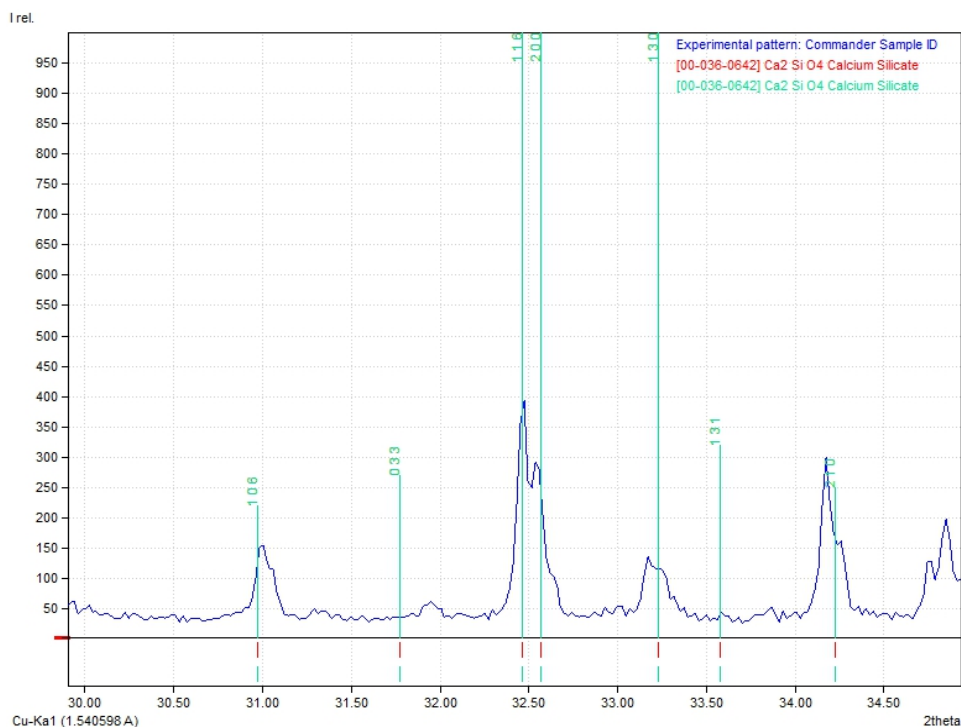
Figure 10. XRD pattern of sample 3 in range 2θ = 30 - 35°. Are also marked the crystallographic Miller indexes. The best fitting belite standard has orthorhombic symmetry (α'- polymorph).

CONCLUSIONS

The optical features of belite presented here mirror the raw mix chemical compositions, relative low burning temperatures, slow cooling rate, differences in absorption of impurities, sometimes reduction conditions during firing. Taking into consideration the correlation between optical properties of clinker belites, firing conditions and hydraulicity of resulted cement, established by Ono and Campbell *[34, 35]*, we can say, that: observed yellowish brown pleochroism of belite grains means slow cooling rate and low hydraulic properties, but sometimes the greenish yellow color indicates a clinker hydraulicity of medium quality. The measured belite birefringence of 0.017 - 0.018 could be interpreted as low hydraulicity of clinkers, low burning grade and very low or missing reactive α- belite content. Microstructures such as ragged belite or corroded rough grain shapes reveal low hydraulic activity and reducing burning conditions.

The details of XRD pattern of the studied clinkers indicate the presence in all samples of β-polymorph reflections and different structural transformations or stabilization forms of α'-belite quenched to room temperature.

The established chemical and mineralogical features of belites could help to improve the clinker raw mixture recipe and sintering conditions. By increasing the quenching rate or by using different belite stabilizing components could induce a greater proportion of reactive belite and interstitial amorphous material, which all lead to the better hydraulic activity of cement.

EXPERIMENTAL SECTION

The raw materials used for the present SAB clinkers experiment are natural (Vârghiș limestone, Bodoc clay, Nucsoara gypsum, Racosul de Jos basaltic scoria, Racosul de Sus volcanic tuff, Filia diatomite) and industrial waste (Oradea red mud), the later resulted in the bauxite ore processing by Bayer method at "Alumina" factory from Oradea. The selected raw material compositions previously were chemically and optically (under polarizing microscope) studied. The chemical compositions of raw materials were analysed by SEM-EDX, or by wet chemical method. (Table 3).

Table 3. Chemical compositions of clinker raw materials, wt%

oxides	Vârghiș Limestone (SEM-EDX)	Bodoc Clay (wet chem)	Oradea Red mud (SEM-EDX)	Racoșul de Jos Basaltic scoria (SEM-EDX)	Racoșul de Sus Volcanic tuff (wet chem)	Filia Diatomite (SEM-EDX)	Nucșoara Gypsum (wet chem)
CaO	89.61	1.66	12.71	10.38	2.88	0.71	28.31
SiO_2	4.01	67.97	8.93	46.10	64.53	92.52	9.83
Al_2O_3	5.16	15.41	17.04	18.78	11.80	3.24	2.73
Fe_2O_3	-	4.88	48.37	9.93	2.57	2.18	1.07
Na_2O	-	1.54	3.68	3.23	1.89	-	0.15
K_2O	-	2.43	-	1.69	2.75	0.46	0.55
MgO	-	1.59	1.30	7.21	0.45	-	0.39
TiO_2	-	0.81	6.80	1.61	0.27	-	0.13
V_2O_5	-	-	0.19	-	-	-	0.04
P_2O_5	1.22	-	0.98	1.07	-	-	0.04
SO_3	-	-	-	-	-	0.89	37.08
Mn_2O_3	-	0.13	-	-	-	-	0.02
L.O.I.	-	3.58	-	-	12.40	-	19.90
Total	100	100	100	100	100	100	100

The raw materials were dried in owen then grinded for two hours in the porcelain mill with balls. The raw materials mixed as in recipes from **Table 2** were homogenized for one hour in the porcelain mill. From the raw mix materials cube - like briquettes of 25x25x25 mm sizes were made, then burned in a laboratory electrical kiln until a constant peak temperature of 1220°C, 1240°C (samples ID marked as „A") and 1260 °C (samples ID marked as „B" in **Figure 8**) for one hour.

For the present chemical-mineralogical study were selected five samples of clinkers, burned at 1220°C (sample 3), 1240°C (Samples 2A, 8A, 11A) and 1260°C (sample 11B) and were studied in dry-prepared *[33]* thin and thick sections under optical transmission and reflexion polarising microscope (using also HF etching). Were took microphotos in plane polarised light (1N) and in cross polarised light (N+)

The crystallised mineral phases from clinkers were also investigated by XRD analyses at the University Babeş- Bolyai using a Bruker D8 Advance diffractometer with Bragg-Brentano geometry, CoKα1 with λ = 1.78897, Fe filter and a one-dimensional detector. Corundum (NIST SRM1976a) was the internal standard. The data were collected on a 2θ = 5 - 64o interval, at a 0.02°, with the measuring step of 0.2 seconds. The identification of the mineral phases was performed with the Match 3.1 software, using the PDF2 (2012) database.

ACKNOWLEDGMENTS

R E F E R E N C E S

[1] L. Zhang, M. Su & Y. Wang, *Advances in Cement Research*, **1999**, *1*, 15-21.

[2] K. Quillin, *Cement Concrete Resources,* **2001**, *31,* 1341.

[3] M. Palou, J. Majling and I. Janotka, *Proceedings of the 11th International Congress on the Chemistry of Cement* (ICCC) Durban, South Africa, **2003**, 1896.

[4] A. Alaoui, A. Feraille, A. Steckmeyer & R. Le Roy, *Proceedings of the 12th International Congress on the Chemistry of Cement* (ICCC), Montreal, Canada paper 258 (W3-11.3) **2007**, 1-8.

[5] İ. Soner, "Utilization of Fluidized Bed Combustion Ashes as Raw Material in the Production of a Special Cement"; In partial fulfilment of the requirements for the degree of Master of Science in Chemical Engineering, Middle East Technical University, Haziran, Turcia, June **2009**.

[6] I.A. Chen & M.C.G. Juenger, *Journal of Material Science,* **2009**, *44*, 2617.

[7] G.S. Li, G. Walenta & E. Gartner, *Proceedings of the 12th International Congress of the Chemistry of Cement* (ICCC), Montreal, CA, paper 398 (TH3-15.3), **2007**,1-12.

[8] G.K. Moir and F.P. Glasser, *Proceedings of the 9th International Congress on the Chemistry of Cement* (ICCC), New Delhi, India, **1992**, 125-152.

[9] P. Barnes, C.H. Fentiman & J.W. Jeffery, *Acta Crystallographica,* **1977**, *A36*, 353.

[10] S.A. Guinier and M. Regourd, *5th International Symposium on Cement and Concrete*, **1969**, Vol. 1, p. 1.

[11] P.B. Moore, *American Mineralogist,* **1973***, 58*, 32.

[12] S. Udagawa, K. Urabe, M. Natsume, and T. Yano, *Cement and Concrete Research,* **1980**, *10*, 139.

[13] W.G. Mumme, R.J. Hill, G. Bushnell-Wye and E.R. Segnit, *Neues Jahrbuch für Mineralogie,* **1995**, *169*, 35.

[14] L. Bonafous, C. Bessada, D. Massiot, J.-P. Coutures, B. Le Rolland, & P. Colombet, *Journal of the American Ceramic Society,* **1995**, *78*, 2603.

[15] Y.J. Kim, I. Nettleship and W.M. Kriven, *Journal of the American Ceramic Society*, **1992**, *75*, 2407.

[16] D.H. Campbell, "Microscopical Examination and Interpretation of Portland Cement and Clinker". Edited by: Natalie C. Holz, Portland Cement Association, Published by: Portland Cement Association USA, **1999**.

[17] N. Yannaquis and A. Guinier, *Bulletin de la Société Française de Minéralogie et de Crystallographie*, **1959**, *82*, 126.

[18] C.J. Chan, W.M. Kriven, and J.F. Young, *Journal of the American Ceramic Society,* **1988**, *71*, 713.

[19] T. Taylor, "Cement chemistry", second edition, Thomas Telford Publishing, **1997**, London.

[20] M. Regourd, M. Bigare, J. Forest and A. Guinier, in *5th International Symposium on Cement and Concrete*, **1969**, Vol. 1, p. 44.

[21] Y. Ono, S. Kawamura and Y. Soda, in *5th International Symposium on Cement and Concrete*, **1969**, Vol. 1, p. 275.

[22] Y. Ono, "Microscopic Analysis of Clinker," Onoda Cement Co., Central Research Laboratory, 1973/12/15 and 1975/6/22. Paper supplied to students at Hawaiian seminar, **1975**.

[23] G. Yamaguchi and S. Takagi, in *5th International Symposium on Cement and Concrete*, **1969**, Vol. 1, p. 181.

[24] H. Insley, "Structural Characteristics of Some Constituents of Portland Cement Clinker," *Journal of Research of the National Bureau of Standards*, Vol. 17, Research Paper RP917, Washington, D.C., September **1936**, pp. 353-361.

[25] H. Kühl, „Der Kalkstandard der Portlandzemente". Tonindustrie-Zeitung, **1933**, 57, Heft 40, S. 460-464.

[26] H. Kühl, „Hydraulischer modul und Hydraulefaktoren- Verhältnis im Portland-zement". Protokoll des VDPCF, **1913**, S. 399-408.

[27] H. Kühl, „Der junge Zementchemiker"*, Zement* **1926**, 15, Heft 36. S. 636/639,

[28] H. Kühl, Der Kalksättigungsgrad, *Zement,* **1931**, 20, Heft 6, S. 123-125.

[29] S. Nasir and H. El Etr, *Qatar University Science Journal*, **1996**, *16(2)*, 315.

[30] M.S. Idris, K.N. Ismail, S.B. Jamaludin, C.R., Ghazali and K. Hussin, *American Journal of Applied Sciences*, **2007**, *4(5),* 328.
[31] N.H. Deborah & D.E. Thomas, *Journal of Cleaner Production*, **2009**, *17*, 668.
[32] C. Hall and K.L. Scrivener. *Journal of Advanced Cement-Based Materials*, **1998**, *7(1)*, 28.
[33] J. Ingham, „Geomaterials under the microscope, a colour guide, building stone, roofing slate, aggregate, concrete, mortar, plaster, bricks, ceramics and bituminous mixtures, in transmitted polarised light, under Jenapol petrographic microscope and by XRD method". Manson Publishing, **2013**.
[34] Y. Ono, *Proceedings of the Third International Conference on Cement Microscopy*, International Cement Microscopy Association, Houston, Texas, **1981**, pp. 198-210.
[35] D.H. Campbell, "Microscopical Examination and Interpretation of Portland Cement and Clinker". Edited by: Natalie C. Holz, Portland Cement Association, Published by: Portland Cement Association USA, **1999**.

BEHAVIOUR OF TWELVE SPHERICAL CODES IN CW EPR POWDER SIMULATIONS. UNIFORMITY AND EPR PROPERTIES

CORA CRĂCIUN[a*]

ABSTRACT. This paper assesses the efficiency of twelve spherical codes in CW EPR powder simulations. The spherical codes are either regular or are generated using optimisation methods. The EPR simulations are performed for spin systems with axial and rhombic symmetry. The spherical codes are compared using Voronoi tessellation-based homogeneity and EPR properties.

Keywords: CW EPR powder simulations, spherical code, uniformity degree, EPR metrics

INTRODUCTION

Continuous-wave electron paramagnetic resonance (CW EPR) powder simulations use spherical sets of points to approximate numerically the EPR spectrum. The quality of the EPR simulations depends both on the spherical codes' properties (size, uniformity degree) and the EPR characteristics of the spin system investigated (spin state, symmetry).

Previous assessments of the spherical codes for magnetic resonance simulations were based on the codes' homogeneity [1], the convergence rate of the simulations [2,3], and on EPR metrics [4]. The EPR metrics defined in [4] and some of the homogeneity metrics [4,5] depend on the spherical codes' Voronoi tessellation generated on the unit sphere.

This paper assesses the behaviour in CW EPR powder simulations and computes some homogeneity and EPR properties for the following spherical codes (the grids' abbreviations used in the paper are given in parentheses): Concentric map (CM) [6,7], HEALPix (HPX) [8,9], Cubed-sphere (CS) [10-13], Minimum Energy (ME) [14-16], Maximum Determinant (MD) [14,15,17], Symmetric Spherical grid (SS) [14,15,18], Icosahedral - covering arrangement (icover) [19],

---

[a] *Babeş-Bolyai University, Faculty of Physics, 1 Kogălniceanu str., RO-400084 Cluj-Napoca, Romania*
* Corresponding author: cora.craciun@phys.ubbcluj.ro

Icosahedral - packing arrangement (ipack) [19], Icosahedral - maximal volume arrangement (ivol) [19], Hammersley (Ham) [20-24], Repulsion (Rep) [3,25], and Spherical Centroidal Voronoi Tessellation (SCVT) spherical code [26-29].
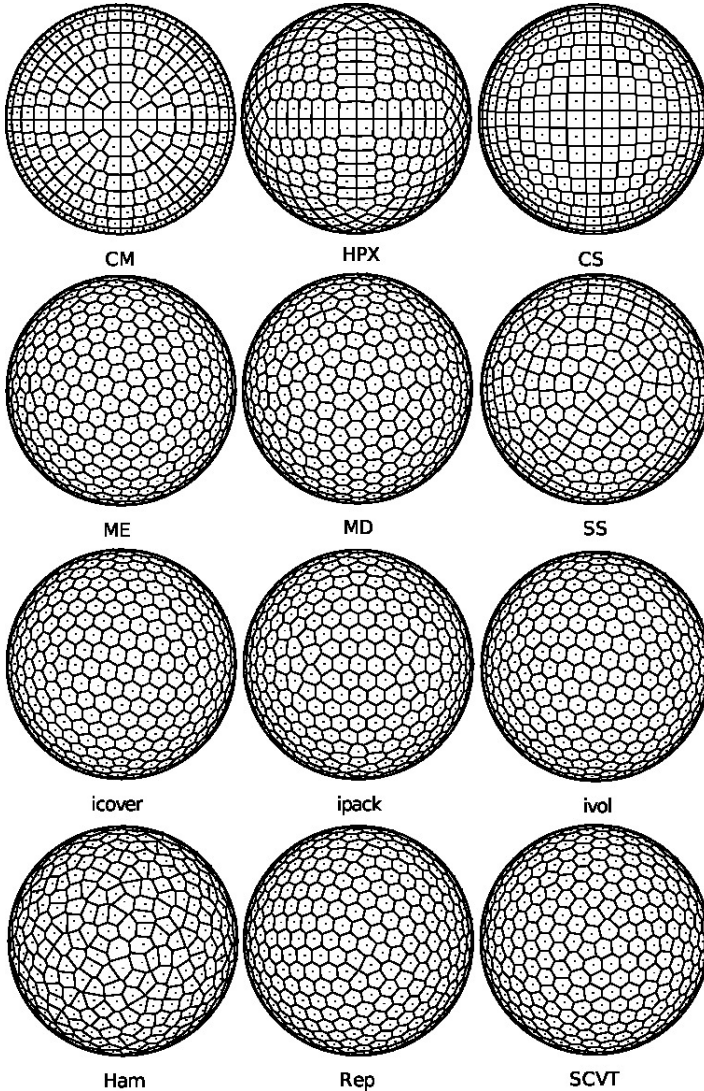
Figure 1. The upper hemisphere and the Voronoi tessellation of the following spherical codes (the full sphere number of points is given in parentheses): CM (580), HPX (588), CS (602), ME (576), MD (576), SS (564), icover (572), ipack (582), ivol (572), Ham (578), Rep (578), and SCVT (578).

(a) *Concentric map* (CM) has been proposed for ray tracing applications in computer graphics, in order to maintain the adjacency and relative proportions when mapping patches from one surface to another [6,7]. First, CM maps square grids on disks, by transforming concentric squares of points into concentric circles of points [7]. Then, the points on the disk are uniformly projected onto the upper hemisphere [7]. The points on the lower hemisphere are obtained by mirror symmetry with respect to the xOy plane.

(b) *HEALPix* (Hierarchical Equal Area isoLatitude Pixelization) was developed for astronomy applications involving fast processing of functions, such as spherical harmonic transforms, on spherical regions [8,9]. The HEALPix tessellation partitions the sphere in quadrilateral regions of equal areas, called pixels. The pixel centres (the grid nodes) are equally spaced on curves of constant latitude [8].

(c) The original *Cubed-sphere* grid was introduced by Sadourny, in order to avoid the pole problems in the context of atmospheric motion numerical modelling [10]. The grid is obtained by projecting the six faces of a cube onto the circumscribed sphere. Different projection methods have been proposed, including the gnomonic [11] and conformal [12] mappings. This paper uses the gnomonic equiangular central projection, which yields a non-orthogonal cubed-sphere grid with higher uniformity than other projections [13].

(d-f) The *Minimum Energy*, *Maximum Determinant*, and *Symmetric Spherical* grids were computed by R. S. Womersley and I. H. Sloan for numerical integration on the sphere [14-18]. The Minimum Energy points were obtained by minimizing their Coulomb-type potential energy [14-16]. The Maximum Determinant (Extremal) points were computed by maximizing the determinant of an interpolation matrix, in the space of spherical polynomials [14,15,17]. The Symmetric (antipodal) Spherical code belongs to the category of spherical t-designs, having equal cubature weights for all points [14,15,18].

(g-i) The *Icosahedral* arrangements of points were computed by R. H. Hardin, N. J. A. Sloane, and W. D. Smith [19]. The covering arrangement was obtained by minimizing the covering radius, that is the maximal distance from any point on the sphere to the closest grid point [19]. The packing arrangement was generated by maximizing the minimal distance between the grid points [19]. At its turn, the maximal volume arrangement was computed by maximizing the volume of the points' convex hull [19].

(j) The *Hammersley* spherical code, introduced in [20], is a deterministic low-discrepancy finite point set, based on radical inversion [21]. This point set has proved useful for quasi-Monte Carlo integration [21] and has been used, for example, in various applications in computer graphics [22]. The Hammersley point set on the unit sphere is obtained by projecting a two-dimensional Hammersley set, using a mapping such as Lambert cylindrical equal-area projection [22,23].

(k)   The *Repulsion* spherical code has been proposed for Nuclear Magnetic Resonance powder simulations [3,25]. This spherical code is generated iteratively by adjusting the positions of a set of equal electrical charges on the unit sphere. The charges repel each other by Coulomb forces and perform small movements on the sphere until the system reaches equilibrium [25]. At equilibrium, the potential energy of the charge system is minimal.

(l)   The *SCVT* grid belongs to the category of energy minimization spherical codes and uses the unit sphere Voronoi tessellation [26-29]. The grid is generated iteratively, the points' positions being adjusted until they coincide with the mass centres (centroids) of their corresponding Voronoi cells [26-29].

The original grids use different tessellations to partition the unit sphere in patches or cells. This paper uses the Voronoi tessellation for all spherical codes, in order to compute the weight corresponding to each grid point in EPR simulations. The Voronoi tessellations of the twelve spherical codes with about 580 points are presented in Figure 1.

RESULTS AND DISCUSSION

1. CW EPR powder simulations

CW EPR powder spectra of the twelve spherical codes have been simulated as described in [4], for a spin system $S = 1/2$ characterised by electron Zeeman interaction with the static magnetic field. Two different symmetries of the gyromagnetic matrix **g** have been considered: one axial (C3), with the principal values ($g_x = 2.0$, $g_y = 2.0$, $g_z = 2.2$), and one rhombic (C4), with ($g_x = 2.0$, $g_y = 2.1$, $g_z = 2.2$). The two g-cases were denoted as in reference [4], to ease comparison with the results presented there. Pure axial spin systems do not require a spherical code, a quarter of a spherical meridian being sufficient for powder simulations [30]. Nevertheless, the axial case is considered here as an extreme case for nearly axial spin systems. EPR simulations have also been performed for the EasySpin grid [1] with a very high number of points. These simulations illustrate how the experimental spectra would look like for the spin system and symmetries considered in this paper. Based on the EPR simulations (Figures 2 and 3), we make the following observations:

(a)   In the *axial case* (C3), the Ham, Rep, ME, MD, ipack, and SCVT spherical codes generate simulated spectra with lower simulation noise than the other spherical codes. However, they do not behave better, for instance, than the Fibonacci grid presented in [4], which yields a nearly noise-free simulated spectrum in the (C3) g-case.
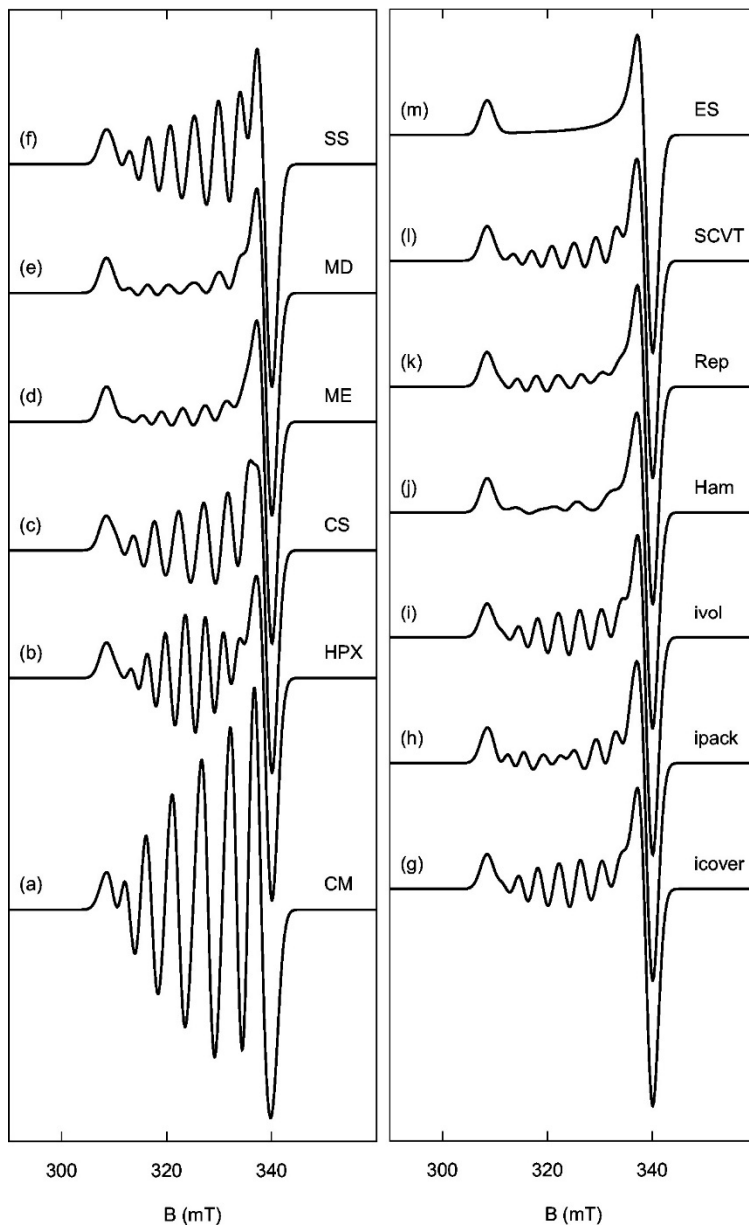
Figure 2. Simulated CW EPR powder spectra for (a-l) the twelve spherical codes with about 580 points and (m) the EasySpin spherical code with 9606 points, in the axial (C3) g-case.
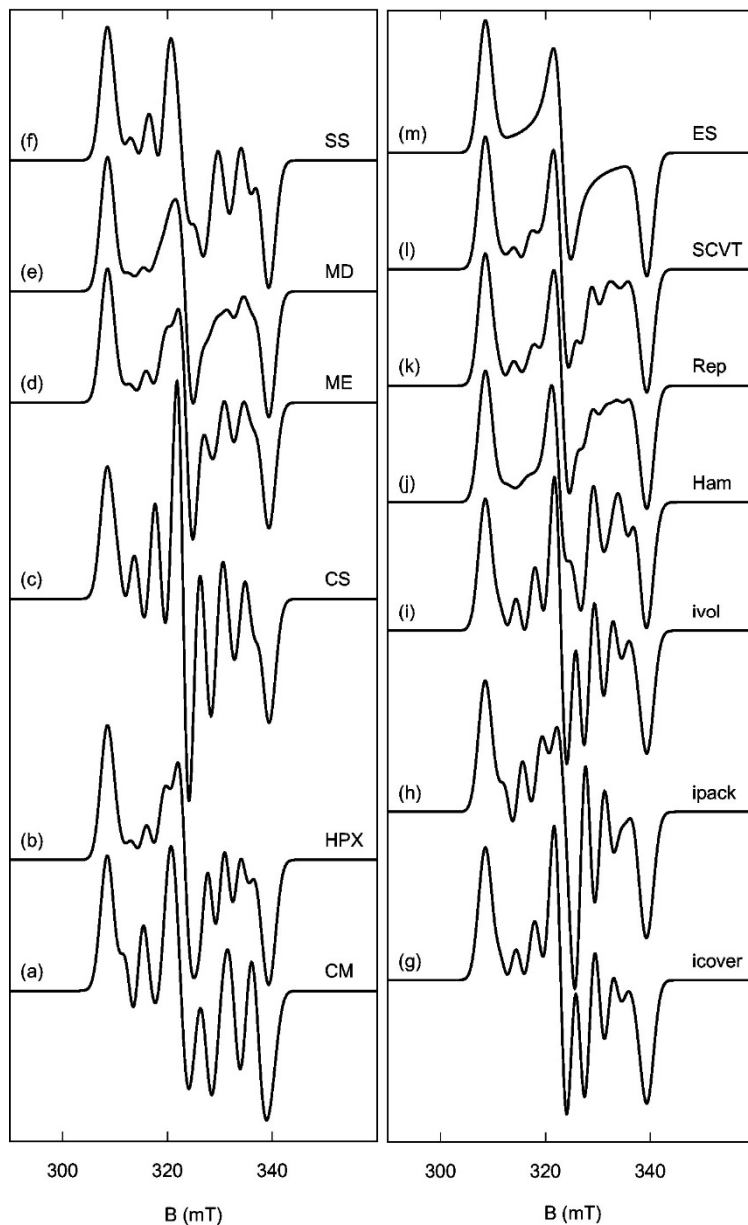
Figure 3. Simulated CW EPR powder spectra for (a-l) the twelve spherical codes with about 580 points and (m) the EasySpin spherical code with 9606 points, in the rhombic (C4) g-case.

(b) In the *rhombic case* (C4), the MD, Rep, and SCVT spherical codes generate less noisy simulated EPR spectra then the other spherical codes. The spectra of these grids have similar quality with the Fibonacci grid's spectrum, but are noisier than the EasySpin grid's spectrum from [4].

2. Homogeneity properties

By Voronoi tessellation, each spherical code generates a structure of Voronoi cells on the unit sphere (Figure 1). If we take the mean distance, $h_{mean}(k)$, between any grid point P_k (k = 1,...,N) and the vertices of its Voronoi cell V_k, we obtain a measure of the grid's homogeneity [4,5].

Figure 4 presents the h_{mean} distributions (the $h_{mean}(k)$ values for all grid points) for the twelve spherical codes discussed in this paper. The icover, ME, and Rep grids, followed by ivol, SCVT, and MD, have the h_{mean} distributions with the smallest spread between the lower and upper whiskers of the boxplot representations. This means that most Voronoi cells of each of these spherical codes are geometrically similar.

3. EPR properties

The two EPR metrics defined in [4] have been calculated for the spherical codes discussed here. The first metric, $B_{dev}(k)$, is the deviation of the resonance magnetic field at the grid point P_k from the mean magnetic field of the corresponding Voronoi cell V_k [4]. The mean field of the Voronoi region is calculated by averaging the resonance magnetic fields at a set of randomly generated points inside this region. The second EPR metric, $B_{ov,max}(k)$, is the maximum overlapping degree between the resonance magnetic field intervals of the Voronoi cell V_k and its adjacent Voronoi cells [4]. This metric quantifies how much the EPR signals generated by adjacent Voronoi regions are overlapping.

The B_{dev} distributions of the grids are presented in Figure 5, for the (C3) and (C4) g-cases. In each case, most spherical codes have similar spread of data, excepting Ham and ipack with the highest range distributions. Compared to the previously investigated EasySpin grid [4], all twelve spherical codes have wider B_{dev} distributions and thus are less EPR homogeneous.

Unlike the B_{dev} metric, $B_{ov,max}$ (Figure 6, Table 1) differentiates better the grids in the axial (C3) g-case. In this case, the CM spherical code presents the highest maximum overlapping degree and behaves as the previously investigated Rectangular grid [4]. In the rhombic (C4) g-case, the twelve spherical codes behave similarly.
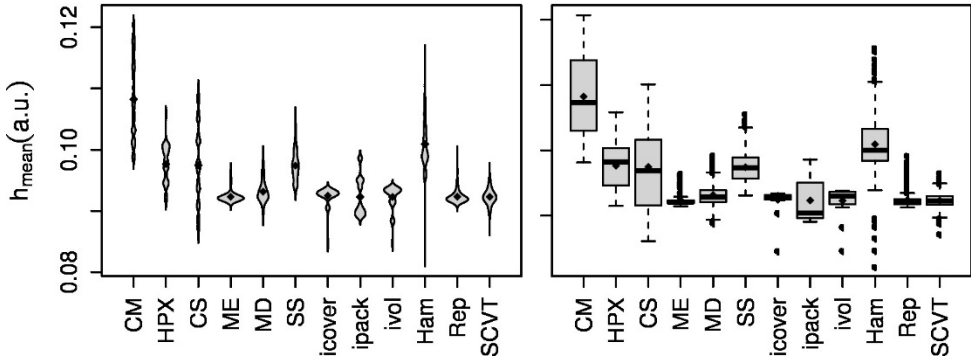
Figure 4. The h$_{mean}$ distributions for the spherical codes with about 580 points, in beanplot (left) and boxplot (right) representation. In the boxplots, the boxes cover the interquartile range and the whiskers extend to the most extreme data point, but not further than 1.5 times the interquartile range [34]. The full knots inside the beans and boxes are the data's mean values and the horizontal lines inside the boxes are the data's median values.
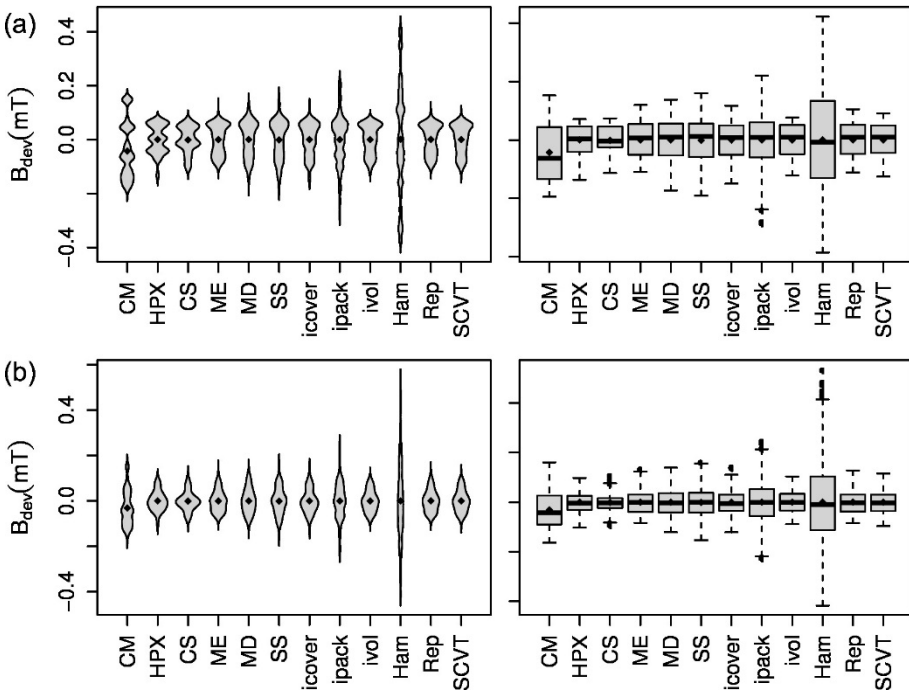
Figure 5. The B$_{dev}$ distributions for the spherical codes with about 580 points, in beanplot (left) and boxplot (right) representation: (a) (C3) g-case, (b) (C4) g-case.
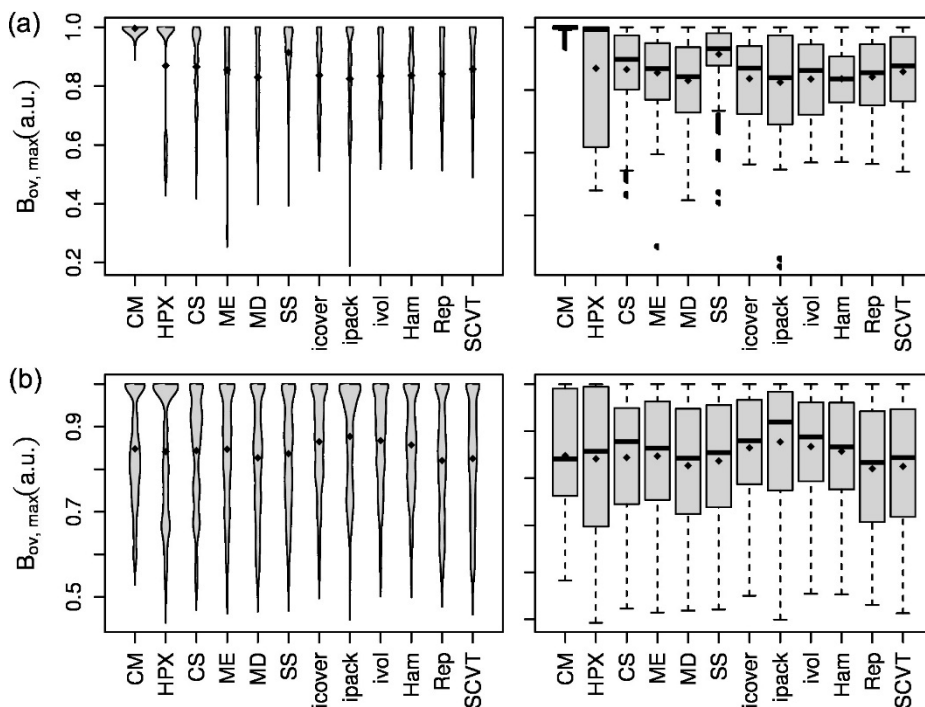
Figure 6. The $B_{ov,max}$ distributions for the spherical codes with about 580 points, in beanplot (left) and boxplot (right) representation: (a) (C3) g-case, (b) (C4) g-case.

Table 1. The mean and median values[1] of the $B_{ov,max}$ distributions, in the axial (C3) and rhombic (C4) g-cases

Grid	(C3)	(C4)
CM	0.996 (1.000)	0.848 (0.840)
HPX	0.869 (0.994)	0.841 (0.855)
CS	0.866 (0.898)	0.844 (0.877)
ME	0.855 (0.869)	0.847 (0.864)
MD	0.830 (0.841)	0.827 (0.842)
SS	0.914 (0.934)	0.836 (0.850)
icover	0.836 (0.867)	0.865 (0.879)
ipack	0.824 (0.840)	0.877 (0.920)
ivol	0.835 (0.859)	0.867 (0.887)
Ham	0.835 (0.837)	0.857 (0.864)
Rep	0.838 (0.852)	0.842 (0.860)
SCVT	0.828 (0.831)	0.839 (0.856)

[1]The median values are given in parentheses. The reported values are the averages on three different sampling experiments of the grids, as described in [4]. Three variants of the Rep and SCVT grids have been used, each sampled once.

CONCLUSIONS

This paper has compared twelve spherical codes regarding their behaviour in CW EPR powder simulations and their homogeneity and EPR properties. The grids' EPR simulations and metrics are only partially consistent. The grids with high geometric and EPR homogeneity do not always generate low-noise simulated EPR spectra. For example, the Repulsion, MD, and SCVT grids generate relatively low-noise simulated EPR spectra and present geometrically and EPR (regarding the B_{dev} metric) homogeneous Voronoi cells. The CM grid, at its turn, generates noisy EPR simulated spectra and has geometrically inhomogeneous and highly EPR-overlapping Voronoi regions. However, the Ham spherical code generates a relatively low-noise simulated EPR spectrum for an axial symmetry spin system, but has geometrically and EPR (B_{dev}) inhomogeneous Voronoi cells.

COMPUTATIONAL DETAILS

The HEALPix spherical code was generated using the `HEALPix` (Hierarchical Equal Area isoLatitude Pixelation of the sphere) software (version 3.30, C language routines) [9]. The Minimum Energy (`me23.0576`) [16], Maximum Determinant (`md023.00576`) [17], and Symmetric Spherical (`ss033.00564`) [18] codes were computed by R. S. Womersley and I. H. Sloan. The Icosahedral arrangements of points (`icover.3.572.7.1.txt`, `ipack.3.582.txt`, and `ivol.3.572.7.1.txt`) were computed by R. H. Hardin, N. J. A. Sloane and W. D. Smith and made available at [19]. The Hammersley spherical code with base 2 was computed with the `udpoint` archive [24]. The Repulsion grids were generated as described in reference [31], using the `repulsion.c` program [25]. The SCVT grids were computed as described in [31], using the FORTRAN90 `sphere_cvt` library (`sphere_cvt.f90`, J. Burkardt) [29]. The Repulsion and SCVT spherical codes were generated in three variants. The Voronoi tessellations of the grids were computed using the `STRIPACK` package (R. J. Renka) [32], in the implementation available at [33] (`stripack.f90`, version 2007).

All CW EPR powder simulations used the microwave frequency v = 9.5 GHz and Gaussian lineshapes with the full width at half maximum of 3 mT. The cubature weight of each grid point to the simulation was approximated with the area of the corresponding Voronoi cell. The homogeneity and EPR metrics were computed as described in reference [4] and the figures were generated within R software environment [34].

R E F E R E N C E S

[1]. S. Stoll, Ph.D. Thesis, ETH Zurich, Switzerland, **2003**.
[2]. A. Ponti, *J. Magn. Reson.*, **1999**, *138*, 288.
[3]. M. Bak, N.C. Nielsen, *J. Magn. Reson.*, **1997**, *125*, 132.
[4]. C. Crăciun, *J. Magn. Reson.*, **2014**, *245*, 63.
[5]. H. Nguyen, J. Burkardt, M. Gunzburger, L. Ju, Y. Saka, *Comput. Geom.*, **2009**, *42*, 1.
[6]. P. Shirley, In *Proceedings on Graphics Interface '90*, **1990**, p. 205-212.
[7]. P. Shirley, K. Chiu, *J. of Graphics Tools*, **1997**, *2*, 45.
[8]. K.M. Górski, E. Hivon, A.J. Banday, B.D. Wandelt, F.K. Hansen, M. Reinecke, M. Bartelmann, *The Astrophysical Journal*, **2005**, *622*, 759.
[9]. http://healpix.sourceforge.net
[10]. R. Sadourny, *Mon. Wea. Rev.*, **1972**, *100*, 136.
[11]. C. Ronchi, R. Iacono, P.S. Paolucci, *J. Comput. Phys.*, **1996**, *124*, 93.
[12]. M. Rančić, R.J. Purser, F. Mesinger, *Quart. J. Roy. Meteor. Soc.*, **1996**, *122*, 959.
[13]. R.D. Nair, S.J. Thomas, R.D. Loft, *Mon. Wea. Rev.*, **2005**, *133*, 814.
[14]. R.S. Womersley, I.H. Sloan, *Adv. Comput. Math.*, **2001**, *14*, 195.
[15]. I.H. Sloan, R.S. Womersley, *Adv. Comput. Math.*, **2004**, *21*, 107.
[16]. http://web.maths.unsw.edu.au/~rsw/Sphere/Energy/index.html
[17]. http://web.maths.unsw.edu.au/~rsw/Sphere/Extremal/New/index.html
[18]. http://web.maths.unsw.edu.au/~rsw/Sphere/EffSphDes/ss.html
[19]. R.H. Hardin, N.J.A. Sloane, W.D. Smith, "Tables of spherical codes with icosahedral symmetry", published electronically at http://neilsloane.com/icosahedral.codes/
[20]. J.M. Hammersley, *Ann. New York Acad. Sci.*, **1960**, *86*, 844.
[21]. H. Niederreiter, "Random Number Generation and Quasi-Monte Carlo Methods", *CBMS-NSF Regional Conference Series in Applied Mathematics*, SIAM, Philadelphia, **1992**.
[22]. T.-T. Wong, W.-S. Luk, P.-A. Heng, *J. of Graphics Tools*, **1997**, *2*, 9.
[23]. J. Cui, W. Freeden, *SIAM J. Sci. Comput.*, **1997**, *18*, 595.
[24]. http://www.cse.cuhk.edu.hk/~ttwong/papers/udpoint/udpoints.html
[25]. http://bionmr.chem.au.dk/download/repulsion/repulsion.c
[26]. Q. Du, M.D. Gunzburger, L. Ju, *SIAM J. Sci. Comput.*, **2003**, *24*, 1488.
[27]. Q. Du, M.D. Gunzburger, L. Ju, *Comput. Methods Appl. Mech. Eng.*, **2003**, *192*, 3933.
[28]. J. Burkardt, M. Gunzburger, J. Peterson, R. Brannon, Technical Report: SAND2002-0099, Sandia National Laboratories, February **2002**.
[29]. http://people.sc.fsu.edu/~jburkardt/f_src/sphere_cvt/sphere_cvt.html
[30]. S. Stoll, A. Schweiger, *J. Magn. Reson.*, **2006**, *178*, 42.
[31]. C. Craciun, *Appl. Magn. Reson.*, **2010**, *38*, 279.

[32]. R.J. Renka, *ACM Trans. Math. Softw.*, **1997**, *23*, 416.
[33]. http://people.sc.fsu.edu/~jburkardt/f_src/stripack/stripack.html
[34]. http://www.r-project.org/

SOLUTIONS IN THE COAGULATION OF OIL WASTEWATER

SMARANDA MASU[a], EUGENIA GRECU[b]

ABSTRACT. Coagulation is one of the most important stages of the oil wastewaters pre-treatment. Oil wastewaters coagulation that we have studied and which had a content of 95.9-270.6mg Total Petroleum Hydrocarbon (TPH)•L^{-1} required optimal doses of polyaluminum chloride (PAC) coagulant between 12.0-16.4mgAl•L^{-1}. In the PAC coagulation, the use of various coagulants aids with absorbent properties, such as: indigenous volcanic tuff, charcoal, anaerobic biologic sludge led to: 1. The PAC dose reduction with 30-50%; 2. Turbidity, Total Organic Carbon (TOC), TPH and absorbance at wavelength 254 nm, A254, of treated samples in the presence of aids and reduced PAC doses were similar vs. samples treated with non-reduced PAC doses in aids absence. The use of indigenous volcanic tuff as coagulation aid led to coagulation sludge which are able to sediment with faster than the sludge obtained with PAC coagulation but without aid. More the volume of the coagulation sludge obtained is reduced with 50% vs. one obtained in other variants. By adding coagulation aids there was a reduction of coagulation reagent costs up to 50%. The correlation between A254 and TPH parameters can be useful in establishing on-line relationships that could ease the operators' activity in wastewater treatment plants.

Keywords: Total Petroleum Hydrocarbons, wastewater coagulation, polyaluminum chloride, coagulant aids, costs

INTRODUCTION

It is well known that a lot of wastewaters loaded with organic pollutants result from the oil processing operations. Out of them there are large amounts of oil compounds, among which a high percentage consists of aromatic compounds. Out of these oil compounds, the Total Petroleum Hydrocarbons (TPH), is very toxic in water and more than this they persist in the environment [1-6].

a *National Research and Development Institute for Industrial Ecology-ECOIND, Branch of Timisoara, Queen Mary Square, No.1, RO-300004, Timisoara, Romania, smarandamasu@yahoo.com*
b *Politehnica University of Timisoara, Faculty of Management in Production and Transports, Remus Street, No.14, RO-300191, Timisoara, Romania, eugeniagrecu@yahoo.com*

It was noticed a decrease of algae productivity in natural water when oil compounds are found. The presence of these compounds often causes the alteration of the natural colour, taste and odour of water surfaces. More than this, the oils and the fats present in the wastewater tend to agglomerate on the water passages, in the premises units, on the side parts causing odour formation as a result of anaerobic degradation. Furthermore, TPH cause severe corrosion of the passages or of the storage units. As a whole, oil wastewaters are carcinogenic, causing a series of hazards for the natural water ecosystem components even extending onto the human health [2, 7-8].

There are methods of treating the oil wastewaters with physical / chemical treatments, such as: settling, filtration, centrifugation, foaming and coalescing, adsorption, coagulation, chemical oxidation and biological techniques. However, there are new technologies mentioned in the specialty literature [9-12], such as: membrane processes, catalytic oxidation, etc.

There are certain treatment methods, such as: adsorption, coagulation, flocculation, membrane processes etc. through which pollutants are transferred from one medium to another; this step is necessary because it eliminates the organic compounds from water. The organic compounds are removed from water in several concentrated phases that can be subsequently stored, processed, monitored.

The biological techniques have serious limitations caused by the presence of recalcitrant compounds, low speed biodegradation, voluminous treatment units, etc. However in the literature there are reported, good efficiencies in the reduction of TPH from wastewater by the coagulation processes associated with adsorption phenomena [13-15].This is the reason for which the authors used Al or Fe salts as coagulation reagent and associated materials as aids: polymeric compounds, natural gums, polyacrylamides, substances that contain sequences of carbohydrates and/or polysaccharides and proteins such as chitin, chitosan, together with various plant debris, such as: cane sugar, shredded coconut shells, charcoal, cellulose, etc. [7,16-19]. The aids addition in coagulation stage with coagulation reagent determines the formation of coagulation aggregates as flocks. The adding of the coagulation aids causes the absorption phenomena of TPH, and thus contributes to the increase of the flock's size and the efficient separation of the pollutants. The analytical control of the coagulation stage has an important role in the management and the optimization of the processes involved in the industrial oil wastewater treatment plants. The control parameters are the following: pH, TPH, Chemical Oxygen Demand (COD), Total Organic Carbon (TOC), suspensions, etc. [3, 10, 17-18, 20]. The process control can be supplemented with specific parameters such as the ultraviolet absorbance at a wavelength of 254 nm (A254) [21-23].

The purpose of this study is to identify the natural materials that can be used as aids in the coagulation processes with PAC agent in the context of the oil wastewaters pre-treatment. The study monitored the efficiencies of the TPH reduction from wastewater by coagulation variants with: 1. the Optimal Dose (OD) of Al^{3+} salts, using PAC coagulant agent, 2. the low dose (LD) of Al^{3+} salts *vs.* OD using PAC coagulant agent and the coagulation aids with absorbent properties, such as: indigenous volcanic tuff, charcoal, biological sludge, 3. the correlation of the conventional control parameters TPH of treated/ untreated waters with the unconventional spectrophotometric parameter - absorbance at 254nm wavelength, A254, 4. the improvement of the coagulated sludge settling rate, 5. coagulant agent costs analysis.

RESULTS AND DISCUSSIONS

Table 1 shows the initial characteristics of the oil wastewaters. The conditions of discharging the treated oil wastewater into the sewerage networks of localities and directly in wastewater treatment plants are in compliance with HG 352/2005 NTPA 002 [24]. The pH of the wastewaters ranges between 7.16-8.2 (admissible values according to HG 352/2005 - NTPA 002 [24]). COD of wastewaters range between $161.3-376.5 mgO_2 \cdot L^{-1}$ and do not exceed the values admitted by current norms of $500 mgO_2 \cdot L^{-1}$ [24/]. It is known that the substances with aromatic character cannot oxidize by dichromate oxidation of organic compounds in strong acidic medium; and the oil wastewaters under study are heavily loaded with aromatic hydrocarbons.

Table 1. The initial characteristics of the oil wastewaters
(three repetitions for each treated variants)

No	Parameters	Wastewaters		
		WW 1	WW 2	WW 3
1	pH	8.20±0.5	7.85±0.3	7.16±0.2
2	Turbidity [°NTU]	65.2±2.5	64.0±2.0	33.5±0.7
3	COD [$mgO_2 \cdot L^{-1}$]	376.5±32.5	230.4±27.5	161.3±12.5
4	TPH [$mg \cdot L^{-1}$]	270.6±35.4	160.6±25.5	95.9±22.3
5	TOC [$mgC \cdot L^{-1}$]	101.3±16.3	59.7±13.7	32.7±9.5
6	* Absorbance A254 [cm^{-1}]	2.235±0.5	1.031±0.7	0.89±0.2

* Samples filtered through filtering paper.

The turbidity of the wastewaters ranges between 33.5-65.2°NTU and the TOC of wastewaters between $32.7-101.3 mgC \cdot L^{-1}$. As for A254 of wastewaters this ranges between 0.890-2.235cm^{-1}. We have to mention that the TOC and the A254 are not set by national regulations. As it can be seen the TPH of

wastewaters ranges between 95.9-270.6 mg·L^{-1} while the amount of TPH exceeds by 19.2 to 54.0 times the amount of 5mg TPH·L^{-1} admissible, according to HG 352/2005 - NTPA 002. [24]. The pre-treatment of WW 1, WW 2 and WW 3 wastewaters with PAC coagulant agent, at the optimal dose (OD) performed by the Jar-Test method, has determined a significant reduction of the efficiencies for COD, turbidity, TPH, TOC and A254.

Table 2 presents the characteristics of the water samples treated with optimal doses (OD) of PAC coagulation agent as far as the reduction efficiencies of turbidity and the organic loading are concerned; such as COD, TOC and A254. It can be observed that the reduction efficiency of the turbidity is high: from 68.2 up to 80.7%. The residual turbidity is ≤12.5 o NTU. It can also be seen that the reduction efficiency of the total organic load is high, from 46.8 to 63.9% for TOC, between 65.2 to 74.1% for TPH and for A254 between 15.7-39.0%.

Table 2. Characteristics of the treated water samples with OD of PAC coagulant agent [mgAl·L^{-1}] (three repetitions for each variants)

Wastewaters		Parameters	Treated water samples	
Type	OD of PAC coagulant agent [mgAl·L^{-1}]		Residual values	Removal efficiency [%]
WW1	16.4	Turbidity [ºNTU]	12.5±3.5	80.7
		TPH [mg·L^{-1}]	39.7±5.3	74.1
		TOC [mgC·L^{-1}]	37.2±3.9	63.1
		* Absorbance A254 [cm^{-1}]	1.58±0.05	39.0
WW 2	16.0	Turbidity [ºNTU]	12.5±5.3	80.5
		TPH [mg·L^{-1}]	67.6±6.6	67.0
		TOC [mgC·L^{-1}]	21.5±4.8	63.9
		* Absorbance A254 [cm^{-1}]	0.72±0.02	30.1
WW 3	12.0	Turbidity [ºNTU]	10.75±3.3.	68.2
		TPH [mg·L^{-1}]	33.5±5.2	65.2
		TOC [mgC·L^{-1}]	17.6±1.9	46.8
		* Absorbance A254 [cm^{-1}]	0.75±0.01	15.7

water samples filtered through filtering paper

It can be seen that the residual TOC is up to 37.2mgC·L^{-1}, while the residual TPH up to 67.6mg·L^{-1}. It is worth mentioning that the coagulation variants applied caused the removal from the wastewater WW 1 of a high quantity of TPH·L^{-1}, *i.e.:* 230.9mg·L^{-1}; from wastewater WW 2 was removed 103.0mgTPH·L^{-1}, and from the polluted waters WW 3 the total quantity removed

was 62.6mg TPH·L^{-1}. However, the TOC and the TPH residual values of the treated samples water were high. The TPH residual was 4.3-7.9 times higher than the national norms limits. In order to improve the reduction efficiency of the total organic compounds in the WW 1-WW 3 wastewaters at the stage of coagulation various inorganic or organic aids were added: indigenous volcanic tuff, charcoal, anaerobic biological sludge.

In tables 3, 4 and 5 there are presented the residual values of the turbidity, COD, TOC, A254 parameters in treated samples, at the coagulation stage, with reduced doses (RD) of PAC coagulant agents and coagulation aids. It is observed that the addition of aids in the coagulation stage with PAC led to:

1. Reductions of PAC coagulant agent dose by 30-50% vs optimal dose;

2. The turbidity in treated samples water with RD of PAC coagulant agent and indigenous volcanic tuff aid was 8.3-15.5 ° NTU, a RD of PAC coagulant agent and the charcoal were 4.5-5.5 ° NTU, a RD of PAC coagulant agent and the *biological* sludge were 7.5-10.5 ° NTU. Treated waters have had a turbidity which is below a 15.5°NTU and can be downloaded into the sewerage networks of localities and directly in wastewater treatment plants [24]

3. TOC in treated samples water with RD of PAC coagulant agent and indigenous volcanic tuff aid were 13.3-24.5mgC·L^{-1}, with RD of PAC coagulant agent and charcoal aid were 18.6-30.1mgC·L^{-1}, RD of PAC coagulant agent and biological sludge aid were 14.7-23.7mgC·L^{-1}.

4. TPH in treated samples water with PAC coagulant agent doses, RD, in aids presence were: for and indigenous volcanic tuff in the range 5.0-46.2mg·L^{-1}, for charcoal in the range 6.5-29.7mg·L^{-1}, and for biological sludge in the range 4.2-27.4mg·L^{-1}.The lowest residual concentrations TPH were within the range of 4.2-6.5mg·L^{-1}, which were obtained in case WW 3. It is worth mentioning that the water WW 3 indicated the lowest initial loading with petroleum products. Residual values of 4.2-5.0mg TPH·L^{-1} in WW 3 treated water with RD of PAC coagulant agent and indigenous volcanic tuff or biological sludge on can be discharged in accordance with the current Romanian rules. Even so, residual values of TPH = 6.5mg•L^{-1} in WW 3 treated with RD of PAC coagulant agent and charcoal were above the limit admitted at discharge [24].

It can be seen in tables 2, 3, 4, 5 that the efficiencies to reduce turbidity and TOC were similar for PAC coagulant agent used at OD or RD in coagulation stage in absence/presence of coagulation aids.

Figure 1 shows the results in the TPH reduction efficiencies, in WW 1 - WW 3 samples treated PAC coagulant agent used at OD or RD in coagulation stage in absence/presence of coagulation aids. It can be seen that by applying the coagulation variants with PAC coagulant agent RD and the indigenous volcanic tuff we can obtain the highest TPH reduction efficiencies, within the range of 88.6-94.5%. Also, high TPH reduction efficiencies in WW 1 - WW 3

samples treated with the PAC coagulant agent RD and biological sludge and charcoal were obtained in the range 64.3-93.2%. The TPH reduction efficiencies, in WW 1 - WW 3 samples treated PAC coagulant agent used at OD in coagulation stage in absence aids were under 72%.

Table 3. Treated samples WW 1 with RD of PAC coagulant agent and coagulate aids (three repetitions for each variants)

No	Treated variants WW 1	Parameters		
		Turbidity [°NTU]	TPH [mg·L^{-1}]	TOC [mgC·L^{-1}]
1	RD of PAC coagulant agent 11.5 mgAl·L^{-1} Coagulation aids: indigenous volcanic tuff 0.5mg·L^{-1}	8.3±1.6	46.2±4.8	24.5±3.2
2	PAC coagulant agent RD= 11.5 mgAl·L^{-1} Coagulation aids: charcoal 0.5 mg·L^{-1}	5.5±0.8	18.6±2.3	18.6±1.0
3	PAC coagulant agent RD= 11.5 mgAl·L^{-1} Coagulation aids: biologic sludge (0.4g·L^{-1} D.M.)	8.5±1.8	41.2±5.3	23.7±3.4

Table 4. Treated samples WW 2 with PAC coagulant agent RD and aids (three repetitions for each treated variants)

No	Treated variants WW 1	Parameters		
		Turbidity [°NTU]	TPH [mg·L^{-1}]	TOC [mgC·L^{-1}]
1	PAC coagulant agent RD=8.0 mgAl·L^{-1} Coagulation aids: indigenous volcanic tuff 0.5mg·L^{-1}	15.5±1.8	18.0±4.2	20.4±2.8
2	PAC coagulant agent RD=8.0 mgAl·L^{-1} Coagulation aids: charcoal 0.5 mg·L^{-1}	4.5±0.5	29.7±2.6	30.1±4.3
3	PAC coagulant agent RD=8.0 mgAl·L^{-1} Coagulation aids biologic sludge (0.4g·L^{-1} D.M.)	10.5.±1.6	27.4±3.9	23.7±3.5

Table 5. Treated samples WW 3 with RD of PAC coagulant agent and coagulate aids (three repetitions for each treated variants)

No.	Treated variants WW 1	Parameters		
		Turbidity [°NTU]	TPH [mg·L^{-1}]	TOC [mgC·L^{-1}]
1	PAC coagulant agent RD=8.4 mgAl·L^{-1} Coagulation aids: Indigenous volcanic tuff 0.5mg·L^{-1}	8.5±1.5	5.0±3.3	13.3±4.0
2	PAC coagulant agent RD=8.4 mgAl·L^{-1} Coagulation aids: charcoal 0.5 mg·L^{-1}	5.5±1.4	6.5±1.6	20.2±3.2
3	PAC coagulant agent RD=8.4 mgAl·L^{-1} Coagulation aids: biologic sludge (0.4g·L^{-1} D.M.)	7.5±0.9	4.2±0.8	14.7±2.4
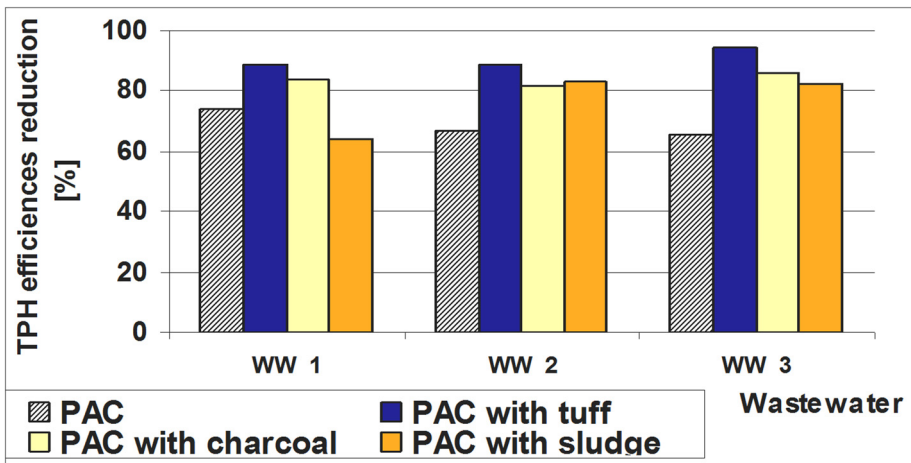
Figure 1. TPH reduction efficiency in WW 1- WW 3 samples treated with PAC coagulant agent used OD or RD in coagulation stage in absence/presence of coagulation aids.

In figures 2, 3 and 4, UV absorbance (A254) determined for WW 1-WW 3 untreated/treated waters are presented. The addition of PAC coagulant agent RD in coagulation stage in presence of coagulation aids led to the reductions absorbance *vs.* absorbance determinated for PAC coagulant agent OD in coagulation stage in absence of coagulation aids.
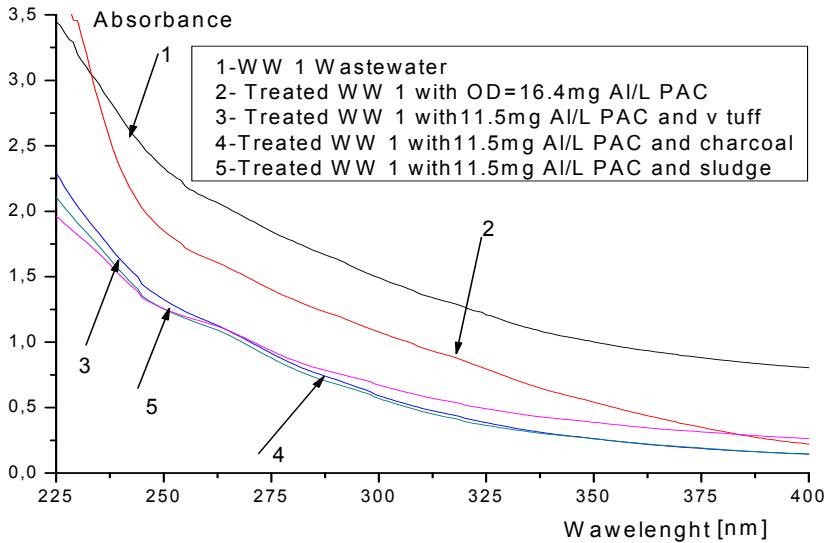
Figure 2. Selective UV VIS spectrum for untreated/treated WW 1 waters
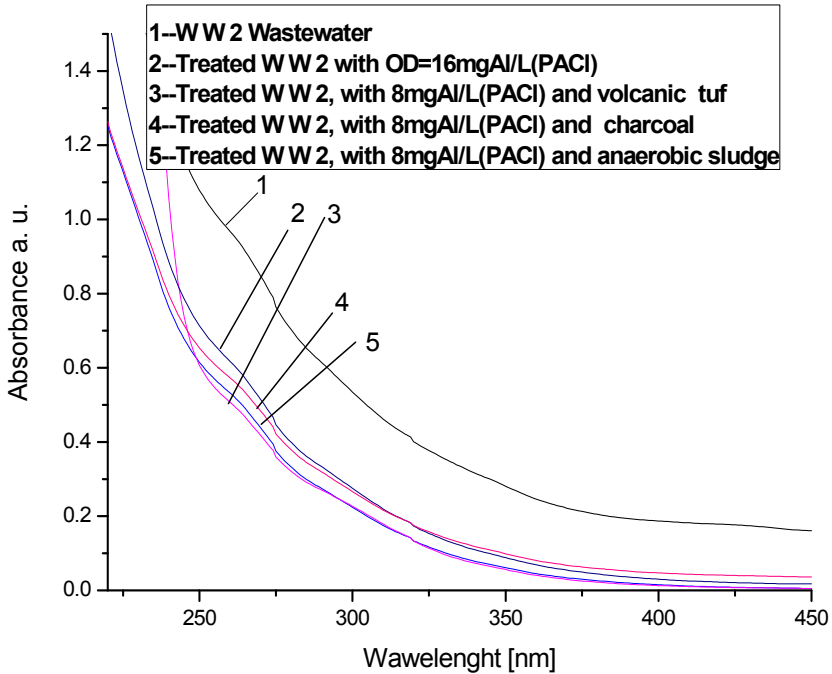
Figure 3. Selective UV VIS spectrum for untreated/ treated WW 2 waters
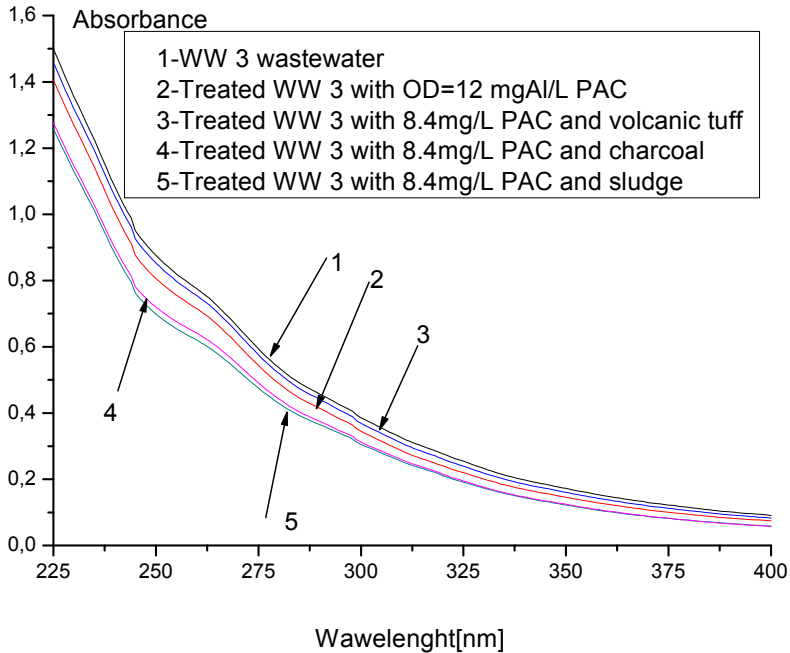
Figure 4. Selective UV VIS spectrum for untreated/ treated WW 3 waters

From figure 2, 3 and 4 the resulting reduction of global parameter A254 was:

- 11.7-44.1% at treating wastewater WWW 1-3 with PAC coagulant agent RD in coagulation stage in presence of coagulation aids indigenous volcanic tuff,

- 25.8-46.5% after treatment with PAC coagulant agent RD in coagulation stage in presence of coagulation aids biological sludge,

- 26.0-46.0% after the treatment of PAC coagulant agent RD in coagulation stage in presence of coagulation aids charcoal.

A254 reduction efficiencies was similar when wastewaters it were treated with PAC coagulant agent OD in coagulation stage in absence of aids. The absorbance variation was correlated with the variation of TPH.

Given the correlations between the two parameters TPH and A254, A254 parameter can be used as an indicator of untreated/treated water quality. A254 can be determined quickly without altering the water quality; thus the time spent for water analysis by classical procedure can be reduced. The correlation between A254 and TPH parameters can be useful in establishing on-line relationships that could ease the operators' activity in wastewater treatment plants.

Table 6 presents the quantities of coagulated sludge from water samples treated with PAC coagulant agent OD or RD in coagulation stage in absence/presence of coagulation aids. We have to state that in the samples treated with PAC coagulant agent RD in coagulation stage in presence of coagulation aids such as indigenous volcanic tuff and biological sludge, in the sedimentation stage, the coagulation flocs were large and heavy. Coagulation with PAC coagulant agent RD and indigenous volcanic tuff or biological sludge aids after 30 minutes have determinated the sludge sedimentation and the clear supernatant (see Jar Test settles flocs coagulation in the stage of sedimentation). Samples treated with PAC coagulant agent RD and charcoal aid require filtering operation for separating sludge coagulation. The flocks that do not sediment are to be removed when filtering.

Table 6. Quantities of sludge from water samples treated with PAC coagulant agent OD or RD in coagulation stage in absence/presence of coagulation aids

No	Wastewater treatment with PAC coagulant agent	Sedimentation time [min]	Sludge quantities [ml·L^{-1}]	Observation
1	Optimal dose (OD)	30	40-60	Large and light flocs sediment
2	RD=0.7 OD PAC coagulant agent + indigenous volcanic tuff	10	20-30	Large and heavy flocs sediment
3	RD=0.5 OD PAC coagulant agent + charcoal	30	40-60	partially settled some float
4	RD=0.5 OD PAC coagulant agent + biological sludge	30	28-45	medium flocs sediment

In Table 6 it can be observed that the addition of indigenous volcanic tuff to PAC coagulant agent OD caused the formation of heavy flocs; they settle three times faster than those formed with PAC coagulant agent OD in the absence of coagulation aids. The addition of indigenous volcanic tuff has determined a high reduction of coagulated sludge, i.e. 50% (in volumes).

Table 7 presents a comparison between the costs of the coagulant agents for wastewaters treated with PAC coagulant agent OD or RD in coagulation stage in absence/presence of coagulation aids [Euro•m^{-3}].

Table 7. Coagulants cost comparison

No	Coagulant type	Cost of coagulants for wastewaters treated with PAC coagulant agent OD or RD in coagulation stage in absence/ presence of coagulation aids [Euro•m⁻³]		
		WW 1	**WW 2**	**WW 3**
1	PAC coagulant agent OD	89.1	87.9	65.9
2	PAC coagulant agent RD with indigenous volcanic tuff aid	63.4	45.0	47.1
3	PAC coagulant agent RD with charcoal aid	64.5	46.1	48.2
4	PAC coagulant agent RD with biological sludge aid	62.4	44.0	46.1

The addition of the coagulation aids reduces the cost of coagulation agents needed to achieve efficacy as following: with 27.6-30% when the dose was reduced by 30% PAC coagulant agent; with 47.55-50% if the PAC coagulant agent was reduced by 50%.

To the waters treated with PAC coagulant agent RD in coagulation stage in presence of coagulation aids the next stage can be applied, i.e: gravitational separation (sedimentation) or filtration. The cost of the industrial sedimentation and filtration are calculated based on: the water flow, the types of decanters, filters, process time, etc. The filtering operation is estimated as being 1.62- 1.89 more expensive than sedimentation [25].

The advantages and disadvantages in using aids are determined by nature and their behaviour in the coagulation process:

- for charcoal is a better water treatment quality; but the sludge separation (filtering) operation is more expensive than settling;

- for volcanic tuff is high capacity of sedimentation (compacting the coagulation sludge) and a reduced processing cost in a subsequent stage;

- for the biological sludge is a industrial waste recycling and the capacity of sedimentation [26].

CONCLUSIONS

The optimal dose of PAC coagulant determined for the studied wastewaters ranged from 12.0 -16.4 [mg·L⁻¹] Al. Reduction efficiencies were high: 68 to 80.7% for turbidity, between 46.8 to 63.9% for TOC, for TPH between 65.2 to 74.1%, from 15.7.to 39.0% for A254. However, residual values of global parameters, *i.e.* TPH and TOC of treated water samples, have remained high. TPH have remained

above the allowed limit of 5 mg·L^{-1}, being exceeded by 4.3-7.9 times vs. Romanian regulations. The use of adjuvants for wastewater coagulation has determined: 1. Reductions of the PAC coagulation dose by 30-50%; 2. Efficiencies of reduction of turbidity and TOC it was higher than the reduction efficiencies obtained for the coagulation with optimal dose in the absence of adjuvants; 3. TPH reduction efficiency was 64.3-94.5%. 4. Reduction efficiencies of A254 were 11.7-46.5%; The absorbance for treated water correlated with the TPH content. The correlation between A254 and TPH can be useful in establishing relationships that could ease the operators' activity in wastewater treatment plants. The addition of indigenous volcanic tuff in PAC coagulation has determined the formation of heavy and large flocs which settled three times faster than those formed at the coagulation with optimal dose of PAC in adjuvant absence, and the coagulated sludge volume was reduced by 50%. Moreover, the addition of coagulation aids has reduced costs coagulation reagents necessary to obtain optimum efficiency [7, 25, 26].

EXPERIMENTAL SECTION

Materials

1. Coagulation agents: polyaluminum chloride coagulant (PAC), from B.A.D.S. Brasov. Characteristics: name PAC 17 with 17.2% Al_2O_3; 2. Coagulation aids: indigenous volcanic tuff from Cemacom Zalau with ground particle size < 0.2 mm; charcoal from Letea Energo Prest SRL, Pitesti; anaerobic biological sludge (8.3 mg·L^{-1} D.M.) from a municipal waste plant; 3. Sources of wastewaters. Wastewaters were taken periodically from drilling wells in operation. Wastewaters were stored at 4°C.

Methods

Coagulation was performed with a stirrer equipped with variable speeds (Phipps & Bird Company, USA). The PAC coagulant agent OD or RD in coagulation stage in absence/presence of coagulation aids for maximum pollutant removal were done by Jar Test method (in three steps: rapid stirring, slow stirring and gravitational settling). Rapid stirring time of water sample with the optimal amount of coagulant in the presence / absence of aids was 3 minutes; Slow stirring time was 15 minutes; Settling time of coagulated water sample was 30 minutes;Coagulation pH =7.3. The wastewaters were introduced in 6 coagulation vessels. The volume of each sample coagulated it was 250 ml.

In the separated supernatant from coagulated samples were analyzed according to conventional parameters of the standard rules: pH determined pH-meter model 290A ORION RESEARCH USA, turbidity caused by Micro 100

Laboratory Turbidimeter, Scientific Inc. USA, COD (Chemical Oxygen Demand) determined by hot dichromate oxidation in strongly acidic medium of K. TOC (Total Organic Carbon) was determined by TOC Analyzer Multi N/ C 2100 Analytik Jena, Germany. Non-conventional parameter absorbance at wavelength 254 nm, A 245, was analyzed by UV VIS spectrophotometer, Specord 205, Analytik Jena, Germany. UV VIS Samples were filtered through Sartorius filter papers FT 2-206

TPH were determined according to the Romanian standardized norms by solvent (tetrachlorethylene) extraction with (SR 7877-1) *i.e.* TPH is extracted from a volume of wastewater corrected to pH=1 with hydrochloric acid d=1.19 $g \cdot L^{-1}$, (V) by mixing with solvent. Extracts number is four. Solvent extracts dried by passing through a filter with anhydrous Na_2SO_4 p.a. Then solvent extracts are placed in capsule C1, with m_1 [g]. The solvent is evaporated and weigh the capsule with TPH residuum, C2 m_2 [g]. Calculate the amount of TPH, TPH $g \cdot L^{-1} = [(m_2 - m_1) \cdot V^{-1} \cdot 1000$. Studied waters must have the characteristics required by national norm [24] to be discharged into the sewerage networks of localities and directly in wastewater treatment plants.

The volume of sludge it was determined after a period of 30 minutes sedimentation in cones Imhoff [27].

R E F E R E N C E S

[1]. American Petroleum Institute, "Management of Water Discharges: Design and Operations of Oil-Water Separators", 1st ed., Washington D.C., USA, **1990**, chapter 1-5.

[2]. B.H. Diyauddeen, W.M.A.W. Daud, A.R.A. Ayiy, *Process Safety and Environmental Protection,* **2011***, 89*, 95.

[3]. C. Majdik, G. Katona, M. Chintoanu, M. Roman, E. Luca, S.M. Simon,T. Rusu, C. Roman, *Studia UBB Chemia*, **2011**, *1,* 275.

[4]. N. Ilias, A. Draghici, D. Draghitoiu, S. Ghelagiu, A. Cornescu, *Analele Universitatii „Constantin Brancusi" Tg Jiu, Seria Inginerie,* **2009**, *3*, 147.

[5]. J. Saththasivam, K. Loganathan, S. Sarp, *Chemosphere*, **2016**, *144,* 671.

[6]. V.K. Gupta, I. Ali, T.A. Saleh, A. Nayak, S. Agarwal, *RCS Advances*, **2012**, *2*, 6389.

[7]. R. Crisafully, M.A.L. Milhome, R.M. Cavalcante, E.R. Silviera, D. de Keukeleire, R.F. Nascinto, *Bioresource Technology*, **2008**, *99,* 4515.

[8]. M. Senila, E. Levei, L. Senila, O. Cadar, M. Roman, M. Miclean, *Studia UBB Chemia*, **2015**, *2,* 137.

[9]. W. Tian, J. Bai, K. Liu, H. Sun, Y. Zhao, *Ecotoxicological Environmental Safety,* **2012**, *8,* 1.

[10]. J.T. Alexander, F.I. Hai, T.M. Al-aboud, *Journal Environmental Management*, **2012**, *111,* 195.
[11]. R. Fabris, C. Chow, T. Tran, S. Gray, M. Frikas, Development of Combined Treatment Processes for the Removal of Recalcitrant Organic Matter, Research Report no. *38*, Salisbury, Australia, CRC for Water Quality and Treatment, **2008**, chapter 1.
[12]. M. Carbureanu, G. Catalina, *Revista de Chimie*, **2014**, *65,* 1498.
[13]. S.C. Cheu, H. Kong, S.T. Song, K. Johari, N. Saman, M. A. C. Yunus, H. Mat., *Journal of Environmental Chemical Engineering*, **2016**, *4(1),* 864.
[14]. C.E. Santo, V.J.P. Vilar, C.M.S. Botelho, A. Bhatnagar, E. Kumar, R.A.R. Bonaventura, *Chemical Engineering Journal,* **2012**, *183*, 117.
[15]. H. Farajnezhad, P. Gharbani, *IJRRAS,* **2012**, *13,* 306.
[16]. S.M. Koch, J.B. Dixon, *Applied Clay Science*, **2001**, 1*8,* 111.
[17]. B. Guo, H. Yu, B. Gao, H. Rong, H. Dong, D. Ma, R. Li, S. Zhao, *Colloids and Surfaces A: Physicochemical and Engineering Aspects*, **2015**, *481*, 476.
[18]. M. Sueyoshi, R.S. Al – Maamari, B Jibril, M. Tasaki, Kazuo Okamura, H. Kuwagaki, H. Yahiro, K. Sagata, Y. Han, *Journal Analytical and Applied Pyrolysis*, **2012**, *97,* 80.
[19]. M. Ng, A.E. Liana, S. Liu, M. Lim, C.W.K. Chow, D. Wang, M. Drukas, R. Amal, *Water Research,* **2012**, *46,* 4614.
[20]. A. Ghirisan, S. Dragan, *Studia UBB Chemia*, **2011,** *2,*115.
[21]. A.M. Steele, Thesis Ultraviolet Absorbance at 254 nm as an Indicator of Petroleum Hydrocarbon Removal by Activated Carbon: a case study, University of California, Davis, **2013**, chapter 2-3.
[22]. S. Masu, Proceedings of the 20th International Symposium on Analytical and Environmental Problems, Szeged, Hungary, 22nd, September, **2014**. 71.
[23]. S. Mâșu, *Revista de Chimie*, **2011**, *62(1),* 64.
[24]. ***HG 352/2005 NTPA 002 amending and supplementing Government Decision no 188/2002 to approving the rules on the condition of discharging wastewater into the aquatic environment, Government of Romania, Monitor Official, Bucharest, **2005**, *378*.
[25]. D.S. Barwon, Proceedings of 72 [nd] Annual Victorian Water Industry Engineers and Operators Conference Bendigo, Australia, **2009**, www.wioa.org.au/vic*/*
[26]. Water Treatment - Yearly OM Costs Problems, CIVL, 1-7, www.ce.memphis.edu/1112/.../group_problem_treatment_
[27]. G. Degremont, "Water Treatment Handbook - 1991 sixth edition", Lenntech B.V., Rotterdamseweg, **1991**, volume1-2, http://www.lenntech.com/scientific-books/water-treatment/degremont-water-treatment-handbook.htm#ixzz4FQ1YCKTB

RAPID DETERMINATION OF INDOOR AIR CONTAMINANTS IN SHOE SHOPS USING PHOTOIONIZATION DETECTORS

VICTOR BOCOȘ-BINȚINȚAN[a], ALINA SMOLENSCHI[a], ILEANA-ANDREEA RAȚIU[a*]

ABSTRACT. Recently, indoor air quality (IAQ) has become a serious concern. More and more people are facing health problems due to the poor air quality at the workplace; most of them are exposed to pollutants without even realizing it. Therefore, it is important to monitor the indoor air quality to prevent an unsafe environment. In the shoe making process, various volatile compounds – like toluene, found especially in adhesives – are used. These chemicals tend to slowly desorb from the final products and to accumulate ultimately inside the shoe shops. We report here the total volatile organic compounds (tVOCs) that are prone to be ionized by the UV radiation; measurements were performed over eight weeks inside six shoe shops located in Cluj-Napoca, Romania, with a ppbRAE Plus instrument manufactured by RAE Systems Inc. USA. We found with this ultra-sensitive photoionization detector (PID) maximum concentrations up to 7 ppmv of tVOCs (isobutene units) in air for each shoe shop investigated. The obtained results demonstrate that people working in the selected shoe stores may be exposed to significant tVOCs concentrations during a working day. Thus, PID devices are useful tools for quickly surveying the indoor air quality.

Keywords: photoionization detection PID, indoor air quality IAQ, volatile organic compounds VOCs, toluene.

INTRODUCTION

People spend most of their life (80-90%) in indoor spaces, such as houses, cars, office buildings and other public spaces. If we assume that people inhale more than 22 m^3 of air per day, the contaminants present in the air can constitute a serious threat to their health. The most common indoor air quality problems in buildings were already considered, such as insufficient ventilation rate, too high particle concentration, poor filtration effectiveness and hygienic conditions [1].

[a] *Babeş-Bolyai University, Faculty of Environmental Science & Engineering, Str. Fântânele nr. 30, 400294 Cluj-Napoca, Romania*

[*] *Corresponding author: andreea_ratiu84@yahoo.com*

The World Health Organization (WHO) estimates that more than 30% of all buildings where commercial activities are running have problems with indoor air quality. Indoor air pollution in homes, public buildings and offices is produced mostly by activities of the occupants of these spaces and by using various devices, chemicals, clothing, by releasing gas phase compounds from structural or decorative materials, and also by intrusion of outdoor pollutants [1].

Pollutants from the indoor environment may pose an important stress on human health and welfare. When they reach high concentrations, following acute or chronic exposure they can cause discomfort, irritation and illness [2]. One of the most dangerous category of VOCs, the BTEX group (benzene, toluene, ethylbenzene and xylenes), receives special attention, due to their toxicity. Exposure at work can take place for instance in the industry – such as printing, furniture and footwear. The most dangerous of these is benzene, a carcinogenic compound; therefore, its use was banned in several applications [3]. Toluene is used in adhesives, the dilution of the dyes, paint industry, as an additive for gasoline, etc. Acceptable concentration of volatile organic compounds in indoor air is between 0.2-0.5 mg m^{-3} [4]. Toluene is an aromatic hydrocarbon widely used in footwear industry; it is also found sometimes as a metabolic product by some bacteria [5]. Toluene C_7H_8 (CAS No. 108-88-3, MW 92.14 g mol^{-1}) is a colorless, flammable and water insoluble liquid (m.p. -93°C; b.p. 110-111°C; density 0.865 g cm^{-3} at 25°C); it is volatile (vapor pressure of 22 mm Hg at 20°C) and its vapors are heavier than air (vapor density: 3.2 vs. air). Odor threshold for toluene is about 3 ppm$_v$ [6]. The first effects of toluene exposure can be observed at a concentration of ca. 50 ppm$_v$. Exposure to 100-200 ppm$_v$ (375-750 mg m^{-3}) is associated with headache, respiratory irritation; at concentrations of 400 ppm$_v$ one may experience eye irritation, vomiting, ataxia, and dizziness. Chronic exposure of personnel at toluene concentrations of 30-130 ppm$_v$ (113-488 mg m^{-3}) can have adverse effects on hearing and visual system (color differentiation) [7]. In the U.S.A., the Occupational Health and Safety Administration (OSHA) indicates an Immediately Dangerous To Life or Health concentration (IDLH value) of 500 ppm$_v$, and a permissible exposure limit (TWA value) of only 10 ppm$_v$ (37.5 mg m^{-3}) [8]. In order to limit human exposure to BTEX group and to toluene especially, it is imperative that their sources can be detected, identified and removed/diminished.

Some rapid instrumental techniques suitable for detecting pollutants in indoor air are cationic sensors („hot bead"), colorimetric techniques, electrochemical sensors, or photoionization detectors. A hybrid, portable sensor which combines two orthogonal sensing principles (a selective molecular binding with a microfabricated quartz tuning fork detector, and then separation of analytes with a column), was developed for monitoring vapors of BTEX in air in the presence of interferents, at ppb$_v$ levels [9].

The PID utilizes ultraviolet light to ionize gas molecules, and is commonly employed for quick, real-time detection of volatile organic compounds (VOCs). Preliminary studies for the analysis of total VOCs were undertaken, to evaluate the

performance characteristics of a portable analyzer equipped with a PID; they successfully demonstrated the possibility of using PID application for indoor environments that can be made fairly effectively under certain environments such as a newly built apartment [10]. In another study, three ppbRAE PGM-7240 PIDs were employed to concurrently measure the spatial and temporal distributions of ethanol concentration from a gas-pollutant leaking source with the aims to examine the pollutant dispersion flow field in a clean room [11].

The PID technique may be used in stand-alone instruments, but PID devices are also used in tandem with other analytical instruments, such as gas chromatographs (GCs). Cost-effective indoor air quality surveys and making on-site decisions to control VOC emissions were studied [12]; one determined concentrations of five target VOCs (BTEX and hexane) in several buildings in Waterloo, Canada, using solid-phase microextraction technique. Fast separation and speciation of common indoor air pollutants was possible with the use of a modified portable GC instrument, equipped with a PID, a FID, and a dry electrolytic conductivity detector in series. The detection limits for the target compounds in air were between 1 and 9 ppb_v [12]. Using the same instrumentation and technique described in [12], monitoring and analysis of VOCs, formaldehyde, and particulate matter in air were done by Koziel et al.; concentrations measured were as low as 700 parts-per-trillion and the authors considered their work as being a simple approach for fast, cost-effective sampling and analysis of common VOCs in indoor air [13].

PID devices in tandem with gas chromatography/mass spectrometry (GC/MS) were often used in the analysis of environmental pollutants. Volatile coal tar and petroleum hydrocarbons, and an integrated system for detecting pollutants on-line, in real-time by photoionization detection and quantitation by GC/MS was described [14]. Ghira et al. detected very low levels of pyridine vapors in controlled atmospheres from indoor air [15], using both PID and IMS (Ion Mobility Spectrometry), sensitive and powerful analytical techniques with multiple applications in trace detection.

Talking about the occupational exposure to organic solvents, dust, chromium, degradation products of synthetic materials, in particular about people working in shoe & clothes, electronics, food, or cosmetics shops Several studies have shown the presence of chemicals (such as toluene, benzene, or n-hexane) in urine and/or blood samples [16-18]. Studies have been undertaken on the toxicity of shoe soles [16], the exposure of persons who work in indoor environments such as the shoe stalls at dust, portable gas ranges, organic solvents, adhesives and shoe polish [17]. Neurophysiological and psychological disorders caused by occupational exposure to organic solvents were also addressed [18].

The microenvironments of a multi-store shopping mall in Guangzhou, China, were analyzed using a thermal desorption system and a GC-MS system in order to verify the VOCs produced by indoor emission sources. The fast-food court and a leather products department store have had the highest concentrations

of benzene, toluene, ethylbenzene, xylenes and chlorinated hydrocarbons. The authors considered that the emission sources of monocyclic aromatic hydrocarbons might include cooking, while chlorinated hydrocarbons were possibly connected with their use as cleaning agents or deodorizers. [19]

However, there is no doubt that leather and several other materials (textile, rubber and plastic) from which the shoes are made, plus the adhesives used, embed a wide range of different chemicals; consequently, there are health risks associated with the use of products and with the exposure of personal employed in shoe shops, as well. Unfortunately the most often there is insufficient knowledge about which chemical substances these products contain; also, the properties of these substances are in many cases not known in sufficient detail. This lack of knowledge can potentially affect the human health and the environment.

Because nowadays the effects of harmful substances on human health and well-being represent a major topic of interest to scientists, in the present study we aimed to investigate in real time the indoor air quality of six shoe shops from Cluj-Napoca, Romania. For this purpose we measured total volatile organic compounds prone to be ionized by the UV radiation (tVOCs) inside the shoe stores located in different points of Cluj-Napoca, over eight weeks, using a ultra-sensitive PID detector Model *ppbRAE Plus* manufactured by RAE Systems Inc., USA. We have done 15 sets of measurements in all six shops, starting April until the end of May. The obtained results have shown that people working in the selected shoe stores may have been exposed to significant VOCs concentrations during a work day. Because each group of air contaminants carries its own particular danger, and the higher concentrations of constituents fundamentally affect the quality of indoor air and peoples' health, we strongly suggest the use of portable, autonomous PID devices for monitoring the indoor air quality during a working day. The PIDs are simple, rugged, hand-held, lightweight devices, with high availability on the market and with a relatively low cost (up to 1,000 USD per unit). We are also convinced that PID will be a useful tool for improving the indoor air quality and the global environment in the next future.

RESULTS AND DISCUSSIONS

Through data collection and analysis we found relatively high concentrations of photoionizable chemical compounds in indoor air. We suppose that the largest amount is from toluene, widely used in the manufacture of adhesives for the footwear industry.

Because the purpose of this study was to observe and analyze the variation profile of total VOCs over 15 days in six shoe stores, in order to assess the trend of concentration evolution over time, as summarized in **Table 1** and displayed in **Figures 1** and **2**. The average and maximum values for each data set / day, together with the surface of each shop and the ambient temperature in

commercial spaces were also displayed in **Table 1**. Temperature variation was between 13 and 32°C during the experimental time period. As expected, we have noticed that tVOCs concentrations were higher during a day with a higher temperature.

Table 1. The average values and maximum values (expressed in isobutene units) of total photoionizable compounds concentrations found in each shop

T [°C]	Shop #1 S = 18m² [ppbᵥ]		Shop #2 S = 28m² [ppbᵥ]		Shop #3 S = 35m² [ppbᵥ]		Shop #4 S = 15m² [ppbᵥ]		Shop #5 S = 24m² [ppbᵥ]		Shop #6 S= 21m² [ppbᵥ]	
	Average	Maximum	Average	Maximum	Average	Maximum	Average	Maximum	Average	Maximum	Average	Maximum
19	351	1564	631	1473	536	2515	568	3388	708	939	595	3095
20	305	1295	545	2429	460	2924	1053	5208	676	1084	563	1621
19	583	881	1743	2823	798	1106	1052	1959	565	1902	861	2004
13	859	1063	942	1571	944	1255	756	1930	326	730	689	1997
20	1208	1976	411	625	849	1003	746	1721	208	257	320	1071
21	954	1812	910	4229	2144	3216	1291	3993	534	1784	829	3725
23	415	815	699	1658	1211	1395	625	1187	1184	3272	686	1664
24	540	1848	976	1284	1316	1761	785	1501	1216	3316	538	2738
25	967	2296	1401	7224	623	766	304	1023	969	3106	888	3479
22	1204	2011	1043	2994	313	1233	1145	2416	812	2208	1126	3280
23	653	2325	351	636	1144	1846	908	2426	517	2632	314	2020
21	378	944	1777	2452	783	1237	567	1288	791	3497	570	2506
22	756	889	1045	2706	2230	3612	2138	4639	643	3269	1661	1967
32	405	649	2806	4418	1530	2835	1482	2264	696	3570	1038	3807
28	1996	2203	972	4442	2292	2788	1073	2853	861	3876	1079	2628

However, considering all the cases, we cannot conclude that the temperature is always the decisive factor influencing the concentration of the detected compounds. Also, from data in the Table 1 one can notice that the surface area of stores varies between 15 m² (Shop #4) and 35 m² (Shop #3). By comparing the values recorded in Shop #3 (the smallest space) and Shop #4 (the largest space) for each day, and the graphic representation in **Figure 1**, we observe that in Shop #3 no higher values of total photoionizable compounds were recorded than in Shop #4. From this standpoint, taking in account the values recorded in all 15 days, we still cannot conclude that in small areas the concentrations are always higher than in large spaces. Probably, the ventilation plays the most important role here.
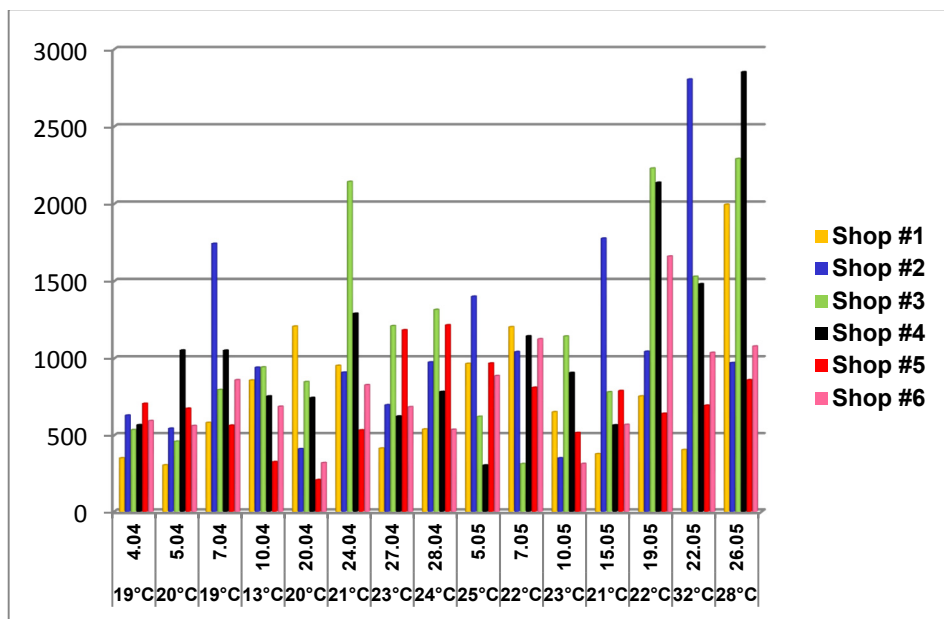
Figure 1. Average concentrations of tVOCs recorded (expressed in isobutene units) for 15 days in the six stores

In conclusion, the differences between compounds concentrations measured daily may be influenced by differences in temperature or store space, but are not caused by temperature fluctuations and surface area of the store. Factors such as the presence or absence of ventilation, organization, placement of goods in store, quantity of goods, customer turnover and movement (which indirectly determines the ventilation space) certainly affect contaminant concentrations inside the store.

For better understanding and interpreting our experimental results we divided the data in two categories: (1) the maximum concentration values (when the instrument was near by the shoes) recorded by PID, represented in **Figure 2** and (2) the average concentration values, which represents the arithmetic average of total recorded values for a distinct shop in each day (**Figure 1**). For each shop a measurement session took about 5 min.

Observing **Figure 1**, we can see that the smallest concentrations of average values were recorded in Shop #5, where only in two days the value of 1000 ppb$_v$ (isobutene units) was exceeded. Followed by shop #5, the smallest concentrations recorded were in Shop #1 and then in Shop #6. The highest values of average concentrations were found in Shop #3, where in three days the average concentration values ware more than 2000 ppb$_v$ isobutene units, followed by Shop # 2 and #4.
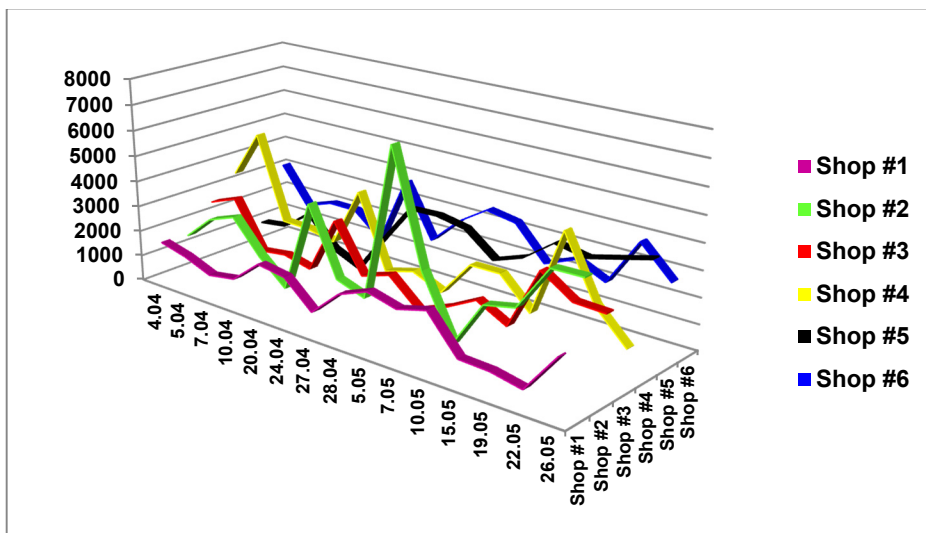
Figure 2. Maximum concentration of tVOCs (expressed in isobutene units) for 15 days in the six stores

In **Figure 2** maximum concentration values of total photoionizable chemical compounds recorded over 15 days were displayed. The smallest values for maximums were recorded in Shop #1, followed by Shop #5 and Shop #6. This can be explained by the continuous ventilation and by location of the store in the basement, with direct access from outside. We could also notice during the experimental sessions that these shops are selling leather shoes only, and not shoes made of synthetic materials.

Higher concentrations of maximum values were identified in Shop #2 and Shop #4. Shop #2 has direct access from outside and ventilation systems, nonetheless, it operates in a very busy area, and the shoes are made from leatherette (synthetic materials). We believe that these are the possible reasons that can account for the high maximum concentration of chemical compounds released in the stores.

Given that a concentration of over 500 ppb_v (isobutene units) in indoor air indicates the existence of a relatively high air contamination [20], we can infer with some worry that in those stores where we performed measurements there is a permanent exposure to volatile organic compounds. Among the tVOCs, the most common in footwear industry is toluene. Toluene has a PID correction factor CF of 0.5 (for a 10.6 eV lamp) and is very easily detected by PID devices; therefore, the PID instrument is more sensitive to toluene than to isobutene, which is used as calibration standard. Assuming that the majority of vapor amounts in shoe shops is represented by toluene, the toluene concentration is equal to the displayed PID concentration (in isobutene units) multiplied by the CF.

CONCLUSIONS

Our research, performed over 15 days and over a total period of 8 weeks, aimed to determine whether there is a chronic exposure of the staff working in shoe shops to volatile organic compounds coming especially form adhesives and leatherette. Our investigation encompassed six different shoe shops from Cluj-Napoca, Romania. Results confirmed the presence in the air of photoionizable compounds at ppm levels, thus approaching the admitted TWA limits for toluene. After a detailed analysis of the collected data, we concluded that one should address urgently the occupational exposure to compounds from the category of dangerous volatile organic compounds; we consider that the principal indoor air contaminant is toluene.

We expect that in the near future the PID devices alone and / or coupled with other analytical instrumentation (GC-MS, IMS, etc.) will be a very useful tool for monitoring and improving the indoor air quality and the global environment.

EXPERIMENTAL SECTION

The concentration of volatile photoionizable compounds was measured in six different shoes shops from Cluj-Napoca, Romania, using the sensitive PID instrument **ppbRAE Plus** device model PGM-7620 (made by RAE Systems Inc., USA), during 15 days (in April and May). The measurement time in each shop was about 5 minutes / day. With its highly compact design (size $21.8 \times 7.62 \times 5.0$ cm and weighing only 553 g), this VOCs detector is used on a large scale as a fast monitor.

In this study, the PID device was able to detect in real time (2-3 s) very low vapor concentrations of volatile organic compounds, down to 1 ppb_v, while the range is up to 200 ppm_v. The main components of the PID instrument are the photoionization sensor and the UV lamp. Once the vapors of organic compounds are passing through the sensor and are exposed to the UV photons from the lamp, they are photoionized and the electrons and positive ions generate an ion current, which is then amplified and displayed on the device's display directly in concentration units (ppb_v).

The used PID device was equipped with a standard UV lamp with photon energy of 10.6 eV. The lamp consists of a glass body, provided with a window transparent to UV radiation at the end; this body is filled with a noble gas (Kr) at reduced pressure. The PID sensor is positioned above of the UV lamp. PID uses a pump with a flow rate of 450-550 cm^3 min^{-1}. The air drawn by the pump is then evacuated through an outlet after passing through the PID sensor [21]. A diagram of the photoionization detector in presented in **Figure 3**.

Prior to measurements, the PID instrument has been calibrated using a standard atmosphere containing 10 ppm$_v$ of isobutene in purified air (from a pressure cylinder). All data stored in the internal memory of the instrument were transferred to a PC computer using a RS-232 interface and the appropriate software.
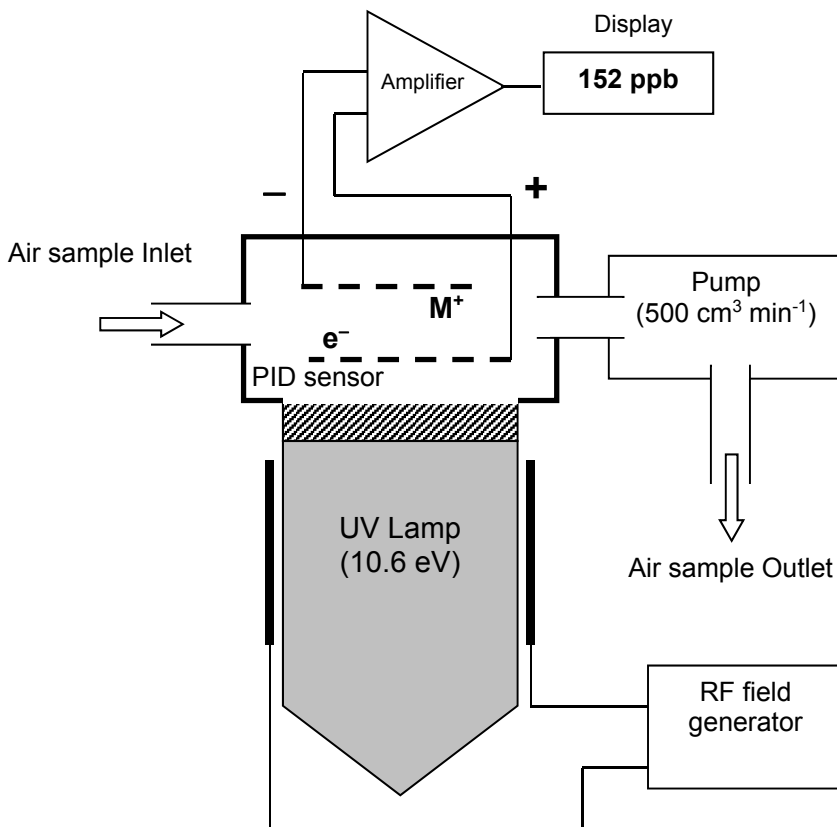
Figure 3. Schematic of the photoionization detector and associated experimental setup. The UV lamp, filled with Kr gas at low pressure, generates photons with the energy of 10.6 eV by using a RF field that induces and sustains a glow discharge when applied onto a set of two opposite metallic plates placed externally to the lamp body. The lamp is a glass body (1/2" o.d. and ca. 4 cm length) with a soldered disc of material transparent to ultraviolet radiation (MgF$_2$ for 10.6 eV lamps).

R E F E R E N C E S

[1]. Care For Your Life: A guide to Indoor Air Quality, **2008**, available on-line at http://www.epa.gov/iaq/pubs/careforyourair.html, accessed in 10.05.2016.

[2]. I. Haiduc, L.D. Boboş, A. Oltean, Environment & Progress, **2004**, 2, 153.

[3]. S.K. Kang, M.Y. Lee, T.K. Kim, J.O. Lee, Y.S. Ahn, *Chemico-Biological Interactions*, **2005**, *153-154*, 65.

[4]. C. Klaassen, Cassarett & Doull's Toxicology - The Basic Science of Poisons (6nd ed.), McGraw-Hill Publishers, **2001**, chapter 24.

[5]. I.A. Raţiu, V. Bocoş-Binţinţan, M. Turner, V.H. Moll, C.L.P. Thomas, *Current Analytical Chemistry*, **2014**, *4*, 488.

[6]. L. Wilkins, *Teratology*, **1997**, *55*, 145.

[7]. Cantox Environmental, Assessment report on toluene for developing ambient air quality objectives, RWDI West Inc., Alberta Environment, **2004**, 12-35.

[8]. U.S. Department of Labor - Occupational Safety and Health Administration, https://www.osha.gov/SLTC/toluene/exposure_limits.html [accessed in October 2016]

[9]. C. Chen, F. Tsow, K. Driggs Campbell, R. Iglesias, E. Forzani, N.J. Tao, *IEEE Sensors Journal*, **2013**, *13*, 1748.

[10]. A. Mizukoshi, K. Kumagai, N. Yamamoto, M. Noguchi, K. Yoshiuchi, H. Kumano, Y. Yanagisawa, *International Journal of Environmental Research and Public Health*, **2010**, *7*, 4127.

[11]. Y.C. Shih, A.S. Yang, C.W. Lu, *Building and Environment*, **2011**, *46*, 1104.

[12]. M. Jia, J. Koziel, J. Pawliszyn, *Field Analytical Chemistry and Technology*, **2000**, *4*, 73-84.

[13]. J. Koziel, M.Y. Jia, A. Khaled, J. Noah, J. Pawliszyn, *Analytica Chimica Acta*, **1999**, *400*, 153.

[14]. A. Robbat, Jr., T. Considine, P. M. Antle, *Chemosphere*, **2010**, *80*, 1370.

[15]. G.B. Ghira, I.A. Raţiu, V. Bocoş-Binţinţan, *Environmental Engineering & Management Journal*, **2012**, *12*, 251.

[16]. E. Ingre-Khans, C. Rudén, M. Breitholtz, *Ecotoxicology and Environmental Safety*, **2010**, 1633.

[17]. H. Bae, W. Yang, M. Chung, *Science of the Total Environment*, **2004**, *323*, 99.

[18]. P. Grasso, M. Sharratt, D.M. Davies, D. Irvine, *Food and Chemical Toxicology*, **1984**, *22*, 819.

[19]. J. Tang, C.Y. Chan, X. Wang, L.Y. Chan, G. Sheng, J. Fu, *Atmospheric Environment*, **2005**, *39*, 7374.

[20]. RAE Systems Inc., **2002**, Using PIDs for indoor air quality surveys (Application Note-AP 212).

[21]. RAE Systems Inc., **2003**, Operation and Maintenance Manual, Parts per Billion VOC monitor PMG-7240, pp. 8-20.

SYNTHESIS OF COBALT FERRITE NANOPARTICLES VIA A SOL-GEL COMBUSTION METHOD

RAREŞ-ADRIAN BORTNIC[a], FIRUŢA GOGA[b*], AMALIA MESAROŞ[c], MIRCEA NASUI[c], BOGDAN STEFAN VASILE[d], DUDRIC ROXANA[a], ALEXANDRA AVRAM[b]

ABSTRACT. This paper presents the synthesis of $CoFe_2O_4$ nanoparticles via a sol-gel combustion method. Nanoparticles with the grain size in the range of 20-70 nm were synthesized using hydrated nitrates of cobalt and iron, sucrose and pectin. Sucrose was used as a polycondensation agent for the formation of the gel. The reaction mechanism for the gel formation is discussed in the paper. The addition of pectin facilitated the formation of a hard gel through the drying of the precursor solution at 200°C. Through a thermogravimetric analysis on the gel, the temperature at which the entire organic part has decomposed is concluded. The fine black nanopowder was obtained after a thermal treatment of the gel at a temperature of 700°C. Infrared spectroscopy (FT-IR) highlighted the presence, respectively the absence of organic compounds before and after the thermal treatment. Structural, morphological and magnetic measurements were conducted using X-ray diffraction (XRD), transmission electron microscopy (TEM), vibrating sample magnetometer (VSM).

Keywords: $CoFe_2O_4$, Sol-gel, nanoparticles, magnetic, ferrite

INTRODUCTION

Given the various applications of $CoFe_2O_4$ spinel ferrite, in areas such as magnetic recording, magnetic fluids and micro wave devices [1,2], this paper explores the possibility of synthesizing said particles through a cost-effective, environmentally safe, sol-gel combustion method.

[a] *Faculty of Physics, Babes-Bolyai University, Cluj-Napoca 400084, Romania*
[b] *Babeş-Bolyai University, Faculty of Chemistry and Chemical Engineering, 11 Arany Janos str., RO-400028, Cluj-Napoca, Romania*
[c] *Technical University of Cluj-Napoca, 28 Memorandumului Street, 400114 Cluj-Napoca, Romania*
[d] *Department of Science and Engineering of Oxide Materials and Nanomaterials, Faculty of Applied Chemistry and Materials Science, Polytechnic University of Bucharest, 1–7 Polizu Street, Bucharest 011061, Romania*
* *Corresponding author: fgoga@chem.ubbcluj.ro*

Adapting a technique proven successful in synthesizing other oxide nanoparticles such as NiO, ZrO_2, La_2O_3, $BaFe_{12}O_{19}$ [3,4] a $CoFe_2O_4$ single phase fine powder was obtained.

Recent studies have reported the successful synthesis of spinel cobalt ferrite through various other methods such as the precipitation method [5], the solvothermal method [6], the co-precipitation method [5], the hydrothermal method [7], and the sol-gel PVA method [8].

The reason behind studying and opting for this sol-gel route is that the reactants used for the process are cost effective, and the polycondensation and gelation agents (sucrose and pectin, respectively) are safe and environmentally friendly.

Sucrose was utilized in the synthesis of nanopowders for various purposes: as a source of C for obtaining composites [9-11], as fuel for obtaining nanomaterials through the combustion method [12-22], and as a chelation agent for the sol-gel method [23-32].

Adapting the sucrose-pectin sol-gel method for obtaining $CoFe_2O_4$ following the drying of the precursor solution, a hard porous gel was obtained. For a thorough understanding of the calcination process that followed, a thermogravimetric analysis was conducted. Results from this analysis gave information regarding the quantitative and qualitative composition of the gel, and the temperatures at which the combustion reactions (organic decompositions) occur.

X-ray diffraction and FT-IR techniques were used in order to characterize the structural properties and purity of the obtained powder and TEM imaging was used for the morphological characterization.

By using these characterization methods, the study concludes that the sucrose-pectin sol-gel combustion method is viable in obtaining $CoFe_2O_4$ nanoparticles with the grain size of 20-70 nm.

RESULTS AND DISCUSSIONS

The following mechanism was proposed for the formation of $CoFe_2O_4$ nanoparticles:

Global reaction:

$$Co(NO_3)_2 \cdot 4H_2O + 2Fe(NO_3)_3 \cdot 9H_2O + nC_{12}H_{22}O_{11} + (12n-2)O_2 \rightarrow$$
$$CoFe_2O_4 + 8NO_2 + 12nCO_2 + 11(n+2)H_2O$$
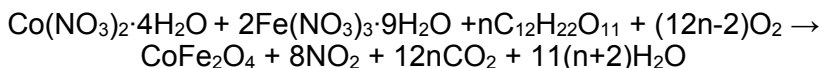
Thermal analysis of the gel decomposition

The thermal analysis (Figure 1) describes the decomposition process of the gel. Correlating the TG curve with the process at hand, we attribute the different stages of weight loss as follows:

214

In the interval of 20-150°C, a 5.89 % weight loss is experienced, attributed to the evaporation of water present in the gel.

The combustion of the gel takes place in the 150-471°C temperature range, in two stages. The first process, between 150-395°C, is slightly exothermic and has a mass loss of approximately 51.17%. The second process, between 395-471°C, is strongly exothermic and has a mass loss of 40.6%.

Above 471°C, no weight loss was recorded.
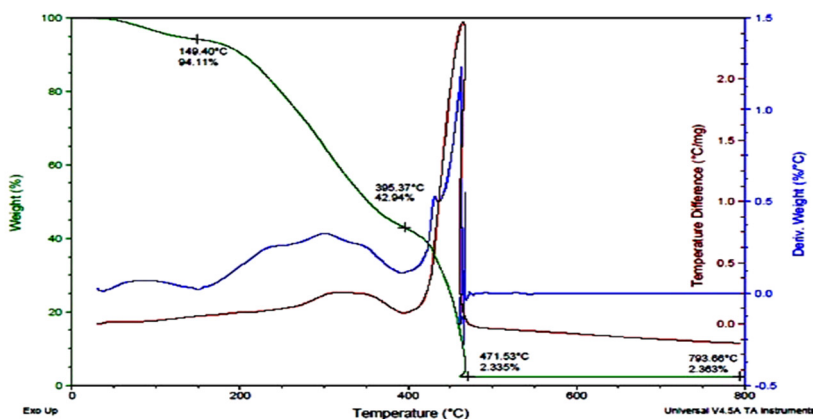
Figure 1. Thermal analysis of the dried gel

X-ray diffraction

The structural characterization was carried out at room temperature by powder X-ray diffraction using a Bruker D8 Advance AXS diffractometer with Cu Kα radiation in the 2θ region 20°-70°. The crystallite sizes were calculated using the Debye-Scherrer formula:

$$D = \frac{k\lambda}{\beta\cos\theta}$$

where β is the peak full width at half maximum (in radians) at the observed peak angle θ, k is the crystallite shape factor (was considered 0.94) and λ is the X-ray wavelength.

The X-ray diffraction pattern (Figure 2) shows that the $CoFe_2O_4$ powder is in a single phase and well crystallized in the cubic spinel structure, with the lattice parameter of 8.382(3) A, obtained from Rietveld analysis. The broadened XRD maxima indicates that the crystallite size is in the nanometer range. The crystallite size calculated using the Debye-Scherrer formula is about 65 nm.
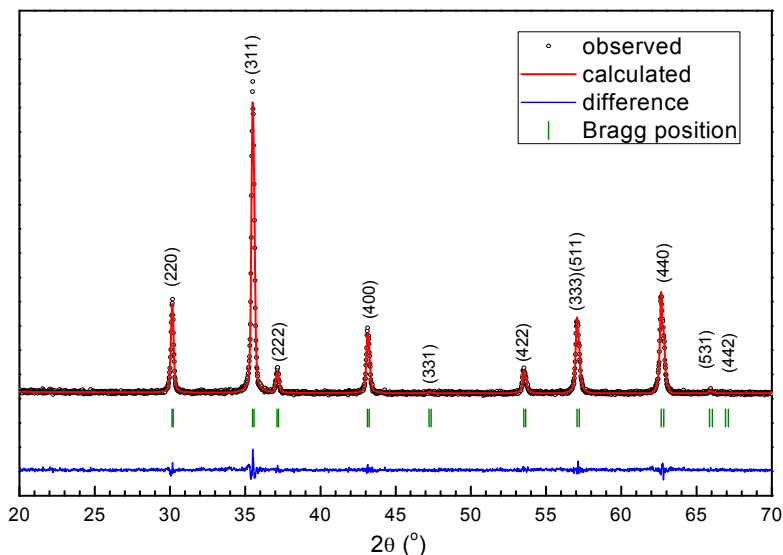
Figure 2. XRD pattern of the CoFe$_2$O$_4$ nanopowder

FT-IR spectroscopy

The FTIR spectra of the precursor and the thermally-treated samples have been presented in Figure 3. The peaks from the precursor spectra can be assigned to the main chemical groups of the starting reagents. The large band observed at approximately 3290 cm^{-1} is attributed to the stretching vibration - ν(OH) of water. The asymmetric ν_{asym}(CH$_2$) and the symmetric ν_{sym}(CH$_2$) stretching modes can be observed at 2932 and 2865 and are in good agreement with the literature [33,34]. The interaction between pectin and metal salts is shown by presence of the asymmetric ν_{asym}(COO$^-$) and the symmetric ν_{sym}(COO$^-$) stretching modes observed at 1630 and 1340 cm^{-1} that correspond to the carboxylic anions coordinated by the metal ions. The difference in their frequencies $\Delta\nu$(COO$^-$)=ν_{asym}(COO$^-$)-ν_{sym}(COO$^-$) is around 290 cm^{-1} suggesting a bidentate coordination between the carboxylate and metal ions. [35] The band at 1539 cm^{-1} is attributed to the stretching vibration of NO^{2-} group, while the CH$_2$ wagging mode is observed at 1447 cm^{-1}. In the 1100-600 cm^{-1} domain the precursor spectrum presents bands corresponding to symmetric stretching mode of C-O-C group (1037 cm^{-1}) and to the wagging mode of C-O bond (778 cm^{-1}). The high intensity band observed in the 600-350 cm^{-1} domain is assigned to the stretching modes of metal-oxygen bonds. The FTIR spectrum of the thermally treated sample confirms the decomposition of the organic part and the stretching vibrations corresponding to the metal – oxygen bonds increase in intensities.

216
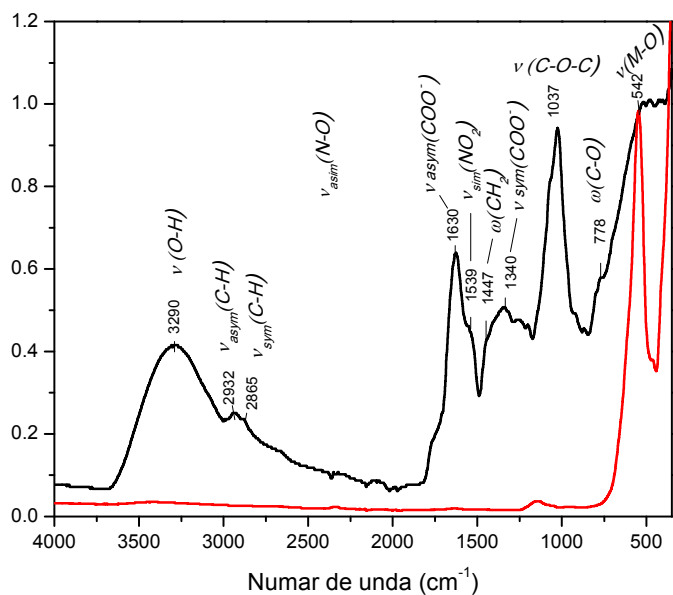
Figure 3. FT-IR spectra of the dried gel (black) and the CoFe$_2$O$_4$ powder (red).

Transmission electron microscopy

The TEM analysis presented in Figure 4 reveals mildly agglomerate pseudo-spherical particles with a grain size ranging between 20 – 75 nm.
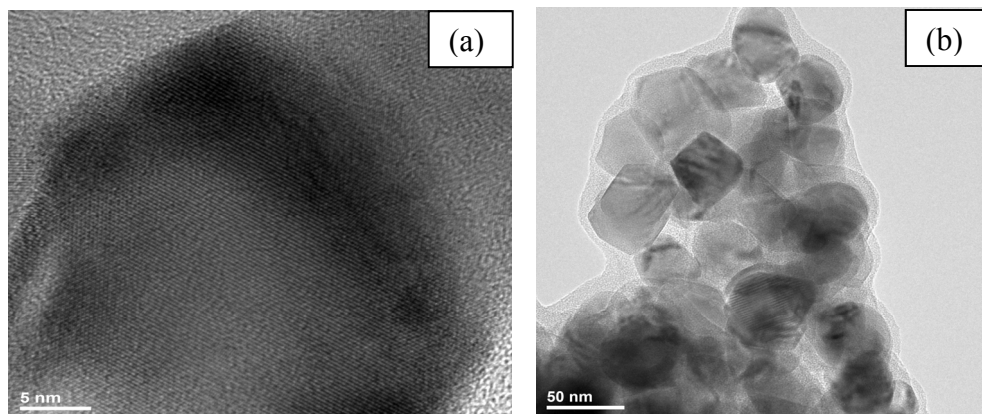
Figure 4. TEM images of the CoFe$_2$O$_4$ nanoparticles at a scale of 5 nm (a), and 50 nm (b)

Vibrating sample magnetometer

Figure 5 shows the field dependence of magnetization for $CoFe_2O_4$ nanoparticles at room temperature. For the $CoFe_2O_4$ nanoparticles the value of the saturation magnetization (Ms) and coercivity (Hc) are found as ~1.2 emu/g and ~55 Oe respectively. The small value of the coercivity of $CoFe_2O_4$ nanoparticles indicates that these nanoparticles are near the superparamagnetic limit. The M(H) curve also contains a linear part at higher fields indicating a very significant paramagnetic contribution to the magnetization.
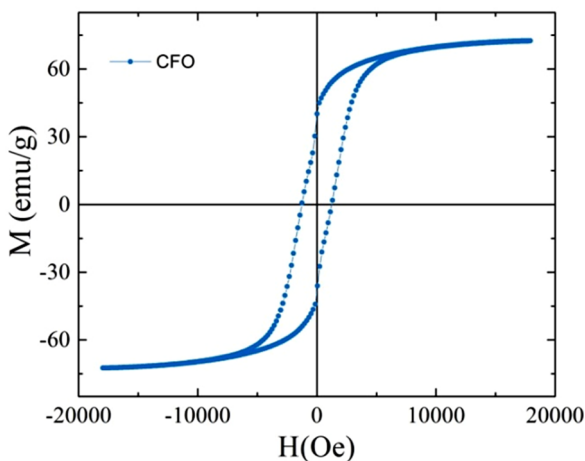
Figure 5. Magnetic hysteresis loops for $CoFe_2O_4$ nanoparticles at room temperature.

CONCLUSIONS

Through this endeavor it has been proven that $CoFe_2O_4$ nanoparticles can be synthesized via the sol-gel, pectin-sucrose route. This method has potential value considering these organic compounds are non-toxic, cheap and available at an industrial scale. Also it is worth mentioning that by proving that $CoFe_2O_4$ can be synthesized through this method, it has again been validated that the sol-gel method has immense applicability, is versatile and could be used for synthesizing various other systems.

Following the information in this paper the process could be easily adapted at a large scale.

The thermogravimetric analysis, besides giving information about the decomposition of the gel can prove useful in devising calcination diagrams for this kind of products.

Using X-ray diffraction and FT-IR spectroscopy it has been proved that the obtained powder is a single phase spinel $CoFe_2O_4$ ferrite.

TEM imaging has permitted the precise view regarding the size and shape of the obtained particles. The results showed mildly agglomerate particles with a grain size of 20-75 nm.

The small value of coercivity of $CoFe_2O_4$ nanoparticles indicates that these nanoparticles are near the superparamagnetic limit.

EXPERIMENTAL SECTION

Synthesis of $CoFe_2O_4$ ferrite nanoparticles

The $CoFe_2O_4$ nanoparticles, were obtained via the sol-gel method, using sucrose as a poly-condensation agent and pectin as a gelation agent. In order to synthesize 2 mmols of $CoFe_2O_4$, 2 mmols of $Co(NO_3)_2 \cdot 4H_2O$ and 4 mmols of $Fe(NO_3)_3 \cdot 9H_2O$, respectively, were separately dissolved in Milli-Q water. The solutions were heated to 60°C and vigorously stirred. The quantity of water needed was deduced by slowly adding droplets to the solutions until the full dissolution of the precursor salts. As the pre-mentioned solutions were getting thoroughly homogenized, 14.6 mmols of sucrose were dissolved in 50 ml Milli-Q water. The obtained sucrose solution was halved, and each half was mixed with the precursor solutions under strong magnetic stirring, lowering the temperature to 40°C. After 30 minutes the two solutions were mixed, continuing the strong magnetic stirring. Following the homogenization of the solution, pectin was added in a quantity of 1:5 weight ratio - pectin: sucrose. After 20 minutes of stirring, using a 1 M solution of nitric acid, the pH was fixed to be in the range of 1.5-3. This final solution was poured in a ceramic capsule and subjected to drying at 80 °C for 24 hours and at 200 °C for another 24 hours. After the annealing of the gel at 700°C for 2 hours, a fine black powder was obtained.

Analysis Techniques

Thermogravimetry and differential thermal analysis (TG/DTA) curves were recorded with a thermal analyzer TA Instruments SDT Q600 up to 800°C, in air, at a heating rate of 10°C/min, using Al_2O_3 as a reference.

The structural characterization has been carried out at room temperature by powder X-ray diffraction using a Bruker D8 Advance AXS diffractometer with Cu Kα radiation in the 2θ region 20°-70°.

FT-IR spectral analysis was conducted using a Nicolet 6700 FT-IR Spectrometer.

The high-resolution images were obtained using a Tecnai G2 F30 S TWIN transmission electron microscope, TEM, (FEI, Nederlands), equipped with a STEM/HAADF detector. The microscope operates at an acceleration voltage of 300 kV (Schottky field emitter) with a TEM point resolution of 2 Å nm and a TEM line resolution of 1 Å.

The magnetization properties were studied using a vibrating sample magnetometer (VSM Lake Shore).

ACKNOWLEDGMENTS

R E F E R E N C E S

[1]. B.M. Berkovsky, V.F. Medvedev, M.F. Krakov, *Magnetic Fluids: Engineering Applications*, Oxford University Press, Oxford, **1993**;

[2]. A. Goldman, *Modern Ferrite Technology*, Van Nostrand Reinhold, New York, 1993;

[3]. C. Suciu, A. Vik, F. Goga, E. Dorolti, R. Tetean, A.C. Hoffmann, *Studia UBB Chemia*, **2009**, LIV, *4*, 261-271;

[4]. C. Suciu, A.C. Hoffmann, P. Kosinski, *Journal of Materials Processing Technology* **2008**, *202*, 316–320;

[5]. M. Houshiar, F. Zebhi, Z.J. Razi, A. Alidoust, Z. Askari, *Journal of Magnetism and Magnetic Materials,* **2014**, *371*, 43-48;

[6]. A. Baykal, H. Deligöz, H. Sozeri, Z. Durmus, M.S. Toprak, *Journal of Superconductivity and Novel Magnetism*, **2012**, *25*:1879–1892;

[7]. D. Zhao, X. Wu, H. Guan, E. Han, *Journal of Supercritical Fluids,* **2007**, *42*, 226–233;

[8]. M. Sivakumar, S. Kanagesan, R. Suresh Babu, S. Jesurani, R. Velmurugan, C. Thirupathi, T. Kalaivani, *Journal of Materials Science: Materials in Electronics*, **2012**, *23*:1045–1049;

[9]. R. Mohammad-Rahimi, H.R. Rezaie, A. Nemati, *Ceramics International,* **2011**, *37*, 1681-1688;

[10]. Seung-Ah Hong, Su Jin Kim, Kyung Yoon Chung, Youn-Woo Lee, Jaehoon Kim, Byung-In Sang, *Chemical Engineering Journal,* **2013**, *229*, 313–323;

[11]. Li Wang, Wenting Sun, Xianyi Tang, Xiankun Huang, Xiangming He, Jianjun Li, Qingwu Zhang, Jian Gao, Guangyu Tian, Shoushan Fan, *Journal of Power*, *Sources,* **2013**, *244*, 94-100;

[12]. Jun Yang,∗, Xiaoci Li, Junyi Zhou, Yu Tang, Yuanming Zhang, Yongwang Li *Journal of Alloys and Compounds* **2011**, *509*, 9271– 9277;

[13]. R. Nagaraja, Nagaraju Kottam, C.R. Girija, B.M. Nagabhushana, *Powder Technology,* **2012,** *215-216*, 91–97;

[14]. Mohamed Aklalouch, José Manuel Amarilla, Rosa M. Rojas, Ismael Saadoune, José María Rojo, *Journal of Power Sources,* **2008**,*185*, 501–511;

[15]. M.A. Gabal, E.A. Al-Harthy, Y.M. Al Angari, M. Abdel Salam, A.M. Asiri, *Journal of Magnetismand Magnetic Materials,* **2016**, *407*,175–181;

[16]. Ibram Ganesh, Paula M.C. Torres, J.M.F. Ferreira, *Ceramics International, 2009* *35*, 1173–1179;

[17]. Abdelfattah Mahmouda, Jose Manuel Amarilla, Karima Lasri, Ismael Saadoune *Electrochimica Acta*, **2013**, *93*,163-172;

[18]. M.A. Gabal, A.A. Al-Juaid, S.M. Al-Rashed, M.A. Hussein, F. Al-Marzouki, *Journal, of Magnetism and Magnetic Materials,* dx.doi.org/10.1016/j.jmmm. **2016**, 10.147;

[19]. Cheng-Gong Han, Chunyu Zhu, Genki Saito, Tomohiro Akiyama, *Advanced Powder Technology*, **2015**, *26*, 665–671;

[20]. Seung-Beob Yi, Hoon-Taek Chung, Ho-Gi Kim, *Electrochemistry Communications,* **2007**, *9*, 591–595;

[21]. G. Ramakrishna, H. Nagabhushana, D.V. Sunitha, S.C. Prashantha, S.C. Sharma, B.M. Nagabhushana, *Spectrochimica Acta Part A: Molecular and Biomolecular Spectroscopy,* **2014**, *127*, 177–184;

[22]. J.G.S. Duque, E.A. Souza, C.T. Meneses, L. Kubota, *Physica B*, **2007**, *398*, 287–290;

[23]. E.A. Souza, J.G.S. Duque, L. Kubota, C.T. Meneses, *Journal of Physics and Chemistry of Solids*, **2007**, *68*, 594–599;

[24]. S.F. Wang, X.T. Zu, G.Z. Sun, D.M. Li, C.D. He, X. Xiang, W. Liu, S.B. Han, S. Li, *Ceramics International*: http//dx.doi.org/10.1016/j. ceramint. **2016**, 09.075;

[25]. Zahra Negahdari, Ali Saberi, Monika Willert-Porada, *Journal of Alloys and Compounds,* **2009**, *485*, 367–371;

[26]. M. Mozafari, M. Gholipourmalekabadi, N.P.S. Chauhan, N. Jalali, S. Asgari, J.C. Caicedoa, A. Hamlekhan, A.M. Urbanska, *Materials Science and Engineering* **2015**, C 50, 117–123;

[27]. J. Jadhav, S. Biswas, A.K. Yadav, S.N. Jha, D. Bhattacharyya, *Journal of Alloys and Compounds*, **2017**, *696*, 28- 41;

[28]. A.G. Khaledi, S. Afshar, H.S. Jahromi, *Materials Chemistry and Physics*, **2012**, *135*, 855-862;

[29]. A. Alhaji, R. Shoja Razavi, A. Ghasemi, M.R. Loghman-Estarki, *Ceramics International*, http://dx.doi.org/10.1016/j.ceramint.2016.11.057;

[30]. Ali Majedi, Fatemeh Davar, Alireza Abbasi, *Journal of Industrial and Engineering Chemistry,* **2014**, 20, 4215–4223;

[31]. K. Agilandeswari, A. Ruban Kumar, *Advanced Powder Technology*, **2014**, *25*, 904–909;

[32]. D. Gingasu, I. Mandru, O.C. Mocioiu, S. Preda, N. Stanica, L. Patron, A Ianculescu, O. Oprea, S. Nita, I. Paraschivescu, M. Popa, C. Saviuc, C. Bleontu, M.C. Chifiriuc, *Materials Chemistry and Physics,* **2016**, *182*, 219-230;

[33]. A.B. Brizuela, L.C. Bichara, E. Romano, A. Yurquina, S. Locatelli, S.A. Brandán, *Carbohydrate Research,* **2012**, *361*, 212–218;

[34]. K. Elen, A. Kelchtermans, H. Van den Rul, R. Peeters, J. Mullens, A. Hardy, M.K. Van Bael, *J. Nanomater*., **2011**, *1/1*, 18.

INFLUENCE OF THERMAL TREATMENT ON STRUCTURAL PROPERTIES OF SOME ZINC-PHOSPHATE GLASSES DOPED WITH IRON IONS

LIVIU CALIN BOLUNDUT[a*] AND VASILE POP[a]

ABSTRACT. Glass ceramics samples with chemical composition $(Fe_2O_3)_x \cdot (P_2O_5)_{40} \cdot (ZnO)_{(60-x)}$ $(0 \leq x \leq 20 \text{ mol\%})$ were prepared by melt-quenching technique, followed by a thermal treatment at two different temperatures for two hours. Structural properties were studied by DTA, XRD, and FTIR measurements. From DTA measurements can be observed that, with increasing in concentration of the dopant (Fe_2O_3), the transition and crystallization temperatures increase. The XRD data show, the presence of two or three crystalline phases, and the FTIR data confirm the existence of ZnO_4 structural units in our samples. So the thermal treatment applied to the samples lead to changes in the structural properties and also to some modification in the glass ceramic network.

Keywords: zinc phosphate glass ceramics, DTA, XRD, transitional metals doped glass ceramics.

INTRODUCTION

Due to their multiple applications and important physical properties, phosphate glasses have fascinated the researchers in the recent years. This kind of materials have potentials applications in a great diversity of technology areas such as: optical and magnetic devices [1], bio-materials [2, 3], memory switching [4], electronics [5, 6], matrix for containment of the waste [7], energy transfer materials [8], battery materials [9], solid state laser hosts [10, 11], etc. Also, the phosphate glasses have some limits due to their poor chemical durability. The presence of water will destroy the P-O-P bonds from the glass network, so the use of this kind of glasses under hydrated conditions is limited [12, 13]. The adding of transition metal ions, in the phosphate glass matrix, will lead to the

---

[a] *Technical University of Cluj-Napoca, Faculty of Materials and Environmental Engineering, Physics and Chemistry Department 28 Memorandumului str., RO-400114, Cluj-Napoca, Romania*
* Corresponding author: liviu.bolundut@chem.utcluj.ro

improving of the chemical durability. When metal ions are incorporated in the glass network, are produced some structural changes. These ions will replace some phosphorus atoms and will form P-O-M^{n+} bonds that are more stable at the water presence [14-16]. This behavior increase the sphere of applications for phosphate glasses.

As example of glasses with transition metals ions, can be mentioned the zinc phosphate and zinc boro-phosphate glasses [14, 15].

In the zinc phosphate glasses, zinc ions act as network modifier, in this way this kind of glasses have a high transparency in the UV region and can be used at the fabrication of liquid crystal screens and withe light-emitting diodes [11].

Glasses containing transition metal ions are also important from scientific point of view due to the presence of free electrons in d orbitals or the presence of free d orbitals at the metallic ions. This cause the modifications of the coordination number, bonding characteristics, covalence state of the substituents metal ions and of the glass networks. All this studies are very helpful in understanding the structure of glassy state [17].

The aim of this work was to obtain some zinc phosphate glasses doped with iron (III) oxide (Fe_2O_3) and investigate them by DTA, XRD, and FTIR measurements in order to establish the structural changes produced by the heat treatments at different temperatures applied to all obtained samples.

RESULTS AND DISCUSSION

DTA (Differential Thermal Analysis) measurements are important because in this way can be determined the glass characteristic temperatures such as: melting temperature T_m, glass transition temperature T_g and crystallization temperature T_c. Using these parameters can be estimated for example the thermal stability of the glasses according with the literature [17-20].

The figure 1 present the DTA curves, for our obtained samples, at the heating rate of 15 °C/minute.

The DTA curve for the glass matrix (x = 0 mol%) show a weak glass transition around temperature of 412 °C, a peak situated at 667 °C, for a slow crystallization process, followed by another two endothermic effects corresponding to the melting of material in two steps that are situated at 776 and 796 °C.

In the case of samples that contain a high concentration of iron ions (x = 10 mol%) a clear glass transition can be observed and also the increase of the transition temperature at 451 °C. On the other hand seems to appear two exothermic effects corresponding to crystallization processes (due to the formation of two crystalline phases) around of 681 and 758 °C, followed by two endothermic ones at 872 and 911 °C due to the melting of material.

For the sample with 20 mol% of iron (III) oxide can be observed that the glass transition and the crystallization temperatures increase.

Also the figure 1 present a single peak due to the glass transition temperature (T_g), indicating the homogeneity of the all obtained samples.
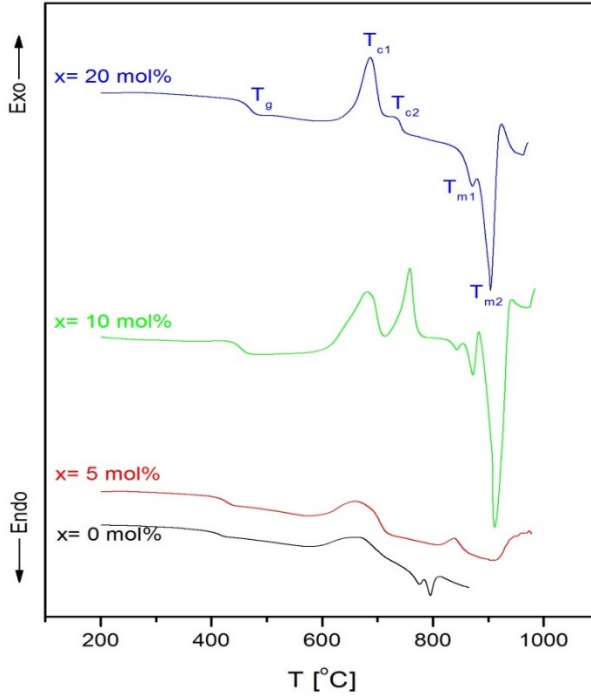
Figure 1. The DTA curves of the $(Fe_2O_3)_x \cdot (P_2O_5)_{40} \cdot (ZnO)_{(60-x)}$ glasses

For our samples were been calculated some parameters such as: activation energy of vitreous transition (E_g), activation energy at crystallization (E_c), fragility index (F), thermal stability (TS) and glass stability (S), parameters that arte listed in table 1.

Table 1. The glass characteristic temperatures (T_g, T_c, T_m), stability parameters (TS, S) and activation energies (E_g, E_c) for the studied $(Fe_2O_3)_x \cdot (P_2O_5)_{40} \cdot (ZnO)_{(60-x)}$ (0≤x≤20 mol%) glasses

x	T_g [ºC]	T_{c1} [ºC]	T_{c2} [ºC]	T_{m1} [ºC]	T_{m2} [ºC]	TS [ºC]	S [ºC]	F	E_g [kJ/ mol]	E_c [kJ/mol]
0	412	667	-	776	796	195	35,7	20,2	264,4	176,3
5	427	672	-	807	909	183	26,6	37,8	309,2	267,1
10	451	681	758	872	911	168	23,1	47,3	408,3	310,4
20	469	687	734	871	904	163	19,1	50,1	449,7	335,4

The thermal stability (TS) was introduced by Dietzel [18] and is expressed by the equation:

$$TS = T_c - T_g \qquad (1)$$

Glass stability parameter (S) introduced by Saad and Poulin [20] was calculated using the relation:

$$S = \frac{(T_p - T_C) \cdot (T_C - T_g)}{T_g} \qquad (2)$$

Another parameter was the fragility index that can be obtained using the equation [21]:

$$F = \frac{E_g}{R \cdot T_g \cdot ln10} \qquad (3)$$

Activation energy of the studied glasses was calculated using the Kissinger formula [22]:

$$\ln\left(\frac{T_g^2}{\beta}\right) = \frac{E_g}{R \cdot T_g} + const. \qquad (4)$$

where β represent the heating rate of DTA (β = 5, 10, 15, 20, 25 ^{0}C/minute), and R is the gas constant.

These parameters express the stability and fragility of the obtained samples, and also provide information about structural changes that take place in the glass ceramic network.

From table 1 can be observed that the glass matrix has the highest thermal stability indicated by all glass stability parameters. Increasing the doping level with iron ions by adding of the Fe_2O_3 leads to the decrease of glass stability probably due to some changes that take place in the glass ceramic network (increase the number of non-bridging oxygen). Also, when iron(III) oxide is introduced, the P-O-P bonds are transformed in Fe-O-P bonds and the chemical character of the bonds from the glass network is modified. The ionic character of the bonds increase and the glasses became more fragile according with the literature data [21].

In figure 2a and 2b are presented the dependences $\ln(T_g^2/\beta)$ versus $10^3/T_g$ and $\ln(T_c^2/\beta)$ versus $10^3/T_c$ for the investigated samples.

From the slopes of the $\ln(T_g^2/\beta)$ versus $10^3/T_g$ and $\ln(T_g^2/\beta)$ versus $10^3/T_g$ graphics can be determined E_g and E_c activation energies for the studied samples. In our case the activation energy of vitreous transition (E_g) and the activation energy at crystallization (E_c) increase with the increasing of the doping level (the concentration of Fe_2O_3).
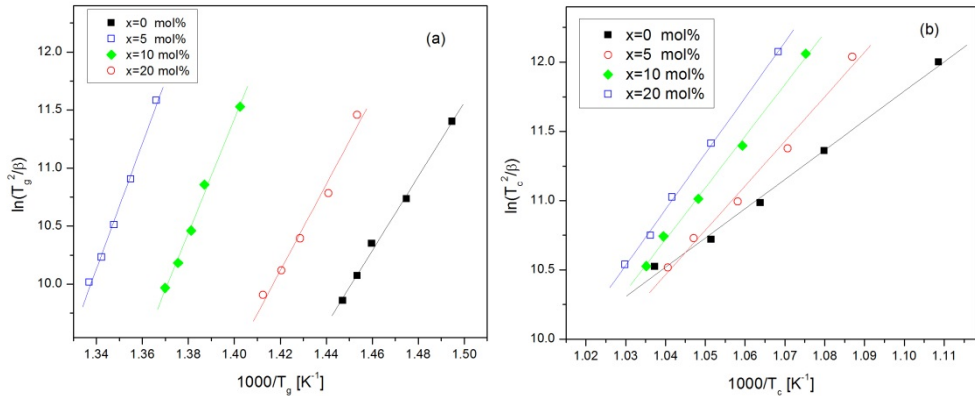
Figure 2a and 2b. The dependences $\ln(T_g^2/\beta)$ on $10^3/T_g$ for the $(Fe_2O_3)_x\cdot(P_2O_5)_{40}\cdot(ZnO)_{(60-x)}$ glasses and the dependences $\ln(T_c^2/\beta)$ on $10^3/T_c$ for the $(Fe_2O_3)_x\cdot(P_2O_5)_{40}\cdot(ZnO)_{(60-x)}$ glasses

The activation energy of glass transition (E_g) seems to be responsible for the molecular motion and rearrangements of the atoms around T_g temperature. According with the literature, a small value of E_g lead to a stable glass sample [23]. So in our case, the sample with the smallest E_g (the most stable one, from this point of view) is the matrix.

The XRD patterns obtained for the studied samples of the glass system $(Fe_2O_3)_x\cdot(P_2O_5)_{40}\cdot(ZnO)_{(60-x)}$ annealed for two hours at different temperatures are shown in figure 3.
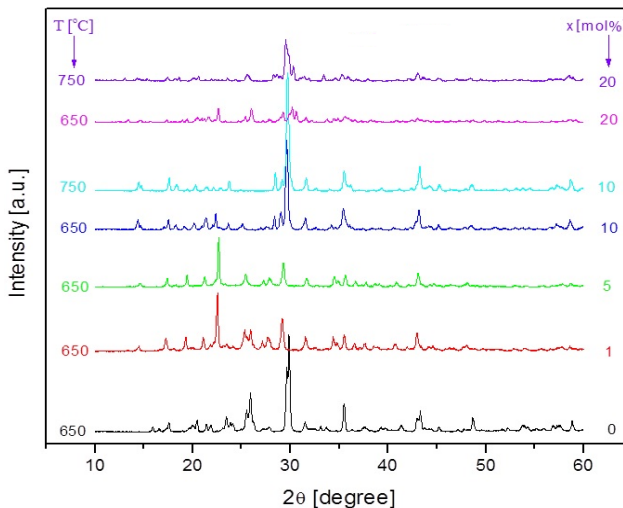
Figure 3. The XRD patterns of $(Fe_2O_3)_x\cdot(P_2O_5)_{40}\cdot(ZnO)_{(60-x)}$ glass ceramics

The matrix $(P_2O_5)_{40} \cdot (ZnO)_{60}$ annealed for two hours at 650 ^{0}C contain two crystalline phases $Zn_2P_2O_7$ (PDF:34-1275) and $Zn(PO_3)_2$ (PDF:30-1488) and the degree of crystallinity for this sample is 71.78%. The degree of crystallinity degree was calculated using Reflex computer program part of Material Studio software [24]. For the samples with concentration of iron (III) oxide equal or higher than x = 10 mol% was identified another crystalline phase that contain iron ($ZnFe_2O_4$ PDF:74-2397). In the table 2 is listed the evolution of crystalline phases obtained for the studied samples that were annealed for two hours at different temperatures.

Table 2. The crystalline phases evolution for the studied samples

x [mol%]	T_{tt} [ºC]	Crystalline Phase
0	650	$Zn_2P_2O_7$, $Zn(PO_3)_2$
3	650	$Zn_2P_2O_7$, $Zn(PO_3)_2$
5	650	$Zn_2P_2O_7$
10	650	$Zn_2P_2O_7$, $ZnFe_2O_4$
10	750	$Zn_2P_2O_7$, $ZnFe_2O_4$
20	650	$Zn_2P_2O_7$, $ZnFe_2O_4$, $Zn(PO_3)_2$
20	750	$Zn_2P_2O_7$, $ZnFe_2O_4$, $Zn(PO_3)_2$

The thermally untreated samples, present XRD patterns that show an amorphous nature of the samples up to a concentration of iron(III) oxide x < 30 mol%. For the sample with iron (III) oxide content of 30 mol% was observed a large halo and peaks characteristic to $FePO_4$ crystalline phase [25]. Due to all mentioned above, the heat treatment increase the degree of crystallinity and also make important changes in the glass ceramic network of the samples.

These changes can be proved also by FTIR measurements that are presented in figure 4a.

The IR spectra were deconvoluted (using a Gaussian type function) in order to obtain some information about the type of structural groups that are present in our glass ceramic network. Also the deconvoluted spectra help us to see the influence of the heat treatment on these structural units (by assignments of the IR vibrations) and the changes that take place in the glass ceramic network. For example we present the deconvolution in case of glass ceramic matrix and for the sample doped with 5 mol% of Fe_2O_3 (figure 5).
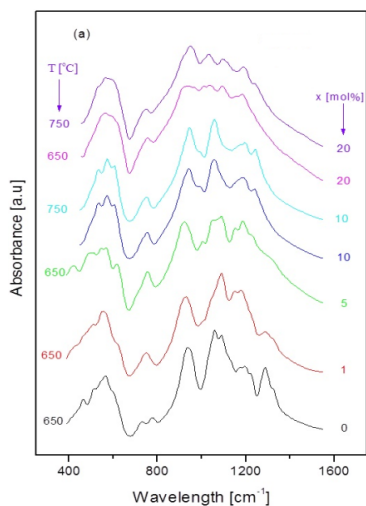
Figure 4. The FTIR spectra for the studied glass ceramics
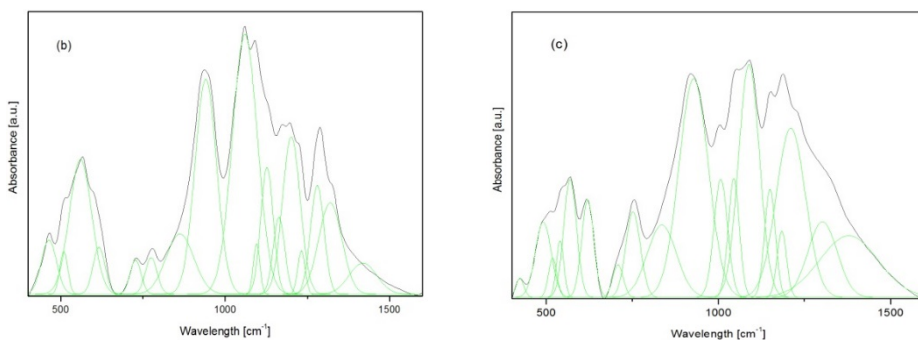
Figure 5. The deconvoluted FTIR spectra for a) the glass ceramic matrix and b) for the sample doped with x = 5 mol% of iron(III) oxide

The assignments for the IR vibrations of the studied samples are listed in table 3.

Analyzing the FTIR spectra of the thermally treated samples can be observed the fact that are more solved then those of the thermally untreated samples [25]. Due to the fact that a solved spectrum correspond to an ordered structure according with literature [25] our obtained samples present a more ordered structure than the thermally untreated samples.

By increasing the concentration of iron(III) oxide the FTIR peaks became broad (see figure 4), due to some structural changes in the network (increase the number of non-bridging oxygen atoms). These changes correspond to a more disordered structure, similar with the case of the untreated samples [25]. The IR results are in agreement with the other obtained data.

Table 3. The assignments, of the IR vibration for the annealed samples from the glass ceramic system $(Fe_2O_3)_x \cdot (P_2O_5)_{40} \cdot (ZnO)_{(60-x)}$

Wavenumber [cm^{-1}]	Assignment	Reference
424-497	δ (O=P-O)	[26]
503-518	Zn-O in ZnO$_4$ units	[27]
535-559	δ (O-P-O)	[28, 29]
560-569	ν (Fe-O) in FeO$_4$ units	[30, 31, 32]
604-625	ν (Zn-O) in ZnO$_4$ units	[27, 33, 34]
706-727	ν_s (P-O-P)	[35]
739-779		
812-862	ν_{as} (P-O-P)	[36]
927-948		
988-1006	ν (P-O$^-$) (Q^0)	[37]
1036-1059	$\nu \left(PO_3\right)^{2-}$ (Q^1)	[38, 39]
1089-1127	$\nu_{as}\left(PO_4\right)^{3-}$ (Q^0)	[38, 39]
1138-1163	$\nu \left(PO_2\right)^-$ (Q^2)	[38, 39]
1184-1201	$\nu_{as}\left(PO_2\right)$ (Q^2)	[37]
1210-1247		
1277-1321	ν_{as} (P=O)	[39]
1355-1419	ν_s (P=O)	[28]

Legend:

δ- bending vibrations

ν- stretching vibrations

ν_{as}- asymmetric stretching vibrations

ν_s- symmetric stretching vibrations

Concluding, the thermal treatment lead to the changes in the glass ceramic network for example the formation of the ZnO$_4$ units, which are not present in the glass ceramic network of the untreated samples [25].

CONCLUSIONS

Some glass ceramic samples with stoichiometric composition $(Fe_2O_3)_x \cdot (P_2O_5)_{40} \cdot (ZnO)_{(60-x)}$ were obtained by melt-quenching technique followed by a heat treatment for two hours at 650 and 750 ^{0}C.

The DTA measurements show that with increasing in concentration of the iron(III) oxide (Fe$_2$O$_3$) the transition and crystallization temperatures increase also. The glass matrix present the highest stability and by increasing of the doping level the stability of glass (TS, S) decreases probably by the increasing of the non-bridging oxygen number from the glass network.

The XRD data for the thermally treated samples show the presence of two or three crystalline phases in the studied samples.

The thermal treatment lead to the formation of ZnO_4 and FeO_4 units confirmed by the FTIR data. Also the FTIR spectra of the samples thermally treated are more solved, this mean a more ordered structure.

In conclusion all the obtained data confirm that the thermal treatment lead to the changes in the glass ceramic network, the structure becoming more ordered, that in the case of the untreated samples.

EXPERIMENTAL SECTION

Samples, using the melt-quenching technique, corresponding to the glass ceramic system $(Fe_2O_3)_x \cdot (P_2O_5)_{40} \cdot (ZnO)_{(60-x)}$ were obtained. The starting materials used (Fe_2O_3, P_2O_5, ZnO) were of high purity Alfa Aesar (99.9 %). The stoichiometric amounts of these oxides were mixed and homogenized into an agate mortar. The mixtures were melted using a porcelain crucible at 1100 ^{0}C for 15 minutes using an electric furnace. Then the molten material was quickly cooled at room temperature by pouring onto a stainless-steel plate. After that the samples were thermally treated for two hours at different temperatures 650 and 750 ^{0}C.

The DTA data were obtained using a PerkinElmer TG/DTA 6300 thermal analyzer under argon gas atmosphere.

The XRD measurements were carried out using a XRD-6000 Shimadzu diffractometer, with a graphite monochromator Cu-K_α radiation ($\lambda = 1.54$ Å) at room temperature.

The FTIR spectra were done using a FTIR apparatus (JASCO FTIR 6200 spectrometer) in the 400-1800 cm^{-1}. The spectra were registered using KBr pellets.

R E F E R E N C E S

[1]. G. Kumar, S.K. Apte, S.N. Garaje, M.V. Kulkarni, S.M. Mahajan, B.B. Kale, *Applied Physics A-Materials Science & Processing*, **2010**, *98*, 531.

[2]. J.C. Knowles, *Journal of Materials Chemistry*, **2003**, *13*, 2395.

[3]. V. Rajendran, A.V. Gayathri Devi, M. Azooz, F H. El-Batal, *Journal of Non-Crystalline Solids*, **2007**, *353*, 77.

[4]. A. Pan, A. Ghosh, *Journal of Materials Research*, **2002**, *17*, 1941.

[5]. A.A. Bahgat, B.A.A. Makram, E.E. Shaisha, M.M. El-Desoky, *Journal of Alloys and Compounds*, **2010**, *506*, 141.

[6]. R.K. Singh, A. Srinivasan, *Journal of Magnetism and Magnetic Materials*, **2010**, *322*, 2018.

[7]. B.C. Sales, L.A. Boatner, *Materials Letters*, **1984**, *2(4B)*, 301.

[8]. P.I. Paulose, G. Jose, N.V. Unnikrishnan, *Journal of Non-Crystalline Solids*, **2010**, *356*, 93.

[9]. B. Kang, G. Ceder, *Nature*, **2009**, *458*, 190.

[10]. B. Tischendorf, J.U. Otaigbe, J.W. Wiench, M. Pruski, B.C. Sales, *Journal of Non-Crystalline Solids*, **2001**, *282*, 147.

[11]. U. Caldino, E. Alvarez, A. Speghini, M. Bettinelli, *Journal of Luminescence*, **2013**, *135*, 216.

[12]. M.G. Mesko, D.E. Day, *Journal of Non-Crystalline Solids*, **1999**, *27*, 327.

[13]. A. Mogusmilankovic, V. Licina, S.T. Reis, D.E. Day, *Journal of Non-Crystalline Solids*, **2007**, *353*, 2659.

[14]. J.F. Ducel, J.J. Videau, *Materials Letters*, **1992**, *13*, 271.

[15]. L. Koudelka, P. Mosner, *Materials Letters*, **2000**, *42*, 194.

[16]. M.K. Hwang, B.K. Ryu, *Journal of the Korean Physical Society*, **2016**, *69*, 157.

[17]. P. Pascuta, M. Bosca, G. Borodi, E. Culea, *Journal of Alloys and Compounds*, **2011**, *509*, 4314.

[18]. A. Dietzel, *Glastechnische Berichte-Glass Science and Technology*, **1968**, *22*, 41.

[19]. A. Hruby, *Physica B*, **1972**, 22, 1187.

[20]. M. Saad, M. Poulin, *Materials Science Forum*, **1987**, *19-20*, 11.

[21]. N. Mehta, R.S. Tiwari, A. Kumar, *Materials Research Bulletin*, **2006**, *41*, 1664.

[22]. H.E. Kissinger, *Analytical Chemistry*, **1957**, *29*, 1702.

[23]. N.S. Saxena, *Journal of Non-Crystalline Solids*, **2004**, *345-346*, 161.

[24]. *Accelrys Software Inc. Materials Studio, Release* 5.5. **2010**.

[25]. P. Pascuta, G. Borodi, A. Popa, V. Dan, E. Culea, *Materials Chemistry and Physics,* **2010**, *123*, 767.

[26]. H. Doweidar, Y.M. Moustafa, K. El-Egili, I. Abbas, *Vibrational Spectroscopy,* **2003,** *339*, 83.

[27]. E. Mansour, G. El-Damrawi, *Physica B*, **2010**, *405*, 2137.

[28]. D.A. Magdas, O. Cozar, V. Chis, I. Ardelean, N. Vedeanu, *Vibrational Spectroscopy*, **2008**, *48*, 251.

[29]. P. Pascuta, G. Borodi, N. Jumate, I. Vida-Simiti, V. Dan, E. Culea, *Journal of Alloys and Compunds*, **2010**, *504*, 479.

[30]. M.G. Ferreira da Silva, B.F.O. Costa, *Journal of Non-Crystalline Solids*, **2001**, *293-295*, 534.

[31]. I. Ardelean, R. Lungu, P. Pascuta, *Journal of Materials Science - Materials in Electronics*, **2007**, *18*, 837.

[32]. I. Ardelean, P. Pascuta, *Materials Letters*, **2004**, *58*, 3499.

[33]. H.S. Liu, T.S. Chin, S.W. Yung, *Materials Chemistry and Physics,* **1997**, *50*, 1.

[34]. P. Pascuta, E. Culea, *Journal of Materials Science - Materials in Electronics*, **2011**, 22, 1060.

[35]. P. Subbalakshmi, N. Veeraiah, *Journal of Non-Crystalline Solids*, **2002**, *298*, 89.

[36]. B.H. Jung, D.N. Kim, H.S. Kim, *Journal of Non-Crystalline Solids,* **2005**, *351*, 3356.

[37]. Y.M. Lai, X.F. Liang, S.Y. Yang, J.X. Wang, L.H. Cao, B. Dai, *Journal of Molecular Structure*, **2011**, *992*, 84.

[38]. L. Baia, M. Baia, W. Kiefer, J. Popp, S. Simon, *Chemical Physics,* **2006**, *327*, 63.

[39]. S. Marzouk, *Materials Chemistry and Physics,* **2009**, *114*, 188.

A NOVEL PLANAR ELECTROCHEMICAL CELL FOR VOLTAMMETRIC MEASUREMENTS IN THIN HYDROGEL FILMS

LÁSZLÓ KÉKEDY-NAGY[a*], FERNANDO GARAY[b] AND ERNŐ LINDNER[a]

ABSTRACT. The fabrication of a planar micro electrochemical cell is presented. The simplicity and the relative low cost of this kind of cells make them very interesting and promising in the development of chemical and biochemical sensors. The utilization of microelectrodes as working electrodes in planar electrochemical cells is preferred to the conventional macro electrodes because microelectrodes can be used in highly resistive media, have short response time, and excellent signal to noise ratio. In electrochemical sensor applications, the microelectrode surfaces are commonly modified with multiple layers to boost selectivity, control sensitivity, or to provide a biocompatible interface between the sensor and its environment. In this work, the fabricated set of bundled electrodes is covered with a hydrogel as an example of its potential use as electrochemical gas sensor. All micro electrochemical cells were characterized by cyclic voltammetry (CV) and the results were analyzed with different statistical methods.

Keywords: Electrochemical gas sensor, microelectrode, planar micro electrochemical cell, cyclic voltammetry

INTRODUCTION

Due to their unique advantages electrochemical (bio)sensors remained in the forefront of sensor research throughout the years [1,2].

Electrochemical gas sensors are widely used for the determination of different gases such as oxygen, carbon dioxide, or ammonia as well as for diagnostic purposes. In this regard, electrochemical sensors are considered to be selective tools for the determination of several analytes in a wide concentration

[a] *University of Memphis, Department of Biomedical Engineering, Memphis, Tennessee 38152, USA*
[b] *INFIQC, CONICET, Dpto. de Físico Química, Fac. de Ciencias Químicas, Universidad Nacional de Córdoba, 5000 Córdoba, Argentina*
* Corresponding author: laszlo@inano.au.dk.

range. Moreover, the robustness, low cost, and small size commonly associated to this kind of sensors make them suitable for the systematic analysis of small volumes of samples [3,4].

The most common gas sensor consist on a working electrode and a reference electrode, which are placed inside a cylinder filled with an electrolyte solution and separated from the sample by a thin gas permeable membrane. The working electrode is placed as close as possible to the membrane so that only a very thin film (~10 μm) of the electrolyte solution is sandwiched between the electrode surface and the gas permeable membrane. In this regard, the gas permeable membrane provides exceptional selectivity for this kind of sensors because only gas molecules can diffuse through the membrane and change the concentration in the thin layer of electrolyte immediately adjacent to the working electrode surface. Additionally, the system usually achieves steady-state conditions in a relatively short time (from few seconds to few minutes) depending on the thickness and resistance of the membrane [7,8]. In order to minimize this resistance, it is intended to add high concentration of the electrolyte into the film and it is also preferred the use of microelectrodes instead of conventional macro-electrodes. It is well-known that microelectrodes have smaller RC time constant and better signal-to-noise ratio than the larger electrodes. As a result, microelectrodes result quite suitable for the quantification of analytes in samples with relatively high resistive media.

Depending on the application, the fabrication strategy and the electrode material of a microelectrode can vary significantly [9]. Some few examples of microelectrode fabrication are the print and peel method [10], electrochemical deposition inside a microfluidic channel [11], electrochemical etching [12], inkjet printing with ultrashort pulsed laser ablation [13] and sonochemical patterning of microelectrode arrays [14].

In this work the development of a planar sensing platform that can be transformed into a variety of sensors by coating the surface with a task specific film is presented. This set of bundled electrodes is the scaffold for a micro-electrochemical cell that can be used for the determination of electroactive species in the gas phase. The bundled electrodes and the electrochemical cells are characterized by cyclic voltammetry and the results analyzed by different statistical methods.

RESULTS AND DISCUSSION

The obtained electrochemical cell consisted in a bundle of three electrodes and the details related to the electrode preparation are indicated in the experimental section. Figure 1 shows a scheme of the side view (A) and a picture of the surface of the bundled electrodes (B). It can be observed from Figure 1B that all three electrodes are relatively close to each other. The close

proximity is beneficial, because it might minimize the ohmic potential drop of the solution. The integrity of the glass-platinum seal was investigated visually, using a digital microscope. There were no cracks or nicks observed around the working electrode, which might modify the surface and therefore the electrochemical characteristics of the working electrode. All indications showed a good seal between the glass and the metal, thus obtaining a microelectrode having disk geometry.
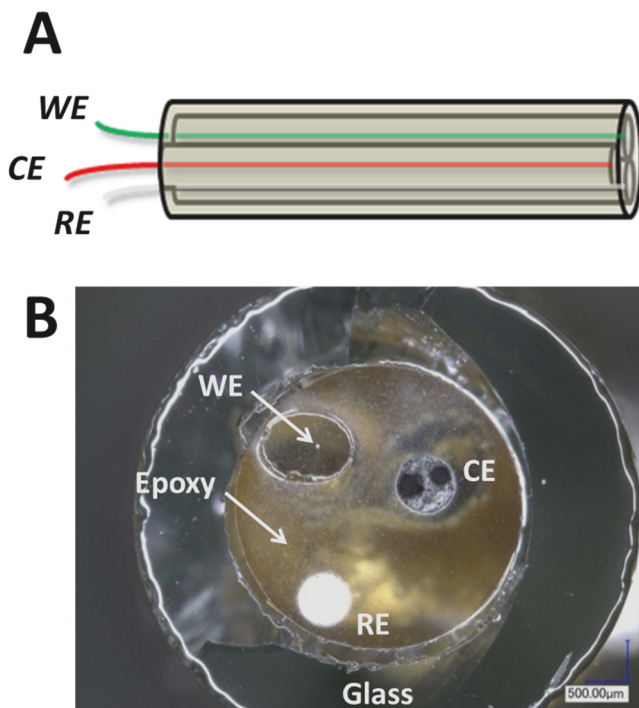
Figure 1. (A) Scheme of the planar micro electrochemical cell. (B) Photograph of a polished planar electrochemical cell surface, WE – working electrode (25 µm diameter Pt disc electrode); RE – reference electrode (0.5 mm diameter Ag disc electrode); CE – auxiliary electrode (0.6 mm diameter graphite disc electrode).

Every set of bundled electrode was tested/characterized by cyclic voltammetry (CV) [15, 16]. Figure 2 shows a cyclic voltammogram recorded in 1 mM FcMeOH in 0.1 M KCl, recorded from -0.1 V to +0.4 V (vs. Ag|AgCl|0.1M KCl) with a scan rate of 0.05 Vs^{-1}, while the solution was stirred vigorously for 10 seconds before each experiment. A very well developed sigmoidal voltammogram was observed, which is characteristic for microelectrodes having disk geometry.

The steady-state of limiting current for microelectrodes of disk geometry is expected to follow the equation [17-19]:

$$i_L = 4nFDCr \qquad (1)$$

where, I is the steady state or limiting current (A), n is the number of electrons, F is the Faraday constant (96,485.3415 Asmol^{-1}), D is the diffusion coefficient of the FcMeOH in aqueous solution (7.6 ± 0.5×10^{-6} cm^{2}s^{-1}) [20], C is the concentration of the FcMeOH in the aqueous solution and r is the radius of the disk microelectrode. Using Equation 1, one can determine the actual radius of the working electrode.
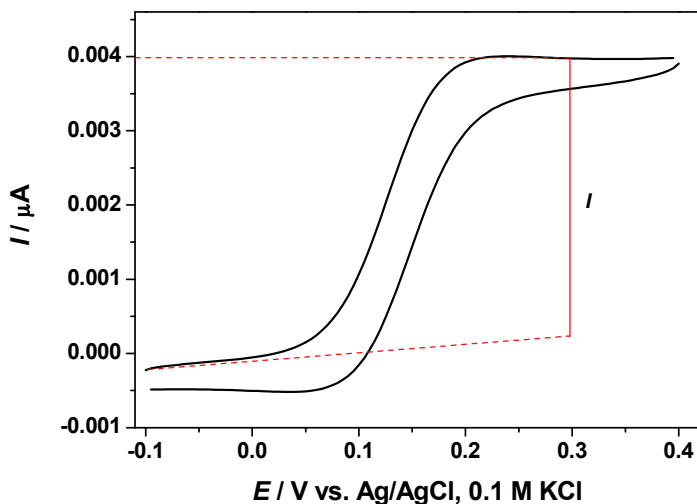
Figure 2. Representative CV recorded with a fabricated micro-electrochemical cell in 1 mM FcMeOH and 0.1 M KCl background electrolyte. Scan rate 0.05 Vs^{-1}.

The steady state current obtained with the Pt disk microelectrode was compared to the expected (theoretical) current obtained from Equation 1. The results are shown in Figure 3. The current expected from the equation was 0.00367 μA.

The average diameter of the fabricated Pt disk microelectrodes was (23.9 ± 0.5) μm after they were bundled to the reference and counter electrodes. Although the obtained average diameter was 4.4% smaller than the 25.0 μm informed by the manufacturer of the Pt wire, a one way analysis of variance (ANOVA) points out no significant difference between the steady state currents of the different microelectrodes and the theoretical steady state current. The statistical study was performed for $α = 0.05$. Tukey and Levene's tests were also in agreement with ANOVA analyses indicating that the newly fabricated set

of bundled electrodes were performing as expected for microelectrodes having disk geometry and also, statistically they were no different from the theoretically calculated values (steady state current or radius).
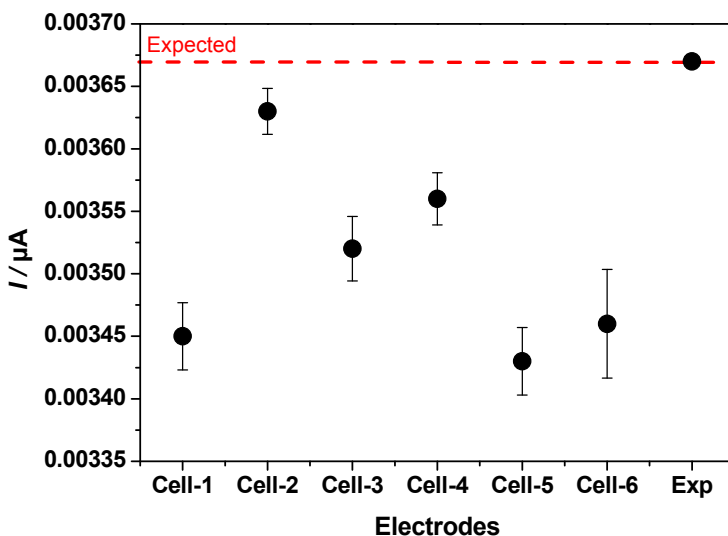
Figure 3. Steady state current values obtained for independently fabricated bundled electrodes. All measurements were in 1.0 mM FcMeOH and 0.1 M KCl as background electrolyte. Experimental results are compared to the expected value of a 25 μm diameter Pt disk.

Once this platform was ready, the electrodes were covered with a hydrogel. In this case, the hydrogel was composed by 0.045 g/mL (3x) gelatin. The hydrogel was placed by drop casting on the surface of the bundled electrodes. Thus, the volume of hydrogel defined the size of planar electrochemical cell.

For a typical electrochemical gas sensor, the electrodes are placed in a cylinder which contains the electrolyte. In our case this electrolyte solution was replaced by the hydrogel which was spin coated on the surface of this electrochemical cell. In this setup, the reproducibility of the sensor it doesn't only depend on the radius of the working micro electrode, but the thickness of the hydrogel as well. The changes within the humidity of the room might drastically influence the thickness of the hydrogel, hence the electrochemical response of the sensor as well. Thus the feasibility of using the planar electrochemical cell as a sensor in the gas phase was evaluated by studying the effect of humidity in the environment. To do this, 1 mM FcMeOH and 0.1 M KCl were added to the composition of the hydrogel. Then the hydrogel film coated electrochemical cell was placed in a sealed 20 mL vial over 5 mL of 0.1 M KCl. Under this

condition, the hydrogel of the sensor slowly incorporates water from the environment. As a result, gradual swelling of the hydrogel occurs until its saturation with water and the current response of the sensor decreases due to the dilution of the electroactive species into the film. Figure 4 shows CVs performed with the planar electrochemical cell every 30 minute. During the first 3 hours, the volume of the hydrogel changes linearly with time. Then, the swelling effect slows down and after 6 hours the humidity of the hydrogel is close to its equilibrium value.
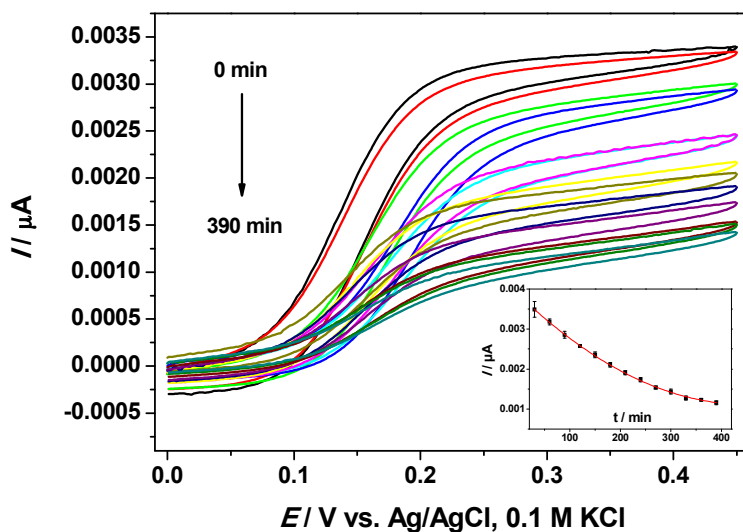
Figure 4. Representative CVs recorded with a gelatin film coated planar electrochemical cell exposed to a humid environment. The gelatin film contained 1 mM FcMeOH as analyte and 0.1 M KCl as background electrolyte. The inset shows the decrease of the steady state current with time. Scan rate 0.05 Vs^{-1}.

Since the decrease of the signal in the first 30 minutes was not significant it projects promising feasibility for the utilization of the homemade planar micro electrochemical cell as a platform for the development of membrane coated gas sensors. The optimization of the experimental protocol and hydrogel film coating was out of scope for this work.

CONCLUSIONS

A novel planar electrochemical cell has been presented. In this work it is shown its preparation and characterization by cyclic voltammetry. In order to minimize IR drop and to maximize the signal to noise ratio a 25 µm Pt microdisk

electrode is used as working electrode. No statistical difference was found between the theoretically expected and experimentally determined steady state currents. The set of bundled electrodes is robust and the surface can be renewed any time simply by polishing with alumina.

The electrochemical measurements showed clearly that the newly prepared electrochemical cells could be a viable option in the development of electrochemical (bio)sensors of species dissolved in the gas phase.

EXPERIMENTAL SECTION

Micro Electrochemical Cell Fabrication

The planar micro electrochemical cell consists of three electrodes, each of them were prepared individually. The working microelectrode (WE) consists of a 25 μm Ø Pt wire, which was inserted in a borosilicate glass tubing (OD = 1.0 mm and ID = 0.5 mm). Before the electrode preparation the glass tubing was cleaned with 1:10 dilute nitric acid solution, and de-ionized water. After several rinses the glass capillaries were dried for 1 hour in an oven at $100°$ C. The cleaned capillaries were pulled with a Sutter Instruments pipette puller (Model P-30) using the following settings: $HEAT_1$ = 825; $HEAT_2$ = 100; PULL = 800. The pulling provided a pair of capillaries of approximately the same length (5 cm) with a short tapered end. The tapered end of the pulled capillaries was sealed with an open flame produced by a Bunsen burner.

The Pt wire was cut into sections of ~2 cm, straightened, cleaned in methanol, dried and inserted into the pulled glass capillary tubes. For visual confirmation a microscope was used to check if the Pt wire had fully descended to the tip of the closed glass capillary tubing. The open ends of the glass tubing were attached then to a vacuum pump for 30 minutes. Heat was carefully applied to the tips of the closed end of the glass tubing, using the same Bunsen burner. The glass tubing was heated slowly, first at the top of the flame, and was pulled in and out of the flame. It was also rotated during the process so that the tubing would not bend. This process was continued until approximately one centimeter of the glass tubing had collapsed around the platinum wire. Finally, each microelectrode was checked with a microscope to ensure that no air bubbles were formed between the glass and the Pt wire. The working electrode was connected to a thin cable by injecting silver epoxy (EPO-TEK H2OE) into the open end of the glass capillary.

The reference electrode was a 0.5 mm Ø Ag wire while the counter electrode was a 0.6 Ø mm spectral purity graphite rod. The connections were prepared by careful alignment of the electrode piece with the copper connecting wire, followed by the sealing with the silver epoxy. The silver epoxy was cured overnight at $100°$ C.

The set of three electrodes were bounded together as tight as possible with parafilm, in order to fit in an external glass tubing (OD = 5.1 mm, ID = 3.0 mm), which was pre-cleaned in a 1:10 dilute HNO_3 solution. The side of this external glass tube that contains the three electrodes was temporarily sealed with scotch tape. Then epoxy resin Epon 828 was prepared according to a protocol by Wightman et al [21]. It consisted of a preheated (~70°C) mixture of m-phenylenediamine and in a weight ratio of 0.16/1.0. Once the resin was prepared, it was injected into the glass tubing containing the electrodes and the epoxy was cured over a period of two days, first overnight at room temperature, and then at 150° C.

After complete curing the scotch tape was removed from the end of the glass tube and the planar electrochemical cell was polished manually using sandpaper of decreasing coarseness in order to obtain a flat smooth surface for each of the three electrodes. Then, the set of bundled electrodes was polished with alumina slurry of 1.0 μm and 0.3 μm. This polishing was performed on a machine-rotating polisher. Prior to each electrochemical experiment, the planar electrochemical cell surface was polished with 0.05 μm grade alumina slurry. This last step was done by hand, and the electrodes were rinsed and sonicated in de-ionized water to ensure that no alumina particles remained on the surface.

Materials

The following chemicals were used: potassium chloride-extra pure (KCl) from Acros Organics (New Jersey, US); ferrocenemethanol (FcMeOH) 97% from Aldrich (St. Louis, MO). For the preparation of the hydrogel film commercially available gelatin was used from a local store. The electrodes of the planar micro cell were fixed together with an epoxy resin constituting of m-phenylenediamine 99+%, from Acros Organics (Belgium); Epon resin 828 from Miller-Stephenson chemical company (Danbury, CT). The tight electric contact of the cell electrodes with the Cu connecting wires was realized via silver epoxy H20E, from Epoxy Technology (Conroe, TX). All solutions were prepared by using de-ionized water (18 MΩ cm) from a Millipore Milli-Q system.

The electrodes prior measurements were polished on the polishing cloth by using wet Alpha micropolish II deagglomerated alumina (1 μm, 0.3 μm, 0.05 μm) powder (Buehler, Lake Bluff, IL).

The planar electrochemical cell was constructed by using a Pt wire of 25 μm Ø and 99.95% purity from Alfa Aesar (Ward Hill, MA), a silver wire of 0.5 mm Ø and 99.99% purity manufactured by Aldrich, and a graphite bar of 0.6 mm Ø, spectral purity by Aldrich, as auxiliary electrode.

Apparatus and Methods

The electrochemical measurements were performed using a potentiostat Model 760C (CH Instruments, Austin TX).

For the electrochemical cell preparation the following instruments were used: P-30 pipette puller; Pittsburgh Universal Bunsen burner; Cooltech (Ashford, Middlesex, UK) high performance vacuum pump Model No. 15600; rotating polisher ST-707B from Sharpner (Saddle Brook, NJ). The electrodes surfaces were observed with the digital microscope VHX-1000 Keyence (Itasca, IL).

R E F E R E N C E S

[1]. A. Turner, *Trends in Biotechnology*, **2013**, *31*, 119.
[2]. A.J. Bandodkar, J. Wang, *Trends in Biotechnology*, **2014**, *32*, 363.
[3]. J.R. Stetter, W.R. Penrose, S. Yao, *Journal of The Electrochemical Society*, **2003**, *150*, S11.
[4]. C.M.A. Brett, *Pure Appl. Chem.*, **2001**, *73*, 1969.
[5]. D. Grieshaber, R. MacKenzie, J. Voros, E. Reimhult, *Sensors*, **2008**, *8*, 1400.
[6]. S.D. Collyer, F. Davis, S.P.J. Highson, *Sensors*, **2010**, *10*, 5090.
[7]. B.D. Pendley, H.D. Abruna, *Anal. Chem.*, **1990**, *62*, 782.
[8]. J.R. Stetter, J. Li, *Chem. Rev.*, **2008**, *108*, 352.
[9]. R.D. O'Neill, S.C. Chang, J.P. Lowry, C.J. McNeil, *Biosensors and Bioelectronics*, **2004**, *19*, 1521.
[10]. C. Hong, D. Bao, M. S. Thomas, J.M. Clift, V.I. Vullev, *Langmuir*, **2008**, *24*, 8439.
[11]. A.D. Bani-Yaseen, *Int. J. Electrochem. Sci.*, **2010**, *5*, 1837.
[12]. H.J. Lim, Y.M. Lim, S.H. Kim, *Jpn. J. Appl. Phys.*, **2003**, *42*, 1479.
[13]. S.H. Lee, D.J. Lee, Y.H. Lee, S.T. Wereley, J.H. Oh, *Phys. Status Solidi A 209*, **2012**, *11*, 2142.
[14]. S.D. Collyer, F. Davis, S.P.J. Higson, *Sensors*, **2010**, *10*, 5090.
[15]. C.M.A. Brett, A.M. O. Brett, "Electrochemistry - Principles, Methods and Applications", Oxford University Press, New York, **1993**, chapter 13.
[16]. P.T. Kissinger, W. R. Heinman, "Laboratory techniques in electroanalytical chemistry", Marcel Dekker, Inc., New York, **1996**, chapter 12.
[17]. J. Wang, "Analytical Electrochemistry", A John Wiley & Sons, Inc., New York, **2000**, chapter 6.
[18]. A.J. Bard, L.R. Faulkner, "Electrochemical Methods Fundamentals and Applications", John Wiley & Sons, Inc., New York, **2001**, chapters 1 and 14.

[19]. C.G. Zoski, "Handbook of Electrochemistry", Elsevier B. V., Amsterdam, **2007**, chapter 2.

[20]. C. Amatore, C. Pebay, L. Thouin, A. Wnag, J.S. Warkocz, *Anal. Chem.*, **2010**, *82*, 6933.

[21]. R.M. Wightman, A. Hermans, A.T. Seipel, C.E. Miller, *Langmuir*, **2006**, *22*, 1964.

ROMANIAN (MĂCICAŞ) ZEOLITIC VOLCANIC TUFF FOR MALACHITE GREEN REMOVAL

RALUCA PLEŞA CHICINAŞ[a], HOREA BEDELEAN[b], ANDRADA MĂICĂNEANU[a,c*]

ABSTRACT. Zeolitic volcanic tuff was tested as a potential adsorbent for malachite green (MG) dye removal from aqueous solutions. The influences of contact time, temperature, dye initial concentration, solid:liquid ratio, and adsorbent grain size over the adsorption capacity and efficiency were considered. Removal efficiencies up to 99% and a monolayer capacity (Langmuir) of 4.05 mg MG/g were calculated. The equilibrium and kinetic study showed that the experimental data were best fitted on the Temkin model and that the intra-particle diffusion could be the rate determining step. Thermodynamic analysis showed that MG adsorption onto ZVT is an endothermic, non-spontaneous process.

Keywords: natural zeolite, malachite green, adsorption, efficiency, equilibrium, kinetic, thermodynamic

INTRODUCTION

Natural zeolite is an abundant resource available all over the world, is usually regarded as a low-cost material and has been used as an adsorbent to remove heavy metals, dyes and ammonia ions [1-3]. Zeolites are able to exchange ions with external medium, having a high ion exchange capacity, which is their significant characteristic. The ion exchange behaviour depends on framework structure, ion size and shape, and charge density of the anionic framework. These properties make zeolites attractive materials that can be successfully used for pollutants removal from wastewaters [4-5].

---

[a] *Babeş-Bolyai University, Faculty of Chemistry and Chemical Engineering, 11 Arany Janos str., RO-400028, Cluj-Napoca, Romania*
[b] *Babeş-Bolyai University, Faculty of Biology and Geology, 44 George Bilaşcu St., 400015, Cluj-Napoca, Romania*
[c] *Indiana University of Pennsylvania, Department of Chemistry, Indiana, PA 15705, USA*
* Corresponding author: Sanda.Maicaneanu@iup.edu

Dyes are important pollutants of water, which are discharged from textile, printing, paper, plastics, food and leather industries. It is estimated that more than 100,000 commercially available dyes with over $7 \cdot 10^5$ tons of dyestuff are produced annually [6]. They affect the nature of the water, reducing the photosynthetic reaction. Also some dyes are toxic and even carcinogenic [5-6]. Malachite green is a basic dye used in ceramic industry, textile industry, leather industry, as a cytochemical dye and in paints manufacturing. Because of its toxicity is used to treat parasites, fungal infections, and bacterial infections in fish and fish eggs [7].

In order to remove dyes from wastewaters, physical, chemical, and biological methods were reported. Between the various methods tested, adsorption proved to give the best results in terms of initial cost, flexibility, simplicity of design and very important does not result in the formation of harmful substances [6].

The purpose of this work was to study the possible use of zeolitic volcanic tuff (ZVT) as an adsorbent for malachite green (MG) removal from aqueous solution. The influence of the reaction parameters such as temperature, adsorbent quantity, MG initial concentration, and adsorbent grain size were considered. Equilibrium (Langmuir, Freundlich, Dubinin-Radushkevich, and Temkin) and kinetic (pseudo-first-, pseudo-second-order, liquid film diffusion, and intra-particle diffusion) models were used to evaluate the adsorption mechanism. Also the thermodynamic parameters ΔG^0, ΔH^0, and ΔS^0 were calculated.

RESULTS AND DISCUSSION

Zeolitic volcanic tuff characterization

The zeolitic volcanic tuff sample used in this work is included in the Dej Formation of Badenian age, located in the north-western part of the Transylvanian Depression. The tuff may be characterized as a vitric tuff. The glass shards in tuffs are replaced by zeolite minerals, clinoptilolite type. Quartz, plagioclases, micas and opal-CT are also present.

X-ray diffraction (XRD) analysis confirms the presence of the clinoptololite as the main zeolite mineral phase [8].

The whole rock chemical analysis showed the acid character of the tuff with SiO_2 >60% [9]. The loss of ignition value (over 13%) indicates that zeolites represent between 60% and 80% of the crystallized fractions of the tuff [8-10].

MG adsorption results

The results obtained for MG removal from aqueous solution using ZVT are presented further and discussed in terms of removal efficiency and adsorption capacity.

The influence of temperature on MG adsorption was investigated using the following reaction conditions: solid:liquid ratio 0.50:10 g/mL, 50 mg MG/L, 0.6-1.0 mm adsorbent grain size, and a reaction time of 360 min. The acquired results, Figure 1, showed that an increase of the contact time has as result a gradually increase of the MG uptake with a higher rate for temperatures between 35 and 55°C in the first 100 min and then slower towards the equilibrium. Adsorption equilibrium was reached in about 300, 240, and 120 min as the temperature increased from 25 to 55°C. Removal efficiency increases from 72 to 93% as the temperature increases from 25 to 55°C.
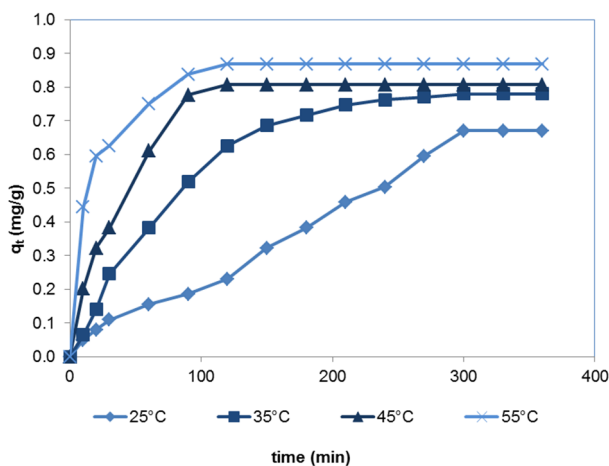
Figure 1. Time evolution of MG uptake for different temperatures
(50 mg MG/L, 0.50:10 g/mL, 0.6-1.0 mm grain size, 360 min).

The results obtained for various initial concentrations of MG solution (10-250 mg/L) are presented in Figure 2. An increase of MG initial concentration led to an increase in the ZVT adsorption capacity, proving that the considered material has a high ability to retain MG even at high concentrations.

The study of the solid:liquid ratio influence upon MG adsorption process was conducted using solid:liquid ratios in 0.25:10-1.00:10 g/mL interval. The results obtained are presented in Figure 3. Thus, an increase in adsorbent quantity led to a decrease in adsorption capacity value due to the fact that for the same initial concentration, a higher surface or adsorbent quantity is available for adsorption. The highest removal efficiency calculated in this case was about 97% for 1.00:10 mg/L.

The influence of the ZVT grain size upon the adsorption capacity in the MG adsorption process was studied for a range of grain sizes in 0.2-0.4 to 1.25-1.6 mm interval. Adsorption capacities values thus obtained for all grain sizes are presented
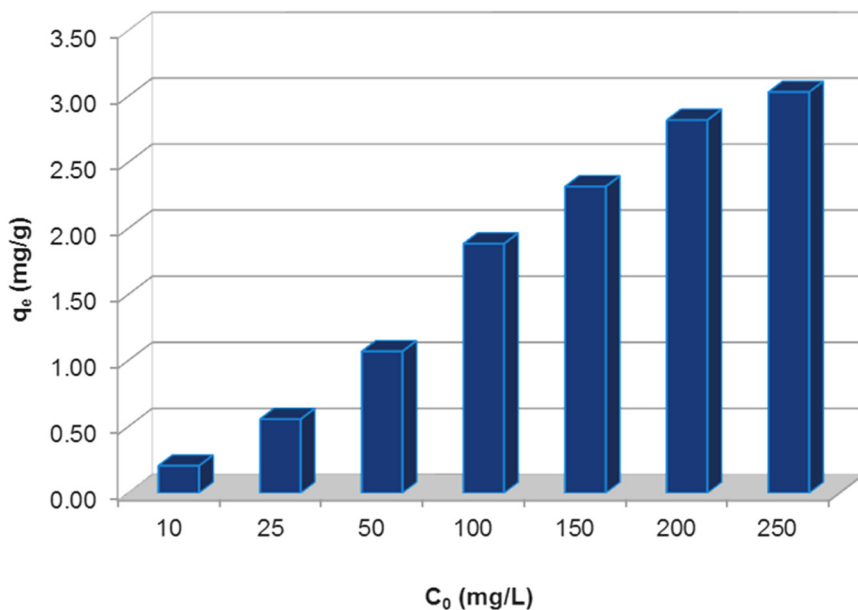
Figure 2. MG initial concentration influence over the adsorption capacity
(25°C, 0.50:10 g/mL, 0.6-1.0 mm grain size and 420 min).
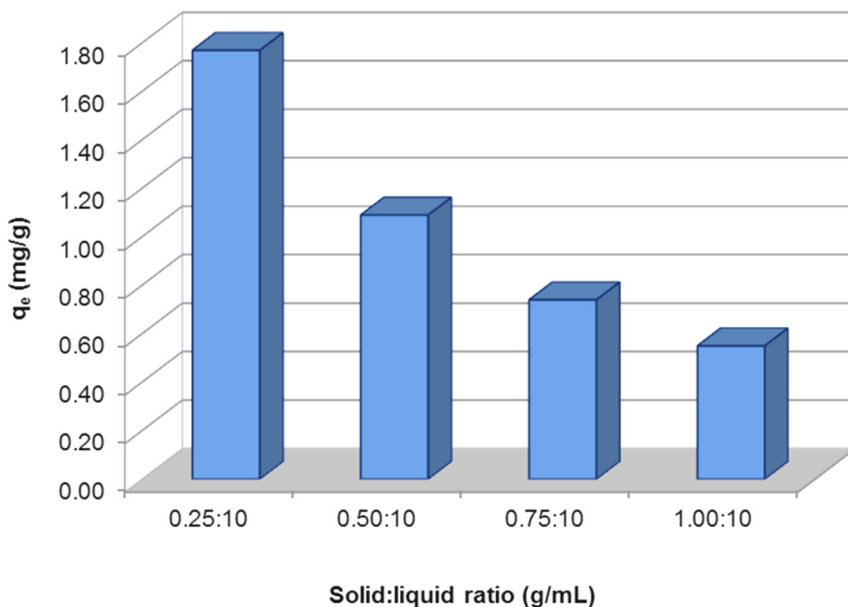
Figure 3. Solid:liquid ratio influence over the adsorption capacity of ZVT in the MG
adsorption process (50 mg/L, 25°C, 0.2-0.4 mm grain size, 360 min).

in Figure 4. This evolution might be correlated with diffusional limitations that occur due to the MG molecule size, adsorption taking place mostly on the external surface of the grain. Removal efficiency values followed the same trend with a maximum value of about 98% for 1.25-1.60 mm.
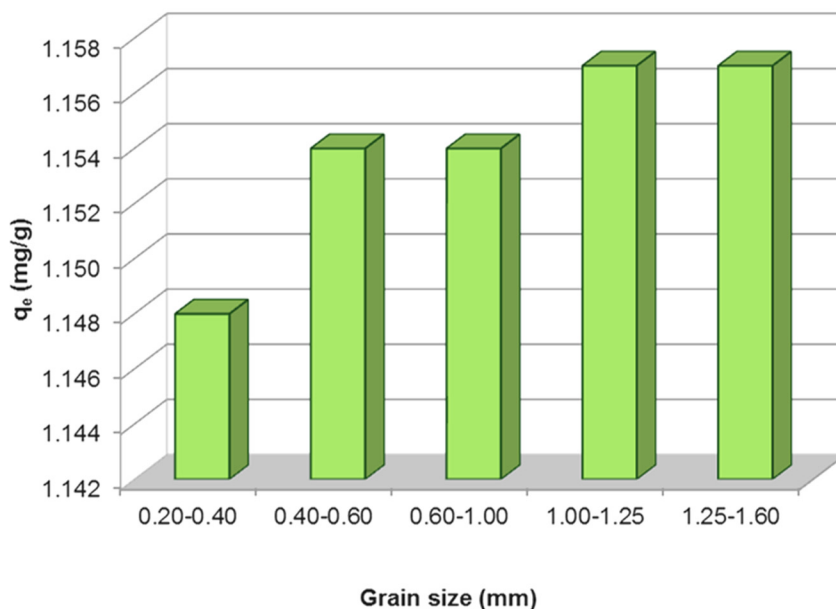
Figure 4. Variation of adsorption capacities obtained for MG adsorption on ZVT at different grain size (50 mg/L, 25°C, 0.50:10 g/mL, 360 min).

Adsorption isotherms

Equilibrium experiments were carried out for different initial concentrations in 10-250 mg/L range at 25°C for 420 min.

In order to establish which isotherm model describes better the adsorption of MG on ZVT, Langmuir, Freundlich, Dubinin-Radushkevich and Temkin equations were considered. The parameters obtained from experimental data and the related correlation coefficients are presented in Table 1. All values of correlation coefficient (R^2) were higher than 0.9, but Temkin model yields a better fit, with a 0.9864 value, than Langmuir, Freundlich and Dubinin-Radushkevich models, with 0.9421, 0.9275, and 0.9490, respectively. Previous studies in similar systems showed that the adsorption of dyes (methyl orange and methyl violet) was best described by Temkin model [11].

Table 1. Langmuir, Freundlich, Dubinin-Radushkevich and Temkin
isotherms parameters for the adsorption of MG onto ZVT
(10-250 mg/L, 25°C, 0.50:10 g/mL, 0.60-1.00 mm, 420 min)

Langmuir			Freundlich			Dubinin-Radushkevich			Temkin		
K_L (L/mg)	q_m (mg/g)	R^2	n	K_F (mg$^{(1-1/n)}$L$^{1/n}$/g)	R^2	K_D (mol^2/kJ^2)	E_D (kJ/mol)	R^2	A_T (L/g)	B	R^2
0.0504	4.0519	0.9421	1.9952	0.2985	0.9275	4×10^{-9}	11.18	0.9490	2.0326	2×10^{-6}	0.9864

Adsorption kinetics

The rate constants and the adsorption mechanism of MG adsorption onto ZVT were evaluated by using different kinetic models, such as pseudo-first-, pseudo-second-order, intra-particle, and liquid film diffusion. The results obtained for all considered kinetic models are presented in Table 2. Taking into consideration the correlation coefficients obtained for all considered models, the fact that $q_{e,calc}$ for pseudo-first- and pseudo-second-order exhibit considerable difference towards the $q_{e,exp}$ values, and also that the intercept values in case of diffusion models are very close to 0 [12], support the conclusion that intra-particle diffusion might be rate-determining step for this system (concentrations higher than 50 mg/L). Experimental results obtained for various grain sizes of the ZVT (adsorption capacity increases with an increase in grain size) also support this conclusion.

Table 2. Pseudo-first-, pseudo-second-order, intra-particle and
liquid film diffusion parameters for the adsorption of MG onto ZVT
(10-250 mg/L, 25°C, 0.50:10 g/mL, 0.60-1.00 mm, 420 min)

C_0	$q_{e,exp}$ (mg/g)	Pseudo-first-order			Pseudo-second-order			Intra-particle diffusion			Liquid film diffusion		
		k_1 (1/min)	$q_{e,calc}$ (mg/g)	R^2	k_2 (g/mg·min)	$q_{e,calc}$ (mg/g)	R^2	k_{ip} (mg/g min$^{1/2}$)	Intercept	R^2	k_{fd} (1/min)	Intercept	R^2
10	0.2031	0.0124	0.1838	0.9847	0.0781	0.2363	0.9982	0.0095	0.0370	0.8975	0.0123	-0.1170	0.9847
25	0.5562	0.0140	0.8254	0.9641	0.0074	0.8260	0.9726	0.0321	-0.0207	0.9437	0.0140	0.3890	0.9641
50	1.0420	0.0082	1.4299	0.9397	0.0011	2.1354	0.9762	0.0635	-0.1956	0.9949	0.0082	0.2884	0.9398
100	1.8225	0.0074	2.4227	0.9178	0.0005	4.1528	0.9861	0.1090	-0.3459	0.9971	0.0074	0.2500	0.9178
150	2.1840	0.0067	2.7451	0.9563	0.0006	4.2409	0.9550	0.1306	-0.3785	0.9955	0.0067	0.1685	0.9563
200	2.7314	0.0075	3.6888	0.9146	0.0002	6.8871	0.9538	0.1649	-0.5542	0.9963	0.0075	0.2675	0.9146
250	2.8993	0.0068	3.5898	0.9321	0.0008	4.6642	0.9483	0.1651	-0.3983	0.9964	0.0068	0.1679	0.9321

The pore diffusion coefficients determined are presented in Table 3, with the smallest value of 8.69×10^{-10} cm^2/s. Although the values are not in the rate determining range (10^{-11} - 10^{-13} cm^2/s) [13-14] it is reasonable to assume that internal diffusion plays a significant role for the considered system especially in the higher concentration range.

Table 3. Pore diffusion coefficients

C_0 (mg/L)	D (cm^2/s)	C_0 (mg/L)	D (cm^2/s)
10	5.90×10^{-9}	150	8.69×10^{-10}
25	1.95×10^{-9}	200	5.44×10^{-10}
50	7.40×10^{-10}	250	1.23×10^{-9}
100	6.41×10^{-10}		

Adsorption thermodynamics

The adsorption of MG dye onto ZVT was studied at temperatures in 298-328 K interval. In order to estimate the effect of temperature for the considered adsorption system, Gibbs free energy (ΔG^0), enthalpy (ΔH^0) and entropy (ΔS^0) were determined. The values obtained are listed in Table 4. ΔH^0 positive value, also less than 84 kJ/mol indicates the endothermic nature and that the process is physical in nature [4]. The small positive value of ΔS^0 confirmed the increased randomness at the solid-solution interface during adsorption [3]. ΔG^0 values for all temperatures are positive, and the value decrease with increase of temperature, which indicates the fact that the considered adsorption process will be promoted by specific temperature conditions, leading to increased adsorption capacities [15].

Table 4. Thermodynamic parameters for the adsorption of MG onto ZVT (50 mg/L, 25-55°C, 0.50:10 g/mL, 0.60-1.00 mm, 420 min)

T (K)	ΔS° (kJ/K·mol)	ΔH° (kJ/mol)	ΔG° (kJ/mol)
298			6.73
308	0.11	39.17	5.64
318			4.55
328			3.46

CONCLUSIONS

This work presents the results obtained for malachite green removal from aqueous solution using a zeolitic volcanic tuff from Măcicaş deposit, Cluj County, as adsorbent. The study of various parameters showed that the ZVT sample has a high capacity to remove MG dye from aqueous solution with removal efficiencies up to 99%. Also as the initial concentration of dye increases, adsorption capacity of the ZVT increases suggesting its increased ability to efficiently remove MG even at high concentrations. The kinetic study showed that intra-particle diffusion might be the rate determining step for this particular system. Thermodynamic analysis showed that MG adsorption onto ZVT is an endothermic, non-spontaneous process. According to the obtained results it can be concluded that the zeolitic volcanic tuff from Măcicaş could be used as an efficient adsorbent for MG dye removal from aqueous solutions.

EXPERIMENTAL SECTION

Materials

In this work, a representative sample of zeolitic volcanic tuff (ZVT) collected from Măcicaş deposit (Cluj County, Transylvania, Romania) was used. Raw ZVT was subjected to a grinding process, followed by size separation in order to obtain the 0.2-0.4, 0.4-0.6, 0.6-1.0, 1.0-1.25 and 1.25-1.6 mm fractions, which were further used throughout the experiments. Raw ZVT was then washed few times with distilled water in order to remove fine particles and dried at 105°C for 24 h.

All reagents were of analytical purity and used as received. Distilled water was used throughout this work.

Adsorption experiments

Malachite green (MG) adsorption process was conducted in batch conditions, in a thermostated batch reactor using a three-dimensional shaker (50 rpm), for 420 min. various parameters that could influence the adsorption process were considered. Thus the experiments were carried out using different contact times (10-420 min), temperatures (25-55°C), MG initial concentrations (10-250 mg/L), solid:liquid ratios (0.25:10-1.00:10 g/mL) and different ZVT grain sizes (0.2-0.4, 0.4-0.6, 0.6-1.0, 1.0-1.25 and 1.25-1.6 mm).

MG concentration in solution was determined using a UV/VIS T70+ spectrophotometer (λ_{MG} = 618 nm). All the experiments were realized in triplicate, the presented values are averaged values.

Adsorption capacity and MG uptake, q_e and q_t (mg/g), respectively, and removal efficiency, E (%) were calculated in order to establish the effectiveness of the considered sample in the dye removal process.

$$q_{e(t)} = \frac{(C_0 - C_{e(t)}) \cdot V}{m}$$

$$E = \frac{C_0 - C_e}{C_0} \times 100$$

where: C_0, C_e, and C_t are the initial, equilibrium, and time t MG concentrations in solution, in mg/L, V is the sample volume, in L and m is the adsorbent quantity, in g.

Adsorption isotherms, kinetics and thermodynamics

The equilibrium analysis of the adsorption process of MG on ZVT was carried out using the Langmuir, Freundlich, Temkin and Dubinin-Raduschevich models. For all considered models the equations in the linear form are given in Table 5.

Pseudo-first-, pseudo-second-order, intra-particle diffusion and liquid film diffusion kinetic models were used in order to explain the adsorption mechanism. The pore diffusion coefficient, D (cm^2/s) for the removal of MG by ZVT was also calculated (assuming a spherical geometry of the adsorbents – average size 0.8 mm). The equations used in order to determine the kinetics parameters and pore diffusion coefficient are given in Table 5.

The thermodynamic parameters, Gibbs free energy (ΔG°), enthalpy (ΔH°), and entropy (ΔS°), for the removal of MG by ZVT were determine using the equations presented in Table 5.

Table 5. Isotherms, kinetics and thermodynamics models.

		Equation	Reference
ISOTHERM	Langmuir	$\frac{1}{q_e} = \frac{1}{q_m K_L} \cdot \frac{1}{C_e} + \frac{1}{q_m}$	[16,17]
	Freundlich	$\log q_e = \log K_F + \frac{1}{n} \cdot \log C_e$	[3,18]

		Equation	Reference
	Dubinin-Radushkevich	$$\ln q_e = \ln q_s - K_D \varepsilon^2$$ $$\varepsilon = RT \ln(1 + \frac{1}{C_e})$$ $$E_D = \frac{1}{\sqrt{2K_D}}$$	[16,19]
	Temkin	$$q_e = B \ln A_T + B \ln C_e$$ $$B = \frac{RT}{b_T}$$	[3,20]
KINETIC	Pseudo-first-order	$$\ln(q_e - q_t) = \ln q_e - k_1 t$$	[21,25]
	Pseudo-second-order	$$\frac{t}{q_t} = \frac{1}{k_2 q_e^{\ 2}} + \frac{t}{q_e}$$	[22,25]
	Intra-particle diffusion	$$q_t = k_{ip} t^{1/2}$$	[23,25]
	Liquid film diffusion	$$\ln(1 - F) = -k_{fd} t$$	[24,25]
	Pore diffusion coefficient	$$D = 0.003 \cdot \frac{r_0^2}{t_{0.5}}$$ $$t_{0.5} = \frac{1}{k_2 q_e}$$	[25]
TERMODYNAMIC	Gibbs free energy	$$\Delta G^\circ = -RT \ln K_d$$	[3,26]
	Enthalpy and entropy	$$\Delta G^\circ = \Delta H^\circ - T\Delta S^\circ$$	

Where,

A_T – Temkin isotherm equilibrium binding constant (L/g)

B – constant related to heat of adsorption

b_T – Temkin isotherm constant (J/mol)

C_e – equilibrium MG concentration (mg/L)

D – pore diffusion coefficient (cm^2/s)

E_D – free energy per molecule of adsorbate (kJ/mol)

F – fraction attainment at equilibrium ($= q_t/q_e$)

K_D – Dubinin-Radushkevich isotherm constant (mol^2/kJ^2)

K_d – thermodynamic equilibrium constant (L/g)

K_F – Freundlich isotherm constant ($mg^{(1-1/n)} L^{1/n}$/g)

k_{fd} – liquid film diffusion rate constant (1/min)

k_{ip} – intra-particle diffusion rate constant (mg/g $min^{1/2}$)

K_L – Langmuir adsorption constant (L/mg)
k_1 – pseudo-first-order rate constant (1/min)
k_2 – pseudo-second-order rate constant (g/mg·min)
n – constant related to intensity of adsorption (Freundlich)
q_e – adsorption capacity (mg/g)
$q_{e,exp}$ – experimental amount of dye adsorbed at equilibrium (mg/g)
$q_{e,calc}$ – calculated amount of dye adsorbed at equilibrium (mg/g)
q_t – amount of dye adsorbed at time t (mg/g)
q_m – monolayer capacity of the adsorbent (mg/g)
q_s – theoretical isotherm saturation capacity (mg/g)
r_0 – average ZVT grain diameter (cm)
R – universal gas constant (8.314 J/mol K)
R^2 – correlation coefficient
t – time (min)
$t_{0.5}$ – time for half adsorption (s)
T – absolute temperature (K)
ΔG° – Gibbs free energy (kJ/mol)
ΔH° – enthalpy (kJ/mol)
ΔS° – entropy (kJ/K·mol)

R E F E R E N C E S

[1]. S. Wang, H. Li, S. Xie, S. Liu, L. Xu, *Chemosphere,* **2006**, *65,* 82.
[2]. S. Wang, Z.H. Zhu, *Journal of Hazardous Materials,* **2006**, *B136*, 946.
[3]. R. Han, J. Zhang, P. Han, Y. Wang, Z. Zhao, M. Tang, *Chemical Engineering Journal,* **2009,** *145*, 496.
[4]. E. Alver, A.Ü. Metin, *Chemical Engineering Journal*, **2012**, *200–202*, 59.
[5]. S. Wang, Y. Peng, *Chemical Engineering Journal,* **2010**, *156*, 11.
[6]. M. Rafatullah, O. Sulaiman, R. Hashim, A. Ahmad, *Journal of Hazardous Materials*, **2010**, *177*, 70.
[7]. R. Han, Y. Wang, Q. Sun, L. Wang, J. Song, X. He, C. Dou, *Journal of Hazardous Materials,* **2010**, *175*, 1056.
[8]. H. Bedelean, M. Stanca, A. Măicăneanu, S. Burcă, 2005, *Studia Universitas Babeş-Bolyai, Geologia,* **2006**, *51,* 43.
[9]. H. Bedelean, V. Codrea, O. Barbu, 2007, *Bulletin of the Geological Society of Greece, Proceedings*, **2007**, *30*, 666.
[10]. A. Măicăneanu, H. Bedelean, S. Burcă, M. Stanca, *Separation Science and Technology*, **2011**, *46,* 1621.
[11]. S. Chen, J. Zhang, C. Zhang, Q. Yue, Y. Li, C. Li, *Desalination,* **2010**, *252*, 149.
[12]. N. Caliskan, A.R. Kul, S. Alkan, E.G. Sogut, I. Alacabey, *Journal of Hazardous Materials*, **2011**, *193*, 27.
[13]. Z. Ioannou, J. Simitzis, *Journal of Hazardous Materials*, **2009**, *171*, 954.
[14]. V. Srihari, A. Das, *Desalination*, **2008**, *225*, 220.

[15]. R.M. Schneider, C.F. Cavalin, M.A.S.D. Barros, C.R.G. Tavares, *Chemical Engineering Journal,* **2007**, *132*, 355.

[16]. S. Veli, B. Alyüz, *Journal of Hazardous Materials,* **2007**, *149*, 226.

[17]. I. Langmuir, *Journal of the American Chemical Society*, **1918**, *40*, 1361.

[18]. H.M.F. Freundlich, *Zeitschrift fur Physikalische Chemie,* **1906**, *57*, 385.

[19]. M.M. Dubinin, *Chemical Reviews*, **1960**, *60,* 235.

[20]. M.I. Temkin, V. Pyzhev, *Acta Physico-Chimica. USSR*, **1940**, *12*, 327.

[21]. S. Lagergren, Kungliga Svenska Vetenskapsakademiens. *Handlingar*, **1898**, *24*, 1.

[22]. Y.S. Ho, G. McKay, *The Water Research,* **2000**, *34*, 735.

[23]. W.J. Weber, J.C. Morris, *Journal of the Sanitary Engineering Division American Society of Civil Engineers,* **1963**, *89*, 31.

[24]. G.E. Boyd, A.W. Adamson, L.S. Myers Jr., *Journal of the American Chemical Society*, **1947,** *69*, 2836.

[25]. L.C. Coteţ, A. Măicăneanu, C.I. Fort, V. Danciu, *Separation Science and Technology*, **2013**, *48*, 2649.

[26]. M. Koyuncu, *Physicochemical Problems of Mineral Processing*, **2012**, *48,* 485.

LIPASE CATALYZED PARALLEL KINETIC RESOLUTION OF IBUPROFEN

BOTOND NAGY[a], MĂDĂLINA ELENA MOISĂ[a], ALINA FILIP[a], LÁSZLÓ CSABA BENCZE[a], MONICA IOANA TOŞA[a*]

ABSTRACT. A series of commercially available lipases in various solvents using several alcohols as nucleophiles were studied for the stereoselective esterification of ibuprofen and alcoholysis of ibuprofen esters respectively. Novel methods were developed for the stereoselective synthesis of both enantiomers of the target compound. The (*S*)-selective alcoholysis and (*R*)-selective hydrolysis in a parallel kinetic resolution procedure in presence of lipase from *Mucor miehei* as catalyst were performed.

Keywords: lipase, Ibuprofen, enzymatic kinetic resolution, stereoselectivity

INTRODUCTION

Ibuprofen is one of the most important members of Nonsteroidal anti-inflammatory drugs (NSAIDs) that belongs to the family of propanoic acid. Their anti-inflammatory action resides primarily in the (*S*)-enantiomer. The undesired (*R*)-profens might bring some health problems, *e.g.* accumulation in fatty tissues, with unknown effects [1].

The preparation of (*S*)-Ibuprofen on industrial scale has been studied in the last three decades, different strategies based on asymmetric synthesis [2] and (enzymatic) kinetic and dynamic kinetic resolution [3] being employed. The resolution methods are prefered while the racemate synthesis on a large scale has been optimized and efficient technologies were developed.

Biocatalysis offers a green alternative for the resolution of racemic profens using usual kinetic resolution processes. Large series of lipases and esterases have been shown to be highly enantioselective towards several

---

[a] *Babeş-Bolyai University, Faculty of Chemistry and Chemical Engineering, Biocatalysis and Biotransformation Research Centre, 11 Arany Janos str., RO-400028, Cluj-Napoca, Romania*
* *Corresponding author: mtosa@chem.ubbcluj.ro*

profens. Not only hydrolytic approaches performed in aqueous media, but also alcoholysis and aminolysis reactions in non-conventional media were reported in the last two decades [4].

Usually, esterifications are limited by the lower activity of the biocatalysts, by the need to shift the equilibrium to the product-side (*e.g.* by removing the water formed in the process) and as well by long reaction times (days) and only moderate enantioselectivities and yields. Lipase-catalyzed esterification [5] or alcoholysis [6] could overcome the disadvantages of hydrolytic procedures due to the limited solubility of ibuprofen-esters in aqueous systems.

The medium engineering is a generally accepted method for fine tuning of the enzymatic activity. The used solvent can modify the enzymatic activity in two ways, namely by enhancing the substrate solubility and by causing conformational changes of the protein [7]. The water content of the reaction mixture is one of the most influent factors on the activity of lipases in organic media. Moreover, the solubility of the residual water of enzymes in the used organic solvents can significantly influence the enzyme activity, selectivity and product distribution in a certain biocatalytic procedure. Nevertheless, down-stream procedures involving the isolation and purification of the reaction products could be significantly improved when enzymatic kinetic resolutions are performed in organic solvents.

In concordance with the mechanism of action of lipases, firstly the serine from the catalytic triad will react with an esteric substrate generating an acyl-enzyme intermediate by releasing the alcoholic residue from the substrate. In the second stage the formed acyl-enzyme can easily react with a nucleophile present in the reaction mixture, generating the reaction product while the acyl-free enzyme is released. The enzyme activity and stereoselectivity could be significantly improved when esters derived from fatty (medium or long chain) alcohols are used as starting materials, by miming the structure of the natural substrates of lipases. In addition, esters derived from profens and fatty alcohols are highly soluble in less polar solvents, which were found to be the most proper reaction media for lipases when they are acting as stereoselective catalysts in non-aqueous systems. Compared with short-chain alcohols which are stripping the essential water from the enzyme and are acting as dead-end inhibitors [8], fatty alcohols are well tolerated by enzymes and also they can be considered as green chemicals.

While in the last decades several lipase-catalyzed biocatalytic reactions (including synthesis and/or hydrolysis) for synthetic natural like fatty acid esters were developed, [9] only a few enzyme mediated (trans)esterification using long chain alcohols as nucleophile are known.

Lipase catalyzed synthesis of non-toxic, non-skin-irritant, odorless and tasteless non-ionic surfactants like biodegradable *n*-Alkyl (C8-C14) esters of glucuronic have been already reported [10]. Further, the optimal conditions

for the enzymatic esterification of lactic and glycolic acids with fatty alcohols (C8–C16) in the presence of a lipase from *Candida antarctica* were also studied [11]. In this way a rapid, nearly complete conversion into the desired ester with high volumetric productivity was achieved. Alternatively, the enzymatic transesterification of ethyl lactate with fatty alcohols increased the yield for the desired (C8–C16) type alkyl lactate (e.g. 87% in 24 h for dodecyl lactate).

Generally, lipases are versatile stereoselective catalysts since are able to mediate the kinetic resolution of several chiral alcohols, carboxylic acids, esters, amides and lactones by hydrolysis, alcoholysis, acidolysis or transesterification [12].

Encouraged by all these results, we turn our attention to the development of an enzymatic procedure for the synthesis of both enantiomers of Ibuprofen. For this scope commercially available lipases were tested as potential catalysts for the efficient parallel kinetic resolution of various ibuprofen based esters. The method was further improved by substrate and medium engineering tools.

RESULTS AND DISCUSSION

Due to the residual water content of the used solvent and/or enzyme, the biocatalytic alcoholysis can be often concurred by secondary hydrolytic reactions, both in a stereoselective manner. Moreover, varying the reaction conditions, enzymes could display opposite stereoselectivities for the same substrate-product pair. Consequently both, *R* or *S* enantiomers of the reaction counterparts could be produced. Last, but not least, the enzyme activity is strongly influenced by the length of the alkyl chain attached to substrate or nucleophile. Increasing enzyme activity with the length of the acyl residue was reported [13] when sixteen different amides were hydrolyzed in presence of lipase B from *C. antarctica*.

Taking into account these facts the potential biocatalytic paths, when Ibuprofen or its (C1-C16) *n*-alkyl-ester are used as substrates in kinetic resolutions, are depicted in Scheme 1.

In order to explore how length of the alkyl chain of nucleophilic alcohols and of the ibuprofen esters influence the sense and the grade of stereoselectivity of lipases but also the product distribution all possible enzymatic routes: esterification, alcoholysis/transesterification and hydrolysis were subjected for investigations.

Moreover, the enzymatic alcoholysis *versus* hydrolysis were both studied with the aim to produce optimally both, optically pure enantiomers of ibuprofen and ibuprofen esters, respectively.
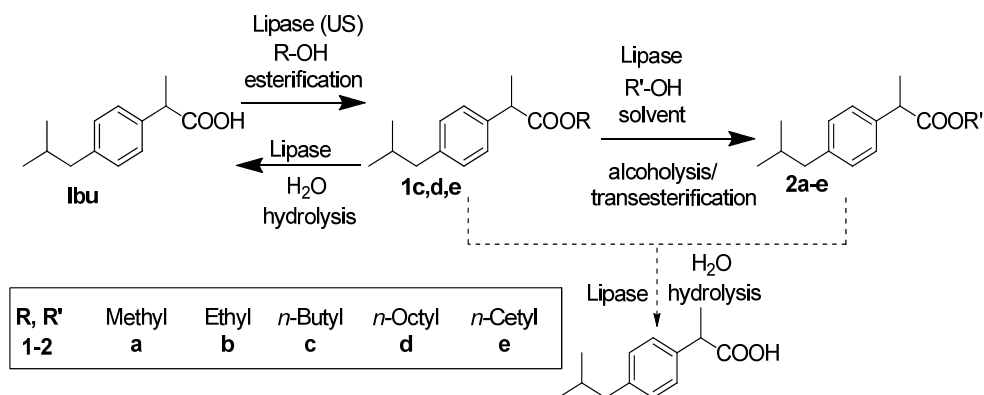
Scheme 1. Possible reaction routes for the biocatalytic transformation of Ibuprofen and its various esters

1. Lipase-catalyzed esterification of *rac*-ibuprofen

Since lipases from *Aspergillus oryzae* and *Rhizopus oryzae* were successfully used for the esterification of racemic phenylacetic and 2-phenyl-1-propanoic acid [14], first the lipase-catalyzed esterification of racemic ibuprofen (*rac*-Ibu) was tested under various conditions. Commercial lipases, such as lipases A and B from *Candida antarctica* CaL-A and CaL-B), lipase from *Candida rugosa* (CrL), lipase from *Pseudomonas cepacia* (PcL), lipase from *Pseudomonas fluorescens* (LAK), *Pancreatic porcine* lipase (PpL), lipase from *Mucor miehei* (MmL) were used as potential biocatalysts for the esterification of ibuprofen in several neat alcohols at 55°C with and without sonication. Using different alcohols as nucleophile (*n*-butanol, *iso*-butanol, *n*-pentanol, *n*-octanol, *n*-cetanol) it was found that the enzymatic activity continuously decreased with the increasing of the alkyl chain length of the alcohols. Best results were obtained with immobilized CaL-B on Eupergite (Novozym 435) in *n*-butanol. Only the *R*-selective CaL-B displayed satisfactory results for esterification, leading *R*-ibuprofen butyl ester (ee=85%) with a conversion of 10% after 1 h. By sonication the reaction rate increased slowly (*c* >13% after 1 h), but the enzyme displayed lower selectivity (ee=73% for *R*-ibuprofen butyl ester). Next this reaction was performed at room temperature in several recommended solvents like MTBE, *n*-octane, acetonitrile, toluene and THF, using 5 *equiv*. of butanol. Best results were obtained in MTBE when the reaction undergoes without a significant improvement of the enzyme activity, but the enzyme selectivity slightly increased of (ee=89% for *R*-ibuprofen butyl ester).

2. Lipase-catalyzed hydrolysis of racemic ibuprofen esters

Next the hydrolysis of three bulkier racemic ibuprofen esters (*rac*-**1c-e**) were performed in the presence of the above mentioned lipases in the same organic solvents. For this scope water, saturated octane, MTBE, toluene or acetonitrile, THF containing 5 *equiv*. of water were used. It was found that at lower conversions (c<5%) the weakly active CaL-B and MmL displayed both high but surprisingly opposite stereosectivities (*E*>200) as depicted in Scheme 2. When higher conversions were reached (c>10%), the enantiopurities of the formed ibuprofen decreased dramatically as shown in Table 1.

Table 1. Hydrolysis of racemic ibuprofen esters (*rac*-**1c-e**, 10 mg) with two lipases (10 mg) in several organic solvents saturated with water or containing 5 *equiv*. of water (after 12 h).

Substrate/solvent		CaL-B				MmL			
		Products		c	*E*	Products		c	*E*
		ee (*S*)-**1**	ee (*S*)-Ibu			ee (*R*)-**1**	ee (*S*)-Ibu		
rac-**1c**	MTBE	6	99	5.7	>200	67	53	55.8	6
	Octane	1	99	1.0	>200	6	99	5.7	>200
	CH₃CN	5	73	6.4	7	1	59	1.7	4
	Toluene	15	75	16.7	8	4	78	4.9	8
	THF	2	99	2.0	>200	1	99	1.0	>200
rac-**1d**	MTBE	7	46	13.2	3	60	40	60.0	4
	Octane	1	99	1.0	>200	3	99	2.9	>200
	CH₃CN	4	34	10.5	2	27	39	40.9	3
	Toluene	1	99	1.0	>200	7	71	9.0	6
	THF	1	78	1.3	8	1	99	1.0	>200
rac-**1e**	MTBE	1	88	1.1	16	51	8	86.4	2
	Octane	1	99	1.0	>200	6	99	5.7	>200
	CH₃CN	5	67	6.9	5	58	14	80.6	2
	Toluene	1	99	1.0	>200	10	99	9.2	>200
	THF	4	99	3.9	>200	1	81	1.2	10

The use of a triple-folded mutant of CaL-A with a 30-fold enhanced activity towards profens, which displayed high enantioselectivities for (*R*)-selective hydrolysis of ibuprofen esters, was earlier reported [15]. Beside the enhanced selectivity, the activity of the mutant remains unsatisfactory as found also for the native lipases. This information and our herein presented results determined us to investigate also the alcoholysis of the racemic bulkier ibuprofen esters with various aliphatic alcohols (Scheme 2).

3. Enantioselective alcoholysis of racemic ibuprofen esters

Next an analytical scale extensive screening for the alcoholysis of *rac*-Ibuprofen octyl ester (*rac*-**1d**) with *n*-butanol in the same five solvents (MTBE, *n*-octane, acetonitrile, THF, toluene) in presence of several lipases was investigated. Most of the lipases (CaL-A, PpL, LAK, CrL, lipase from *Burkholderia cepacia* LPS, and Alcalase) were inactive. Good results were displayed by the *R*-enantioselective CaL-B and by the (*S*)-selective MmL (Scheme 2). Similarly to MmL, lipases from lyophilized mycelia of *Aspergillus oryzae* displayed *S*-selectivity when *rac*-Flurbiprofen based esters [16] were subjected for alcoholysis.
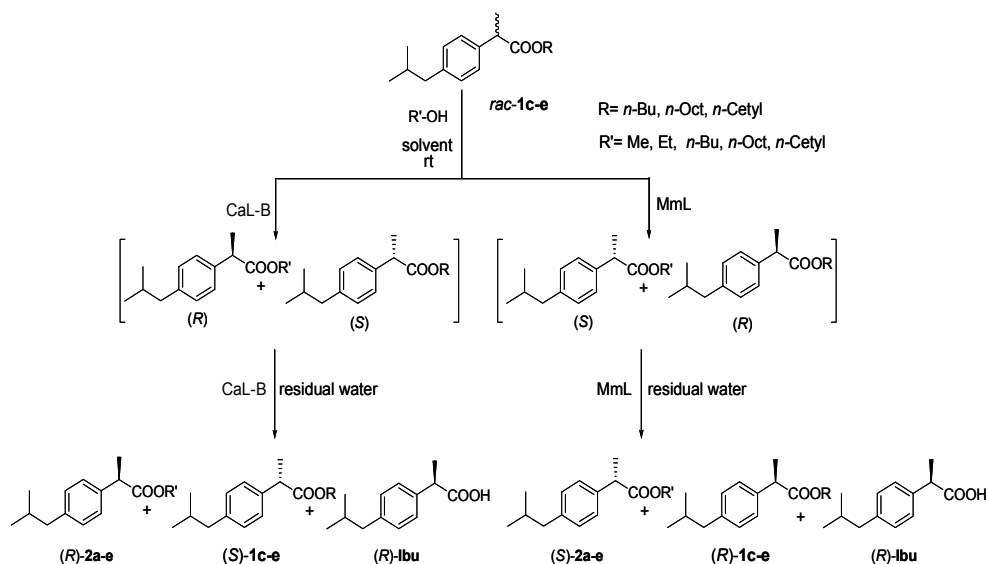
Scheme 2. The opposite enantioselectivity of CaL-B and MmL in the alcoholysis of racemic esters of Ibuprofen
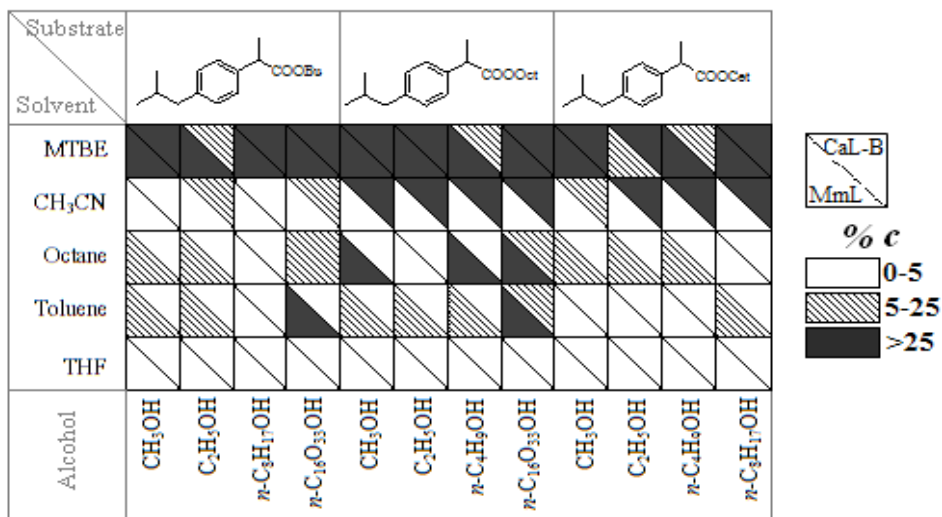
Figure 1. Conversions for the CaL-B and MmL mediated alcoolysis of *rac*-**1c,d,e** in various solvents at room temperature, after 17h

Based on these results further other nucleophiles (methanol, ethanol, *n*-octanol and *n*-cetylic alcohol) were tested for the alcoholysis of all three bulky racemic esters (*rac*-**1c-e**) in presence of these two lipases with opposite enantioselectivity in the same solvents. The obtained most relevant results are presented in Figure 1 (conversion) and Figure 2 (enantiomeric excesses).

Due to the presence of the residual water from the enzymes, a secondary enzymatic hydrolysis of the produced kinetic resolution products occurred in all cases. For these reaction both lipases (CaL-B and MmL) were *R*-selective biocatalyst.

In almost all cases the optical purity of the produced (*R*)-ibuprofen by hydrolytic side reactions was high, while the enantiomeric excesses of the formed (*S*)-**2** or (*R*)-**2** esters and of the remained (*R*)-**1** or (*S*)-**1** esters were moderate to good.

Highest conversions for the MmL catalysed alcoholysis for all three *rac*-**1d-e** esters were obtained in MTBE, excepting the ethanolysis of the cetyl ester *rac*-**1e** which undergoes similarly and slowly both in MTBE and *n*-octane. Generally, the same solvent was appropriate also for the CaL-B mediated transesterifications, excepting the butanolysis of octyl- and cetyl ester *rac*-**1d-e**, when acetonitrile proved to be most convenient reaction media. The CaL-B mediated ethanolysis of butyl ester *rac*-**1c** proceeded slowly in both MTBE and acetonitrile. While *n*-octane was the adequate solvent for the MmL catalyzed alcoholysis of octyl ester *rac*-**1d**, in THF all reactions underwent with insignificant conversions.
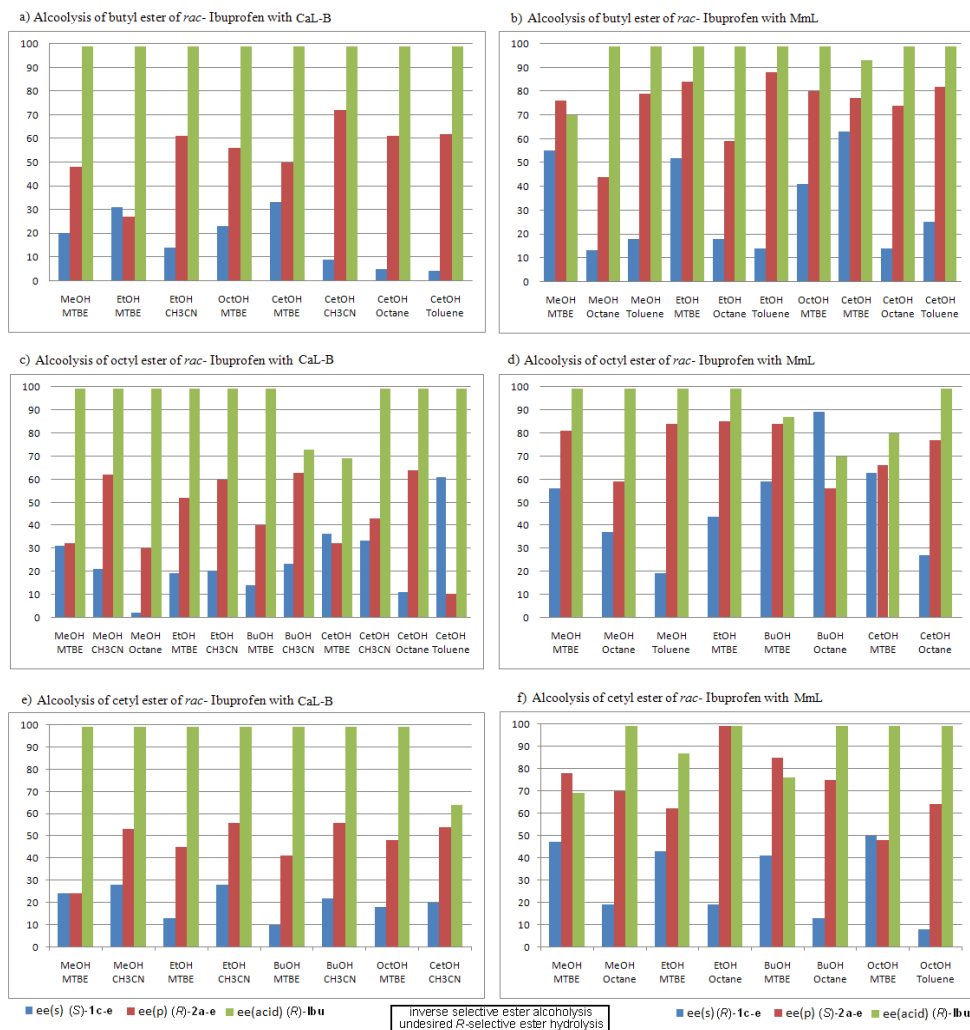
Figure 2. Enantiomeric excesses for the alcoholysis of the *rac*-**1c,d,e** (5 μL) with five different alcohols (5 equiv.) in presence of CaL-B and MmL (25 mg/mL) in various solvents (500 μl) at room temperature, after 17h

Considering all analytical scale results as schematically depicted in Figure 1 and 2 the optimal biotransformation is catalyzed by MmL in MTBE when the octyl ester of ibuprofen (*rac*-**1d**) was the substrate and ethanol was the nucleophile. In this reaction (*S*)-**2b** (ee 86%) and (*R*)-**1d** (ee 44%) were formed. However, by a parallel enzymatic hydrolytic resolution, the (*R*)-Ibuprofen was also formed as by product in a highly enantiomerically enriched form (ee 99%).
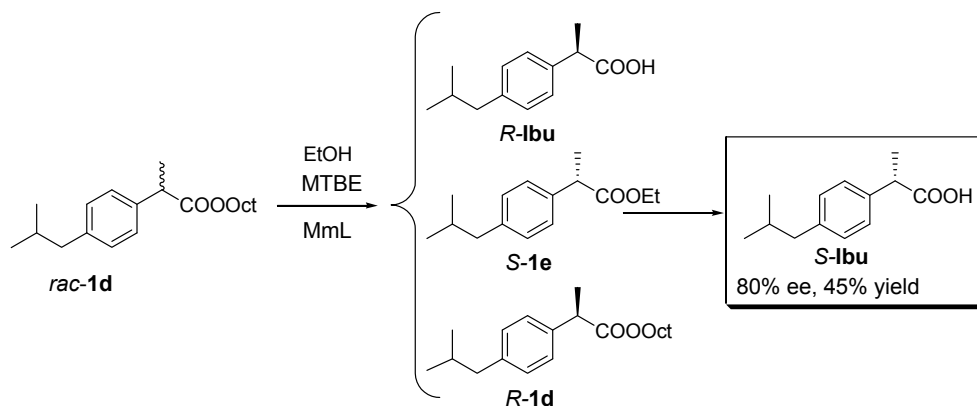
Scheme 3. Preparative scale synthesis of (S)-Ibuprofen

Using the optimal conditions (enzymatic ethanolysis of racemic octyl ester (*rac*-**1d**) catalyzed by MmL in MTBE, followed by hydrolysis of the obtained *S*-ethyl ester (*S*)-**2b**, the preparative scale procedure was performed as depicted in Scheme 3.

CONCLUSIONS

All possible enzymatic routes involving the ibuprofen esters with long chain alcohols *rac*-**1** as product or substrate were studied. A selective and facile strategy to prepare both enantiomers of ibuprofen by lipase mediated kinetic resolution of racemic *n*-octyl ester was developed. Two enzymes with opposite enantioselectivity were tested and the influence of the chain length of alcoholic moiety on the obtained conversion and optical purity of products were systematically investigated.

EXPERIMENTAL SECTION

1. Analytical methods

The ^{1}H and ^{13}C NMR spectra were recorded on a Bruker spectrometer operating at 300 MHz and 75 MHz, respectively, at 25 °C using tetramethylsilane (TMS) as an internal standard and CDCl$_3$ as solvent. Thin Layer Chromatography (TLC) was carried out using Merck Kieselgel 60F^{254} sheets. Spots were visualized

by treatment with 5% ethanolic phosphomolybdic acid solution and heating. Preparative chromatographic separations were performed using column chromatography on Merck Kieselgel 60Å (63-200 μm).

All reagents were purchased from Merck or Sigma-Aldrich and used as received. Solvents and alcohols for enzymatic reactions were stored over molecular sieves unless otherwise stated. Commercially lipases were purchased from Sigma or Novozym.

The enantiomeric separations were performed by HPLC using an Agilent 1200 instrument with DAD detector using a Chiralpak IB column, with n-hexane-2-propanol (99:1, v/v) as eluent for all esteric compounds and n-hexane-2-propanol with 1% acetic acid content (99:1, v/v) for Ibuprofen, at 1 mL/min flow rate.

Table 2. Chromatographic enantiomers separation on IB HPLC column

t_R (min)	Ibu	1,2a	1,2b	1,2c	1,2d	1,2e
R	11.99	11.6	8.33	9.45	9.15	8.3
S	14.45	13.35	10.51	11.27	11.19	11.27

Determination of E was based on the Chen equation [17]:

$$E=ln[(1-c)(1-ee_S)]/ln[(1-c)(1+ee_S)]$$

Racemic esters were obtained by direct esterification with the appropriate alcohol in dioxane as solvent, in the presence of DCC at room temperature. The structures of the obtained purified esters were confirmed by analytical and spectral data which are in agreement with those reported in the literature [18].

2. Lipase mediated kinetic resolutions

2.1. Selective enzymatic esterification

Racemic ibuprofen (200 mg) was solved in the tested solvent (0.4 mL) and the alcohol (5 equiv.) and the lipases (100 mg) were added. The reactions were carried out at 55°C in a US bath. Samples (50 μL) were taken and diluted with n-hexane (1 mL), than filtered and analyzed by HPLC.

2.1.2. Lipase-catalyzed hydrolysis of ibuprofen esters

Racemic esters (rac-**1c-e**, 10 mg) were solved in the tested solvent (1 mL) saturated with water and the lipases (10 mg) were added. The reactions was carried out at 25°C under shaking at 1250 rpm. Samples were taken and diluted with n-hexane, than filtered and analyzed by HPLC.

2.1.3. Lipase-catalyzed alcoholysis of ibuprofen esters

Racemic esters (*rac*-**1c-e**, 10 mg) were solved in the solvent (1 mL) and than the alcohol used as nucleophil (5 equiv.), 3-4 pieces of molecular sieves and t lipase (10 mg) were added. The reaction was carried out at 25°C under shaking at 250 rpm. Samples were taken and diluted with *n*-hexane, than filtered and analyzed by HPLC.

ACKNOWLEDGMENTS

R E F E R E N C E S

[1]. K.M. Williams, R.O. Day, R.D. Knihinicki, A.M. Duffield, *Acta Pharm. Toxicol.* 1986, **59**, 192.

[2]. R.H. Sonawane, N.S. Bellur, J.R. Ahuja, *Tetrahedron:Asymmetry* **1992**, *3,* 163.

[3]. Y. Maryam; M. Mehdi, H. Zohreh, *J. Mol. Catal. B: Enzym.* **2014**, *104,* 87.

[4]. F. Roure, A. Ducret, M. Trani, R. Lortie, *J. Chem. Tech. Biotechnol.* **1997**, *69*, 266; S.W. Tsai, J.J. Lin, C.S. Chang, J.P. Chen, *Biotechnol. Prog*. **1997**, *13*, 82; D. Chavez-Flores, J.M. Salvador, *Tetrahedron: Asymmetry* **2012**, *23,* 237.

[5]. C. Jose, M.V. Toledo, L.E. Briand, *Crit. Rev. Biotechnol.* **2016**, *36(5)*, 891; V. Gotor-Fernandez, E. Busto, V. Gotor, *Adv. Synth. Catal.* **2006**, *348,* 797; A.K. Prasad, M. Husain, B.K. Singh, R.K. Gupta, V.K. Manchanda, C.E. Olsen, V.S. Parmar, *Tetrahedron Lett.* **2005**, *46*, 4511.

[6]. R. Morrone, N. D'Antona, D. Lambusta, G. Nicolosi, *J. Mol. Catal. B: Enzym.* **2010**, *65*, 49.

[7]. A.C. Wu, P.Y. Wang, Y.S. Lin, M.F. Kao, J.R. Chen, J.F. Ciou, S.W. Tsai, *J. Mol. Catal. B: Enzym.* **2010**, *62*, 235.

[8]. W. Tsuzuki, A. Ue, A. Nagao *Biosci. Biotechnol. Biochem.* **2003**, *67*, 1660.

[9]. Chen. J.P., Wang, J.B. *Enzyme Microb. Technol.* **1997**, *20*, 615; Chulalaksananukul, W., Condoret, J.S., Combes, D. *Enzyme Microb. Technol.* **1993**, *15*, 691.

[10]. For examples: J. Brem, M. Naghi, M.I. Tosa, Z. Boros, L. Poppe, F.D. Irimie, C. Paizs, *Tetrahedron: Asymmetry* **2011**, *22*, 1672; M. Liaquat, *J. Mol. Catal. B: Enzym*. **2011**, 68, 59; T. Miyazawa, E. Kaito, T. Yukawa, T. Murashima, T.; Yamada, *J. Mol. Catal. B: Enzym.* **2005**, *37*, 63; E. Santaniello, S. Casati, P. Ciuffreda, G. Meroni, A. Pedretti, G. Vistoli, *Tetrahedron: Asymmetry* **2009**, *20*, 1833; K, Kaewprapan, J. Wongkongkatep, W. Panbangred, P. Phinyocheep, E. Marie, A. Durand, P. Inprakhon, *J. Biosci. Bioeng.* **2011**, *112(2)*, 124.

[11]. C. Blecker; S. Danthine; M. Pétré; G. Lognay; B. Moreau; L.V. Elst; M. Paquot; C. Deroanne *J. Colloid Interf. Sci.* **2008**, *321*, 154.

[12]. C. Torres; C. Otero *Enzyme Microb. Technol.* **1999,** *25*, 745.

[13]. A. Ghanem, H.Y. Aboul-Enein, *Chirality* **2005**, *17(1)*,1; R.D. Schmid, R.A. Verger, *Angew. Chem. Int. Edit.* **1998**, *37*, 1608; V.B. Gotor *Med. Chem.* **1999**, *7*, 2189, U.T. Bornscheuer, R. J. Kazlauskas *Hydrolases in Organic Synthesis*, Wiley–VCH, **1999**

[14]. A. Torres-Gavilán, E. Castillo, A. López-Munguía, *J. Mol. Catal. B: Enzym.* **2006**, *41*, 136.

[15]. R. Gandolfi, R. Gualandris, Ch. Zanchi, F. Molinari, *Tetrahedron: Asymmetry,* **2001,** 12, 501; A. Romano, R. Gandolfi, F. Molinari, A. Converti, M. Zilli, M. Del Borghi, *Enzyme Microb. Technol.* **2005**, *36*, 432.

[16]. K. Engström, J. Nyhlen, A.G. Sandström, J.E. Backväll, *J. Am. Chem. Soc.* **2010**, *132*, 7038; A. G. Sandström, K. Engström; J. Jyhlen; A. Kasrayan; J.E. Bäckvall, *Protein Eng., Des. Sel.* **2009**, *22*, 413.

[17]. P. Spizzo, A. Basso, C. Ebert, L. Gardossi, V. Ferrario, D. Romano, F. Molinari, *Tetrahedron* **2007,** *63,* 11005.

[18]. C.-S. Chen, Y. Fujimoto, G. Girdaukas, C.J. Sih, *J. Am. Chem. Soc.* **1982**, *104*, 7294.

[19]. C.W. Lee, H. Alper, *J. Org. Chem.* 1995 , *60*, 250; S. Koul, J.L. Koul, B. Singh, M. Kapoor, R. Parshad, K.S Manhas, S.C. Taneja, G.N. Qazi, *Tetrahedron: Asymmetry* **2005**, *16*, 2575; A.K. Bansal, R.K. Khar, R. Dubey, A.K. Sharma, *Pharmazie* **1994**, *49*, 422; M. Kapoor, R. Parshad, K.S. Manhas, S.C. Taneja, G.N. Qazi, *Tetrahedron: Asymmetry* **2005**, *16*, 2575, A.K. Bansal, R.K. Khar, R. Dubey, A.K. Sharma, *Pharmazie* **1994**, *49*, 422.

AN ASSESSMENT OF THE WATER QUALITY AND ECOLOGICAL STATUS OF SITNICA RIVER, KOSOVO

HYRIJE KORAQI[a]*, IBUSH LUZHA[b], FATLINDA TËRMKOLLI[a]

ABSTRACT. The aim of this study is to assess and present the contamination with some environmental toxic parameters of water samples of Sitnica River, Kosovo. Sitnica River is one of the main rivers in Kosovo. The river is located in the area with high anthropogenic pressure, were the contamination of river with different pollutants presents a complex long-term environmental problem. The water samples from Sitnica River were collected from five stations every three months. These stations are covering the upstream and downstream sites of major industrial area of Obiliq city close to Thermo Power Plant (TPP) Kosovo "B" as the main power plant in the country. This Thermo Power Plant apart from air and soil pollution is considered as main source of contamination for the river water as well due to the direct discharged of waste water without any prior treatment. International permissible limits (75/440/EEC) and Kosovo National limits (UA13/2008) were applied to assess the river water contamination. Physico-chemical parameters in water samples from Sitnica River were determined to assess the level of contamination. The concentrations of some toxic parameters such: Fe^{2+}, Mn^{2+}, Al^{3+}, Cr^{3+}, NO_2^--N, NO_3^--N, NH_3-N, PO_4^{3-}-P were measured using UV-VIS spectrophotometry in accordance with standard method US EPA 6010C.The results showed that the Sitnica River is heavily polluted. The results were summarized using the program Statistica 6.0 descriptive statistical method. In order to protect the river water from further contamination, the remediation options in order to reduce the anthropogenic discharges are suggested.

Keywords: Physico-chemical, Sitnica River contamination, UV-VIS Spectro-photometry

INTRODUCTION

There are many ways to define water pollution, and yet most of definitions address towards to excessive concentration of the certain substances which for certain time cause effects than can be hazardous for water ecosystems [1].

[a] *University of Prishtina ''Hasan Prishtina'',str. Bulevardi "Dëshmorët e Kombit", Prishtina, Kosovo*
[b] *Ministry of Trade and Industry, Muharrem Fejza street, n.n. Hospital Square 10.000 Pristine, Kosovo*
* *Corresponding author: hyriekoraqi@hotmail.com*

Multidisciplinary collaborative research is essential for understanding the pollution processes. Determination of total quantitative and qualitative metals and distribution of all physical and chemical forms in traces (speciation) in natural water equilibrium resources today is to be considering as the main challenge for most of the scientists. Overexploitation of nature and uncontrolled use of natural resources, including inadequate processing of industrial wastes have caused large contamination of world ecosystems by toxic parameters: Fe^{2+}, Mn^{2+}, Al^{3+}, NO_2^--N, NO_3^--N, NH_3-N, $PO_4^{3-}-P$.

Due to its position and form, Sitnica River is very interesting for hydro biological studies. It originates as a confluence of two mountain rivers (Shtimanka and Sazlija) and with a total length of 154 km, flows in a South-Northwest direction through the central part of the Kosovo until its confluence into Iber River. This is most important river of the Kosovo walleye and the meeting point for the whole hydrographic network. The catchment area occupies 2861 km2 and is characterized by its high potential or raw materials, favorable geographic position and configuration of terrain, traffic network and concentration of industrial and mining complexes. This river is the sole recipient for a large amount of waste water, which changes its ecological characteristics [2][3].

The aim of this study was the quantitative determination of some environmental toxic parameters in polluted waters discharged from TPP Kosova "B" and the possible impact of these waters on the pollution of River Sitnica as surface water resource. International permissible limits (75/440/EEC) and Kosovo National limits (UA13/2008) were applied to assess the river water contamination. Physico-chemical parameters in water samples from Sitnica Rivers were determined to assess the level of contamination. The concentrations of some toxic parameters: Fe^{2+}, Mn^{2+}, Al^{3+}, NO_2^--N, NO_3^--N, NH_3-N, $PO_4^{3-}-P$ were measured using UV-VIS spectrophotometry in accordance with standard method US EPA 6010C.

The sampling sites in Sitnica River are geographically positioned using Geographic Information System (GIS). The results were elaborated using statistical methods that can be used to locate pollution sources. Selected locations, where certain toxic elements should be monitored and remediation possibly performed, were highlighted [4].

Kosovo as a new country aiming the EU integration has harmonized the national water legislation with EU Water Framework Directive. There are a very few references to waters in Kosovo; however, these are all in respect of the chemical quality [5]. The authors reported the level of contamination in rivers of Kosovo, mainly in water and sediments of Sitnica river, their concentrations were very high due to the inputs of industrial discharge and mining waste erosion. No studies have been reported on the assessment of ecological status of the rivers in Kosovo.

RESULTS AND DISCUSSION

The obtained values are shown in Table 1. From results showed that most of the physico-chemical parameters: water temperature, pH, conductivity, total dissolved solids (TOS), chemical oxygen demand (COD), biochemical oxygen demand (BOD), hardness, concentration of Cl^-, NO_3^--N, NO_2^--N, NH_3-N, PO_4^{3-}-P, SO_4^{2-}, Ca^{2+}, Mn^{2+}, Fe^{2+}, Al^{3+}, Cr^{3+} in water of Sitnica river were found out the permissible limits of both European Legislation 75/440/EEC and Kosovo National Administrative Direction UA 13/2008.

Table 1. Physic-chemical parameters in river water Sitnica

Parameters	A_1	A_2	A_3	A_4	A_5
Water temp./ ° C	15.0	16.1	16.5	19.9	15.8
pH/1	11.0	8.41	8.32	10.3	7.64
Conductivity/ µScm^{-1}	475	431	423	459	557
Total dissolved Solids (TDS)/mg/L	18.0	20.4	28.2	37.2	21.2
Chemical oxygen demand (COD)/mg/L	18.0	13.1	15.9	22.1	29.8
Biochemical oxygen demand (BOD) /mg/L	19.3	17.9	20.8	25.2	32.7
Hardness /°dH	4.07	6.52	8.90	11.2	13.9
Chlorine (Cl^-)/ mg/L	296	55.5	75.5	51.9	97.4
NO_3^--N/mg/L	0.64	1.16	1.32	1.14	1.13
NO_2^--N/ mg/L	0.04	0.10	0.12	0.10	0.21
NH_3-N/ mg/L	0.03	0.04	0.21	0.02	0.50
PO_4^{3-}-P/ mg/L	0.77	0.17	0.57	0.72	0.96
SO_4^{2-}/ mg/L	9.0	28.6	52.7	64.3	62.3
Ca^{2+}/ mg/L	2.57	4.80	5.63	9.32	6.88
Mn^{2+}/mg/L	1.02	0.71	0.51	0.55	0.96
Fe^{2+}/mg/L	2.52	2.96	1.82	1.78	3.10
Al^{3+}/ mg/L	0.89	1.87	2.0	2.04	2.89
Cr^{3+}/mg/L	0.97	1.24	1.32	1.45	2.15

Basic statistical parameters for parameters (mg/L) in five water samples are presented in Table 2. Using experimental data (Table 2) and box plot approach of Tukey [6], anomalous values (extremes and outliers) in waters were determined for the whole region. Frequency distributions of each measured ions and two dimensional scaterplot with plots diagrams are presented in Figure 1 and 2. Anomalous values (outliers and extremes) for 7 variables are presented in Table 3.

Table 2. Basic statistical parameters for nine chemical parameters

Variable mg/L	Mean	Geo. mean	Median	Min.	Max.	Variance	Std.Dev.
Al^{3+}	1.85	1.75	1.87	0.89	2.89	0.53	0.72
Fe^{2+}	2.67	2.62	2.96	1.78	3.10	0.30	0.54
Mn^{2+}	0.75	0.72	0.71	0.53	1.02	0.05	0.22
NO_2^-N	0.11	0.10	0.10	0.04	0.21	0.00	0.05
NO_3^-N	1.03	1.01	1.13	0.64	1.16	0.04	0.22
NH_3-N	0.27	0.10	0.04	0.02	0.75	0.11	0.33
$PO_4^{3-}P$	0.56	0.43	0.72	0.71	0.96	0.13	0.36
Cr^{3+}	1.55	1.49	1.45	0.97	2.15	0.24	0.49
Cl^-	141	111	97.4	51.9	296	113	106
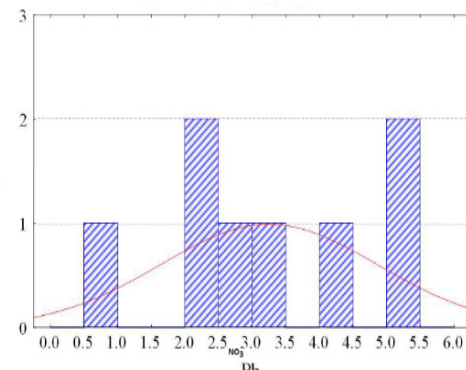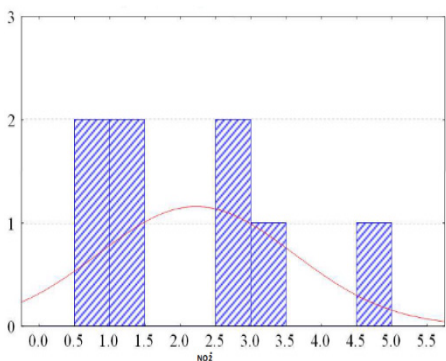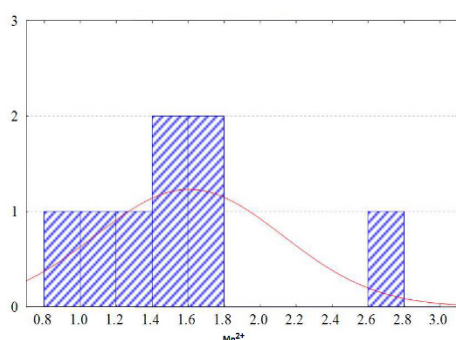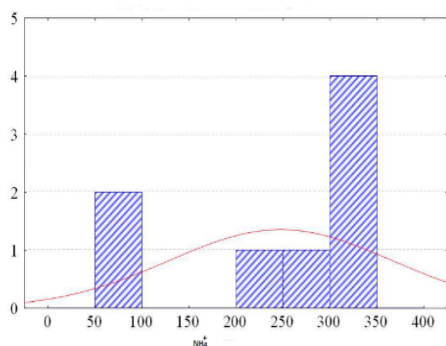
Figure 1. Frequency Histograms of some measured parameters: Mn^{2+}, NH_4^+, NO_2^-, NO_3^-
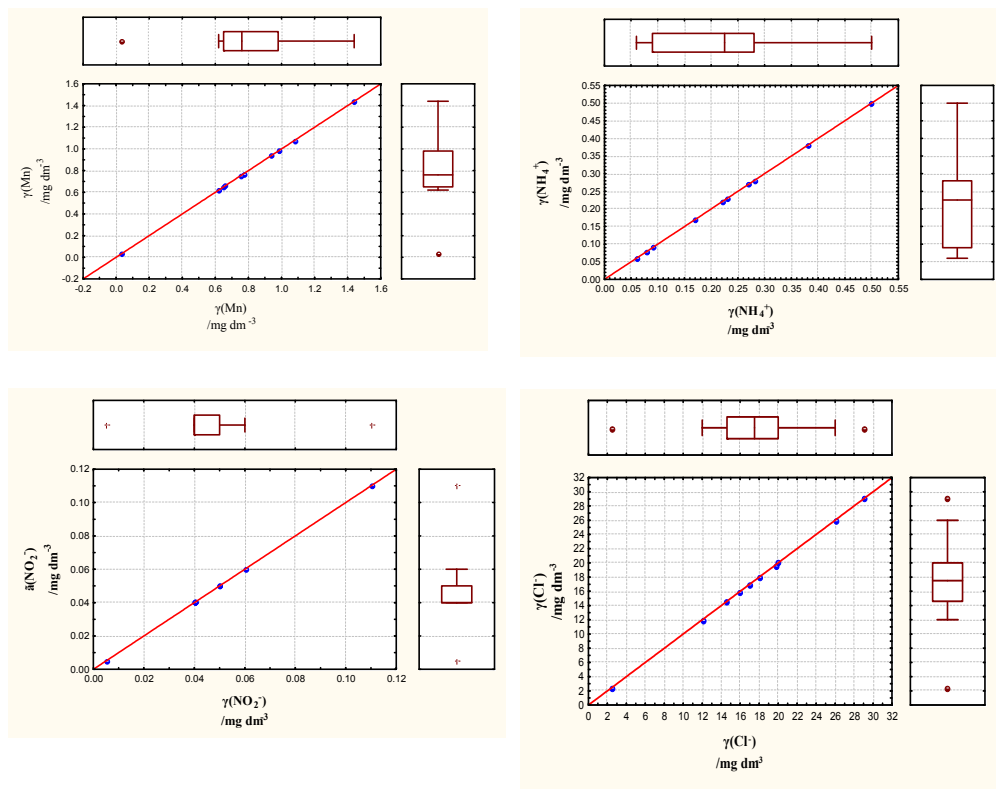
Figure 2. Two dimensional scatterplot with plots diagrams of some measured parameters: Mn, NH_4^+, NO_3^-, Cl^-

Table 3. Water samples with anomalous values (outliers and extremes) from seven variables

Sample	Outliers of elements	Extremes of elements
A_1	Cl^- (296 mg/L) Mn^{2+} (1.02 mg/L)	-
A_2	-	NO_2^--N (0.10 mg/L)
A_3	NH_3-N (0.76 mg/L)	-
A_4	-	-
A_5	Al^{3+} (2.89 mg/L) NH_3-N (0.5 mg/L)	Fe^{2+} (3.10 mg/L) NO_2^--N (0.21 mg/L) Cr^{3+} (2.15 mg/L)

Chemical data presented in the Table 1, Frequency Histograms of some measured ions (Fig.1) and Boxplot diagrams (Fig. 2), can be used for the assessment of water contamination by toxic elements according to the International permissible limits (75/440/EEC) and Kosovo National limits (UA13/2008) and EU directives.

The physic-chemical parameters such as: water temperature, pH, conductivity, total dissolved solids (TOS), chemical oxygen demand (COD), biochemical oxygen demand (BOD), hardness, concentration of Cl^- NO_3^--N, NO_2^--N, NH_3-N, PO_4^{3-}-P, SO_4^{2-} Ca^{2+}, Mn^{2+}, Fe^{2+}, Al^{3+}, Cr^{3+} generally appeared to be significantly concentrated in the River water Sitnica, it is evident that in this River all used waters from Kosovo Power Plants (Kosovo "A" and "B") are discharged there, and the leached waters of all ash disposals and two surface open mine (Mirash and Bardh) of these two power plants also.

Temperature varied at different locations of the river as indicated by the *in-situ* readings. It is not considered coming from heat contamination sources, but from natural warming in different parts of Kosovo. The high pH value at stations A_2 A_3 A_4 A_5 is due to the discharge of water from Thermo Power Plant Kosovo "B" after treatment with lime. Conductivity ranged from 431-584 µScm^{-1} these values were within highest desirable limit (75/440/EEC). If we compare conductivity separately, the lowest value is observed at A_2 station and the highest value is observed at A_3 station. Higher conductivity values indicate the presence of higher content of dissolved salts in the water. The values of hardness of water have described positive correlation with Mg^{2+} and Ca^{2+} concentrations. The lowest Hardness value is observed at A_1 station (4.07°dH) and the higher value of the hardness was observed at station A_5 (13.9°dH). Chemical oxygen demand (COD) and Biochemical oxygen demand (BOD) reaches maximum values at A_5 station (29.8 mg/L COD and 32 mg/L BOD).

The concentrations of chlorines were below 200 mg/L (maximum admissible concentration, according to EU Directive), except for concentration found in A1. The concentration of NO_3^--N above 10 mg/L which causes the lowest toxic effect at all locations A_1-A_5. The concentration of NO_2^--N were above 0.005 mg/L, which causes the significant effect, was found at all stations. The concentration of NH_3-N above 0.1 mg/L causing significant toxic effect were found at stations A_3 and A_5. The concentration of PO_4^{3-}-P above 0.25 mg/L, which causes the significant effect, was found at stations A_3 and A_5. The concentration of Mn above 0.05 mg/L (meaning the maximum admissible concentration, according to EU Directive) causing significant toxic effect were found at all stations A_1-A_5. The highest concentration was found at station A_1 (1.02 mg/L). Concentration of Fe above 0.3 mg/L, which causes the significant toxic effects, was found at all stations A_1-A_5. The highest concentration of Fe was found at station A_3 and A_5 (A_3: 3.02 mg/L and A_5: 3.10 mg/L). The concentrations of Al^{3+} above 0.2 mg/L which causes the toxic effects, were

found at all locations A_1- A_5. The highest concentration of Al^{3+} was found at station A_5 (2.89 mg/L), as a result of anthropogenic pollution. The concentration of Cr above 0.05 mg/L which causes the toxic effects, were found at all locations A_1-A_5. The highest concentration of Cr was found at station A_5 (2.15 mg/L), as a result of anthropogenic pollution.

The presence of toxic parameters and trace metals in the River water Sitnica in these five sample places is in fact the result of the producible activity of Kosovo power plants which use lignite as a combustible material and which after combustion releases a considerable amount of ash. Created disposals from residues after the combustion of lignite are near river Sitnica is the permanent way to indicate in the quality of its water. High concentration of chromium in these sample places can be described as a variety of agricultural and industrial activities in this region. Farmers, with their activity in agro production, use different chemical preparations, which contain chromium, and which together with raw waters from agricultural surfaces, arrive till the river Sitnica. The raw material used for the production of electricity at Kosova Thermal power plants is coal. These plants use large quantities of water and have no wastewater treatment. Working activity in these plants results in water pollution which after discharge into water causes environmental impact. Polluted water discharged from these plants into the Sitnica river results in pollution with significant impact on local and regional level.

The discharge of polluted water from coal mines, thermal power plants and existing ash landfills is a result of disregarding the environmental legislation. The obtained results from the samples taken at different locations before they discharge into the Sitnica River revealed that they are polluted in quality aspect from mines and in quantity aspect from power plants. Advanced wastewater treatments such as classification, treatment, flocculation and filtration of the discharged waters would enable their re-use and minimization the pollution of the river Sitnica which further discharged into the Iber River.

CONCLUSIONS

In order to determine the level of contamination of Sitnica river water, the following parameters: Cl^-, NO_3^--N, NO_2^--N, NH_3-N, $PO_4^{3-}-P$, SO_4^{2-} and trace metals: Al^{3+}, Fe^{2+}, Cr^{3+}, Mn^{2+} concentrations were investigated in five selected sampling sites. The study revealed that the enhanced concentration of toxic parameters of Sitnica river is due to the anthropogenic influences.

International permissible limits (75/440/EEC) and Kosovo national limits (UA13/2008) were applied to assess the river water contamination. The results showed that the Sitnica River is heavily polluted, the highest concentrations were recorded in the sampling spots A_3, A_4 and A_5.

These spots correspond to the locations in Plemetin (A_3), the nearest to the Thermo Power Plant Kosovo "B", between the landfill coal and ash (A_4) and in the Sitnica River where the water used in Thermo Power Plant Kosovo "B" is discharged (A_5).

The results of this study provide the baseline data which can be used by Kosovo authorities for environmental management. It can be concluded that the input of industrial discharge of water from Thermo Power Plant Kosovo "B" into the Sitnica river is responsible for the intense contamination of the water and must be regarded as a major concern.

In order to protect the river water from further contamination, the remediation options in order to reduce the anthropogenic discharges are suggested.

EXPERIMENTAL SECTION

Sitnica River is one of the main rivers in Kosovo. The river is located in the area with high anthropogenic pressure, were the contamination of river with different pollutants presents a complex long-term environmental problem. Summers are warm and dry, while winters are cold and rainy. Annual average air temperature reaches 17.1 ºC.

Average temperature during the coldest month (January) is -2.4 ºC and 24.2 ºC during the warmest month (July). The highest rainfall is recorded between October and March 500-700 mm/year (data from the Meteorological and Hydrological service of the Republic of Kosovo), the lowest between June and August 200-300 mm/year. Precipitation varies from 600 to 1400 mm/year. It is important to evaluate how climate has varied and changed in the seasons. Climate change can directly affect the hydrological cycle and, through it, the quantity and quality of water resources.

The water samples from Sitnica River were collected from five stations every three months at monthly intervals (in triplicate) during the period from June 2015 to September 2015.These stations are covering the upstream and downstream sites of major industrial area of Obiliq city close to Thermo Power Plant (TPP) Kosovo "B" as the main power plant in the country. Geographical positions were determined by GPS, using model "Magelau". The sampling stations are shown in Fig. 3.

Five water samples were taken from along the banks of the sampling station on summer period. Analyses of samples were done according to standards methods for surface water ISO 5667-1(2006) [5,7]. The study area with the sampling locations is shown in Fig.3 and the details about all sampling sites. Sampling tools were washed and dried with water before the next sample was collected. Water samples were collected from 10 cm below the surface water [7]. The collected samples ($1dm^3$) were stored in polythene plastic containers. According to the requirements samples were preserved in the refrigerator after treatment. The study area with the sampling locations is shown in Figure 3 and the details about all sampling sites are presented in Table 4.

Figure 3. Study area with sampling stations

Table 4. Sampling stations with detailed locality description

Sample	Locality	Coordinates	Height above sea level (m)
A₁	To the Thermo Power Plant Kosovo "B"	WPT=451 Y=34505450 X=4721132	541
A₂	Place where discharged water used from facilities the Thermo Power Plant Kosovo "B"	WPT=450 Y=34506102 X=4724197	534
A₃	Plemetin	WPT=448 Y=34504668 X=4726378	536
A₄	The near the Thermo Power Plant Kosovo "B" between the landfill coal and ash	WPT=449 Y=34503772 X=4726063	542
A₅	In the Sitnica River where discharged water used from TPP Kosovo "B''	WPT=447 Y=34503151 X=472840	533

*WPT-Format Waypoint

All instruments were calibrated according to manufacturer's recommendations. All tests were performed at least three times to calculate the average value. Temperature of water was measured immediately after sampling, using digital thermometer, model "Quick 63142". Measurements of pH were performed using pH/ion-meter, "Metrohm". Electric conductivity was measured by conductometer "Metrohm". Some of physic-chemical parameters (NO_2^--N, NO_3^--N, NH_3-N, PO_4^{3-}—P, Al^{3+}, Mn^{2+} and Fe^{2+}) were determined using UV-VIS spectrophotometry method.

A CAMSPEC Model UV-VIS double beam spectrophotometer with a 10mm optical path cell was used for spectrophotometric measurements. Spectral range was 190-1100 nm. Its measurement region, in a cuvette of 10 mm, was λ = 340-800 nm, is dedicated for drinking waters analysis, discharged and sea water.

R E F E R E N C E S

[1]. L.W. Canter, River Water Quality Monitoring, Michigan, **1985**.
[2]. V.N. Živic, J. Šapkarev, Labus, Univerzitetska misao, Pristina, **1997**, 97-101.
[3]. V.N. Živic, B. Miljanovic, V. Kostov, III Congress of ecologists of Macedonia with international participation. Proceedings. Macedonian Ecological Society, **2007**, 13-1.
[4]. F. Gashi, N. Troni, F. Faiku, F. Laha, A. Haziri, I. Kastrati, E. Beshtica, M. Behrami, *American Journal of Environmental Science*, **2013**, *9(2),* 142.
[5]. F. Ferati, M. Kerolli-Mustafa, A. Kraja-Ylli, *Environ Monit Assess*., **2015**, 4524.
[6]. J.W. Tukey, Exploratory data analysis,17th Edn., Addison-Wesley, Reading, Mass., **1997**, 6887.
[7]. ISO 5667-1., Water quality-sampling-part 1: guidance on the design of sampling programs and sampling techniques, **2006**.
[8]. H. David, Water Treatment Unit Processes, Physical and Chemical, Publisher, CRC press, **2005**.
[9]. S. Burca, C. Indolean, A. Maicaneanu, *Studia UBB Chemia*, **2015**, *60*(3), 247.
[10]. M. Davis, S. Maste, Principles of Environmental Engineering and Science, McGraw Hill Company, New York, **2002**.
[11]. B. Baruti, I. Malollari, S. Ferati, N. Lajci, S. Hoda, M. Kelmendi, F. Dobroshi, P. Hoxha, *Journal of Environmental Protection and Ecology*, **2014**, 819.
[12]. Kosovo National Administrative Direction UA 13, AD for the limited values of the effluents discharged on water bodies and on the system of public canalization, **2008**.
[13]. M. Branica, Environmental Research in aquatic systems Scientific Series of the International Bureau Volume 3, Forschungszentrum Julich, Germany, **1990**.

EFFECT OF ABLATION ENVIRONMENT ON THE CHARACTERISTICS OF GRAPHENE NANOSHEETS PRODUCED BY LASER ABLATION

ELNAZ VAGHRI[a], DAVOUD DORRANIAN[a,*]

ABSTRACT. The effect of ablation environment on the characteristics of graphene sheets produced by the laser ablation method in liquid medium has been studied experimentally and reported here. Graphene sheets were synthesized by using Q-switch Nd-YAG laser at 532 nm wavelength and 7 ns pulse width and laser fluence of 0.5 J/cm^2 in liquid nitrogen and distilled water environments. The structure and morphology of the ablation products are characterized by X-ray diffraction method, UV-Visible absorption spectroscopy, transmission electron microscopy (TEM), Raman and Fourier transform infrared spectroscopy (FTIR). Results indicate that the graphene nanosheets synthesized by the laser ablation method in liquid nitrogen environment have larger sp^2 carbon domains and minor structural defects. Therefore, in our experimental conditions, the liquid nitrogen environment seems to be a better medium for producing graphene sheets with high quality, in comparison with the water.

Keywords: Pulsed laser ablation, Graphene, Carbon nanostructures, liquid nitrogen, TEM

INTRODUCTION

Carbon based nano-materials have been extensively studied in the last few decades. Among them graphene, which is a two-dimensional (2D) material with an in-plane hexagonal structure, has attracted more scientific interest, owing to its unprecedented and unique electrical, mechanical, and thermal properties [1,2]. Graphene and graphene based compounds found wide applications in different industrial fields such as electro-photoluminescence devices [3], solar cells [4], artificial muscles [5], beam-scanning planar lens [6], chemical sensors [7], biosensors [8] or organic light emitting diodes [9]. Due to their widespread applications, a large scale production of these materials is needed.

---

[a] *Laser Lab., Plasma Physics Research Center, Science and Research Branch, Islamic Azad University, Tehran, Iran*
* *Corresponding author: doran@srbiau.ac.ir*

To develop the fabrication methods of graphene and its derivatives, many researches have been performed. Currently, numerous techniques are being tested to synthesize graphene such as chemicals vapor deposition, micromechanical exfoliation, epitaxial growth, electric arc graphene production, but among them, pulsed laser ablation (PLA) of a solid target in a confining liquid is emerged as a simple and most efficient technique for synthesizing various kinds of graphene nanoparticles and nanostructures. Laser wavelength, fluency, and pulse duration, as well as the liquid ablation environment and its temperature are the main parameters which could affect on the final production of the laser ablation process [10,11]. Ablation environment can affect the ablation products in two ways. Firstly, the liquid medium in laser ablation process can control the pressure of the plasma plume on the surface of the target, pressure directly proportional to the ablation liquid density; it can change the structure, size, and morphology of the produced nano-structures. Secondly, the aggregation of products can be affected by the nature of liquid environment like polarity or dispersion [10, 11]. During the interaction between the laser beam and the target, the plasma plume, consisting of vaporized atoms or molecules, ablated from the surface of the target, results due to extreme heating; in such conditions, atoms or molecules aggregate together to form nanoparticles. Subsequently, by increasing the pressure of plasma, the number of nanoparticles will also increase. On the other hand, decreasing the plasma pressure (and because of weak Van der Waals bonds between the graphite planes) gives rise to ablation products in the form of graphene planes [10]. The smaller density of the nitrogen in comparison with water and other appropriate liquids, makes this cryogenic a suitable medium for producing graphene nanosheets [10].

Graphene production in liquid nitrogen and distilled water different environments have been recently reported. Mortazavi and co-workers produced graphene sheets by using nanosecond Q-switched Nd:YAG laser ablation of a graphite target in the liquid nitrogen environments [12]. They explained the formation of the laser-ablated produced graphene sheets in liquid nitrogen by the penetration of liquid into the interlayer spacing of graphite. Sadeghi et al. synthesized carbon nanostructures in different liquid environments including distilled water, acetone, alcohol, and CTAB environments by using a 7 ns fundamental wavelength of pulsed Nd:YAG laser at 1064 nm [13]. Their results show that the highest amount of graphene sheets are produced in distilled water environment. Solati and co-workers used nanosecond pulsed laser ablation technique to fabricate colloidal ZnO nanoparticle and graphene nano composite in water environment [14]. Their results show that by increasing the amount of graphene in the suspensions, the band gap energy of mixtures was decreased noticeably. The purpose of the present experimental research is to investigate the effects of the ablation environment on the characteristics of carbon nanostructures produced by the laser ablation technique. In this respect, two different liquid environments: distilled water and liquid nitrogen have been tested.

RESULTS AND DISCUSSION

Raman spectroscopy is a useful and non-destructive diagnostic tool for distinguishing carbonaceous materials. The Raman spectra of the graphene suspensions are illustrated in Fig.1. Output data have been recorded from dried drops of both suspensions on glass substrates. The most prominent peaks in the Raman spectra of graphitic carbon based materials especially graphene are G, D and 2D bands. The G peak is related to plane stretching vibration mode of any pair of SP^2 bonded carbon atoms [15, 16]. The D band is arising from structural defects, edge effects and dangling SP^2 carbon bonds that break the symmetry on the hexagonal SP^2 bonded lattices [17]. The peak at a wave number of 1192 cm^{-1} (named as D* peak) is caused by wrinkled (defective) morphology of the graphene sheets [18]. In Fig. 1(a) two individual peaks at around 1384 cm^{-1} and 1545 cm^{-1} are related to the D and G bands, respectively. Furthermore, another disorder induce-peak which is named as D′ peak at the wave number of 1612 cm^{-1} can be seen in this spectrum. The D′ peak is resulted from intra-valley double-resonance process [19]. As shown in Fig.1 (b) the D peak for the graphene samples produced in distilled water is observed at the same wave number of 1384 cm^{-1} with larger intensity, while the G peak shift to higher wave number at 1633 cm^{-1} and becomes broadens.

The main peaks in the Raman spectra of carbons are the so-called G and D bands, usually appearing at 1560 and 1360 cm^{-1} respectively. The G band has a shift about 73 cm^{-1} to higher wave numbers, due to the conjugation of alkenic C=C bonds with the C=C bonds in aromatic rings (usually longer than those in unconjugated alkenic sp^2 sites), as reported by Kimiagar et al. [20]. Furthermore, there are other additional peaks at approximately 2950 cm^{-1} and 2965 cm^{-1} in the Raman spectra of the samples produced in the distilled water and liquid nitrogen environments, respectively. These peaks are originating from the combination of the D and G bands, called as D+G band [21]. It is worth noting that the intensity of the disorder-induced D band for the graphene sheets produced in liquid nitrogen environment is smaller than for the product in water, indicating the improved quality of graphene nanosheets in liquid nitrogen. The intensity ratio of the disorder-induced D band to the G band (I_D/I_G) is inversely proportional to the in-plane graphitic crystallite size, as given by the formula [22-24]: La= 4.4 (I_G/I_D).

The calculated results show that the I_D/I_G ratio for the graphene sheets produced in liquid nitrogen environment (0.25) is smaller than this ratio in distilled water environment (0.94), indicating that the sp^2 domain of the graphene sheets produced in liquid nitrogen (17.6 nm) is larger than for the product in distilled water environment (4.6 nm). Besides, we can see prominent peaks at the wave numbers of 2688 cm^{-1} and 2757 cm^{-1} in the Raman spectra of the samples produced in liquid nitrogen and distilled water environments, respectively. These peaks are the characteristic peaks of the graphene structure, arising from

a two-phonon double resonance Raman scattering process [25]. The increase of the intensity of 2D band for the graphene nanosheets produced in liquid nitrogen environment indicates that number of layers in the sample produced in liquid nitrogen is smaller than for the product obtained in water [26].
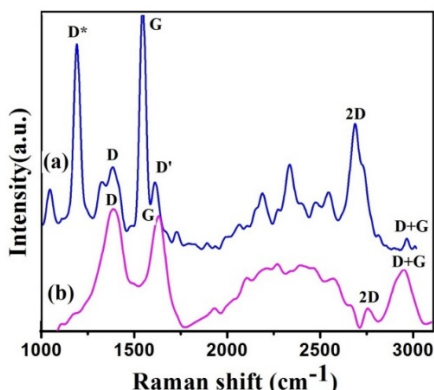
Figure 1. Raman spectra of the samples produced by pulsed laser ablation in (a) liquid nitronen and (b) distilled water environments

The optical spectra of the samples with the transmittance of the liquid environment as the baseline are indicated in Fig. 2. The transmittance spectra of the samples produced in liquid nitrogen environment indicate a high transparency (99%) while the transparency is decreased in the sample produce in distilled water (96%). It is an evidence that the graphene nanosheets produced in distilled water become thicker. This result is in good agreement with the result of the Raman spectra.
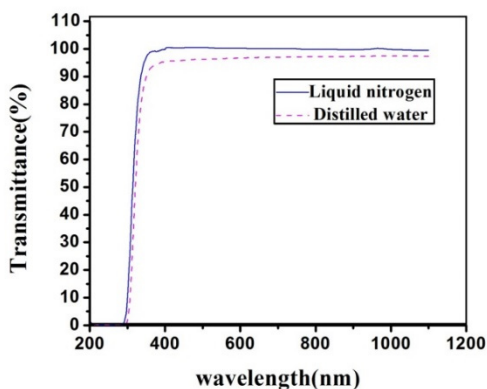
Figure 2. Optical transmittance spectra of the graphene nanosheets Produced in liquid nitrogen and distilled water environments

280

The TEM micrographs of the samples are shown in Fig. 3. Data have been recorded from the dried drops of suspensions on carbon coated copper grids. The images show the transparent silk like structures of graphene. More Darkness in the images is referred to the regions that several graphene layers are stacked on each other. According to the experimental observations, the graphene sheets produced in liquid nitrogen medium have smaller number of layers in compared to those produced in distilled water environment.
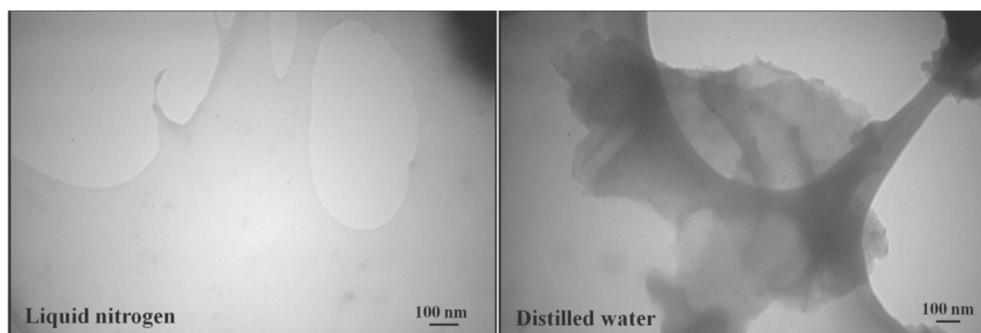
Figure 3. TEM micrographs of the samples

The X-ray diffraction patterns of the samples are presented in Fig. 4. XRD measurement is carried out using the dried drops of every suspension on Si substrates. The XRD pattern of the sample produced in liquid nitrogen environment shows two prominent reflection peaks. The reflection peak at 2θ=32.1° is related to graphitic carbon in graphene while that at 2θ=69.6° corresponds to the Si substrate. One can see a sharp peak at 2θ=69.5° attributed to Si substrate in the XRD pattern of the samples produced in distilled water. The disappearance of graphene peak in XRD diffraction pattern of the product in distilled water may be due to small number of graphene planes resulted in this environment. Basically the peaks in XRD diffraction pattern of materials are the reflected X-ray photons from the atoms on the successive planes of their lattice, which satisfy the Bragg's condition. When the number of planes is small, one may not expect large reflection of X-ray photons [14].

The FTIR transmitted spectra of the studied samples recorded in the range of 500-4000 cm^{-1} are shown in Fig.5. In the low frequency area, there are absorption peaks at the wave numbers of 700 and 732.17 cm^{-1} originating from vibrations of C-H bonds [10]. The aromatic C=C vibrations cause the appearance of a peak at around 1640 cm^{-1}[27]. Beside, the peaks which are located at around 2078.41 cm^{-1}, 2082.7 cm^{-1} can be due to sp^2 C=C groups.

Furthermore, in the high frequency area, the presence of broad absorption band in the range of 3100-3700 cm^{-1} arises from the stretching vibrations of O-H groups. As shown in Fig.5 the intensity of absorption peaks in the samples is similar. The intensity of the absorption peaks in the FTIR spectra depends on the number of the specific bonds present in the samples [10].
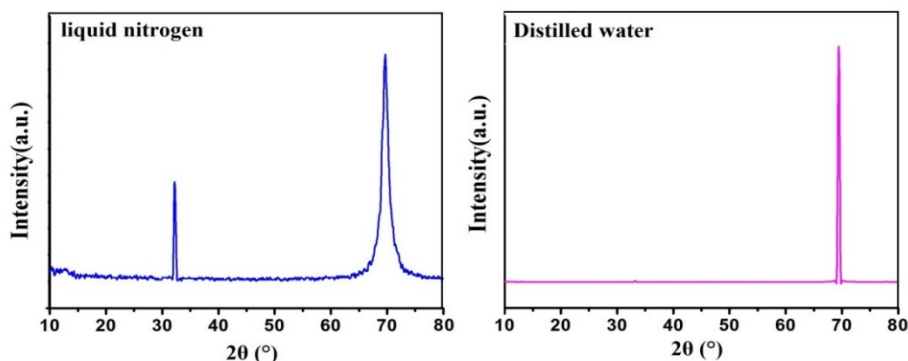
Figure 4. X-ray diffraction pattern of the samples produced by pulsed laser ablation
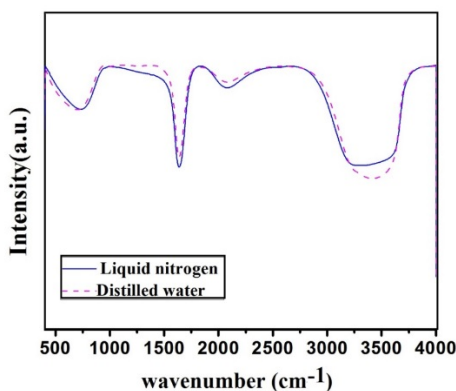
Figure 5. FTIR spectra of the samples

CONCLUSIONS

Graphene sheets were prepared using the second harmonic of a Nd:YAG laser operating at 532 nm wavelength. In this study, the effect of laser ablation environment on the characteristics of the produced graphene sheets

has been investigated. The Raman spectra indicate that the graphene sheets produced in liquid nitrogen environment have larger sp^2 carbon domains, lower structural defects and consequently more acceptable quality compared to the samples produced in distilled water. The X-ray diffraction pattern indicates a smaller number of graphene planes formed in distilled water environment. The TEM micrographs indicate the formation of silk-like structure in the samples. The optical transmittance spectra show the thicker graphene nanosheets are formed in distilled water environment. The FTIR results revealed the existence of sp^2 C=C groups in the graphene nanosheets in suspensions. Coroborating the experimental data, it appears that the liquid nitrogen is a more suitable medium for producing graphene nanosheets with laser ablation method in comparison with the water and other appropriate liquids.

EXPERIMENTAL SECTION

Graphene sheets are prepared by pulsed laser ablation of a high purity graphite target (with 99.99% purity) using the second harmonic of a Nd:YAG laser at a wavelength of 532 nm, with 7 ns pulse width and pulse-repetition rate of 5 Hz and a pulse fluency of 0.5 J/cm^2 at the room temperature. Before starting the experiments, both targets and containers were cleaned ultrasonically in ethanol, acetone and distilled water solutions respectively for 15 minutes. Graphite target was placed at the bottom of a glass cylindrical vessel containing liquid. Height of liquid on the target was 0.8 cm. The laser beam with 6 mm in diameter was focused on the target surface using a lens with a focal length of 80 mm. In order to study the effects of ablation environment on the production quality of Graphene sheets the samples were prepared in distilled water and liquid nitrogen environments. In this study, various analytical techniques have been used to characterize the structure of produced samples. IR spectrum of samples (FTIR), were Cary out using NEXUS870 FTIR spectrometer from Thermo Nicolet Co., in the range of 500-4000 cm^{-1}. Optical transmittance spectra of the samples were measured by UV–Vis–NIR spectrophotometer from PG Instruments (T-80). X-ray diffractions of the dried graphene suspensions on silicon substrates are analyzed using a Cu-Kα radiation (λ=1.54060A°) diffractometer. Raman measurements are performed employing an Almega Thermo Nicolet Dispersive Raman Spectrometer with a 532 nm Nd:YLF laser. Transmission electron microscopy micrographs were taken using a Zeiss-EM10C microscope.

R E F E R E N C E S

[1]. M.J. Allen, V.C. Tung, and R.B. Kaner, *Chem. Rev.*, **2009**,*110*, 132-145.
[2]. Y. LI, N. CHOPRA, the Minerals, *Chemical Methods*, **2015**, *67*(1), 34.
[3]. Z.T. Luo, P.M. Vora, E.J. Mele, A.T.C. Johnson, J.M. Kikkawa, *Appl. Phys. Lett.* **2009**, *94*, 111909.
[4]. H.S. Park, J.A. Rowehl, K.K. Kim, V. Bulovic, and J. Kong, *Nanotechnology* **2010**, *21*, 505204.
[5]. J.J. Liang, Y. Huang, J.Y. Oh, M. Kozlov, D. Sui, S.L. Fang, R.H. Baughman, Y.F. Ma, Y.S. Chen, *Adv. Funct. Mater.*, **2011**, *21*, 3778-3784.
[6]. H.J. Xu, W.B. Lu, Y. Jiang, and Z.G. Dong, *Appl. Phys. Lett.*, **2012**, *100*, 051903.
[7]. A. Salehi-Khojin, D. Estrada, K.Y. Lin, K. Ran, R.T. Haasch, J.-M. Zuo, E. Pop, and R.I. Masel, *Appl. Phys. Lett.*, **2012**, *100*, 033111.
[8]. B. Song, G. Cuniberti, S. Sanvito, and H.P. Fang, *Appl. Phys. Lett.*, **2012**, *100*, 063101/1-4.
[9]. J.B. Wu, M. Agrawal, H.A. Becerril, Z.A. Bao, Z.F. Liu, Y.S. Chen, P. Peumans, *ACS Nano*, **2010**, *4*, 43.
[10]. N. Tabatabaie, D. Dorranian, *Appl. Phys. A*, **2016**, *122*, 558.
[11]. M. Morad, E. Solati, S. Darvishi, D. Dorranian, *Cluster Sci.*, **2016**, *27*, 127.
[12]. Z. Mortazavi, P. Parvin, A. Reyhani, *Laser Phys. Lett*, **2012**, *9*, 547.
[13]. H. Sadeghi, D. Dorranian, *Theor Appl Phys*, **201**6, *10*, 7.
[14]. E.Solati, D. Dorranian, *Appl. Phys. B*, **2016**, *122*, 76.
[15]. J. Ding, M. Wang, X .Zhang, Z. Yang, X. Song, Ch. Ran, *SCI*, **2014**, *416*, 289.
[16]. C. Casiraghi, *Phys. Rev. B*, **2009**, *80*, 233407.
[17]. A. Aregahegn Dubale., Su Wei-Nien, A. G. Tamirat, Ch.J. Pan, B. A. Aragaw, H-M.-Chen, Ch-H Chen, B.J. Hwang, *Mater. Chem. A*, **2014**, *2*, 18383.
[18]. A. Kaniyoor, S. Ramaprabhu, *AIP Advances*, **2012**, *2*, 032183.
[19]. J. Jiang, R. Pachter, F. Mehmood, A.E. Islam, B. Maruyama, J.J. Boeck, A, *carbon*, **2015**, *90*, 53.
[20]. S. Kimiagar, N. Rashidi, *Advanced Research*, **2015**, *3*, 153.
[21]. Y. Kawashima, G. Katagiri, *Physical Review B*, **1995**, *52*, 10053.
[22]. T.V. Cuong, V.H. Pham, E.W. Shin, J.S. Chung, S.H. Hur, E. J. Kim, Q.T. Tran, H.H. Nguyen, P.A. Kohl, *Applied Physics Letters*, **2011**, *99*, 041905.
[23]. M. Shafiei, P.G. Spizzirri, R. Arsat, J. Yu, J.D. Plessis, S. Dubin, R.B. Kaner, K. Kalantar-zadeh, and W. Wlodarski, J. *Phys. Chem. C*, **2010**, *114*, 13796.
[24]. A.C. Ferrari, *Solid State Commun.*, **2007**, *143*, 47.
[25]. R.J. Sereshta, M. Jahanshahia, A. Rashidi, A.A. Ghoreyshia, *APPL SURF SCI*, **2013**, *276*, 672.
[26]. S. Berciaud, S. Ryu, L.E. Brus, T.F. Heinz, *Nano Lett.*,**2009**, *9,* 346.
[27]. O. Akyıldırım, H. Medetalibeyoğlu, S. Manap, M. Beytur, FS. Tokalı, ML. Yola, N. Atar, *Electro.chem. Sci.*, **2015**,*10*, 7743.

QUALITY CONTROL PARAMETERS OF *RIBES NIGRUM* L. BUDS FOR ESTABLISHING THE OPTIMAL HARVESTING PERIOD

ELISABETA CHIŞE[a], RAMONA FLAVIA CÂMPEAN[b], CODRUTA COBZAC[c], DANIELA HANGANU[d], NELI KINGA OLAH[a,b*], VIOLETA TURCUŞ[e*], AUREL ARDELEAN[e]

ABSTRACT. The main extract used by the youngest branch of phytotherapy, named meristemotherapy, is obtained from the freshly processed Blackcurrant buds. Due by the lack of information regarding the optimal harvesting time of the buds and buds chemical composition it was begun a larger study, the results presented in this paper being the preliminary screening of the possible active compounds that can be contained by this vegetal material. The apical and axillar buds from *Ribes nigrum* L shrubs were collected in three different development phases. The bioactive compounds composition screening was performed using monodimensional double development TLC on extracts obtained in ethanol, glycerol and their mixture, according to EPh. The analysis results show that the lipophilic compounds are increased in the maximum development stage and are decreasing when the buds begin to open. In the opened stage are increasing the hydrophilic compounds, like the polyphenols that are secondary metabolites of the plants. These changing in chemical composition indicate also the tissues differentiation. In conclusion of this study can decide that the optimal harvesting time of the buds is before the opening and tissues differentiation, period that is according also with the traditional harvesting time of these type of plant materials.

Keywords: Ribes nigrum L. buds, meristemotherapy, monodimensional double development TLC, optimal chemical composition.

---

[a] *"Vasile Goldis" Western University of Arad, Faculty of Pharmacy, 86 Rebreanu Street, Arad, Romania*
[b] *SC PlantExtrakt SRL, 407059 Rădaia. Cluj, Romania*
[c] *Babes-Bolyai University, Faculty of Chemistry and Chemical Engineering, Cluj-Napoca, Romania*
[d] *Iuliu Haţieganu University of Medicine and Pharmacy, Faculty of Pharmacy, Cluj-Napoca, Romania*
[e] *"Vasile Goldis" Western University of Arad, Faculty of Medicine, 86 Rebreanu Street, Arad, Romania*
* *Correspondent authors: neliolah@yahoo.com, violeta_buruiana@yahoo.com*

E. CHIȘE, R. F. CÂMPEAN, C. COBZAC, D. HANGANU, N. K. OLAH, V. TURCUȘ, A. ARDELEAN

INTRODUCTION

The meristemotherapy, or its more used denomination gemmotherapy, was founded as a distinct branch of the phytoptherapy at the begin of the 20th century when a belgian physician, Pol Henry, put the question if the animal stem cells have regenerating power, what are doing the vegetal stem cells. Following this idea begun to use vegetal stem cells extracts, that are the plants meristematic cells, more concentrated in the buds, sprouts, young parts of the plants. Step by step Pol Henry succeeded to put the basis of this new phytotherapy named phytoembriotherapy, than gemmotherapy, but more correctly is meristemotherapy [1,2].

During the time the meristemotherapy was developed at the border of homeopathy and phytotherapy. The benefits upon the people quality of life of the meristematic tissues extracts were observed by the doctors using the observation method of the homeopathy. Many trees and shrubs buds' were used to obtain specific extracts and experimentaly observed their benefit on the people health. From these observation one extract became more popular, mostly for its major beneficial effect. This was the Blackcurrant buds extract used for its cortizon-like antiinflamatory, antiallergenic effects [1-3].

The Blackcurrant, *Ribes nigrum* L., is a commonly cultivated species in Romania and all around world. There are extended cultures in Russia, Europe and America. Its buds are harvested at the begin of the springtime, processed in fresh state, without drying, using a mixture of ethanol and glycerol according to the method described in French Pharmacopoeia from 1965 and now also in European Pharmacopoeia [4,5].

Recent studies identified in the Blackcurrant buds a lot of polyphenols: proanthocyanidines, like prodelphinidines dimers and trimers [6]; flavonols, like: quercetine, kaempferol and their derivatives [7,8]; phenolic acids, like p-coumaric acid, chlorogenic acid and neo-chlorogenic acid [7,8]. Beside these in the buds were identified the vitamin C and also some important aminoacids: arginine, proline, glycine and alanine [9]. The essential oil obtained from Blackcurrant buds had as main compounds sabinene and delta-3-carene [10].

The clinical observations shown that the Blackcurrant buds extract stimulates the adrenal glands, having a cortison-like antiinflammatory effect, but without the cortisons side effects. The proanthocyanidines contained by buds decrease the pro-inflammatory chemokines [11,12]. Some *in vitro* studies show these proanthocyanidines selectivity for COX-2, enzyme implicated in the inflammatory response and they have no negative effect on the colagen synthesis [13]. The essential oil of the buds has antimicrobial and also antifungal effect [10,14].

As can be seen, both the hydrophilic and lipophilic compounds of Blackcurrant buds, have important therapeutical effects, being important to be in highest possible concentration in the harvested buds and then in the obtained extracts. Because the classical phytotherapy does not use the buds, as usual plant material, there are no special indications regarding the optimal harvesting period. The aim of this paper is to establish the optimal harvesting period of the Blackcurrant buds through a TLC screening of both, hydrophilic and lipohilic compounds profile respectively the biometric determinations.

RESULTS AND DISCUSSION

There were established three development periods for harvesting the Blackcurrant buds: sleeping buds, developed buds and opened buds. Through this three development periods the meristematic tissues are changing and begin the differentiation, more intensively in the opened buds. This process will be reflected also in the change of chemical composition.

This study compare not just the chemical composition of the buds from different development phases, but also the freshly respectively dry processed vegetal material, respectively the influence of used solvent on the bioactive compounds profile.

In the figures 1-3 are presented the chromatograms obtained for different buds extracts.

To can compare the bioactive compounds profile all extracts were concentrated by solid phase extraction. This sample preparation was used also to can eliminate the glycerol, solvent that can prevent the proper TLC separation.

The used TLC mobile phase system separate in the lower part of the chromatogram the hydrophilic compounds, mostly the polyphenols like flavonoids and phenolic acids, eventually coumarins and in upper part the lipophilic compounds, like the terpenic compounds.

It can be observed a similar compound profile, but the concentrations are different. The hydrophilic compounds are better extracted in 70 % vol. ethanol or glycerol. The more lipophilic compounds are better extracted in the mixture of ethanol-glycerol, solvent used also by the standardized pharmacopoeial method.

The extraction process depends from the solvents polarity and viscosity, from the drying stage of the cell membranes, all these influencing the mass transfer trough the lipophylic cell membranes. It can be seen on the TLC chromatograms that the glycerol, a more viscous and more lipophylic

solvent, will extract less compounds from dry buds due by the lack of moisture at the cell membranes level and for this reason will penetrate less the cell membranes. The ethanol, a less viscous and more hydrophylic solvent, will extract more compounds due by its higher penetration potential trough cell membranes. The ethanol-glycerol mixture will benefit both by the ethanol less viscosity and hydrophilicity, but also by the lipophilicity of the glycerol, that will more easier penetrate the cell membranes due by the mixture's less viscosity.

Generally, the freshly processed buds will lead to an extract more concentrated in active compounds in comparison with the dry buds extracts. This is a prove of negative effect of the drying process upon the bioactive compounds profile of the plants.

There can be observed also a difference between the compounds profile from a development stage to other. If the polyphenols content appear to be similar, being present the almost in all cases the same bands, in case of the lipophilic compounds are more differences. The lipophilic compound number increases from 3 in sleeping stage to 6 in developed stage and decreases at the tissues differentiation to 2-3 compounds in opened stage.

The polyphenols are more concentrated, showing more intensive bands, in the extracts obtained from opened buds, these compounds being specifically to the mature plant parts.

In table 1 are presented the biometrical data recorded for 25 buds at each stages. These data will help to give also a numerical parameter for quality control of harvesting period of the Blackcurrant buds.

Table 1. Biometrical determinations

Samples	Minimal size, mm	Maximal size, mm
Sleeping buds	18.4	67.0
Developed buds	53.5	138.6
Opened buds	364.1	462.7

If we correlate the TLC screening and the biometrical data we can conclude that the optimal harvesting time is at developed stage when the buds size not exceed 140 mm in hight and the minimal size is 50 mm.

Due by the fact that we can not find studies with similar aims, our result can not be compared with literature data. But these preliminary results encourage us to continue the study for a complex profiling of the bioactive compounds from Blackcurrant buds extract, results that later can offer us the possibility to made correlations with clinical observations, therapeutic effects or pharmacological studies results.
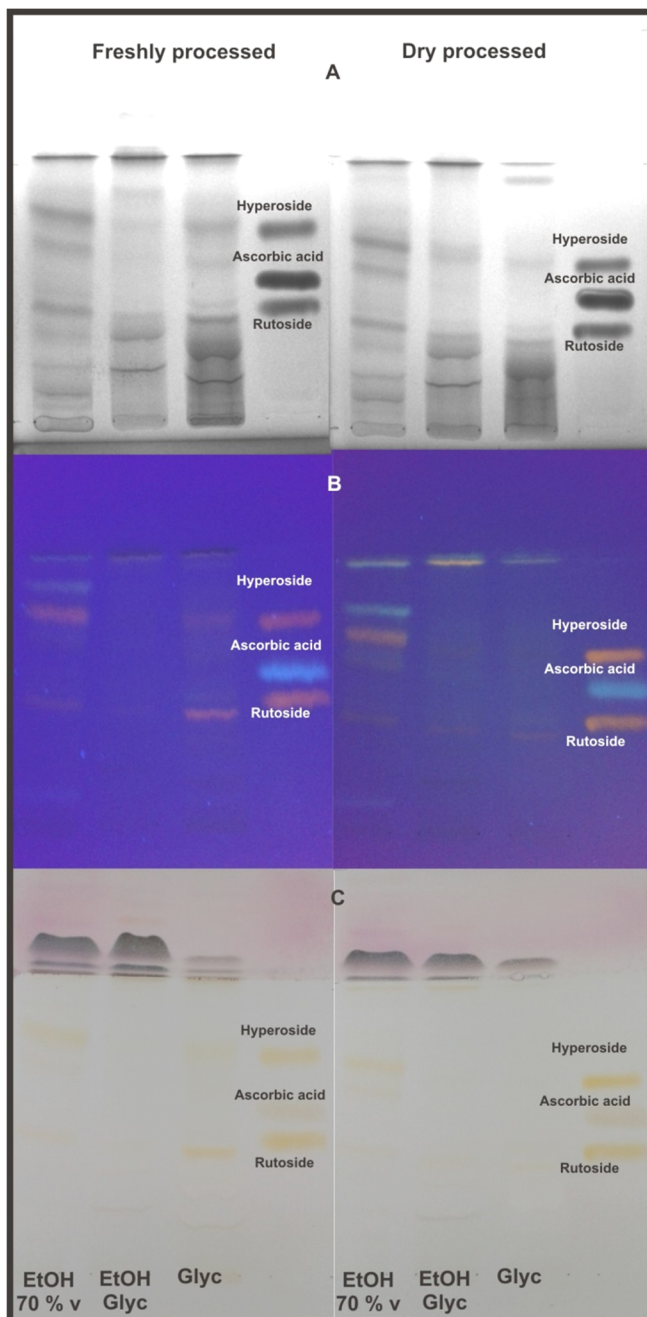
Figure 1. TLC chromatogram of the extracts obtianed from sleeping buds
(A = in UV light at 254 nm, B = fluorescence at 365 nm, C = Visible light)
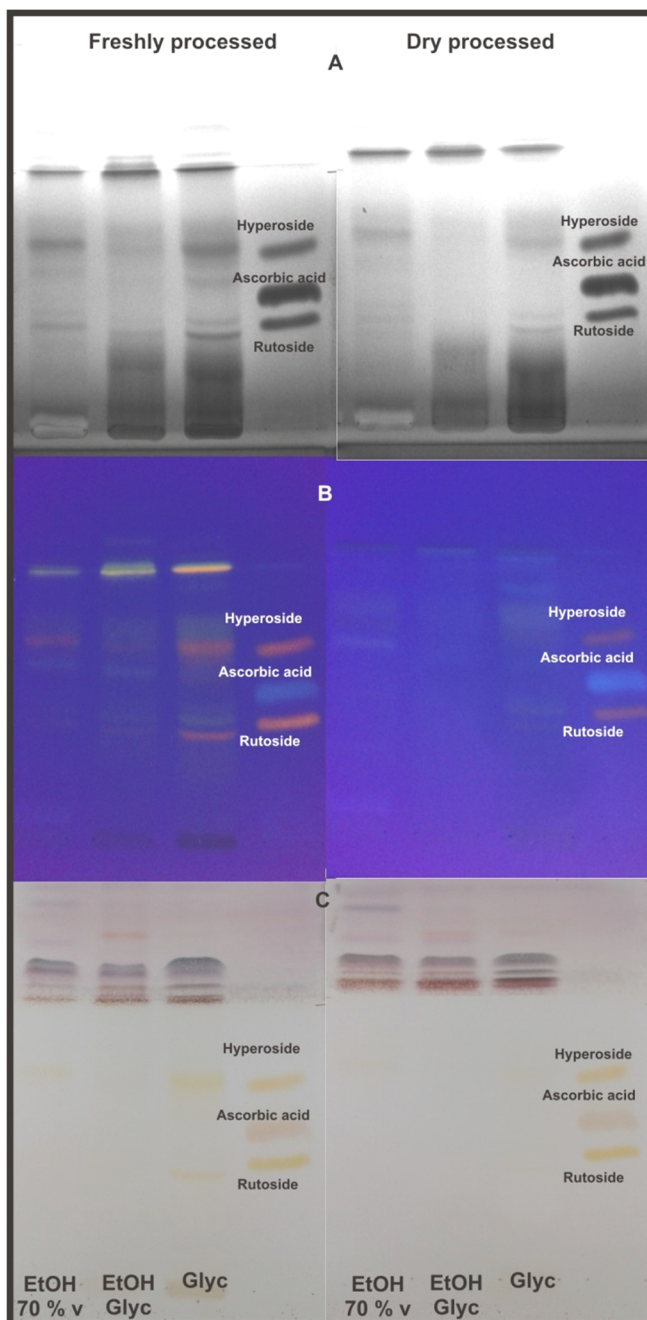
Figure 2. TLC chromatogram of the extracts obtianed from developed buds
(A = in UV light at 254 nm, B = fluorescence at 365 nm, C = Visible light)
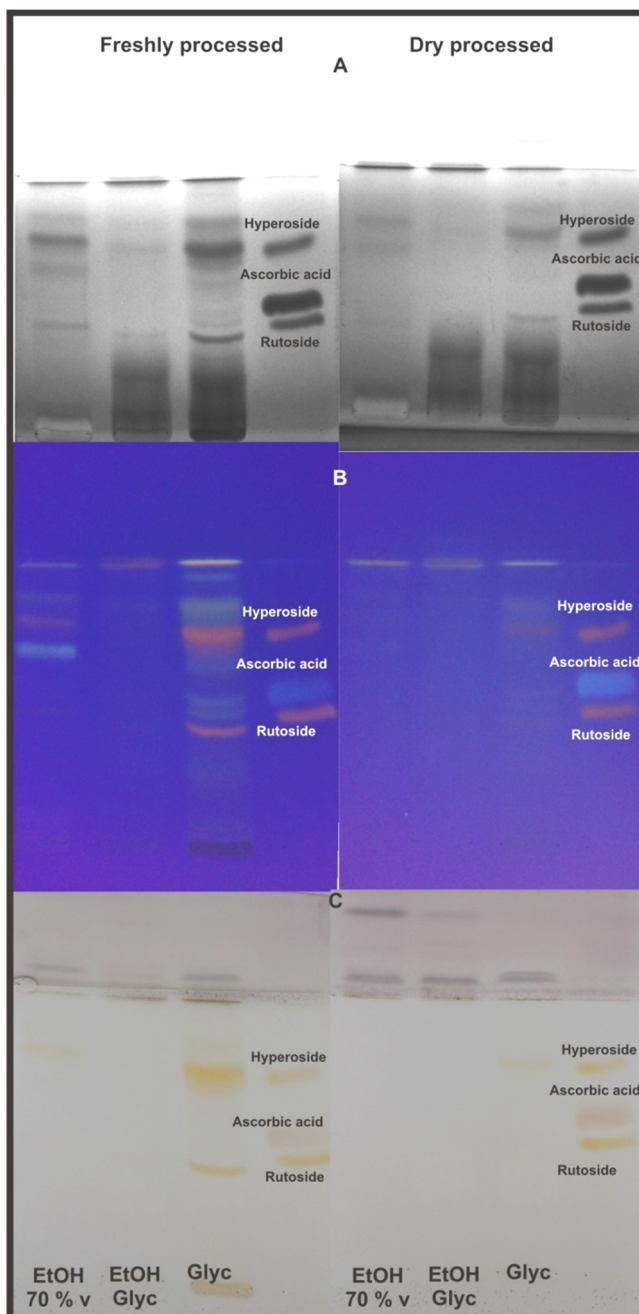
Figure 3. TLC chromatogram of the extracts obtianed from opened buds
(A = in UV light at 254 nm, B = fluorescence at 365 nm, C = Visible light)

CONCLUSIONS

Due by the fact that the meristemotherapy and phytochemical study of the buds and its extracts are appeared recently in the researchers interes, this study is the first that wish to establish parameters for a better control of the plant material harvesting in idea to obtain qualitatively the best possible product.

To have a complex mixture of bioactive compounds the optimal harvesting time of the Blackcurrant buds is at developed stage, at the begin of springtime, before the opening and intensive differentiation of the tissues, at a hight of the buds from 50 to 140 mm.

The fresh processing and the using of ethanol-glycerol mixture for extraction will assure the obtaining of Blackcurrant buds extract with established high quality, efficacy and safety.

EXPERIMENTAL SECTION

Harvesting of plant materials

The Blackcurrant buds were harvested from an organic culture established near Cluj, Romania. The organic state of the culture is certified by EcoInspect Ro-008.

The sleeping buds were collected in January 2016, the developed buds in February 2016 and the opened buds at the begin of March 2016. The harvesting was performed at dry weather, after 10 a.m.

Preparation of the extracts

The ethanolic respectively the glycerolic extracts were obtained from fresh buds respectively dry buds using an extraction ratio of dry part of plant – solvent = 1 :10. As solvents were used the 70 % vol. ethanol respectively 100 % glycerol. The extraction ratio used for fresh buds extraction was computed taking in account the humidity of the fresh vegetal material.

The extracts with solvent mixture were obtained from fresh buds respectively dry buds using an extraction ratio of dry part of plant – solvent = 1 :20. As solvent is used a mixture of ethanol – glycerol 1 :1. The vegetal material – solvent ratio respectively the solvent mixture are according to the European Pharmacopoeia monograph from the special chapter of homeopathic preparations.

All extracts were obtained by cold extraction, being maintained at maceration for 20 days, with daily mixing 2 x 10 minutes. The extracts were decanted and the plant materials with the remained solvent were pressed. The extracts were maintained 5 days for stabilization.

Reagents and materials

HPLC grade methanol, ethyl acetate, ethyl-methyl ketone, formic acid, toluene and analytical grade chlorhydric acid were purchased from Merck (Darmstadt, Germany).

The ethanol and glycerol were of pharmaceutical grade, purchased from Coman Prod (Ilfov, Romania) respectively Glacon Chemie (Germany).

Rutoside and hyperoside were purchased from Roth (Karlsruhe, Germany), ascorbic acid from Merck (Darmstadt, Germany). Standard solution (1 mg/ml) of these compounds was prepared in methanol.

The reagent used for preparing the visualising reagents: Neu-PEG and anisaldehyde, respectively the TLC Sil G F254 (20x20 cm) plates and SPE Sil-C18 cartriges were purchased from Merck (Darmstadt, Germany).

The Neu-PEG reagent is composed from two different solutions, used concomitant: 1 % methanolic solution of diphenyl-borate aminoethanol respectively 5 % ethanolic solution of 4000 polyethyleneglycol.

The anisaldehyde reagent was prepared by mixing 0.5 ml of anisaldehyde with 4.5 ml of concentrated sulphuric acid, 10 ml of glacial acetic acid and 85 ml of methanol.

SPE sample preparation

Each sample was extracted on SPE cartridges with silicagel-C18, using methanol, acidulated at pH = 3,5, for elution. Before each extraction the cartridges were activated by flushing with 5 ml methanol and 5 ml water. The SPE 3 ml from each sample was concentrated to 1 ml by this solid phase extraction [15]. By this extraction was eliminated the glycerol that can negatively influence the TLC separation. The sample preparation was applied to all extracts to can compare the compounds profile.

The TLC analysis

TLC analysis was performed using 13 x 20 cm silica TLC plates with fluorescence indicator at 254 nm. The samples were applied as bands (20 mm) at 15 mm from lower edge of the plate. From ethanolic and glycerolic extracts were applied 20 µl, from solvent mixture extracts were applied 40 µl, to can compare also the bands intensity as a visual semi-quantitative evaluation. Hyperoside, ascorbic acid and rutoside bands were also applied as referenced compounds. A double development was performed to achieve a better separation between hydrophilic and lipophilic compounds. First development was performed on 10 cm with ethyl acetate – ethyl-methyl ketone – formic acid – purified water (50:30:10:10, v/v) as mobile phase. After plate was dry a second development was performed in the same

direction with a less polar mobile phase: toluene – ethyl acetate (95:5, v/v) on 15 cm. Hydrophilic compounds were visualized by spraying the first part of the plate (10 cm) with Neu-PEG reagent. The second part (10-15 cm), the zone associated with lipophilic compounds, was sprayed with anisaldehyde reagent and then heated at 105-110°C for 5-10 minutes. The plates were observed in visible light to have a general view (hydrophilic and lipophilic compounds) and under UV light (254 and 365 nm) for emphasize the similarities and differences between the extracts, especially for polyphenolic compounds. For documentation the plate image was captured using a Camag Reprostar cabinet equipped with a HP digital camera.

The biometrical analysis

At each harvesting were sampled 25 statistically representative buds and the longitudinal sizes were measured using a micrometer. Each bud was measured individually.

R E F E R E N C E S

[1]. F. Pitera, M. Nicoletti, Gemmoterapia. Fondamenti scientifici della moderna Mersitemoterapia, Nova IPSA Ed., Palermo, **2016**.
[2]. F. Pitera, Compendio di Gemmoterapia Clinica, de Ferrari ed., Genova, **2007**.
[3]. Tétau M., Gemmotherapy – a clinical guide. Editions du détail INC, Paris, **1998**.
[4]. ***, French Pharmacopoeia, 11th edition, **2012**.
[5]. ***, European Pharmacopoeia, 8th edition, EDQM, **2016**.
[6]. D. Donno, M.G. Mellano, A.K. Cerutti, G.L. Beccaro, *Pharmaceuticals(Basel),* **2016**, *9(1),* 7.
[7]. F. Ieri, M. Innocenti, L. Possieri, S. Gallori, N. Mulinacci, *J Pharm Biomed Anal.,* **2015**, *115,* 1.
[8]. M. Vagiri, A. Ekholm, S.C. Andersson, E. Johansson, K. Rumpunen, *J Agric Food Chem.*, **2012**, *60(42)*, 10501.
[9]. ***, Black currant (*Ribes nigrum*), Natural Standard Professional Monograph, **2012**.
[10]. B.S. Ethorđević, D.S. Pljevljakušić, K.P. Savikin, T.R. Stević, D.J. Bigović, *Chem Biodivers.*, **2014**, *11(8)*, 1228.
[11]. S.M. Hurst, T.k. McGhie, J.M. Cooney, D.J. Jensen, E.M. Gould, K.A. Lyall, R.D. Hurst, *Mol Nutr Food Res.*, **2010**, *54 (Suppl 2)*, S159.
[12]. N. Garbacki, M. Tits, L. Angenot, J. Damas, *BMC Pharmacol.*, **2004**, *4*, 25.
[13]. N. Garbacki, L. Augenot, C. Bassleer, J. Damas, M. Tits, *Naunyn Schmiedebergs Arch Pharmacol.*, **2002**, *365*, 434.
[14]. E. Oprea, V. Radulescu, C. Balotescu, V. Lazar, M. Bucur, P. Mladin, I.C. Farcasanu, *Biofactors.*, **2008**, *34(1),* 3.
[15]. S. Cobzac, G. Cimpan, N. Olah, S. Gocan, *J. Planar Chrom. Mod. TLC*, **1999**, *12(1)*, 26.

TOTAL PHENOLS, ANTIOXIDANT ACTIVITY AND YIELD, IN TOMATOES AND PEPPERS IN A CLOSED GREENHOUSE AND COMPARISON WITH A CONVENTIONAL GREENHOUSE

NIKOLAOS GOUGOULIAS[a], ALEXANDROS PAPACHATZIS[a], IOANNIS VAGELAS[a], LIVIU GIURGIULESCU[b*], ANASTASIA KARABOULA[a], DIMITRIOS KALFOUNTZOS[c]

ABSTRACT. A study during 36 months, was conducted in a conventional greenhouse (open type) and a geothermal (closed type) of TEI Thessaly to determine the productivity, total phenols content, antioxidant activity and certain qualitative characteristics of hydroponic tomatoes and peppers. At geothermal greenhouse the concentration of total phenols in tomatoes ranged from 151 to 324.5 µg (GAE) /g fresh weight and the antioxidant activity ranged from 3.54 to 3.90 µM (AA) /g fresh weight, while in peppers the total phenols ranged from 597 to 815 µg (GAE) /g fresh weight and the antioxidant activity ranged from 6.3 to 7.2 µM (AA) /g fresh weight. At conventional greenhouse the concentration of total phenols in tomatoes ranged from 163 to 195 µg (GAE) /g fresh weight and the antioxidant activity ranged from 3.3 to 3.9 µM (AA) /g fresh weight, while in peppers the total phenols ranged from 527 to 729 µg (GAE) /g fresh weight and the antioxidant activity ranged from 5.7 to 6.8 µM (AA) /g fresh weight. In tomatoes the yield of the production was higher in the geothermal greenhouse as compared to the conventional greenhouse, while in peppers the yield of the production between of geothermal greenhouse and of conventional greenhouse showed no statistically significant differences.

Keywords: Antioxidant activity FRAP; Hydroponic systems; Peppers; Tomatoes; Total phenols

INTRODUCTION

In an soilless cultivation, the plants are free from diseases, and grow faster than in the soil. The development of the hydroponic systems [1-3], is based on modern distribution systems of nutrient solution [4-6].

---

[a] *Department of Agronomy Technology, Technological Educational Institute of Thessaly, 41110 Larissa, Greece*
[b] *Department of Chemistry and Biology, Technical University of Cluj Napoca, North Universitary Center of Baia Mare, 430122 Baia-Mare, Romania*
[c] *Department of Biosystems Engineering, Technological Educational Institute of Thessaly, 41110 Larissa, Greece.*
[*] *Corresponding author: giurgiulescu@gmail.com*

Geothermal energy is the heat from the earth, clean and sustainable, provides economic benefits, and contributes to a reduction of greenhouse gases [7-10]. The shallow geothermal energy, is derived by absorption of solar radiation, is stored from the earth's surface up to depth 200 m in a temperature 10-18 °C, while obtained from the shallow ground to hot water and is exploited with the heat pumps [11].

Tomatoes and peppers it is natural reservoir of nutrients and of natural antioxidants [12-16]. While, the techniques and cultivation systems, fertilization, irrigation and variety, affect the levels of the antioxidant activity in the tomatoes and peppers [17-19].

The purpose of this study was to compare the geothermal greenhouse with the conventional in the productivity, polyphenols content, antioxidant activity and some qualitative characteristics of hydroponic tomatoes and peppers, for three consecutive seasons.

RESULTS AND DISCUSSIONS

Tomatoes Merilia

Measurements every week in the thickness, number of inflorescences, and number of leaves per tomato plant, showed no statistically significant differences in the two types of greenhouses that were studied during of the growing seasons. Moreover, the mean plant height at the end of the third growing season it was bigger in conventional greenhouse as compared to the geothermal greenhouse (Table 1).

Table 1. Morphological characteristics of tomatoes plants during ripeness of the first, second and third cultivation periods for the conventional and the geothermal greenhouse

Morphological characteristics	Conventional greenhouse			Geothermal greenhouse		
	Cultivation period			Cultivation period		
	First	Second	Third	First	Second	Third
Mean plant height (cm)	160.5c	148c	264a	168.4c	168.1c	224b
Mean plant width (mm)	13.01a	14.07a	14.25a	13.47a	13.82a	14.75a
Mean number of leaves/plant	18b	26b	42a	21b	26b	43a
Mean number inflorescences/plant	13a	10a	9a	15a	9a	9a

Lines with the same letter do not differ significantly according to the Tukey's test (P=0.05).

The juice of the fruit during ripeness showed higher total acidity in the conventional greenhouse as compared to the geothermal greenhouse at the third growing season, while the pH and Brix degrees showed no statistical differences regarding the geothermal greenhouse or the conventional (Table 2). Also, the mean weight of the fruit during the harvest was greater in geothermal greenhouse as compared to the conventional greenhouse, by (11.5, 5.5, and 7) % respectively, for all growing seasons, well as the yield of the production was higher in the geothermal greenhouse as compared to the conventional greenhouse (Table 2). The monitoring of water by the use of water meters during for the three growing seasons revealed that the water consumption in the geothermal greenhouse was 10 % less as compared to the conventional greenhouse.

Table 2. Yield and chemical properties of the tomato juice

Properties	Conventional greenhouse			Geothermal greenhouse		
	Cultivation period			Cultivation period		
	First	Second	Third	First	Second	Third
Total acidity (g citric acid / 100 ml juice)	0.44b	0.45b	0.61a	0.36b	0.41b	0.46b
^{0}Brix	3b	3.5b	4.1a	3.3b	3.2b	4.0a
pH	5.09a	4.46b	4.23b	5.22a	4.51b	4.21b
Mean weight of fruit	208c	208c	225b	235a	220b	242a
Yield (tons /ha)	240.9	219.81	267.50	248.34	232.49	287.71

Lines with the same letter do not differ significantly according to the Tukey's test (P=0.05).

During the fruit ripeness in the first crop season (winter crop), the total phenols content in tomato of the geothermal greenhouse was higher than that of the conventional greenhouse, while in the second and third growing season (spring crops) the content of total phenols in tomato showed no statistically significant differences between the two greenhouses. While the antioxidant capacity FRAP of hydroponic tomato showed no statistical differences regarding the geothermal greenhouse or the conventional greenhouse in all the growing seasons (Figure 1).

Peppers Shelby

In hydroponic peppers cultivation, the geothermal greenhouse as compared to the conventional greenhouse showed no statistical differences regarding the mean plant width, and mean number inflorescences per plant. Also, mean number of leaves per plant at the end of the first and third growing season it was greater in conventional greenhouse as compared to the geothermal greenhouse (Table 3). Moreover, at the end of the second growing season, the mean plant height of the pepper was greater in geothermal greenhouse as compared to the conventional greenhouse (Table 3).
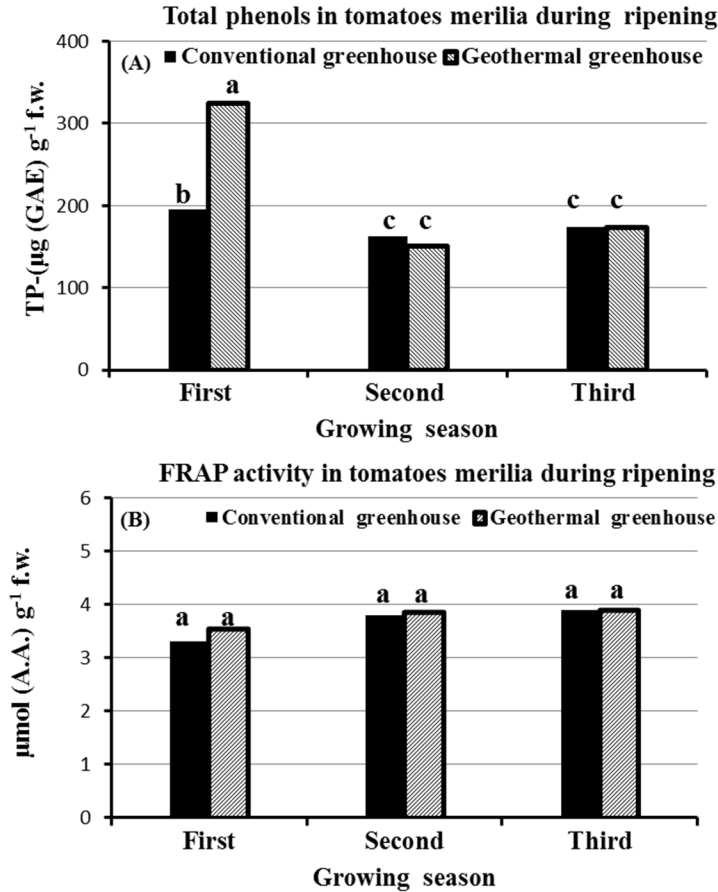
Figure 1. Total phenolic content (A) and antioxidant activity FRAP (B) of tomatoes merilia at the stage ripening in geothermal and conventional greenhouse. Columns in each graph with the same letter do not differ significantly according to the Tukey's test (P=0.05).

The juice of the fruit during ripeness showed higher Brix degrees (soluble solids) in conventional greenhouse as compared to the geothermal greenhouse at the second growing season (spring crop), while the pH and total acidity of juice in conventional greenhouse as compared to the geothermal greenhouse showed no statistical differences (Table 4). Also, the mean weight of the fruit during the harvest showed no statistically significant differences regarding the geothermal greenhouse or the conventional greenhouse in all the growing seasons, well as the yield of the production between of geothermal greenhouse and conventional (Table 4).

Table 3. Morphological characteristics of peppers plants during ripeness
of the first, second and third cultivation periods for the conventional
and the geothermal greenhouse

Morphological characteristics	Conventional greenhouse			Geothermal greenhouse		
	Crop season			Crop season		
	First	Second	Third	First	Second	Third
Mean plant height (cm)	139.25c	161.5b	138c	141c	185.4a	119c
Mean plant width (mm)	13.38a	18.75a	14a	15.5a	18a	13a
Mean number of leaves/plant	146b	196a	144b	116c	187a	119c
Mean number inflorescences/plant	14c	59a	42b	19c	62a	41b

Lines with the same letter do not differ significantly according to the Tukey's test (P=0.05).

Table 4. Yield and chemical properties of the peppers juice

Properties	Conventional greenhouse			Geothermal greenhouse		
	Crop season			Crop season		
	First	Second	Third	First	Second	Third
Total acidity (g citric acid / 100 ml juice)	0.09a	0.13a	0.12a	0.12a	0.13a	0.13a
^{0}Brix	2.8c	3.70a	3.9a	2.7c	3.20b	4.0a
pH	6.26a	6.31a	5.64b	6.38a	6.13a	5.75b
Mean weight of fruit	94a	100a	102a	95a	102a	105a
Yield (tons /ha)	99.33	105.6	113.18	102.9	113.1	113.73

Lines with the same letter do not differ significantly according to the Tukey's test (P=0.05).

During ripeness of the fruit, the total phenols content and antioxidant activity FRAP of the peppers was higher in geothermal greenhouse as compared to the conventional greenhouse in all the growing seasons (Figure 2).
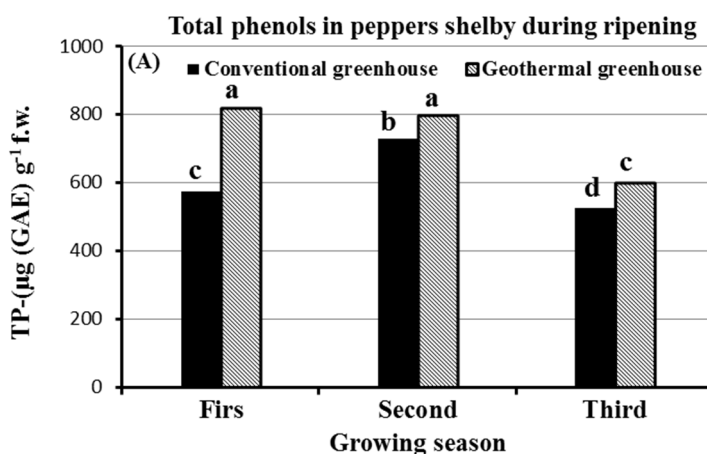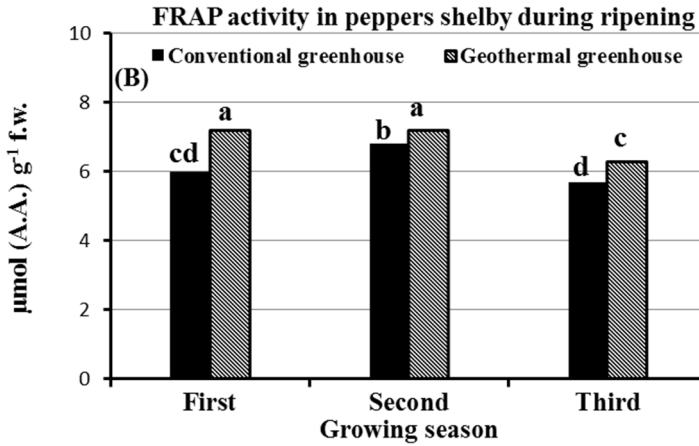
Figure 2. Total phenolic content (A) and antioxidant activity FRAP (B) of peppers at the stage ripening in geothermal and conventional greenhouse. Columns in each graph with the same letter do not differ significantly according to the Tukey's test (P=0.05).

Studies have shown that the total content of phenols and antioxidant activity in hydroponic peppers and tomatoes depends on the differently extracts, maturity stage and cultivars [20-22].

CONCLUSIONS

Total phenols content of hydroponic tomatoes at the ripening stage, was higher in geothermal greenhouse as compared to the conventional greenhouse at the wintry growing season. Total phenols content and antioxidant activity FRAP of hydroponic peppers at the ripening stage, was higher in geothermal greenhouse as compared to the conventional greenhouse in all the growing seasons.

Mean weight of tomatoes fruit during the harvest was greater in geothermal greenhouse as compared to the conventional greenhouse, by (11.5, 5.5, and 7)% respectively, for the three growing seasons, well as the yield of the production was higher in the geothermal greenhouse as compared to the conventional greenhouse. Mean weight of peppers fruit during the harvest, well as the yield of the production showed no statistically significant differences regarding the geothermal greenhouse or the conventional greenhouse in all the growing seasons.

The geothermal greenhouse as compared at the conventional greenhouse, showed higher production on tomato crop, while about of the pepper crop showed greater total phenols content and greater antioxidant activity, for the three growing seasons.

EXPERIMENTAL SECTION

Greenhouse facilities

The experiment was conducted in two greenhouses of Technological Educational Institute of Thessaly. The greenhouse (A), closed type to the system water recycling, that based on shallow geothermal energy and the greenhouse (B), conventional. For the geothermal greenhouse, the energy requirements covered by ground heat exchangers, that constructed adjacent to from the glasshouse at a depth of 100 meters, while the air dehumidifying system it includes the air collection duct, heat exchangers for the cooling of air and plastic tank to collect water for the irrigation. Also in the geothermal greenhouse are located tubes for collection of the nutrient solution during outflow from the greenhouse. The remaining ventilation systems in both greenhouses are identical, as well as dimensions and cover materials. Also, for the air conditioning of both greenhouses, there is system with both heat pumps.

Nutrient solution

The overall flow of the nutrient solution in the greenhouses is controlled by modern automation. The crops was fertilized through a stable chemical nutritive solution at the rates of 58.9 ml/min for 3 minutes, repetitively 4 times a day. The nutritive solution consisted of Ca^{2+} = 169 meq/L, K^+ = 253.4 meq/L, Mg^{2+} = 64.8 meq/L, NH_4^+ = 18.3 meq/L, H^+ = 112 meq/L, Fe^{2+} = 0.6 meq/L, NO_3^- = 281.3 meq/L, PO_4^{3-} = 143.3 meq/L and SO_4^{2-} = 193.5 meq/L, while its pH was about 6 and electrical conductivity EC about 2dS m^{-1}.

Cultivation

In an area of 200 m^2 for each greenhouse, was cultivated hydroponic tomatoes Merilia (100m^2) and peppers Shelby (100m^2) for three consecutive seasons. The substrate it was from stone wool slabs in double rows, with a distance of plants for each slab 30 cm, namely three plants. The duration of the first growing season was from 21- 10-2014 to 21-01-2015, the second growing season from 05-03-2015 to 17- 06-2015, and the third growing season had duration from 04-02-2016 to 28-06- 2016. Eight plants from each greenhouse were selected for measurements. The four of those were always the same, while the other four were selected randomly. The width and the height of plants, the number of leaves and inflorescences were measured once per week.

Preparation of the methanol extracts

The fruits harvested in the ripeness (Figure 4). Ten g of the fruit samples were two rounds treated by 20 ml of 80% aqueous methanol. Samples were incubated for 24 h in the extractant at stirring; the supernatant material was

removed. The pellet was re-treated with aqueous methanol for 2 h at stirring at ambient temperature. The extract was gathered after centrifugation/filtration and the volume was made up to 50 ml with aqueous methanol and used for further chemical analysis [23].

Determination of total polyphenolics (TP)

Total polyphenolic content was determined with the Folin-Ciocalteu (F-C) reagent according to the method of [24] using the microvariant proposed by [25] and the results were expressed as gallic acid equivalent (GAE) in µg/g fresh weight.

Determination of ferric reducing antioxidant power (FRAP)

The antioxidant activity of the methanol extracts was determined on the basis of the method of [26] and was expressed as ascorbic acid equivalent (AA) in µM /g fresh weight.

Determination of total acidity, pH and Brix degrees

The pH, the Brix degrees and the total acidity were measured in fruit juice. The Brix degrees by a Zeiss refractometer while the total acidity by titration with 0.1N NaOH solution and expressed in g of citric acid / l00 ml juice.

Statistical analysis

Data were analyzed using the MINITAB [27] statistical package. The experiment had eight replications. Analysis of variance was used to assess treatment effects. Mean separation was made using Tukey's test when significant differences (P=0.05) between treatments were found.

ACKNOWLEDGMENTS

REFERENCES

1. A.K. Azad, K. Ishikawa, J.C. Diaz-Perez, T.E.J. Eaton, N. Takeda, *Agricultural Sciences*, **2013**, *4(07),* 1.
2. F. Buwalda, E.A., Van Os, G. Giacomelli, G. Samperio Ruiz, T. Vermeulen, P.A. van Weel, M.N.A. Ruijs, *In International Symposium on Growing Media and Soilless Cultivation*, **2013**, *1034*, 201-207.

3. N. Gougoulias, L. Giurgiulescu, D. Kalfountzos, A. Papachatzis, I. Vagelas, D. Ftakas, D. Pateras, A. Chouliara, *Studia UBB Chemia,* **2015**, LX, 2, Tom 1, 177-185.
4. W.M. Bissonnette, R.E. Wainwright, C. Payne, J. Thompson, R. Bromley, C. Morgan, "Systems and methods for controlling liquid delivery and distribution U.S. Patent No. 8, 261, 486. Washington, DC: U.S. Patent and Trademark Office, **2012**.
5. D.S. Domingues, H.W. Takahashi, C.A. Camara, S.L. Nixdorf, *Computers and Electronics in Agriculture,* **2012**, *84*, 53-61.
6. H. Inden, A. Torres, *Acta Horticulturae (ISHS),* **2004**. *644*, 205-210.
7. M. I. Alhamid, Y. Daud, A. Surachman, A. Sugiyono, H. B. Aditya, T. M. I. Mahlia, *Renewable and Sustainable Energy Reviews,* **2016**, *53*, 733-740.
8. K.K. Bloomfield, J.N. Moore, R.N. Neilson, *Geothermal Resources Council Bulletin,* **2003**, *32(2),* 77-79.
9. J. W. Lund,T. L. Boyd, *Geothermics,* **2016**, *60*, 66-93.
10. K. Popovski, Geothermally-Heated Greenhouses in the World, Proceedings of the Workshop: Heating Greenhouses with Geothermal Energy, International Summer School, Azores, **1998**, 425-430.
11. S. Hähnlein, P. Bayer, G. Ferguson, P. Blum, *Energy Policy,* 2013, *59*, 914-925.
12. T. Bahorun, A. Luximon-Ramma, A. Crozier, O.I. Aruoma, *Journal of the Science of Food and Agriculture*, **2004**, *84(12),* 1553-1561.
13. J. de Jesús Ornelas-Paz, J. M. Martínez-Burrola, S. Ruiz-Cruz, V. Santana-Rodríguez, V. Ibarra-Junquera, G.I. Olivas, J.D. Pérez-Martínez, *Food Chemistry*, **2010**, *119(4)*, 1619-1625.
14. C.G. Fraga, (Ed.). Plant phenolics and human health: biochemistry, nutrition and pharmacology **2009** (vol. 1), John Wiley & Sons.
15. N. Gougoulias, A. Papachatzis, H. Kalorizou, I. Vagelas, L. Giurgiulescu, N. Chouliaras, *Carpathian Journal of Food Science and Technology*, **2012**, *4(2)*, 46-51.
16. V.R. Preedy, R.R. Watson, Tomatoes and tomato products. Nutritional, medicinal and therapeutic properties. Published by Science Publishers, Enfield, NH, USA, **2008**.
17. J.J. Benton, Tomato plant culture: In the field, greenhouse and home Garden 2nd Edition CRC press Taylor and Francis Group, **2008.**
18. M.M. Hussein, S. Y. El-Faham, A. K. Alva, *Agricultural Sciences,* **2012**, *3(2)*, 241.
19. F. Nunez-Ramirez, D.A.N.I.E.L. González-Mendoza, O.N.É.S.I.M.O. Grimaldo-Juárez, L.C. Díaz, *International Journal of Agriculture and Biology,* **2011**, *13(5)*, 827-830.
20. M. Anza, P. Riga, C. Garbisu, *Journal of food quality*, **2006**, 29(1), 16-37.
21. M. Ghasemnezhad, M. Sherafati, G. A. Payvast, *Journal of functional foods*, **2011**, *3(1)*, 44-49.
22. R. K. Toor, G. P. Savage, C. E. Lister, *Journal of Food Composition and Analysis*, **2006**, *19(1)*, 1-10.
23. J. Kanner, E. Frankel, R. Granit, B. German, J.E. Kinsella, *Journal of Agricultural and Food Chemistry*, **1994**, *42(1)*, .64-69.
24. V.L. Singleton, J.A. Rossi, *American journal of Enology and Viticulture,* **1965**, *16(3)*, 144-158.
25. B. Baderschneider, D. Luthria, A. L. Waterhouse, P. Winterhalter, *VITIS-Journal of Grapevine Research*, **2015**,*38(3)*, 127-131.
26. I.F. Benzie, J.J. Strain, *Methods in enzymology*, **1999**, *299*, 15-27.
27. B.F. Ryan, B.L. Joiner, J.D. Cryer, MINITAB Handbook: Updated for release 14, 5th edition, **2005**.